

# **PERFORMANCE-BASED FIRE DESIGN OF COLD-FORMED STEEL STRUCTURES MADE OF NEW HIGH-STRENGTH STEELS**

by

Xia Yan

A dissertation submitted to Johns Hopkins University in conformity with the requirements for  
the degree of Doctor of Philosophy

Baltimore, Maryland

June 2022

© 2022 Xia Yan

All rights reserved

## **Abstract**

The development of new structural materials is a key enabler of innovation in the building construction sector, but their adoption requires the ability to assess the safety of the design under various loading cases, including fire. The performance-based fire design approach provides a rigorous framework to assess the structural fire safety of structures, provided the appropriate data and methods are available to evaluate the response of the structures under fire conditions.

This thesis describes a study on the behavior, modeling strategy, and design method of cold-formed steel (CFS) structures made of a new class of materials. The study is based on material testing, advanced fire modeling, and numerical and analytical methods, for enabling the assessment of the structural response in fire.

First, experimental studies are carried out on the elevated temperature and post-fire material properties of high-strength dual-phase and martensitic steels. Tests performed under steady-state, transient, and residual heating conditions show proportionally larger reductions in strength at elevated temperature and after cooling down for the investigated high-strength steels than for conventional cold-formed steels. New models are proposed for the temperature-dependent properties of the materials for implementation in design methods and finite element codes.

Second, various computational modeling strategies are evaluated to assess temperatures in structural members exposed to fires. Based on modeling of experimental tests measuring the temperatures in steel members exposed to localized fires, a modeling decision flowchart is proposed for supporting the computational fire-thermal modeling in performance-based fire design analyses. An application to open car parks illustrates the range of applicability of different models for capturing the effects of localized fires on steel frames.

Third, numerical analyses are used to investigate the stability under fire of CFS members made of the dual-phase and martensitic steels. A parametric study using validated finite element models allows evaluating the local buckling strength of hollow section columns at ambient and elevated temperatures. A modification to the current analytical Direct Strength Method (DSM) is introduced for estimating the local buckling capacity of hollow section columns at elevated temperatures, valid for the different steel grades at ambient and elevated temperatures up to 700 °C.

Finally, the developed material data and modeling methods are applied to conduct the performance-based structural fire design of cold-formed steel assemblies from a prototype metal building. The results show that this fire design approach enables explicitly verifying achievement of the performance objectives while allowing enhanced flexibility and efficiency in design.

Overall, this thesis proposes a roadmap to address structural fire safety when adopting new materials for enabling more efficient, sustainable, and resilient designs.

Advisor: Dr. Thomas Gernay

Readers: Dr. Benjamin W. Schafer

Dr. Nicola Tondini

## **Acknowledgments**

The author would like to thank the people who made this research possible for the past four years at the Johns Hopkins University.

First of all, I would like to express my greatest gratitude to my advisor Prof. Thomas Gernay. His guidance, patience, encouragement, and enthusiasm towards scientific study inspired and stimulated me to move forward. No matter what difficulties we were faced with, he was always calm and optimistic, and provided insightful idea to solve the problems. He is not just a mentor in research, but also a friend in life.

I would like to thank Prof. Benjamin W. Schafer and Prof. Nicola Tondini for serving on my thesis committee and for their review and suggestions on this work. I also would like to thank Prof. Jaafar El-Awady for chairing my GBO committee and thank Prof. James Guest as my GBO committee member. Their kind help is greatly appreciated.

I would like to acknowledge the financial support provided by Hopkins Extreme Materials Institute, American Iron and Steel Institute, Metal Building Manufactures Association, Steel Deck Institute, and ArcelorMittal.

Besides, I would like to thank the Department of Civil and Systems Engineering at Johns Hopkins University for providing such a pleasant environment for this study. Special thanks to the Senior Academic Program Coordinator Elena Shichkova, Administrative Coordinator Carla Diaz, and Administrative Manager Deborah Lantry. I want to thank Senior Technician Nickolay Logvinovsky, Dr. Shahab Torabian, Prof. Michael Shields, and Aakash Bangalore Satish for their assistance with the lab testing. I also want to thank my coauthors for their support in our work.

Last but not least, I would like to thank my parents for their unconditional love and support through this journey. Mom and Dad, thank for always being there whenever difficulties I was faced with.

I want to thank my friends Shiyong Tan, Weixin Zhang, Qi Tong, Chenzhi Ma, James, Wanqu Liu, Chu Ding, Shuna Ni, Zhidong Zhang, Qi Huang, and Yi Li for making my life so colorful. I also want to thank my cat Bella for keeping me company during the COVID 19 pandemic.

## Preface

This dissertation is submitted to the Johns Hopkins University for the degree of Doctor of Philosophy. Several supporting papers which are based on the work presented in the dissertation have been published in conjunction with Assistant Professor Thomas Gernay and other coauthors as listed:

1. Yan, X., Xia, Y., Blum, H. B., & Gernay, T. (2020). *Elevated temperature material properties of advanced high strength steel alloys*. Journal of Constructional Steel Research, 174, 106299.
2. Yan, X., Xia, Y., Blum, H.B., Gernay, T. (2020). *Experimental study on the high temperature properties of advanced high-strength cold-formed steels*. Proceedings of the Cold-Formed Steel Research Consortium Colloquium (cfsrc.org), Oct 20-22.
3. Yan, X., Batista Abreu, J.C., Glauz, R.S., Schafer, B.W., Gernay, T. (2020). *Cold-formed steel properties at elevated temperature: Review and proposed equation*. Proceedings of the Cold-Formed Steel Research Consortium Colloquium (cfsrc.org), Oct 20-22.
4. Yan, X., Xia, Y., Blum, H.B., Gernay, T. (2020). *Experimental investigation of the behavior of martensitic high-strength steels at elevated temperature*. Structures in Fire (Proc. of the 11th Int. Conf.) (pp. 791-821). The University of Queensland, Australia, Nov 30-Dec 2.
5. Yan, X., Xia, Y., Blum, HB., Gernay, T. (2021). *Post-fire mechanical properties of advanced high-strength cold-formed steel alloys*. Thin-Walled Structures, 159, 107293.
6. Yan, X., Batista Abreu, JC., Glauz, B., Schafer, BW., Gernay, T. (2021). *Simple three-coefficient equation for temperature dependent mechanical properties of cold-formed steels*. Journal of Structural Engineering ASCE, 147(4): 04021035.

7. Yan, X., Gernay, T. (2021). *Numerical modeling of localized fire exposures on structures using FDS-FEM and simple models*. Engineering Structures, 246, 112997.
8. Yan, X., Gernay, T. (2021). *A comparative analysis and experimental validation of modeling strategies for structures subject to localized fires*. 12th Asia-Oceania Symposium on Fire Science and Technology (AOSFST 2021). The University of Queensland, Australia, Dec 7-9.
9. Ni, S., Yan, X., Hoehler, M., Gernay, T. (2022). *Numerical modeling of the post-fire performance of strap-braced cold-formed steel shear walls*. Thin-Walled Structures, 171, 108733.
10. Xia, Y., Yan, X., Gernay, T., Blum, HB. (2022). *Elevated temperature and post-fire stress-strain modeling of advanced high-strength cold-formed steel alloys*. Journal of Constructional Steel Research, 190, 107116.
11. Yan, X., Gernay, T. (2022). *Structural fire design of load-bearing cold-formed steel assemblies from a prototype metal building*. (Under review)
12. Yan, X., Gernay, T. (2022). *Local buckling of cold-formed high-strength steel hollow section columns at elevated temperatures*. (Under review)
13. Yan, X., Charlier, M., Gernay, T. (2022). *Thermal response of steel framing members in open car park fires*. (Under review)

## Table of contents

Abstract.....	ii
Acknowledgments.....	iv
Preface.....	vi
List of tables.....	xv
List of figures.....	xix
Chapter 1 Introduction.....	1
1.1 Background and motivation.....	1
1.2 Research scope and objectives.....	5
Chapter 2 Mechanical properties of cold-formed steel at elevated temperatures: review and proposed relationship.....	9
2.1 Introduction.....	9
2.2 Literature review.....	10
2.2.1 Materials and Testing Methods.....	10
2.2.2 Tests by Yan et al.....	12
2.2.3 Tests by Batista Abreu.....	14
2.2.4 Review of published data for cold-formed steels.....	16
2.3 Data.....	17
2.4 Relationships for Retention Factors.....	22
2.4.1 Standardized retention factor equation.....	22
2.4.2 Retention factors for CFS mechanical properties.....	23
2.5 Comparison with codes.....	27
2.6 Conclusions.....	30



Chapter 3	Mechanical properties of advanced high-strength steels (AHSS) at elevated temperature .....	32
3.1	Introduction .....	32
3.2	Literature review .....	34
3.3	Experimental protocol and materials.....	35
3.3.1	Test apparatus .....	35
3.3.2	Test specimens .....	36
3.3.3	Test procedure.....	38
3.3.4	Definition of material properties.....	39
3.4	Steady-state test results .....	41
3.4.1	Failure modes.....	41
3.4.2	Test results .....	42
3.5	Transient-state test results .....	46
3.5.1	Failure modes.....	46
3.5.2	Thermal strain .....	47
3.5.3	Test results .....	47
3.6	Comparison and discussion.....	51
3.6.1	Elastic modulus.....	51
3.6.2	Yield stress.....	54
3.6.3	Ultimate stress.....	57
3.6.4	Elongation at fracture.....	58
3.7	Predictive models .....	59
3.8	Conclusions .....	62

Chapter 4	Mechanical properties of advanced high-strength steels (AHSS) after cooling down	65
4.1	Introduction	65
4.2	Literature review	66
4.2.1	Published residual properties for hot-rolled steels	66
4.2.2	Published residual properties for cold-formed steels	68
4.3	Post-fire testing of AHSS: materials and method	70
4.3.1	Specimens	70
4.3.2	Test procedure	71
4.3.3	Definition of material properties	73
4.4	Post-fire testing of AHSS: data	75
4.4.1	Failure mode	75
4.4.2	Test results	76
4.5	Comparison and discussion	79
4.5.1	Elastic modulus	79
4.5.2	Yield stress	81
4.5.3	Ultimate stress	83
4.5.4	Elongation at fracture	85
4.5.5	Influence of cold working and steel grade	86
4.6	Predictive equations for post-fire mechanical properties of AHSS	87
4.6.1	Elastic modulus	87
4.6.2	0.2% proof stress and ultimate stress	88
4.7	Conclusions	91

Chapter 5	Numerical modeling of localized fire exposure on structures: comparative study and application to open car park fires.....	93
5.1	Introduction .....	93
5.2	Literature review .....	94
5.2.1	Simple localized models .....	94
5.2.2	CFD models .....	99
5.3	Proposed modeling strategy for structures subjected to localized fire.....	102
5.4	Case study: Steel beam under localized fire.....	106
5.4.1	Description of the experiment.....	106
5.4.2	FDS-FEM model.....	107
5.4.3	Heskestad/LOCAFI model.....	113
5.5	Case study: Steel column next to a localized fire.....	114
5.5.1	Description of the experiment.....	114
5.5.2	FDS-FEM model.....	114
5.5.3	LOCAFI model .....	118
5.5.4	Analysis of the effect of spatial interpolation in the FDS-FEM interface model .	118
5.6	Case study: Steel beam under ceiling subjected to localized fire .....	123
5.6.1	Description of the experiment.....	123
5.6.2	FDS-FEM model.....	123
5.6.3	Hasemi model .....	124
5.6.4	Maximum heat flux between Hasemi model and Heskestad model .....	125
5.7	Application: Open car park fires .....	127
5.7.1	Car park.....	127

5.7.2	Fire scenarios .....	128
5.7.3	Methods for fire-thermal modeling.....	130
5.7.4	Fire analysis .....	132
5.7.5	Thermal analysis.....	135
5.7.6	Results.....	136
5.7.7	Discussion.....	145
5.8	Conclusions .....	152
Chapter 6 Numerical study of local buckling behavior of cold-formed high-strength steel hollow section columns at elevated temperatures..... 156		
6.1	Introduction .....	156
6.2	Literature review .....	157
6.3	Finite element model.....	158
6.3.1	Method and experimental data for benchmarking .....	158
6.3.2	Description of the finite element model.....	159
6.3.3	Validation of the finite element model against experimental data .....	163
6.4	Parametric study.....	167
6.4.1	Approach for the parametric study .....	167
6.4.2	Material properties .....	167
6.4.3	Finite element models.....	169
6.4.4	Ultimate capacities of cold-formed SHS and RHS columns at elevated temperatures .....	171
6.5	Comparison between FE analysis and Direct Strength Method.....	175
6.5.1	At ambient temperature.....	175

6.5.2	At elevated temperatures.....	178
6.6	Modified Direct Strength Method for SHS and RHS columns.....	184
6.7	Conclusions .....	186
Chapter 7	Structural design of cold-formed steel C-shaped column assemblies under fire conditions .....	189
7.1	Introduction .....	189
7.2	Literature review .....	190
7.3	Scope and fire design objectives .....	191
7.3.1	Prototype building.....	191
7.3.2	End wall columns.....	192
7.3.3	Fire protection assemblies.....	194
7.3.4	Performance objectives .....	195
7.3.5	Design loads.....	196
7.4	Design-basis fires .....	197
7.5	Thermal response of cold-formed steel columns .....	200
7.5.1	Thermal properties .....	200
7.5.2	Finite element model.....	202
7.5.3	Thermal analysis of the column assemblies.....	202
7.6	Structural response of cold-formed steel columns .....	206
7.6.1	Analysis by Direct Strength Method/AISI S100 .....	207
7.6.2	Analysis by finite element modeling .....	211
7.7	Verification of the fire performance of the metal steel building end walls.....	215
7.8	Conclusions .....	216

Chapter 8	Conclusions and future work .....	220
8.1	Summary .....	220
8.2	Conclusions and future work .....	223
References	.....	226

## List of tables

Table 1. Retention factors for the mechanical properties of CFS-395 and CFS-340. ....	13
Table 2. Retention factors for the mechanical properties of tested ASTM A653 steels.....	15
Table 3. Test data for conventional grade steels.....	17
Table 4. Test data for G550. ....	17
Table 5. Coefficients to determine retention factors for elastic modulus of cold-formed steel....	25
Table 6. Coefficients to determine retention factors for 0.2% proof stress of cold-formed steel.	25
Table 7. Coefficients to determine retention factors for 2% stress of cold-formed steel. ....	26
Table 8 Coefficients to determine retention factors for ultimate stress of cold-formed steel.....	27
Table 9. Coefficients to determine retention factors for mechanical properties of cold-formed steel. .....	28
Table 10. Steel grade and nominal thickness of steel specimen. ....	37
Table 11. Chemical components of materials. ....	37
Table 12. Mechanical properties obtained from ambient temperature tension testing. ....	44
Table 13. Retention factors of elastic modulus, yield stress, and ultimate stress, and elongation at fracture for Mild-395 from steady-state tests.....	44
Table 14. Retention factors of elastic modulus, yield stress, and ultimate stress, and elongation at fracture for HSLA-700 from steady-state tests. ....	44
Table 15. Retention factors of elastic modulus, yield stress, and ultimate stress, and elongation at fracture for DP-340 from steady-state tests. ....	45
Table 16. Retention factors of elastic modulus, yield stress, and ultimate stress, and elongation at fracture for DP-700 from steady-state tests. ....	45

Table 17. Retention factors of elastic modulus, yield stress, and ultimate stress, and elongation at fracture for MS-1030 from steady-state tests.....	45
Table 18. Retention factors of elastic modulus, yield stress, and ultimate stress, and elongation at fracture for MS-1200 from steady-state tests.....	46
Table 19. Failure temperatures at various stress level for transient-state tests.....	49
Table 20. Retention factors of elastic modulus and yield stress for DP-700 from transient-state tests. ....	51
Table 21 Retention factors of elastic modulus and yield stress for MS-1200 from transient-state tests. ....	51
Table 22. Coefficients to determine the retention factors for the mechanical properties of cold-formed AHSS steels.....	60
Table 23. Residual test information of hot-rolled steels.....	68
Table 24. Residual test information of cold-formed steels.....	70
Table 25. Steel grade with nominal properties and thickness of specimens.....	70
Table 26. Mechanical properties obtained from ambient temperature tension testing.....	77
Table 27. DP-340 post-fire retention factors of elastic modulus and yield stress, and elongation at fracture.....	78
Table 28. DP-700 post-fire retention factors of elastic modulus and yield stress, and elongation at fracture.....	79
Table 29. MS-1030 post-fire retention factors of elastic modulus and yield stress, and elongation at fracture.....	79
Table 30. MS-1200 post-fire retention factors of elastic modulus and yield stress, and elongation at fracture.....	79



Table 31. Proposed coefficients for residual properties of AHSS. ....	89
Table 32 Peak and average temperatures of galvanized and ungalvanized profiles under localized fire scenarios (obtained from FDS-FEM AST method). ....	148
Table 33 Dimensions of the column used for validation of the model. ....	159
Table 34 Material properties of G450 generated from the test at ambient and elevated temperatures [120]. ....	161
Table 35 Ultimate capacities of 90x90x2 column with and without residual stress. ....	163
Table 36. Failure modes for 90x90x2 column. ....	166
Table 37. Comparison of ultimate capacities. ....	167
Table 38 Coefficients for the predictive model of retention factors. ....	168
Table 39 Cold-formed steel SHS and RHS columns in the parametric study. ....	170
Table 40 Material properties at ambient temperature. ....	171
Table 41 Averaged ratios of FEM to DSM evaluations of capacity at ambient and elevated temperatures. A ratio lower than 1.00 indicates that the FEM predicts a lower capacity than the DSM. ....	177
Table 42 Section dimensions and unbraced length of the end wall columns. ....	194
Table 43 Fire protection assemblies of the cold-formed steel columns. ....	195
Table 44 Applied design forces for LRFD in the end wall columns under the load combination applicable in the fire situation. ....	197
Table 45 Steel temperature in the end wall columns at 60 minutes under ASTM E119 fire. ....	204
Table 46 Temperature in the end wall columns at 60 minutes under OZone fires. Note: the different considered fuel loads do not affect the temperatures at 60 min. ....	205

Table 47 Average steel temperatures (°C) at 60 minutes under ASTM E119 fire in the columns of the end wall line 7 using different fire protection assemblies. ....	206
Table 48 Capacity of the columns at ambient temperature as evaluated by DSM. ....	208
Table 49 Coefficients for retention factors of steel mechanical properties. ....	209
Table 50 Capacity of the columns at 60 minutes subjected to ASTM E119 by DSM. ....	210
Table 51 Failure temperature and failure time by DSM for ASTM E119 fire. ....	211
Table 52 Capacity of the columns at ambient temperature by FE analysis and DSM.....	213
Table 53 Failure temperature and failure time by FEM analysis for ASTM E119 fire.....	214

## List of figures

Figure 1. Specimen for pin-loaded tensile testing of metallic materials at elevated temperatures, as per ASTM E21 [17]. Dimensions are in mm.....	11
Figure 2. Test setup in the Structures Lab at Johns Hopkins University [18]. .....	13
Figure 3. Stress-strain curves of tested steels by Yan et al. [18]. .....	13
Figure 4. Test setup used by Batista Abreu [19].....	15
Figure 5. Stress-strain curves of tested steels by Batista Abreu [19].....	15
Figure 6. Retention factors of elastic modulus of conventional grade steels and G550 at elevated temperature. ....	19
Figure 7. Retention factors of 0.2% proof stress of conventional grade steels and G550 at elevated temperature. ....	20
Figure 8. Retention factors of 2.0% stress of conventional grade steels and G550 at elevated temperature. ....	21
Figure 9. Retention factors of ultimate stress of conventional grade steels and G550 at elevated temperature. ....	22
Figure 10. Proposed retention factors for elastic modulus at elevated temperature. ....	25
Figure 11. Proposed retention factors for 0.2% proof stress at elevated temperature. ....	26
Figure 12. Proposed retention factors for 2.0% stress at elevated temperature.....	26
Figure 13. Proposed retention factors for ultimate stress at elevated temperature. ....	27
Figure 14. Comparison of proposed retention factors for elastic modulus with design codes. ....	29
Figure 15. Comparison of proposed retention factors for 0.2% proof stress with design codes. .	29
Figure 16. Comparison of proposed retention factors for 2.0% stress with design codes.....	30
Figure 17. Comparison of proposed retention factors for ultimate stress with design codes. ....	30

Figure 18. Definition of symbols used for the material properties. ....	40
Figure 19. Failure modes of specimens in steady-state tests. ....	42
Figure 20. Stress-strain curves obtained from steady-state tests. ....	43
Figure 21. Failure modes of specimens in transient-state tests.....	46
Figure 22. Comparison of measured thermal strain with EC3 [35] and test data in literature. ....	47
Figure 23. Comparison of stress-strain curves obtained from steady-state and transient-state tests (transient-state test results are marked with ‘T’ in the legend).....	50
Figure 24. Comparison of elastic modulus (transient-state test results are marked with ‘T’ in the legend).....	54
Figure 25. Comparison of 2.0% yield stress (transient-state test results are marked with ‘T’ in the legend).....	56
Figure 26. Comparison of 0.2% proof stress (transient-state test results are marked with ‘T’ in the legend).....	57
Figure 27. Comparison of ultimate stress obtained from steady-state tests.....	58
Figure 28. Elongation at fracture $\epsilon_f$ obtained from steady-state tests. Note 40% is the maximum measurable strain in the test setup, which was exceeded at 600°C and 700°C. ....	59
Figure 29 Comparison of proposed retention factors with test data. ....	62
Figure 30. Measured temperature curves of the heating process.....	72
Figure 31. Definition of symbols used for the material properties. ....	74
Figure 32. Failure modes of the specimen from residual tests. (White paint was used for improving contrast for the DIC) .....	76
Figure 33. Stress-strain curve obtained from post-fire residual tests.....	78
Figure 34. Retention factors for residual elastic modulus of cold-formed steels. ....	81

Figure 35. Retention factors for residual 0.2% proof stress of cold-formed steels. ....	83
Figure 36. Retention factors for residual stress at 2.0% strain of cold-formed steels. ....	83
Figure 37. Retention factors of residual ultimate stress for cold-formed steels. ....	85
Figure 38. Elongation at fracture $\epsilon_f$ obtained from residual tests.....	86
Figure 39. Residual retention factor of 0.2% proof stress and ultimate stress for hot-rolled and cold-formed steels.....	87
Figure 40. Proposed model for post-fire elastic modulus of AHSS. ....	88
Figure 41. Proposed model for post-fire 0.2% proof stress of AHSS.....	90
Figure 42. Proposed model for post-fire ultimate stress of AHSS. ....	90
Figure 43. Virtual solid flame models [81].....	97
Figure 44. Modeling strategy for analyzing a structural member subjected to a localized fire..	103
Figure 45. Relative position of fire area and structural member. ....	104
Figure 46. Experimental setup for the steel beam fire test [77].....	107
Figure 47. FDS numerical model of the steel beam fire test. ....	109
Figure 48. Effect of mesh size on the time-averaged adiabatic surface temperatures in the beam. ....	109
Figure 49. Location of adiabatic surface temperature sensors and time-averaged AST's from FDS. ....	110
Figure 50. Test data and computed steel temperatures in the lower flange of the mid-span section. ....	112
Figure 51. Test data and computed steel temperatures at mid web of the mid-span section.....	112
Figure 52. Test data and computed steel temperatures in the upper flange of the mid-span section. ....	112

Figure 53. Experimental setup (unit: m) [95]. .....	114
Figure 54. FDS model of steel column test.....	115
Figure 55. Location of adiabatic surface temperature sensors and time-averaged AST from FDS. .....	116
Figure 56. Test data and computed steel temperature on the front surface in the cross section at 0.4 m height. ....	117
Figure 57. Test data and computed steel temperature on the side surface of the cross section at 0.6 m height. ....	117
Figure 58. Test data and computed steel temperature on the back surface of the cross section at 0.6 m height. ....	118
Figure 59. Interpolation in the domain to transfer information from the fire to the thermal model, based on the location of cell nodes in FDS (blue dots) and structural nodes in SAFIR (S-1)....	119
Figure 60. Gas temperature and incident heat flux output from FDS cell nodes.....	120
Figure 61. FDS models of case study with structure modeled in FDS. ....	121
Figure 62. Computed steel temperatures in the cross section at 0.4 m height, Case 1. ....	122
Figure 63. Computed steel temperatures in the cross section at 3 m height, Case 2. ....	122
Figure 64. Experimental setup and FDS model of Hasemi test [89]. ....	123
Figure 65. Comparison of the steel surface temperatures at lower flange of the center section. ....	126
Figure 66. Comparison of the steel surface temperatures at mid web of the center section.....	126
Figure 67. Comparison of the steel surface temperatures at upper flange of the center section. ....	126
Figure 68 Dimensions of the steel profiles (unit: mm). ....	128
Figure 69 Fire scenarios considered for the modeling of the thermal exposure on steel beams and columns (burning cars are shown in orange, structure of interest is shown in red).....	130

Figure 70 Application domain of localized fire modeling approaches for car park fires (not to scale) (adapted from [114]).	132
Figure 71 FDS modeling domains for the open car park fire analyses.	135
Figure 72 Finite element thermal analysis.	136
Figure 73. Temperature evolution in the web and lower flange of HE600A and IPE450 in fire scenario 1 (results obtained from FDS-FEM AST method is used as benchmark).	140
Figure 74. Temperature evolution in the web and lower flange of HE600A and IPE450 in fire scenario 2 (results obtained from FDS-FEM AST method is used as benchmark).	141
Figure 75 Fire scenario and location of maximum temperature tested by CTICM [116].	142
Figure 76 Temperature in the HE240M in fire scenario 3 (results obtained from FDS-FEM AST method is used as benchmark).	145
Figure 77 Temperatures distribution on the cross section.	146
Figure 78 Average temperatures reached in HE600A and IPE450.	148
Figure 79 The FDS simulation of the localized fire scenario 1 shows that the flame does not touch the ceiling for most of the fire duration.	150
Figure 80 Cross section of SHS and RHS.	159
Figure 81 Boundary conditions for the fixed-fixed SHS column under controlled axial displacement.	160
Figure 82 Idealized residual stress model proposed for hollow sections [120].	163
Figure 83 Axial force-displacement curves for the 90x90x2 SHS column loaded to failure at different temperatures (experimental measurements and numerical results from Abaqus are reported by Balarupan [120]).	165

Figure 84 Retention factors for cold-formed steels of different grades, from Chapter 2 and Chapter 3.....	169
Figure 85 Normalized reduction of ultimate capacity with temperature for the SHS and RHS columns.....	173
Figure 86 Ultimate capacity in local buckling at elevated temperature for the 90x90x2 section column with steel grades G450, DP-700, MS-1200. ....	173
Figure 87 The normalized reduction with temperature of section capacity in local buckling lies in between the retention factors for yield strength and elastic modulus. ....	174
Figure 88. At ambient temperature, the DSM predicts higher section capacities than the FE model for the hollow sections, both for conventional and advanced high-strength steels. ....	175
Figure 89. At ambient temperature, the DSM predicts higher capacities than the FE model for hollow sections, especially when the plates width ratio ( $b_1/b_2$ ) is close to 1.....	177
Figure 90. At ambient temperature, the plate width-to-thickness ratio ( $b/t$ ) of the hollow sections does not noticeably influence the ratio between the DSM and FE predictions of the ultimate capacity. ....	178
Figure 91 Section capacities obtained from FEM and DSM at elevated temperature. (Note the vertical scale is adjusted on each plot for readability.).....	181
Figure 92. Variation of the ratio between FE and DSM predictions of the capacity for each of the 46 hollow sections as a function of temperature.....	182
Figure 93 $P_u/P_y$ versus $\lambda l$ at elevated temperatures obtained from DSM.....	183
Figure 94 Comparison of DSM and modified DSM curves and FEM data for the SHS and RHS columns.....	186
Figure 95. Performance-based design procedure.....	191



Figure 96. Prototype warehouse building. ....	192
Figure 97. Floor plan of the warehouse. ....	192
Figure 98. End wall framing line 1. ....	193
Figure 99. C-shaped sections used for the columns of the end walls. ....	194
Figure 100 Fire protection assemblies for the columns. ....	195
Figure 101 Gas temperature – time curves obtained from fire modeling with OZone for a range of fuel loads and two ventilation conditions. ....	200
Figure 102 Thermal properties of Type X gypsum board. ....	201
Figure 103 Finite element model of columns subjected to fire on 4 sides. ....	202
Figure 104 Temperature distribution in the cold-formed steel column assemblies after 60 minutes of exposure to the ASTM E119 fire. ....	203
Figure 105 Global and local eigenmodes obtained from elastic buckling analysis in Abaqus...	212
Figure 106 Failure modes of columns at ambient temperature. ....	213

## **Chapter 1 Introduction**

### **1.1 Background and motivation**

Design and construction of modern structures need to satisfy multiple criteria. While life safety is the most important one, other goals such as economy, serviceability, sustainability, and robustness bring forward new challenges to the engineers. Even though current code-based (prescriptive) building design approach strives to consider different load conditions and environmental actions, it is not sufficient to only meet the minimum design requirements. While engineers believe the structures we design do provide some degree of safety, we cannot give quantitative judgement on how much safety margin the structures have.

Performance-based design method is established based on the application of engineering principles and physics-based modeling to achieve specific performance targets [1]. By setting the end goal as the starting point, performance-based design is usually carried out by the means of advanced simulation, modeling, testing to find the optimal solution to the multiple objectives. The performance objectives are set to describe the damage level or service states sustained for various hazard acting at specific intensities. By practicing the performance-based design, the owners and engineers work together to achieve the expected performance levels that are appropriate and satisfy their needs.

While performance-based design has been practiced in the field of seismic and wind design of structures for decades, its application in the field of fire hazards is still limited. According to the statistics from CTIF-World Fire Statistics Center, economic cost of fire hazards is almost equal to 1% of GDP in developed countries [2]. In the US, the total cost of fire accidents in the US rose from around 200 billion dollars in 1980s to around 350 billion dollars in 2010s [3]. Fire Estimate Summary published by the United States Fire Administration (USFA) reveals that over the 10-

year period of 2010 to 2019, the residential building fires show a 0.3% decrease in fires but a 14% increase in deaths and a 6% increase in dollar loss. At the meantime, nonresidential building fires exhibit a 30% increase in fires, 50% increase in deaths, and 3% increase in dollar loss. For instance, in 2016, a fire started in a mixed-use property rebuilt from a former warehouse caused 35 deaths. In 2019, 354400 residential building fires happened, which contributed to 2830 deaths and 12625 injuries. 110900 nonresidential building fires happened, which contributed to 100 deaths and 1125 injuries. The number of fire-induced loss are alarming and highlights the importance of fire safety design.

Traditional fire protection design relies on the prescriptive code requirements for structural fire protection and does not explicitly evaluate the structural performance under fire conditions. The prescriptive design is based on the standard fire testing on individual assemblies. However, standards fires do not necessarily reflect the actual fire scenarios in terms of heating rate, peak temperature, fire duration, and possible cooling phase. Since the actual structural performance is not assessed, the level of safety and robustness is unknown to the engineers. Besides, optimum solution in terms of life safety, economic impact and environmental damage cannot be obtained.

To conquer the abovementioned challenges, performance-based fire design provides an alternative with the approval of the Authority Having Jurisdiction (AHJ). An applicable performance-based framework can be found in the Appendix E: Performance-Based Design Procedures for Fire Effects on Structures of the loading standard ASCE 7-16 Minimum Design Loads and Associated Criteria for Buildings and Other Structures [4]. This design framework allows the structural fire engineers to explicitly evaluate the structural performance under realistic fire conditions and assess if the design can achieve a broader range of fire safety goals and objectives.

The first step of performance-based structural fire design is to identify the goal and performance objectives. Performance objectives, which depend on the project specificities, must be defined at the outset of a project, with the relevant stakeholders. They must be explicit so their fulfillment can be assessed at the end of the process. The second step consists in selecting (a range of) design fires. These design fires are based on identified fuel loading and building characteristics. Third, once the thermal exposure conditions have been quantified, their effect on the structure needs to be assessed. Assessment of the structure response requires two steps, namely the thermal (heat transfer) analysis to evaluate temperatures inside the members, and the structural analysis to evaluate internal forces and displacements. Herein, these evaluations are conducted through both numerical and analytical analyses. Finally, the predicted response is checked against the required performance.

With the innovation in materials and construction techniques, cold-formed steel (CFS) members are increasingly used in construction due to their advantageous strength-to-weight ratio. Compared with hot-rolled steel members which require heat treatment in their manufacturing, cold-formed steel members are formed either by press bracing or roll forming at room temperature. The cold working during the manufacturing process enhances the strength of the material, which allows designing members with reduced thickness. Cold-formed steel members are used in load-bearing structures for residential, commercial, and office buildings. For example, cold-formed steel shear wall panels are used to resist lateral loading or racking loading caused by wind, earthquake, or transportation during manufacturing. Proper bracing of the panels with boards, cold-formed steel sections or flat straps increases the strength and stiffness of the frame to carry vertical and lateral load.

Owing to recent progress in manufacturing, Advanced High-Strength Steels (AHSS) with nominal yield stress up to 1200 MPa and ultimate stress up to 1500 MPa are available in the market [5,6]. Recent projects have shown the increasing demands for high performance steels; for example, substantial amounts of high-strength low-alloy Q390 and Q460 steels were used in the Daxing International Airport in China and One World Trade Center in the US. Given the advantageous mechanical properties of these new grades of steels, cold-formed steel members fabricated with novel steels could be used in the construction industry to further reduce the section geometry, self-weight, and construction costs [7] and improve the sustainability. While stability considerations govern the design of many cold-formed steel members, there exist members and assemblies in which the use of higher strength steel can provide benefits, such as steel deck systems and bracing members in cold-formed steel shear walls, in addition to gains in post-buckling behavior.

Research on the behavior of cold-formed members notably needs to address the issue of structural fire response due to the nature of steel of which the strength degrades rapidly with increasing temperatures. Test data show that CFS is more susceptible to temperature than hot rolled, as the increased strength caused by cold-forming fades away [8,9]; this effect is even more severe for cold-formed high-strength steels [10]. With the new material and structural system used in the construction, fire safety of the of cold-formed steel structures need to be verified.

With the climate crisis, innovations in the building industry are set to accelerate. One of the main manifestations of these innovations is the development and adoption of new materials, which enable building lighter, faster, and greener structures. To adopt these new materials in their designs, engineers need data and methods to assess the response of the structures under the various loading cases, including fire. Absent these data and methods, conservative assumptions are made, and traditional (prescriptive) design methods are adopted which rely on extrapolation of limited

empirical evidence on traditional materials. This thesis aims to propose a roadmap to characterize the fire response of a new class of materials and the performance-based fire designs of structures made of these new materials. To achieve this goal, the thesis focuses on material testing, advanced fire modeling, and numerical and analytical methods for assessing the structural fire response. The framework that is applied in the thesis can be applied to other new materials as they become available, in order to rationally analyze the structural fire safety of buildings. Emphasis is also put on the derivation of material properties and design methods for building codes and standards, in order to disseminate largely the knowledge and tools to the engineering community and facilitate the large-scale adoption of new materials enabling more efficient, sustainable, and resilient designs.

## **1.2 Research scope and objectives**

This research focuses on the performance-based design of cold-formed steel structures under fire conditions, aiming to provide models to estimate material properties of conventional and advanced high-strength cold-formed steels at elevated temperature and after cooling down, provide strategies to more accurately capture the member temperature distribution under realistic fire conditions, models to predict the structural performance of typical cold-formed members fabricated with novel steels in fire, and demonstrate the application of performance-based design approach in the field of cold-formed steel structures.

In Chapter 2, a simple, consistent, equation format has been proposed to capture the reduction of mechanical properties of cold-formed steel with temperature. To establish relationships for the reduction in elastic modulus, yield stress, and ultimate stress of cold-formed steels at elevated temperatures, data have been collected from the literature as well as from tests conducted by the

authors. The data include steady-state and transient tests performed on a range of material grades from America, Europe, Asia, and Australia. The proposed relationships for the reduction factors are continuous functions of temperature characterized by three coefficients. The same format is used for the modulus and strength properties. The coefficients are calibrated from the collected data using a regression method. The relationships are valid within the 20°C-1000°C temperature range and for material grade up to and including 550 MPa. The retention factors proposed in this chapter, combined with the stress-strain relationships lie the foundation of structural analysis of cold-formed steel members in fire.

In Chapter 3, an experimental study on the mechanical properties of cold-formed AHSS at elevated temperatures are presented. The tested materials include two AHSS, namely a dual-phase steel (DP) and a martensitic steel (MS), in addition to conventional mild steel and high-strength low-alloy steel (HSLA) specimens as benchmarks. Steady-state and transient-state tests are conducted from room temperature to 700°C. Material properties are obtained from the tests including elastic modulus, yield stress (defined at different strain levels), ultimate stress, and elongation at fracture. Predictive models are proposed to determine the mechanical properties of the cold-formed advanced high-strength steels at elevated temperatures.

In Chapter 4, an experimental study on the post-fire mechanical properties of cold-formed AHSS are presented. First, a review of existing data on steel residual properties is conducted. The collected data includes tests on hot-rolled and cold-formed steels with grades varying from 235 MPa to 960 MPa. Second, a new experimental investigation is performed on AHSS. Two dual-phase (DP) steels and two martensitic (MS) steels with nominal yield stress ranging from 340 MPa

to 1200 MPa and thickness of 1.4 mm and 1.0 mm were tested after exposure to temperatures up to 700°C. Post-fire mechanical properties including elastic modulus, yield stress at different strain levels, ultimate stress, and elongation at fracture were obtained. A set of new equations is proposed to capture the post-fire properties of the AHSS.

In Chapter 5, numerical modeling strategies of localized fire exposure to the structures have been proposed. A brief summary of the theories of the most commonly used fire models is conducted. Based on the application field of each model, a numerical modeling strategy is proposed. Then, three experimental tests of structural members subjected to localized fires, collected from the literature, are simulated using the proposed modeling strategy. The predicted member temperatures are compared with the test measurements to benchmark the different available models against test data, explore the limitations and range of validity of the models, and provide recommendations regarding the adequate use of the methods to capture localized fire exposure conditions on structures. The applicability of the proposed modeling strategy has been further verified by the analysis of the temperatures reached in open car park steel framing members under fire. The proposed flowchart can provide guidance for structural fire engineers to apply the models in adequate manner and ensure the safety requirements for structures subjected to localized fires.

In Chapter 6, the proposed material properties of conventional and advanced high-strength cold formed steels from Chapter 2 and 3 are used to numerically study the local buckling behavior of cold-formed hollow section columns at elevated temperatures. Finite element models (FEM) are calibrated based on experimental data to capture the local buckling behavior of cold-formed SHS and RHS columns at ambient and elevated temperatures. A parametric study is then carried out



with the FE models covering a range of width-to-thickness, plate width ratios, cross section dimensions, member thicknesses, and steel grades. The ultimate capacities gathered from the numerical results are used to evaluate the applicability of the Direct Strength Method (DSM) [11] specified in AISI S100 [12]. A modified DSM in the context of cold-formed SHS and RHS columns made of high strength steels has been proposed. Results show that the proposed equation provides accurate estimates for the SHS and RHS section capacities for the different steel grades at ambient and elevated temperatures up to 700 °C.

In Chapter 7, application of analysis-based methods to evaluate the behavior of cold-formed steel column assemblies taken as part of a realistic cold-formed steel building structure in the fire situation is investigated. Analysis-based methods allow explicit evaluation of the anticipated response under fire loading. A performance-based fire design approach can therefore be adopted where the achievement of the desirable performance objectives in the event of a fire is explicitly evaluated. By adopting a prototype metal building structure designed by industry partners and conducting a complete performance-based structural fire design procedure on selected assemblies part of this structure, the research aims to describe a systematic methodology that can be applied to design realistic cold-formed steel structures for fire. Explicit analysis of assemblies not qualified through standard fire resistance testing provides data about their expected fire performance and supports their use as solutions equivalent to current fire rated assemblies. Finally, the application of several methods of analysis also allows drawing conclusions on their applicability and usefulness to complete such structural fire assessment.

Chapter 8 summarizes the research findings. Future research needs are identified and presented.

## **Chapter 2    Mechanical properties of cold-formed steel at elevated temperatures: review and proposed relationship**

### **2.1 Introduction**

To enable performance-based structural fire design, elevated temperature mechanical properties of construction materials need to be established. For cold-formed steel (CFS), while the Australian and European provisions provide valuable benchmarks, it is useful to independently assess the currently available data (including data not available at the time of the development of the Australian and European provisions) to investigate the development of provisions within the U.S. context. Through this process, it is also recognized that existing provisions have specific features that may have been deemed adequate in their context but are not necessarily desirable in the U.S. context. For example, the AS/NZS 4600:2018 [13] provides distinct curves for low strength and high strength steels to AS 1397, respectively, which do not necessarily correspond with the steels typically used in the U.S. Also, the temperature dependent ultimate stress is not provided. The EN1993-1-2 [14] gives values of elastic modulus and 0.2% proof stress at discrete temperature with a step of 100°C, rather than a continuous equation. Further, the material properties in EN1993-1-2 [14] are said to be applicable to both hot-rolled and cold-formed steel members, but data show that cold-formed steel is more susceptible to temperature than hot-rolled steel, thus deserving specific provisions. Therefore, there is a need for temperature dependent reduction factors for properties of cold-formed steel that can be adopted in the U.S.

In this chapter, as part of a Task Group within the American Iron and Steel Institute (AISI) Committee on Specifications for the Design of Cold-Formed Steel Structural Members, a study has been conducted to establish relationships for the reduction in elastic modulus, yield stress, and ultimate stress of cold-formed steels at elevated temperatures. The testing material and methods,

as well as the existing test data on the elevated temperature mechanical properties of cold-formed steels are reviewed. Based on the data, relationships for the reduction factors are proposed with a simple, consistent equation format. The proposed relationships are also compared with the Australian, French and European codes.

## **2.2 Literature review**

### **2.2.1 Materials and Testing Methods**

#### **2.2.1.1 Cold-formed steels**

Cold-formed steel structural members for building construction utilize coiled sheet steel with thickness typically ranging from 0.8 to 3.0 mm. The most commonly used steel grades in the U.S. are mild steels produced to ASTM A1003/A1003M [15] or ASTM A653/A653M [16], with 0.2% proof stress  $F_y$  of 228 MPa or 345 MPa, and under certain conditions low ductility G550 with  $F_y$  of 550 MPa. Roll-forming machines are used to bend mild steels into structural member shapes such as channels, lipped channels, lipped zees, and deck. These members are then used in repetitive framing schemes to frame vertical (wall) and horizontal (floor, roof) panels. Based on the commonly used steels for cold-formed members, as well as the available data, this work focuses on steel sheet with thickness up to 3.5 mm and yield stress up to 550 MPa.

Data on elevated temperature mechanical properties are obtained through testing specimens cut from cold-formed steel sheets. In the U.S., specimen sizes are prescribed by ASTM E21 [17]. For instance, Figure 1 shows a pin-loaded tensile specimen, with 50 mm gauge length and 12.7 mm width. These specimens are tested to failure through a combination of thermal and tensile loading. Two testing procedures are used in the literature, namely steady-state testing and transient-state testing, as described below.

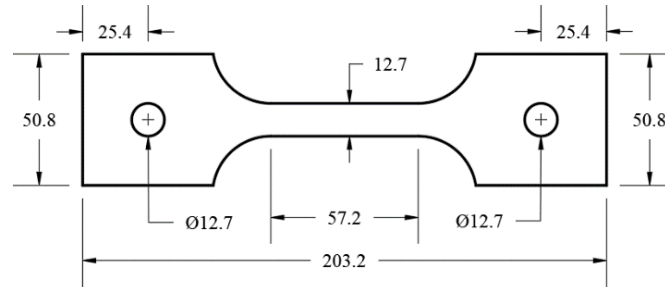


Figure 1. Specimen for pin-loaded tensile testing of metallic materials at elevated temperatures, as per ASTM E21 [17]. Dimensions are in mm.

### 2.2.1.2 Steady-state tests

In a steady-state test, the steel specimen is first heated to a target temperature with a controlled heating rate. A force-controlled mode is implemented to allow unrestrained thermal expansion of the specimen. Once the target temperature is reached, a wait time is observed to ensure stabilization and uniformity of the steel temperature. Then, while maintaining the elevated temperature constant, the specimen is loaded in tension at a controlled loading rate (e.g. 0.005 mm/mm/min according to ASTM E21 [17]) in a displacement-controlled mode. The loading is applied until fracture of the specimen. Continuous stress-strain curves can be directly obtained from steady-state tests.

### 2.2.1.3 Transient tests

In order to more accurately mimic the loaded structures in, transient test is usually carried out. In a transient test, the steel specimen is first loaded in tension to a target stress level. The specimen is then heated, while maintaining the stress level constant, with a controlled heating rate until fracture. During the heating phase, a load-controlled mode is required to maintain the stress level constant, since the temperature increase generates thermal expansion. An unstressed test is also conducted to obtain the free thermal strain as a function of temperature. Transient tests yield

temperature-strain curves at several stress levels. The obtained data are then post-processed to construct stress-strain curves at several temperatures.

### 2.2.2 Tests by Yan et al.

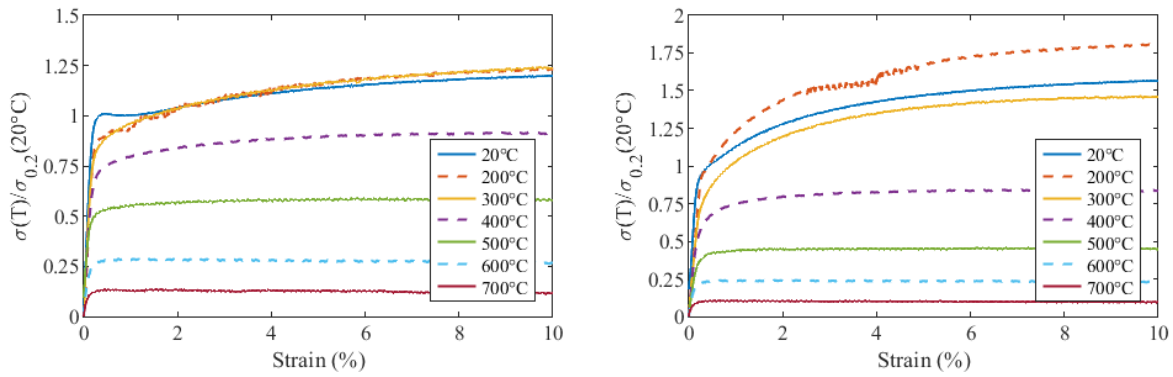
Tests have been conducted by Yan et al. [18] at Johns Hopkins University on specimens cut from a mild steel sheet with  $F_y$  of 395 MPa (CFS-395) and a dual-phase steel sheet with  $F_y$  of 340 MPa (CFS-340). The sheets thickness for both grades was 1.4 mm. The pin-loaded tensile specimens were prepared in accordance with ASTM E21 [17] (Figure 1).

The tests were conducted using a three-zone ATS 3210 furnace with maximum temperature of 1150°C mounted on an MTS load frame, as shown in Figure 2. The furnace includes three internal K-type thermocouples at three independent heating zones to control the furnace temperature. In addition, three external K-type thermocouples applied on the specimen are used to measure the real-time surface temperature of the steel. Strains are measured using both an Epsilon high temperature extensometer (-10%/+20%) and a Digital Image Correlation (DIC) system (+40%).

The tests were conducted in steady state using a heating rate of 10°C/min followed by a 15 min wait time. Once the target temperature was reached the tensile load was applied by controlling the displacement of the rods at a rate of 0.005 mm/mm/min. Tests were carried out for three times on CFS-395 at 20°C, 300°C, and 400°C to verify the repeatability. Results show that the coefficient of variance for the repeated tests is smaller than 5%. Thus, only one test was carried out for the two steel types at various temperatures. The normalized stress-strain curves are shown in Figure 3. Retention factors for elastic modulus  $E$ , 0.2% proof stress  $\sigma_{0.2}$ , 2% stress  $\sigma_{2.0}$ , and ultimate stress  $\sigma_u$  are listed in Table 1.



Figure 2. Test setup in the Structures Lab at Johns Hopkins University [18].



(1) CFS-395

(2) CFS-340

Figure 3. Stress-strain curves of tested steels by Yan et al. [18].

Table 1. Retention factors for the mechanical properties of CFS-395 and CFS-340.

T (°C)	CFS-395				CFS-340			
	$\frac{E(T)}{E(20^\circ\text{C})}$	$\frac{\sigma_{0.2}(T)}{\sigma_{0.2}(20^\circ\text{C})}$	$\frac{\sigma_{2.0}(T)}{\sigma_{2.0}(20^\circ\text{C})}$	$\frac{\sigma_u(T)}{\sigma_u(20^\circ\text{C})}$	$\frac{E(T)}{E(20^\circ\text{C})}$	$\frac{\sigma_{0.2}(T)}{\sigma_{0.2}(20^\circ\text{C})}$	$\frac{\sigma_{2.0}(T)}{\sigma_{2.0}(20^\circ\text{C})}$	$\frac{\sigma_u(T)}{\sigma_u(20^\circ\text{C})}$
20	1.00	1.00	1.00	1.00	1.00	1.00	1.00	1.00
200	0.86	0.90	1.01	1.01	0.83	1.01	1.12	1.14
300	0.75	0.89	1.01	1.06	0.73	0.85	0.93	0.92
400	0.66	0.74	0.81	0.75	0.64	0.65	0.62	0.53
500	0.55	0.53	0.55	0.48	0.55	0.41	0.35	0.29
600	0.43	0.28	0.27	0.24	0.47	0.23	0.19	0.15
700	0.28	0.13	0.13	0.11	0.36	0.10	0.08	0.07

### 2.2.3 Tests by Batista Abreu

Tests have been conducted by Batista Abreu [19] on specimens cut from the web of CFS 600S162 structural studs (according to AISI nomenclature [20]). The specimens were formed from ASTM A653 steel, with nominal yield strengths of 230 MPa and 345 MPa, and thicknesses of 2.58 mm, 1.44 mm, and 1.15 mm. The specimens were flat and had two holes for pinned connections with dimensions according to the standard [21].

An ATS 3710A furnace with maximum temperatures of 621°C was used in the testing (Figure 4 (1)). The specimens were located inside the furnace and connected to MTS 647 hydraulic wedge grips on an MTS 810 load frame through high temperature stainless steel bars with pins (Figure 4 (2)). An MTS 634 axial extensometer was used to measure the changes along the length of the specimens while the axial load was applied (Figure 4 (3)). The extensometer was connected outside the oven to a high-temperature steel mounting which was attached to the specimen inside the oven, within its gage length (Figure 4 (4)).

After placing the specimen and calibrating the load cell and extensometer, the specimen was heated up at an average rate of 10 °C/min. During the heating process, free thermal expansion was allowed by releasing the bottom grip. The temperature levels in this study were 25 °C, 100 °C, 200 °C, 300 °C, 400 °C, 500 °C and 600 °C. Temperature was monitored by two type-K thermocouples. One thermocouple was attached to the specimen and the other was used to measure air temperature inside the oven. After the target temperature was stable, the specimens were maintained under constant temperature for a period of 10 minutes. The extensometer was calibrated to zero and then the load was applied by controlling the displacement of the hydraulic grip until fracture occurred. A total number of 21 specimens were tested. The stress-strain curves are shown in Figure 5 and the retention factors are listed in Table 2.

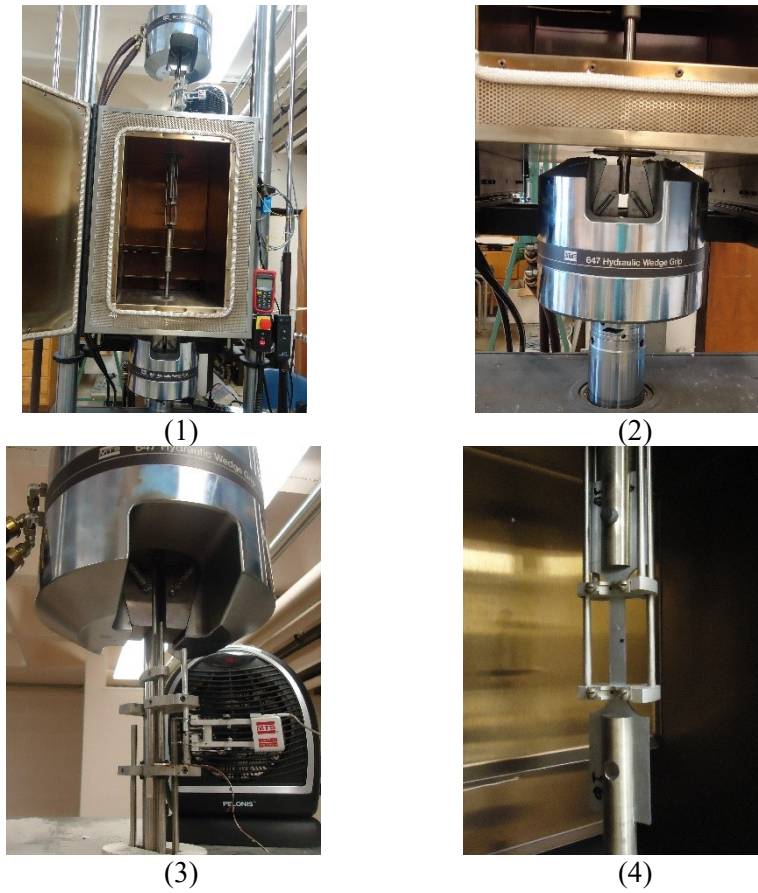


Figure 4. Test setup used by Batista Abreu [19].

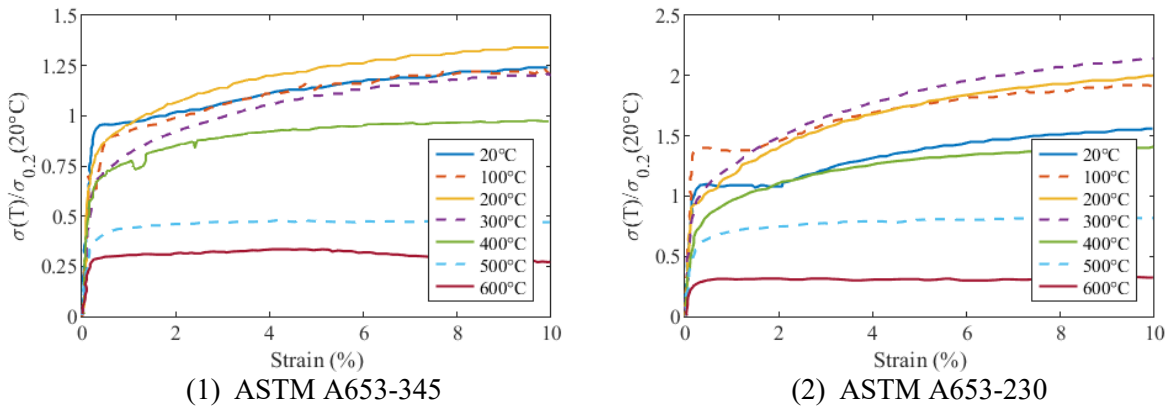


Figure 5. Stress-strain curves of tested steels by Batista Abreu [19].

Table 2. Retention factors for the mechanical properties of tested ASTM A653 steels.

T (°C)	ASTM A653-345MPa-2.58mm			ASTM A653-345MPa-1.15mm			ASTM A653-230MPa-1.44mm		
	$E(T)$	$\sigma_{0.2}(T)$	$\sigma_u(T)$	$E(T)$	$\sigma_{0.2}(T)$	$\sigma_u(T)$	$E(T)$	$\sigma_{0.2}(T)$	$\sigma_u(T)$
	$E(20^\circ\text{C})$	$\sigma_{0.2}(20^\circ\text{C})$	$\sigma_u(20^\circ\text{C})$	$E(20^\circ\text{C})$	$\sigma_{0.2}(20^\circ\text{C})$	$\sigma_u(20^\circ\text{C})$	$E(20^\circ\text{C})$	$\sigma_{0.2}(20^\circ\text{C})$	$\sigma_u(20^\circ\text{C})$
20	1.00	1.00	1.00	1.00	1.00	1.00	1.00	1.00	1.00
100	0.87	0.93	0.96	0.92	0.95	1.02	0.90	1.32	1.24



200	0.83	0.89	1.05	0.99	0.83	1.10	0.88	0.95	1.40
300	0.70	0.72	0.88	0.77	0.76	1.10	0.70	1.02	1.47
400	0.58	0.75	0.73	0.69	0.63	0.80	0.62	0.75	0.95
500	0.42	0.43	0.37	0.45	0.38	0.38	0.39	0.61	0.53
600	0.35	0.42	0.35	0.38	0.16	0.19	0.36	0.29	0.23

#### 2.2.4 Review of published data for cold-formed steels

Data on elevated temperature mechanical properties of cold-formed steels from steel sheets and sections, gathered from the literature [9,10,28–32,18,19,22–27] and from the authors' tests described in Section 2.2.2 and 2.2.3. Collected test data are summarized in Table 3 (conventional grade) and Table 4 (G550). To be consistent with the applicable steel grade specified in AISI and AN 4600, the test data collected in this study cover steel grade up to 550 MPa. The G550 data is provided separately to compare it with conventional grade data for determining whether the latter and former can be aggregated. Table 3 and Table 4 specify the main test parameters including heating rate, steel type, thickness, test type (steady-state vs transient-state), and temperature range. Steel types cover American grades ASTM A653, Australian G250, G300 and G450, European S355, Chinese Q345, among others. Specimen thicknesses range from 0.4 mm to 3.5 mm. Test temperatures range between 20°C and 1000°C. The mechanical properties of interest can be extracted from the test measurements at different elevated temperature. The reduction of these properties with increasing temperature is then described by retention factors, determined as the ratio of the measured value at elevated temperature to that at ambient temperature.

Table 3. Test data for conventional grade steels.

Source	# of specimens	Heating rate (°C/min)	Steel type	Thickness (mm)	Test type*	Temperature (°C)
Lee [27]	81	15-20	G300	0.4, 0.6, 1.0	SS	20-800
Outinen [9]	21	10, 20, 30	S355J2H	3	TS	20-1000
Chen [22]	40	100	G450	1.9	SS/TS	20-1000
Ranawaka [10]	56	10-25	G250	0.6, 0.8, 0.95	SS	20-800
Kankanamge [25]	72	10-20	G250	1.55, 1.95	SS	20-700
			G450	1.5, 1.9		
Ye [32]		20	Q345	1.5	SS/TS	30-700
Landesmann [26]	13	10	ZAR-345	2.7	SS	20-600
McCann [29]	40	10	S355J2H		SS/TS	20-1000
Imran [24]	124		G350	2, 3.5	SS	20-800
Batista Abreu (Batista Abreu 2015)	21	10	ASTM A653	1.44, 2.58, 1.15	SS	20-600
	7	10, 20	ZAR-345	1.55		20-700
Craveiro [23]	27	10	S280GD+Z	2.5	SS	20-800
Rokilan [30]	40		G300	0.8, 1.0	SS	G300
Yan [18]	7	10	CFS-395	1.4	SS	20-700
	7		CFS-340	1.4		20-700

\* 'SS': steady-state test; 'TS': transient-state test.

Table 4. Test data for G550.

Source	# specimens	Heating rate (°C/min)	Steel type	Thickness (mm)	Test type*	Temperature (°C)
Lee [27]	27	15-20	G550	0.42, 0.6, 0.95	SS	20-800
Chen [22]	23	100	G550	1	SS	20-1000
Ranawaka [10]	59	10-25	G550	0.6, 0.8, 0.95	SS	20-800
Rokilan [30]			G550	0.55, 0.75, 0.95	SS	20-700

\* 'SS': steady-state test.

## 2.3 Data

Retention factors for elastic modulus, 0.2% proof stress, 2% stress, and ultimate stress from the tests collected in Table 3 and Table 4 are shown in Figure 6 to Figure 9. Filled symbols are used

for steady-state tests data while empty symbols are used for transient tests data. Conventional grade steel data are plotted in black and blue, while G550 data are plotted in red.

The mechanical properties decrease with increasing temperature. The reduction in elastic modulus is progressive (almost linear) while the reductions in strength parameters exhibit an S-shape with a marked drop between 300°C and 600°C. An increase in ultimate stress is observed for the A653-230 and G250 grades in the range of 100°C-300°C. The variance in strength is large in the range of 300°C-600°C. Generally, G550 data show similar reduction trend with the conventional grade data, suggesting that a unique relationship can be adopted to capture the data for these different grades up to G550. Similarly, the steady-state and transient tests data do not show a clear discrepancy. The lower bound data for the elastic modulus was obtained in transient conditions [32], but the other transient test data for the modulus fit with the average of the steady-state data. This suggests that steady-state and transient data can be aggregated. This assumption will be confirmed in the next section by comparing the fitted relationships on the separated and aggregated datasets.

Regarding thickness, the dataset for 3.5 mm [24] obtained with G350 aligns with the rest of the data. This suggests that there is no marked effect of thickness on the reduction of properties within the studied range. Therefore, it is valid to propose relationships that hold up to 3.5 mm.

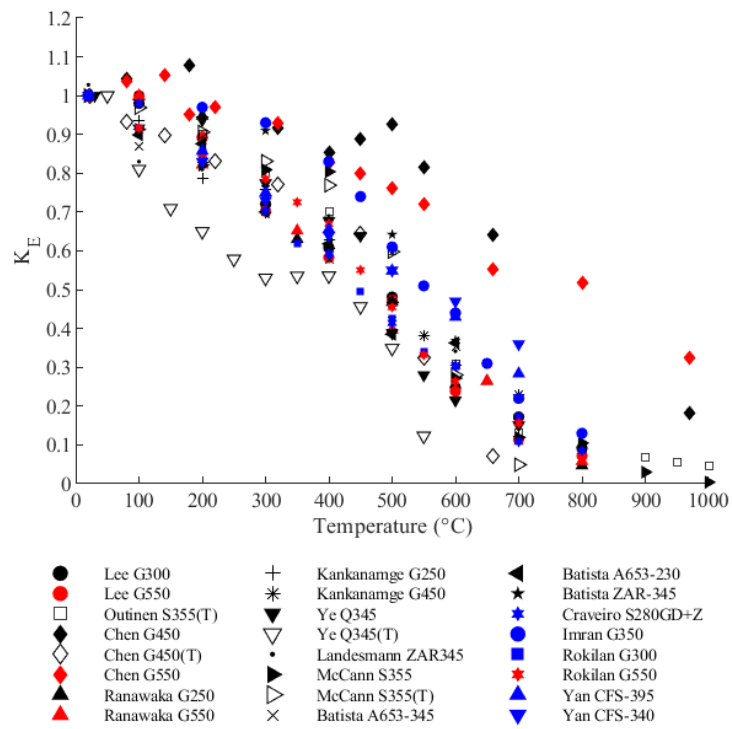


Figure 6. Retention factors of elastic modulus of conventional grade steels and G550 at elevated temperature.

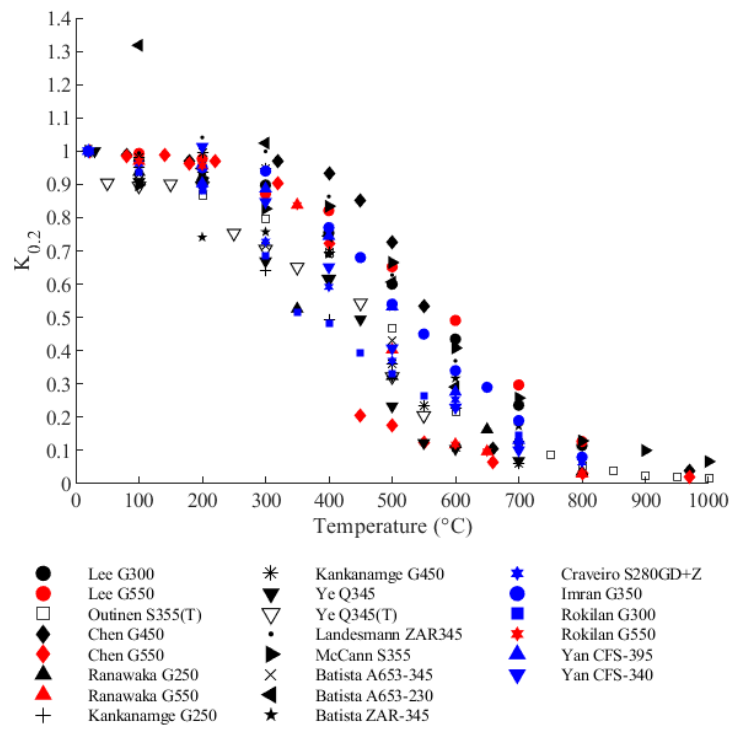


Figure 7. Retention factors of 0.2% proof stress of conventional grade steels and G550 at elevated temperature.

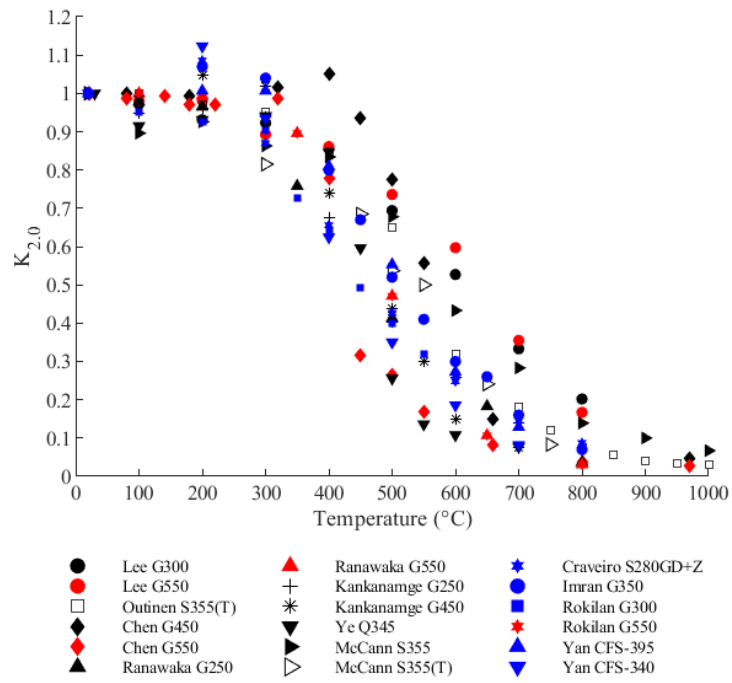


Figure 8. Retention factors of 2.0% stress of conventional grade steels and G550 at elevated temperature.

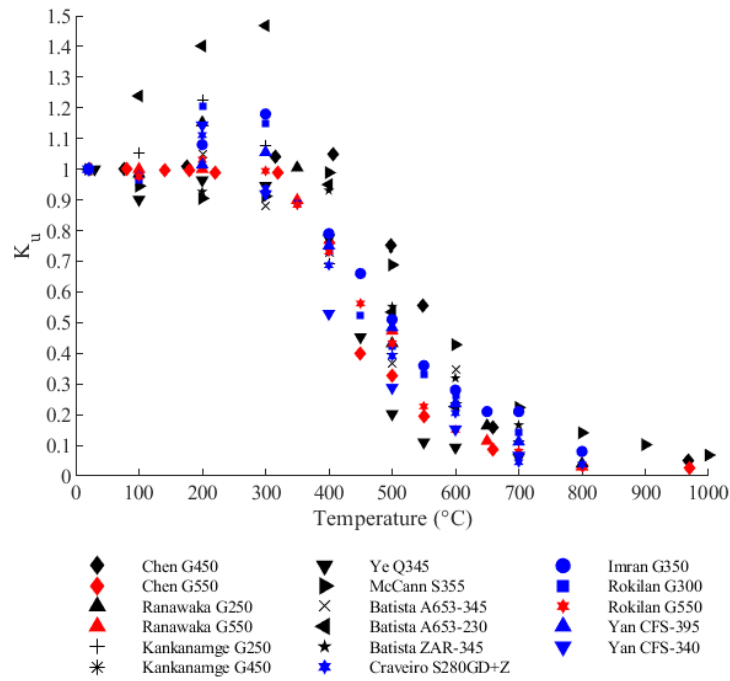


Figure 9. Retention factors of ultimate stress of conventional grade steels and G550 at elevated temperature.

## 2.4 Relationships for Retention Factors

### 2.4.1 Standardized retention factor equation

Retention factors for elastic modulus, 0.2% proof stress, 2% stress, and ultimate stress were developed based on the data reported in Section 2.3. The standardized format of Eq. (1) developed through committee work with the American Iron and Steel Institute was adopted for the retention factor relationships.

$$k = (1 - c) \frac{1 - x^b}{1 + ax^b} + c \quad (1)$$

where

$$x = \frac{T - T_1}{T_2 - T_1} \quad (2)$$

The coefficients  $a$ ,  $b$  and  $c$  are established from the test data by nonlinear least square regression method [33]. The limit temperatures  $T_1$  and  $T_2$  specify the temperature range of the equation, with  $k = 1$  at  $T_1$  and  $k = c$  at  $T_2$ . Here, the range is 20°C-1000°C based on the available data; hence  $T_1 = 20^\circ\text{C}$  and  $T_2 = 1000^\circ\text{C}$ .  $T$  is the steel temperature in °C.

#### 2.4.2 Retention factors for CFS mechanical properties

The developed retention factors are provided in Table 5 to Table 8 and compared with available data in Figure 10 to Figure 13. For each property, retention factors are provided separately for (1) conventional grade under steady state, (2) conventional grade under transient state, and (3) G550 under steady state (no G550 transient data was found). Then, retention factors for the whole dataset are provided, in terms of (4) best statistical fit and the (5) final proposed (rounded) values.

For elastic modulus (Table 5, Figure 10), the curve for the whole dataset agrees with the one for the conventional grade steady-state test data. The G550 curve yields slightly higher values at temperatures above 600°C. In contrast, the transient curve yields a lower prediction of elastic modulus. However, this is due to the single dataset [32] which sits noticeably lower than the rest of the transient test data. Further, it is notoriously difficult to experimentally obtain the elastic modulus from transient tests, because transient tests yield temperature-strain measurements and reconstructing the initial part of the stress-strain curve requires a large number of tests. Therefore, it seems reasonable to adopt a single curve for the whole dataset.

For the 0.2% proof stress (Table 6, Figure 11), the curve for the whole dataset agrees with the one for the conventional grade steady-state test data. The G550 curve yields slightly lower values between 400°C and 800°C. The transient curve yields lower predictions across all temperatures in a similar fashion as the elastic modulus curve. However, this difference is not observed for the 2%



stress (Table 7, Figure 12) where separate and aggregated dataset align closely. Results for the ultimate stress (Table 8, Figure 13) suggest slightly lower values for G550 compared with conventional grade steels at temperatures exceeding 400°C. In the end, the separate and aggregated curves for the modulus and strength properties do not show a clear enough discrepancy to justify incorporating different provisions for the steel grades or testing method in U.S. practice. In other words, this exercise justifies the use of a single curve per property for steel grades up to 550 MPa. The R-square value is provided for each row in the tables. The R-square shows that the fit for the final proposed values is close to that of the best fit for the whole dataset, i.e., there is no noticeable loss in accuracy in adopting the proposed rounded values for the coefficients.

Table 5. Coefficients to determine retention factors for elastic modulus of cold-formed steel.

#	Data type	a	b	c	R-square
1	Steady-state test	3.626	2.434	0.01283	0.8796
2	Transient-state test	4.467	2.139	0.019178	0.8723
3	G550	5.989	2.944	0.09080	0.8152
4	All (SS+TS+G550, fit)	3.902	2.354	0.04268	0.8609
<b>5</b>	<b>All (SS+TS+G550, proposed)</b>	<b>8</b>	<b>3</b>	<b>0.04</b>	<b>0.8518</b>

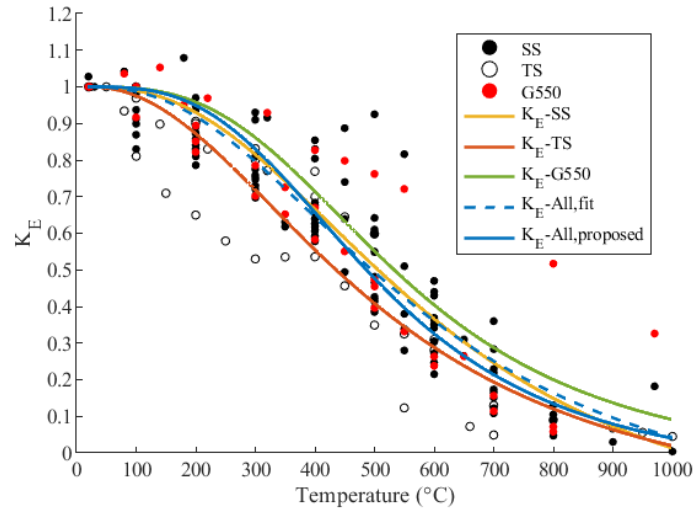


Figure 10. Proposed retention factors for elastic modulus at elevated temperature.

Table 6. Coefficients to determine retention factors for 0.2% proof stress of cold-formed steel.

#	Data type	a	b	c	R-square
1	Steady-state tests	20.92	4.099	0.03563	0.8887
2	Transient-state tests	11.24	2.985	-0.002006	0.9683
3	G550	67.80	5.103	0.04879	0.9255
4	All (SS+TS+G550, fit)	20.72	3.987	0.02485	0.9021
<b>5</b>	<b>All (SS+TS+G550, proposed)</b>	<b>20</b>	<b>4</b>	<b>0.03</b>	<b>0.9005</b>

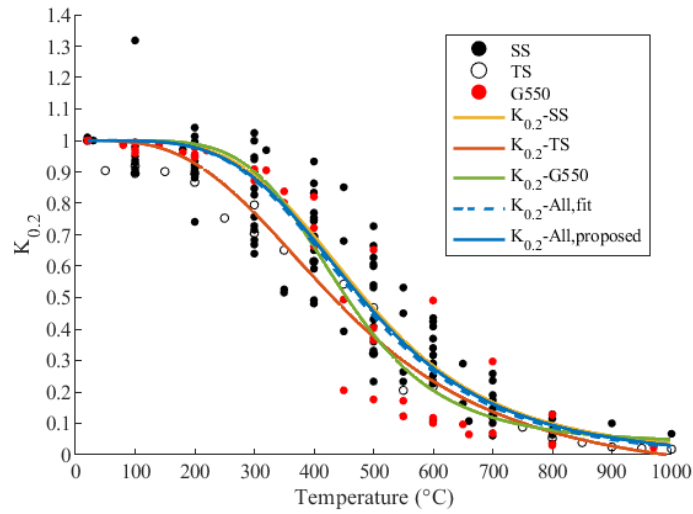


Figure 11. Proposed retention factors for 0.2% proof stress at elevated temperature.

Table 7. Coefficients to determine retention factors for 2% stress of cold-formed steel.

#	Data type	a	b	c	R-square
1	Steady-state tests	83.96	6.103	0.07364	0.9223
2	Transient-state tests	39.95	5.634	0.02550	0.9877
3	G550	53.74	5.219	0.06861	0.9105
4	All (SS+TS+G550, fit)	49.42	5.470	0.05002	0.9265
<b>5</b>	<b>All (SS+TS+G550, proposed)</b>	<b>70</b>	<b>6</b>	<b>0.05</b>	<b>0.9238</b>

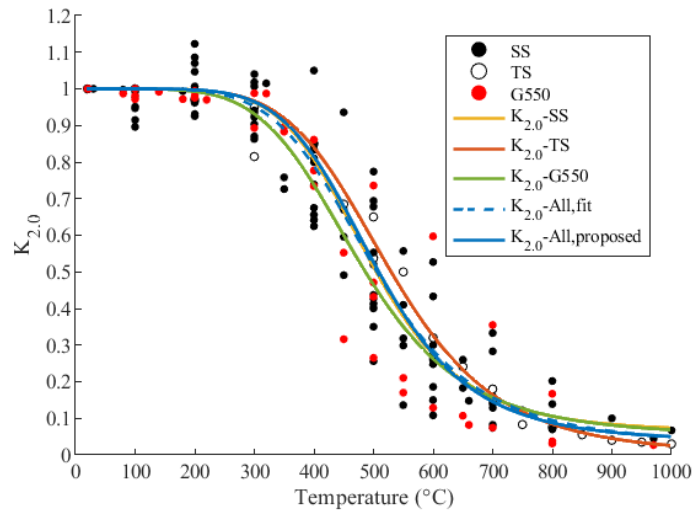


Figure 12. Proposed retention factors for 2.0% stress at elevated temperature.

Table 8 Coefficients to determine retention factors for ultimate stress of cold-formed steel.

#	Data type	a	b	c	R-square
1	Steady-state tests	161.8	6.849	0.05985	0.9101
3	G550	363.6	7.235	0.03201	0.9890
4	All (SS+G550, fit)	133.2	6.573	0.03674	0.9224
<b>5</b>	<b>All (SS+G550, proposed)</b>	<b>185</b>	<b>7</b>	<b>0.04</b>	<b>0.9221</b>

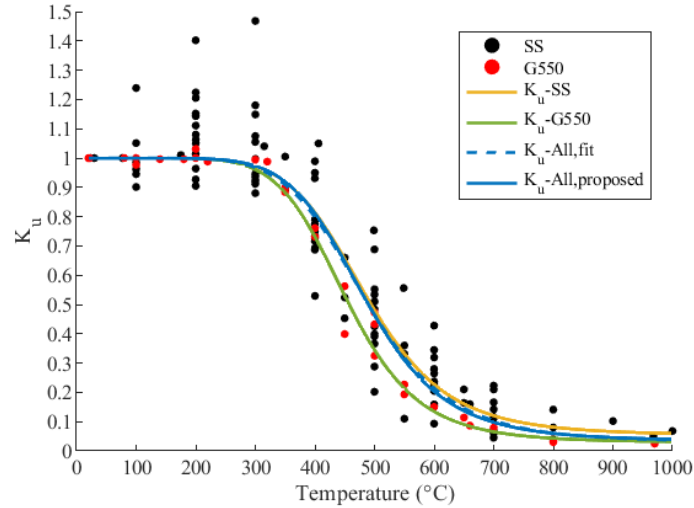


Figure 13. Proposed retention factors for ultimate stress at elevated temperature.

## 2.5 Comparison with codes

The coefficients of the proposed retention factors are summarized in Table 9, for use with Eq. (1) and Eq. (2). The proposed predictive models are compared with the models in the European EN1993-1-2 [14], the Australian standard AS/NZS 4600 [13], and the French National Annex NF EN 1993-1-2/NA [34].

Figure 14 shows the comparison for the elastic modulus. The proposed retention factors agree with the code models. The AS/NZS 4600 [13] provides more conservative values while the EN [14] provides slightly higher prediction at 400°C~600°C. The French National Annex [34] agrees well with the proposed models at temperature up to 500°C, beyond which the French National Annex

[34] exhibits more conservative values. Figure 15 compares the retention factors for the 0.2% proof stress. The AS4600 [13] provides a curve for low strength steels and one for high strength (low ductility G550) steels. The proposed retention factors lie within the range of the code values. The prediction from AS4600 [13] generally provides a lower bound. The low-strength model is generally conservative across all temperatures while the high-strength (low ductility) model provides a lower bound when the temperature exceeds 500°C. The Eurocode EN1993-1-2 [14] and the French National Annex [34] show similar values up to 400°C and they are slightly lower than the proposed models in this study, while at temperature higher than 500°C they show general agreement with the proposed models. Figure 16 shows the 2% stress retention factors. The values in Eurocode EN1993-1-2 [14] for the 2.0% stress are based on hot-rolled steel test data, which exhibit a lower strength reduction at elevated temperature compared with cold-formed steel. AS4600 [13] does not provide relationships for the 2% stress of CFS. Therefore, no direct comparison with a code model can be performed for the 2% stress. Figure 17 shows the ultimate stress retention factors. The proposed model predicts lower values than the EN [14] model.

Table 9. Coefficients to determine retention factors for mechanical properties of cold-formed steel.

Property	a	b	c
Modulus	8	3	0.04
0.2% proof stress	20	4	0.03
2% stress	70	6	0.05
Ultimate stress	185	7	0.04

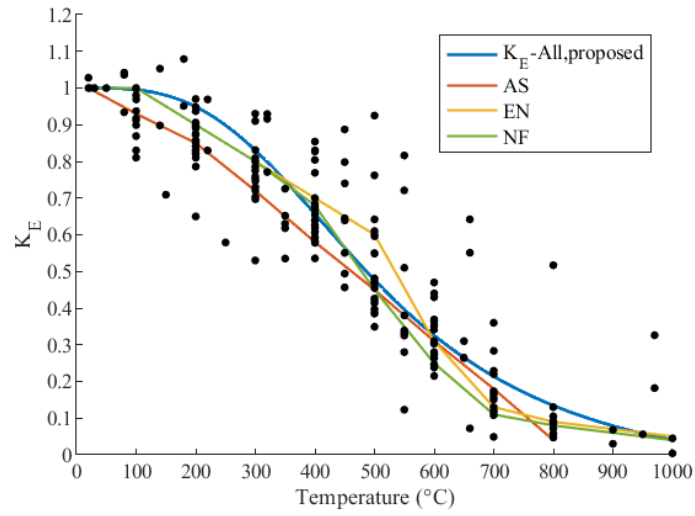


Figure 14. Comparison of proposed retention factors for elastic modulus with design codes.

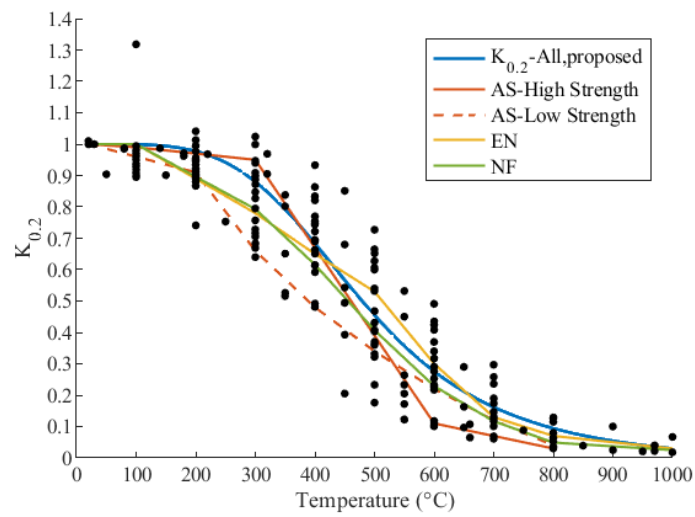


Figure 15. Comparison of proposed retention factors for 0.2% proof stress with design codes.

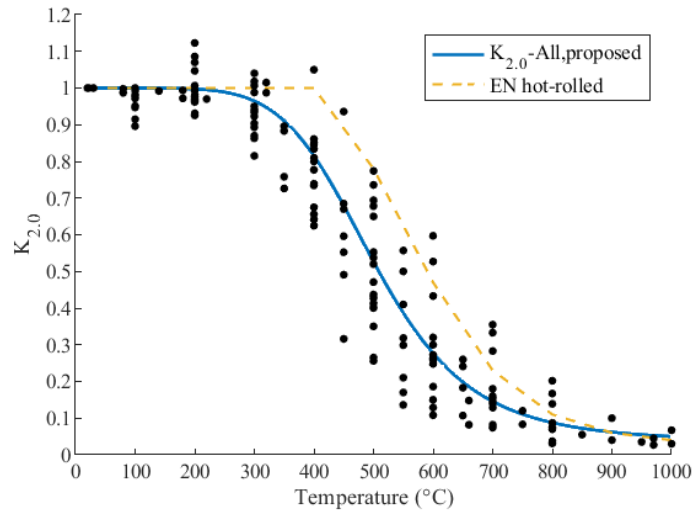


Figure 16. Comparison of proposed retention factors for 2.0% stress with design codes.

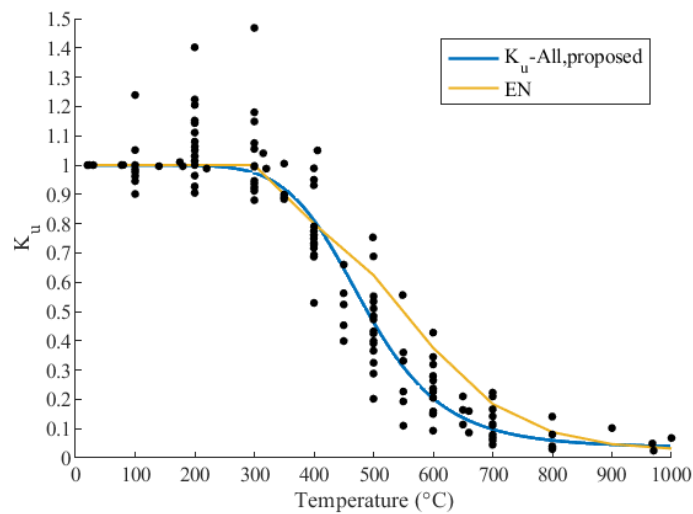


Figure 17. Comparison of proposed retention factors for ultimate stress with design codes.

## 2.6 Conclusions

A simple, consistent, equation format has been proposed to capture the reduction of mechanical properties of cold-formed steel with temperature. The equation (Eq. (1)-(2)), which is a continuous function of temperature, includes three coefficients. The coefficients (Table 9) have been derived from test data to characterize the reduction of elastic modulus, 0.2% proof stress, 2% stress, and

ultimate stress of cold-formed steel – all using the same equation form. The established relationships are applicable to material grades up to 550 MPa and thickness up to 3.5 mm, at temperatures up to 1000°C.

Comparison with Australian, French and European codes show general agreement; however, the proposed relationships have the advantage of being continuous, adopting a consistent format, and providing a single curve for a given property. Further, they provide 2% stress and ultimate stress which are not included specifically for cold-formed steels in other codes. The relationships are under consideration for adoption in the next version of the AISI specification for Cold-Formed Steel Structural Members.



## **Chapter 3 Mechanical properties of advanced high-strength steels (AHSS) at elevated temperature**

### **3.1 Introduction**

Owing to recent progress in manufacturing, Advanced High-Strength Steels (AHSS) with nominal yield stress up to 1200 MPa and ultimate stress up to 1500 MPa are available in the market [5,6]. AHSS refers to a new generation of steels that feature chemical components and multiphase microstructures resulting from precise heating and cooling processes from the austenite or austenite/ferrite phase. As a result, AHSS exhibit a multiphase microstructure containing one or more phases other than ferrite, pearlite, or cementite. These phases could include martensite, austenite, bainite, and/or retained austenite sufficient in quantities to produce high-strength and durability while maintaining formability [6]. AHSS includes dual phase (DP), martensitic (MS), ferritic-bainitic (FB), and some other complex-phase steels. The variety of alloys and processing combination can achieve a wide range of strength, ductility, toughness, and fatigue properties. AHSS can be hot-rolled or cold-formed. The terminology ‘AHSS’ is based on the metallurgical microstructure of the product (which is multiphase), not on the steel grade. Conventional steels are typically referred to as low-strength or high-strength depending on whether their yield stress exceeds a threshold, currently typically defined as 460MPa [35] (although this convention has been evolving with advances in material strengths). AHSS, especially dual-phase (DP) steel and transformation-induced plasticity (TRIP) steel, can have strength grades that span the two conventional strength designations. Yet conventional high-strength steels have single-phase ferritic microstructure (e.g. high-strength low-alloy (HSLA) steels and bake-hardenable (BH) steels), while AHSS have multiphase microstructure. As a convention, this study will thus use the

general term ‘AHSS’ to designate steels with advanced multi-phase microstructure, regardless of their yield strength.

Characterization of material properties at elevated temperatures is required to assess the performance of cold-formed steel structures in the fire situation, as presented by several authors for more conventional grades [36–39]. To fill this gap, an experimental study on the mechanical properties of cold-formed AHSS at elevated temperatures is reported and discussed in this chapter. A total number of 88 specimens were cut from cold-formed steel sheets with nominal yield stress ranging from 340 MPa to 1200 MPa. The tested materials include two AHSS, namely a dual-phase steel (DP) and a martensitic steel (MS), in addition to conventional mild steel and high-strength low-alloy steel (HSLA) specimens as benchmarks. Elevated temperature tension tests were performed in steady-state (66 tests) and transient-state (22 tests) conditions. Tensile specimens were loaded after heating to different elevated temperatures from room temperature to 700°C in steady-state tests, while in transient-state tests specimens were heated after being loaded to predefined stress levels. The temperature of 700°C was selected as maximum in this test campaign because it resulted in a reduction of more than 90% of the measured strength of the AHSS. In structural applications, cold-formed steel components need fire protection, with gypsum wallboard being the most common material, which limits the temperature increase in the steel. Material properties were obtained from the tests including elastic modulus, yield stress (defined at different strain levels), ultimate stress, and elongation at fracture. The test results were compared with the predictions in design codes and literature. Finally, predictive models to determine the mechanical properties of the cold-formed advanced high-strength steels were proposed.

### 3.2 Literature review

Reduction factors for steel material properties at elevated temperatures are available in design codes, such as European code (EC3) [35], American standard (AISC Specification 360) [40], British standard (BS5950) [41], Australian standard (AS 4100) [42], and Chinese standard (CECS 200) [43]. However, the provisions in these standards are mostly based on data for hot-rolled steel and for common grades material, typically up to about 460 MPa yield stress. The cold-working process that increases the yield stress and ultimate stress may reduce quickly at elevated temperature; this effect is even more severe for cold-formed high-strength steels [10].

Experimental investigations of mechanical properties of cold-formed steel at elevated temperatures have attracted increasing attention in recent years [9,10,32,44,22–25,27–30]. Lee et al. [27] tested light gauge cold-formed steels with three steel grades (G300, G500, and G550) and six thicknesses (from 0.4 to 1.2 mm), and presented empirical equations to predict the deterioration of material properties at elevated temperatures. Outinen and Makelainen [9] tested the mechanical properties of cold-formed material taken from S355J2H (355 MPa nominal yield stress; 3 mm thickness) rectangular hollow sections with different heating rates (10°C/min, 20°C/min, 30°C/min, and 45°C/min). Chen and Young [22] studied the mechanical properties of G550 and G450 with thickness of 1.0 and 1.9 mm respectively. Kankanamge and Mahendran [25] conducted an experimental study on the elevated temperature mechanical properties of G250 (1.55 and 1.95 mm) and G450 (1.50 and 1.90 mm) cold-formed steels. Ye and Chen [32] tested the material properties of Q345 with thickness of 1.5 mm under elevated temperatures and concluded that current standards provided an overestimation for the mechanical properties of Q345 under elevated temperatures. McCann et al. [29] tested the mechanical properties of cold-formed S355J2H steel cut from circular, rectangular, and square hollow sections. Craveiro et al. [23] tested the thermal

properties and mechanical properties of galvanized S280GD+Z steel with thickness of 2.5mm at elevated temperature. Li and Young [28] conducted elevated temperature tests on the material properties of cold-formed high strength steel with nominal yield stresses of 700 and 900 MPa and thickness of 4 mm and 6 mm for temperature up to 1000°C. Imran et al. [24] tested cold-formed G350 steel (thickness ranging from 2 to 3.5 mm) cut from circular, rectangular, and square hollow sections. Rokilan and Mahendran [30] tested the mechanical properties of cold-formed low strength G300 steel sheets and high strength G550 steel sheets and steel sections and concluded cold-formed section experienced higher reduction in strength at elevated temperature than cold-formed sheets due to the higher levels of cold working. Overall, the test data from these studies show that the retention factors provided in the codes on the basis of hot-rolled steel materials are not applicable for cold-formed steels and the difference is especially marked for high strength cold-formed steel grades. Meanwhile, the review of previous experimental studies reveals that test data remain scarce on advanced high strength cold-formed steel with grades up to 1200 MPa at elevated temperatures.

### **3.3 Experimental protocol and materials**

#### **3.3.1 Test apparatus**

A three-zone ATS 3210 series high temperature furnace with maximum temperature of 1150°C was mounted on an MTS load frame, as shown in Figure 2. The furnace is controlled by an ATS temperature control system which can set up the target temperature and heating rate. Three internal K-type thermocouples are located in the middle of the three independent heating zones to measure the furnace temperature. In addition, three external K-type thermocouples are used to measure the real-time surface temperature of the steel specimens. These three external thermocouples are

located at the two ends and center of the reduced parallel section [45]. A specifically developed LabVIEW program was used to control the loading process and record the test data.

The strain was measured using both an Epsilon model 3549 high temperature extensometer (strain range: -10% to +20%) and a Digital Image Correlation (DIC) system (strain range: 0 to +40%). For the DIC method, speckles were applied onto the surface of the specimens [46] and an open source MATLAB-based program *ncorr* [47] was used to analyze the displacement of the speckles, which then allowed calculation of the strain. A combination of white base paint and black speckles was applied when the test temperature was below 500°C. In 600°C and 700°C tests, only the white speckles were applied, because the base paint layer was not stable at these high temperatures. Besides, the surface of the specimens became dark at 600°C and 700°C, which made the white speckles stand out. As radiation from the heated steel specimen can significantly alter the intensity of images captured by the DIC camera at high temperature, a blue light illumination and blue band pass filter (BP470, Midwest Optical System, Inc) were used to reduce the error due to the intensity change [48].

### **3.3.2 Test specimens**

Tensile specimens were cut from cold-formed steel sheets in the rolling direction. The steel sheets are of four materials and six grades, namely Mild-395, HSLA-700, DP-340, DP-700, MS-1030, and MS-1200. The first word (e.g. ‘Mild’) indicates the material type while the number (e.g. ‘395’) indicates the nominal yield stress. Here, ‘HSLA’ stands for high-strength low-alloy steel, which provides improved mechanical properties with small amounts of alloying elements (e.g. Manganese, Chromium) added to its chemical composition. ‘DP’ stands for dual-phase steel, which is a high strength steel having a ferritic-martensitic microstructure. ‘MS’ stands for

martensitic steel, which is rich in martensite with smaller amounts of bainite or ferrite and is typically produced by quenching at very high rates from the austenite-ferrite region. Table 10 lists the nominal yield stress, nominal ultimate stress, and nominal thickness of each specimen type. Table 11 gives the typical chemical composition for the test materials (note: the exact composition of the tested steels could not be provided for the DP and MS steels because it is proprietary information from the manufacturer).

Table 10. Steel grade and nominal thickness of steel specimen.

Steel type	Coating	Thickness (mm)	$f_{y,20}$ (MPa)	$f_{u,20}$ (MPa)
Mild-395	Coated	1.4	395	482
HSLA-700	Coated	0.6	700	980
DP-340	Uncoated	1.4	340	590
DP-700	Coated	1.4	700	980
MS-1030	Uncoated	1.0	1030	1300
MS-1200	Uncoated	1.0	1200	1500

Table 11. Chemical components of materials.

Steel type	C (max %)	Si (max %)	Mn (max %)	P (max %)	S (max %)	Al (%)	Nb+Ti (max %)	Cr+Mo (max %)	V (max %)	B (max %)	Cu (max %)
HSLA-700	0.104	0.012	2.32	0.013	0.004	0.031	-	0.606	0.001	0.0001	0.02
DP-340	0.12	0.4	1.6	0.025	0.01	0.015-1.5	0.1	1	0.2	0.005	0.2
DP-700	0.17	0.4	1.7	0.02	0.01	$\geq 0.01$	0.15	1	-	0.005	0.2
MS-1030	0.16	0.4	1.8	0.02	0.01	0.015	0.1	1	-	0.005	0.2
MS-1200	0.28	0.4	1.3	0.02	0.01	0.015	0.1	1	-	0.01	0.2

Note: For DP steel and MS steel, composition is as publicly available for the listed type, not a specific composition from the manufacturer.

The specimens were prepared in accordance with ASTM E21 [45] for pin-loaded tensile testing of metallic materials at elevated temperatures with 50 mm gauge length and 12.7 mm width, as shown in Figure 1. The specimens were cut by waterjet and then milling was applied for accuracy. Measurements of the thickness and width at the two ends and center of the gauge length were carried out by caliper and screw micrometer. For the coated specimens, the zinc coating was removed by HCl acid and the averaged zinc coating thickness was 0.04 mm. The measured

thickness (where coating thickness was subtracted for the coated specimens) and width of each specimen were used for the stress calculation.

### **3.3.3 Test procedure**

Steady-state tests were carried out on the six steel types at temperatures from ambient to 700°C. In a steady-state test, the specimen was first heated to the target temperature with a heating rate of 10°C/min. During the heating process, the upper pin was fixed, while the lower pin was adjusted continuously by the operator through the control software to allow the specimens to expand thermally without incurring compression. A force-controlled method was used where a very small pretension force (within 5MPa) was maintained throughout the heating phase in the specimens. Once the target temperature was reached, a 15 min wait time was observed (at constant elevated temperature and without loading) to ensure the uniform temperature distribution inside the specimens. After 15 min, and while maintaining the constant elevated temperature, the tension force was applied onto the steel specimens at a loading rate of 0.25mm/min in a displacement control mode (evaluated from the strain rate specified in ASTM E21 [45]). The loading was increased at this rate until fracture of the specimen. At the beginning of the test campaign, the steady-state tests were repeated three times on selected steel types (Mild-395, HSLA-700, DP-700, and MS-1200) and at selected temperatures (ambient, 300°C, and 400°C) to confirm the repeatability of the tests.

Transient-state tests were carried out on DP-700 and MS-1200 steels. In the transient-state tests, the specimens were loaded in tension to target stress levels and then heated at a constant rate (while maintaining the stress level constant) until fracture. The applied stress levels applied in this study were based on the nominal yield stress of the tested materials, ranging from 0.05 to 1.2 times the

nominal yield stress of the specimen. For instance, in a transient-state test of DP-700 with 0.1 load level, a force was applied to the specimens to reach a stress level of 70 MPa before heating. An unstressed test was also conducted to obtain the free thermal strain as a function of temperature. The first phase thus consisted of loading the specimen to reach the target stress level. Afterwards, the furnace was activated and proceeded to heat up the specimens with a rate of 5°C/min. During the heating phase, the stress level was maintained constant using a load control method (thus the position of the pins had to be adjusted to compensate for thermal expansion). The temperature of the specimens was measured by the average readings of the three external thermocouples throughout the test. Heating continued until fracture of the specimen. The transient-state tests generate temperature-strain curves at different stress levels, which then compiled together can be converted into stress-strain curves at different temperatures.

### **3.3.4 Definition of material properties**

During the test, the applied force was recorded from the load cell, while the strain was measured by both extensometer and DIC method. As long as the strain was smaller than 20%, the value measured from the extensometer was used. Once the strain exceeded 20%, the value measured from the DIC was used up to the threshold of 40%. Material properties obtained from the tests include the elastic modulus  $E$ , 0.2% proof stress  $f_{0.2}$ , yield stresses at strain level of 0.5%  $f_{0.5}$ , 1.5%  $f_{1.5}$ , and 2.0%  $f_{2.0}$ , ultimate stress  $f_u$ , and elongation at fracture  $\epsilon_f$ , which are defined in Figure 18. The ultimate stress  $f_u$  is the maximum stress value measured during the loading. The elongation at fracture  $\epsilon_f$  is the strain at the onset of fracture. The 0.2% proof stress is defined as the stress needed to impart 0.2% plastic strain; its evaluation requires knowledge of the elastic modulus.



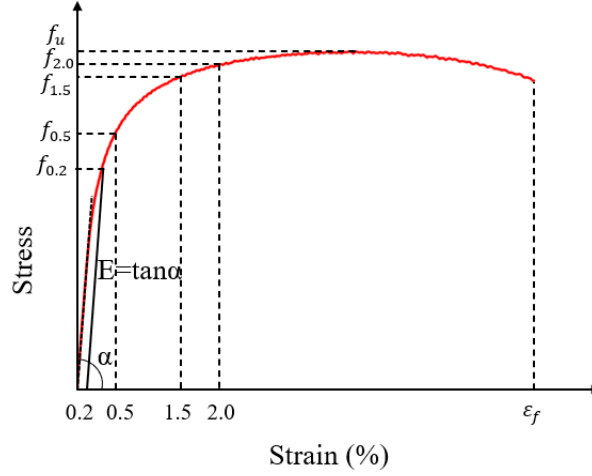


Figure 18. Definition of symbols used for the material properties.

The elastic modulus is defined as the initial slope of the stress-strain curve. However, elastic modulus measurement from a tension test is difficult in practice due to the finite resolution of the extensometers and to the measurement errors which pollute the measurements at very small strain levels. Therefore, it is common to measure the elastic modulus  $E$  as the slope of the region of the stress-strain curve between stress levels of 0.20 and 0.45 times the nominal yield stress [49]. Here, the elastic modulus is defined according to Eq. (3) and Eq. (4), where it is noted that the elevated temperature yield stress is a priori unknown (since it depends on the modulus) and hence is approximated as the product of its ambient temperature value times the retention factor on the ultimate stress:

$$E_t = \frac{0.45f_{y,t} - 0.2f_{y,t}}{\varepsilon(\sigma = 0.45f_{y,t}) - \varepsilon(\sigma = 0.2f_{y,t})} \quad (3)$$

$$f_{y,t} = \frac{f_{u,t}}{f_{u,20}} f_{y,20} \quad (4)$$

where  $f_{y,t}$  is the nominal yield stress at elevated temperature;  $\varepsilon(\sigma = 0.45f_{y,t})$  is the strain measured when the stress equals 45% of the nominal yield stress at elevated temperature;  $f_{u,t}$  is

the measured ultimate stress at elevated temperature;  $f_{u,20}$  is the measured ultimate stress at ambient temperature;  $f_{y,20}$  is the nominal yield stress at ambient temperature.

The reduction in mechanical properties due to temperature is described through the definition of retention factors, defined as the ratio of the value of the property obtained at elevated temperature to the value obtained at ambient temperature. These retention factors are noted as  $k_E$  for elastic modulus,  $k_{0.2}$  for the 0.2% proof stress,  $k_{0.5}$  for the stress at 0.5% strain,  $k_{1.5}$  for the stress at 1.5% strain,  $k_{2.0}$  for the stress at 2.0% strain, and  $k_u$  for the ultimate stress.

### **3.4 Steady-state test results**

#### **3.4.1 Failure modes**

The specimens after the steady-state tests are shown in Figure 19. The specimens became darker with increasing temperature, and showed flaking when the temperature was above 600°C. The failure always occurred in the reduced parallel section, as expected. For Mild-395, HSLA-700, DP-340 and DP-700, the specimens did not show clear necking up to 200°C. When the temperature was above 300°C, the specimens became softer, and the failure mode showed more ductile failures. MS-1030 and MS-1200 showed a similar trend in failure mode. With increasing temperature, the specimens became softer and showed more ductile failures, with increasing fracture strain and clear necking phenomena.

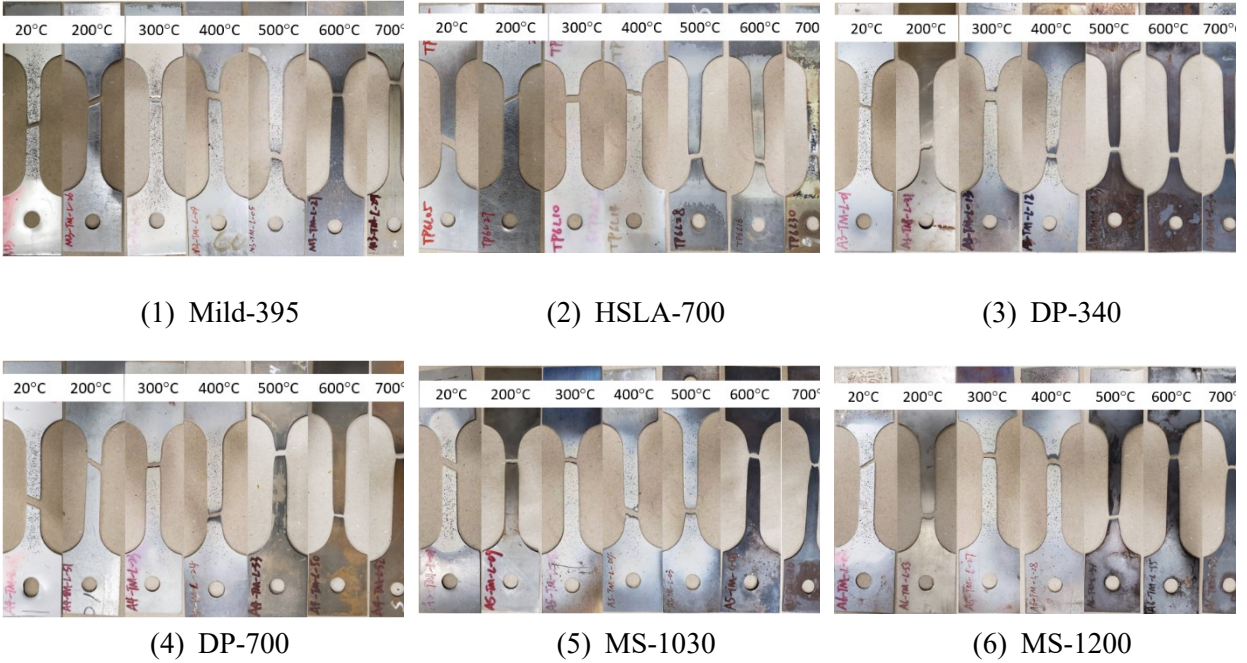
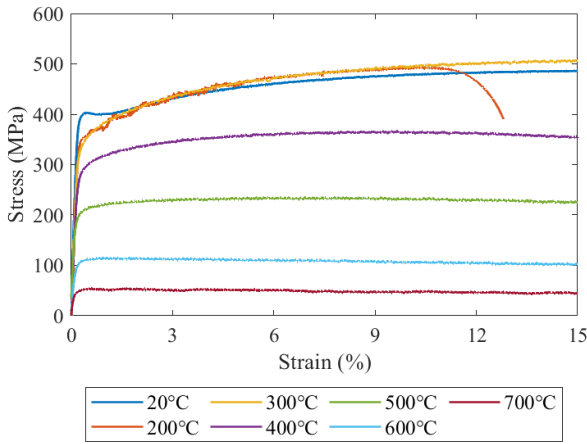


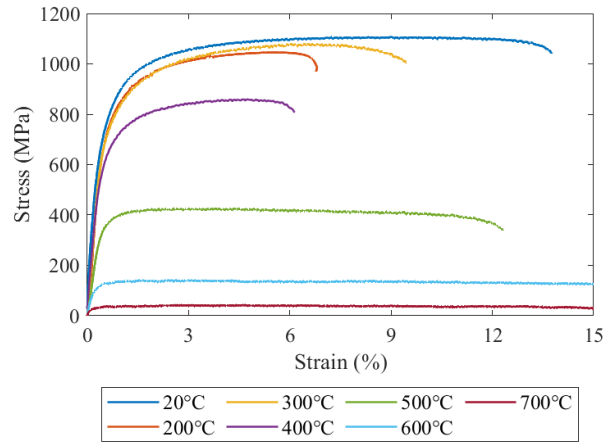
Figure 19. Failure modes of specimens in steady-state tests.

### 3.4.2 Test results

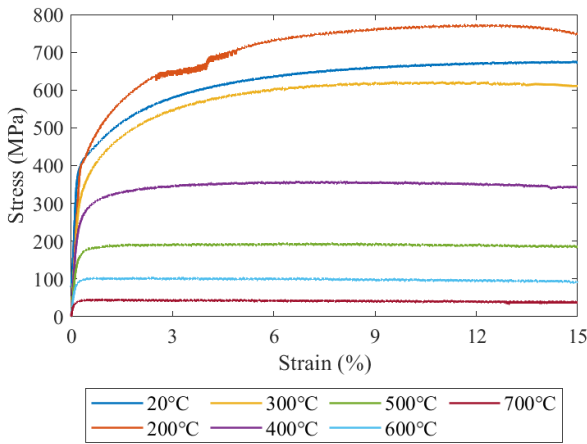
The stress-strain curves obtained from the steady-state tests are presented in Figure 20. The overall trend of reduced strength and stiffness with increasing temperature is observed. Table 12 lists the mechanical properties of the six steel types obtained from ambient temperature tension testing. Using the measured ambient temperature properties and the measured elevated temperature properties, the retention factors can be derived. Table 13 to Table 18 give the retention factors for the elastic modulus  $k_E$ , the 0.2% proof stress  $k_{0.2}$ , the stress at 0.5% strain  $k_{0.5}$ , the stress at 1.5% strain  $k_{1.5}$ , the stress at 2.0% strain  $k_{2.0}$ , and the ultimate stress  $k_u$  obtained from the steady-state tests. The measured elongation at fracture  $\epsilon_f$  is also given. For the tests that were repeated thrice, the mean values and coefficient of variation were calculated. Results show that the coefficient of variation for the repeated tests is smaller than 5%. Thus, in the subsequent test campaign, only one test was carried out for each type of steel at the other elevated temperatures. For the repeated tests, the averaged values are provided in the tables.



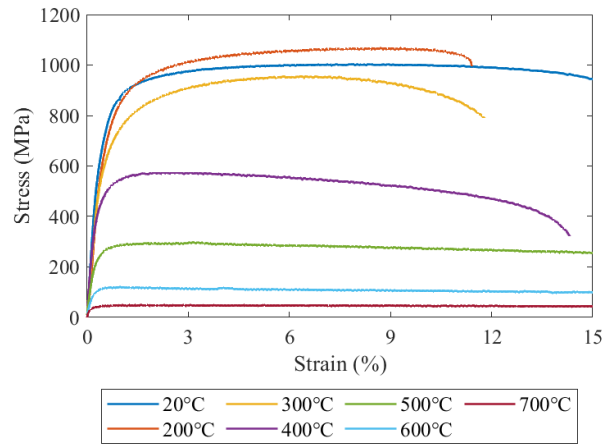
(1) Mild-395



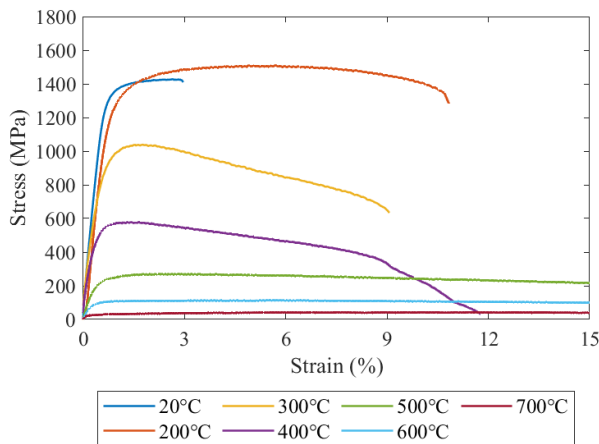
(2) HSLA-700



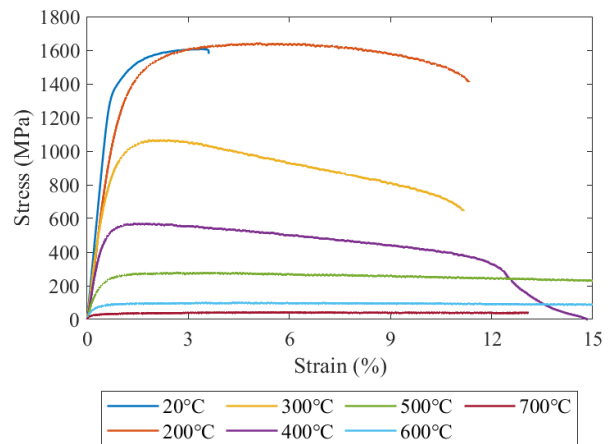
(3) DP-340



(4) DP-700



(5) MS-1030



(6) MS-1200

Figure 20. Stress-strain curves obtained from steady-state tests.

Table 12. Mechanical properties obtained from ambient temperature tension testing.

Steel type	Elastic modulus (MPa)	$f_{0.2}$ (MPa)	$f_{0.5}$ (MPa)	$f_{1.5}$ (MPa)	$f_{2.0}$ (MPa)	$f_u$ (MPa)	$\epsilon_f$ (%)
MS-395	213,021	399	399	403	410	485	28.20
HSLA-700	217,988	752	729	974	1013	1106	13.77
DP-340	206,767	424	431	514	542	675	20.81
DP-700	209,772	762	723	947	971	1026	16.87
MS-1030	215,648	1327	1085	1406	1418	1428	2.95
MS-1200	208,609	1387	1030	1528	1572	1608	3.61

Table 13. Retention factors of elastic modulus, yield stress, and ultimate stress, and elongation at fracture for Mild-395 from steady-state tests.

T (°C)	$k_E$	$k_{0.2}$	$k_{0.5}$	$k_{1.5}$	$k_{2.0}$	$k_u$	$\epsilon_f$ (%)
20	1.00	1.00	1.00	1.00	1.00	1.00	28.20
200	0.86	0.90	0.90	0.99	1.01	1.01	12.80
300	0.75	0.89	0.89	1.00	1.01	1.06	21.74
400	0.66	0.74	0.75	0.81	0.81	0.75	24.23
500	0.55	0.53	0.54	0.55	0.55	0.48	31.26
600	0.43	0.28	0.28	0.28	0.27	0.24	>40.00
700	0.28	0.13	0.13	0.13	0.13	0.11	>40.00

Table 14. Retention factors of elastic modulus, yield stress, and ultimate stress, and elongation at fracture for HSLA-700 from steady-state tests.

T (°C)	$k_E$	$k_{0.2}$	$k_{0.5}$	$k_{1.5}$	$k_{2.0}$	$k_u$	$\epsilon_f$ (%)
20	1.00	1.00	1.00	1.00	1.00	1.00	13.77
200	0.83	0.98	0.93	0.95	0.96	0.94	6.81
300	0.76	0.98	0.93	0.94	0.95	0.98	11.72
400	0.80	0.95	0.91	0.92	0.93	0.94	5.79
500	0.68	0.82	0.80	0.80	0.78	0.75	13.79
600	0.31	0.16	0.18	0.14	0.14	0.13	>40.00
700	0.23	0.04	0.05	0.04	0.04	0.04	>40.00

Table 15. Retention factors of elastic modulus, yield stress, and ultimate stress, and elongation at fracture for DP-340 from steady-state tests.

T (°C)	$k_E$	$k_{0.2}$	$k_{0.5}$	$k_{1.5}$	$k_{2.0}$	$k_u$	$\epsilon_f$ (%)
20	1.00	1.00	1.00	1.00	1.00	1.00	20.81
200	0.83	1.01	1.02	1.11	1.12	1.14	17.32
300	0.73	0.85	0.86	0.93	0.93	0.92	21.45
400	0.64	0.65	0.67	0.64	0.62	0.53	22.88
500	0.55	0.41	0.42	0.37	0.35	0.29	35.24
600	0.47	0.23	0.23	0.20	0.19	0.15	>40.00
700	0.36	0.10	0.10	0.09	0.08	0.07	>40.00

Table 16. Retention factors of elastic modulus, yield stress, and ultimate stress, and elongation at fracture for DP-700 from steady-state tests.

T (°C)	$k_E$	$k_{0.2}$	$k_{0.5}$	$k_{1.5}$	$k_{2.0}$	$k_u$	$\epsilon_f$ (%)
20	1.00	1.00	1.00	1.00	1.00	1.00	16.87
200	0.84	0.97	0.92	1.01	1.03	1.07	11.41
300	0.78	0.88	0.90	0.91	0.93	0.97	12.01
400	0.70	0.65	0.67	0.61	0.61	0.58	16.08
500	0.51	0.34	0.37	0.32	0.31	0.30	34.45
600	0.32	0.15	0.16	0.13	0.12	0.12	>40.00
700	0.22	0.05	0.06	0.05	0.05	0.05	>40.00

Table 17. Retention factors of elastic modulus, yield stress, and ultimate stress, and elongation at fracture for MS-1030 from steady-state tests.

T (°C)	$k_E$	$k_{0.2}$	$k_{0.5}$	$k_{1.5}$	$k_{2.0}$	$k_u$	$\epsilon_f$ (%)
20	1.00	1.00	1.00	1.00	1.00	1.00	2.95
200	1.01	0.85	0.80	0.99	1.02	1.06	10.83
300	0.80	0.70	0.73	0.74	0.73	0.73	9.07
400	0.54	0.41	0.47	0.41	0.40	0.40	11.78
500	0.29	0.17	0.20	0.19	0.19	0.19	24.55
600	0.19	0.07	0.09	0.08	0.08	0.08	>40.00
700	0.09	0.02	0.03	0.02	0.02	0.03	>40.00

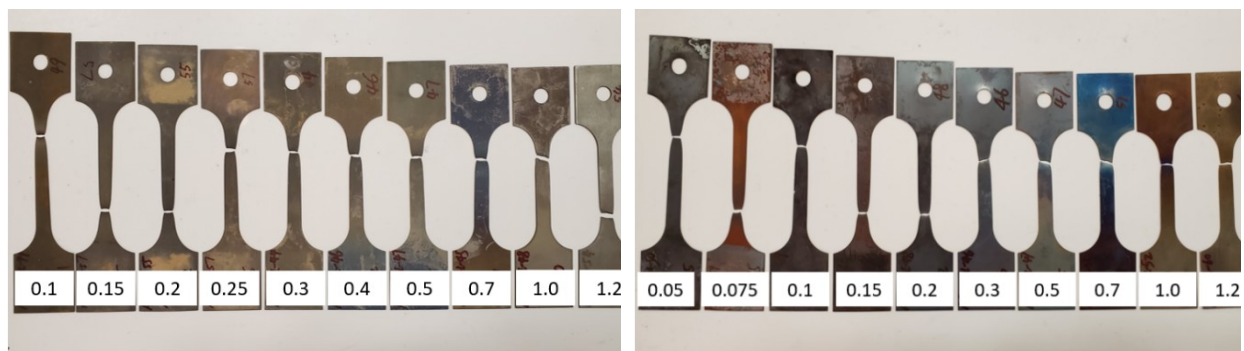
Table 18. Retention factors of elastic modulus, yield stress, and ultimate stress, and elongation at fracture for MS-1200 from steady-state tests.

T (°C)	$k_E$	$k_{0.2}$	$k_{0.5}$	$k_{1.5}$	$k_{2.0}$	$k_u$	$\epsilon_f$ (%)
20	1.00	1.00	1.00	1.00	1.00	1.00	3.61
200	0.85	0.88	0.86	0.95	0.97	1.01	11.03
300	0.73	0.64	0.68	0.69	0.68	0.67	11.17
400	0.54	0.37	0.44	0.37	0.36	0.35	14.94
500	0.32	0.16	0.21	0.18	0.17	0.17	30.18
600	0.18	0.06	0.08	0.06	0.06	0.06	>40.00
700	0.09	0.02	0.03	0.02	0.02	0.03	>40.00

### 3.5 Transient-state test results

#### 3.5.1 Failure modes

The specimens after the transient-state tests are shown in Figure 21. The failure always occurred in the reduced section, as expected. For both DP-700 and MS-1200, with the load level decreasing (from the right of the picture to the left), the failure temperature increased, and the specimens showed extended necking with higher ductility. The thermal expansion of the specimen with increasing fracture temperature (from the right of the picture to the left) is also visible.



(1) DP-700

(2) MS-1200

Figure 21. Failure modes of specimens in transient-state tests.

### 3.5.2 Thermal strain

For the transient-state tests, the measured strain under a given stress state at elevated temperature is composed of mechanical strain and thermal strain. To obtain the mechanical strain, it is thus necessary to subtract the thermal strain from the total (measured) strain. Therefore, zero-load tests were carried out for both DP-700 and MS-1200 to measure the thermal strain. The obtained free thermal strain of DP-700 and MS-1200 are compared with the models in EC3 [35] and the test results from Li and Young [28], in Figure 22. The thermal strain evolution is similar for the DP-700 and MS-1200 steels; additionally they agree well with the results from Li and Young [28]. The EC3 [35] model is slightly higher than the measured thermal strain for temperatures up to 670°C. Overall, the thermal expansion of AHSS is independent of the steel type. The prediction of thermal expansion given by EC3 [35] is applicable for the tested cold-formed AHSS steels for temperature up to 700°C.

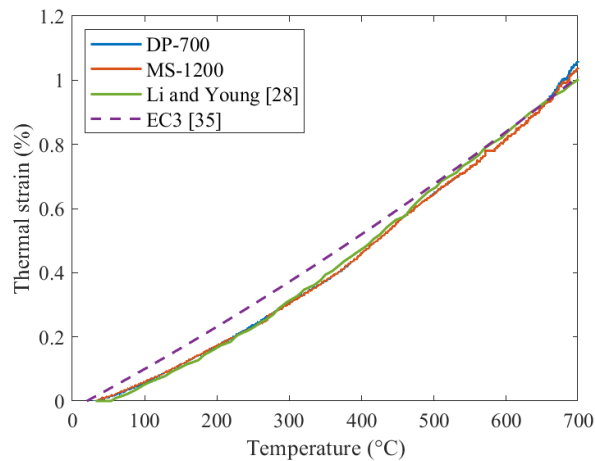


Figure 22. Comparison of measured thermal strain with EC3 [35] and test data in literature.

### 3.5.3 Test results

In the transient-state tests, the total strain in the specimen gauge section is measured as a function of the temperature which is increasing at a constant rate. A constant tension stress value is



maintained in the specimen. The failure temperatures at different stress levels are listed in Table 19 for the two tested materials, DP-700 and MS-1200. The failure temperature is defined as the temperature of the steel when the specimen fractures under the constantly applied stress.

After subtracting the thermal strain (characterized in Section 3.5.2) from the total strain (measured), the relationship between the mechanical strain and the temperature is obtained at different stress level. The full set of temperature-mechanical strain curves obtained from different stress levels were converted into stress-strain curves at different elevated temperature levels as shown in Figure 23. Since the number of stress levels is limited, it is not possible to extract a (continuous) full stress-strain curve and the curve is described by a number of discrete points. Notably, the post-yield behavior is difficult to capture. The ultimate stress at a specific temperature cannot be established (rather, the ultimate temperature at a specific stress is obtained from the test; in general, this ultimate temperature is not a round value of interest such as 500°C, 600°C etc.). Further, the higher the temperature at which the stress-strain curve is established, the smaller the number of data points on the stress-strain curve is, because specimens stressed at high level have already failed at lower temperatures. Here, the applied stress levels range from 0.05 to 1.2 times the nominal yield stress of the specimen, for a total of 11 tests per steel type (including the free thermal strain test). Stress-strain curves are reconstructed for temperatures up to 600°C.

Table 19. Failure temperatures at various stress level for transient-state tests.

Steel type	Load level (of $f_{y,20}$ )	Load level (of $f_{u,20}$ )	Applied stress (MPa)	Failure temperature (°C)
DP-700	0.1	0.07	70	672
	0.15	0.11	105	640
	0.2	0.14	140	600
	0.25	0.18	175	577
	0.3	0.21	210	562
	0.4	0.29	280	525
	0.5	0.36	350	504
	0.7	0.50	490	466
	1.0	0.71	700	417
	1.2	0.86	840	363
MS-1200	0.05	0.04	60	670
	0.075	0.06	90	648
	0.1	0.08	120	599
	0.15	0.12	180	558
	0.2	0.16	240	524
	0.3	0.24	360	477
	0.5	0.4	600	400
	0.7	0.56	840	366
	1	0.8	1200	306
	1.2	0.96	1440	271

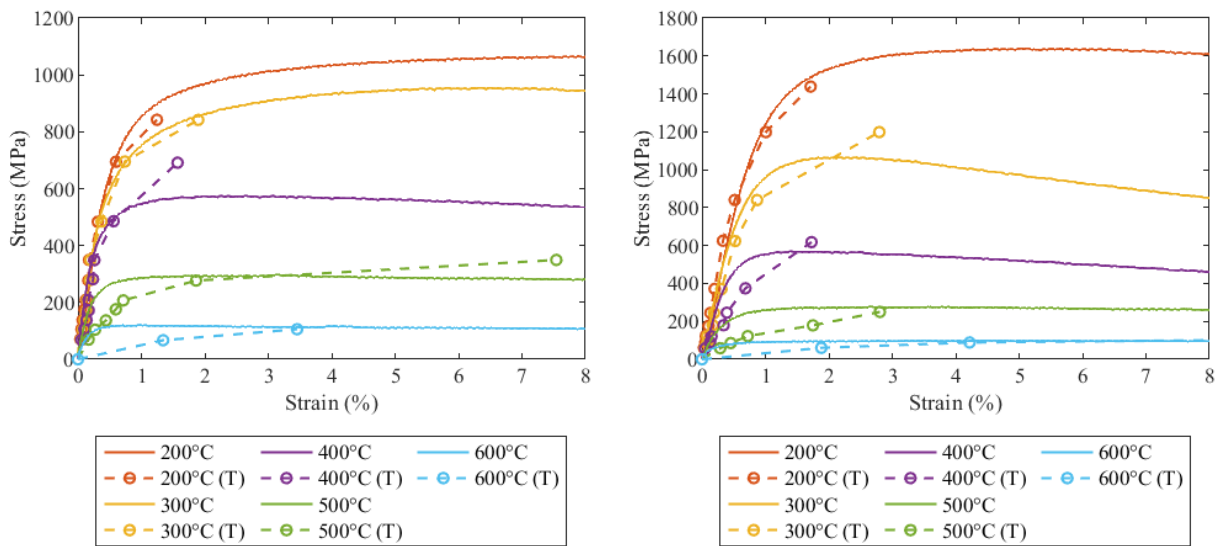
The material properties are listed in Table 20 and Table 21. These include the elastic modulus  $E$ , the 0.2% proof stress  $f_{0.2}$ , the stress at 0.5% strain  $f_{0.5}$ , the stress at 1.5% strain  $f_{1.5}$  and the stress at 2.0% strain  $f_{2.0}$ . The stress at 1.5% and 2.0% strain were not obtained for some of the lower temperatures because the measured strain at 1.2 times the nominal yield stress (which was the highest investigated stress level) was smaller than 1.5% or 2.0%, respectively. The ultimate stress and elongation at fracture cannot be obtained from transient-state tests as explained above.

Calculation of the elastic modulus  $E$  requires a minor modification of Eq. (3)-(4) for transient-state tests. Since the ultimate stress at a specific temperature cannot be measured from transient-state tests, Eq. (4) for the nominal yield stress at elevated temperature  $f_{y,t}$  is modified into Eq. (5):

$$f_{y,t} = \frac{f_{0.5,t}}{f_{0.5,20}} f_{y,20} \quad (5)$$

where  $f_{0.5,t}$  is the stress at 0.5% strain at elevated temperature;  $f_{0.5,20}$  is the stress at 0.5% strain at ambient temperature. The meaning of replacing Eq. (4) by Eq. (5) is that the *a priori* unknown retention factor for the nominal yield stress is taken as the measured retention factor for the stress at 0.5% strain (Eq. (5)) instead of that of the ultimate stress. That retention factor is used to evaluate  $f_{y,t}$  which is required to evaluate the elastic modulus  $E$  (Eq. (3)).

The elevated temperature retention factors are listed in Table 20 and Table 21 for the elastic modulus  $k_E$ , the 0.2% proof stress  $k_{0.2}$ , the stress at 0.5% strain  $k_{0.5}$ , the stress at 1.5% strain  $k_{1.5}$ , and the stress at 2.0% strain  $k_{2.0}$  obtained from transient-state tests.



(1) DP-700

(2) MS-1200

Figure 23. Comparison of stress-strain curves obtained from steady-state and transient-state tests (transient-state test results are marked with 'T' in the legend).

Table 20. Retention factors of elastic modulus and yield stress for DP-700 from transient-state tests.

T (°C)	$k_E$	$k_{0.2}$	$k_{0.5}$	$k_{1.5}$	$k_{2.0}$
100	0.88	0.95	0.94	-	-
150	0.80	0.95	0.91	-	-
200	0.75	0.95	0.87	-	-
250	0.76	0.90	0.83	-	-
300	0.75	0.81	0.78	0.85	-
350	0.72	0.71	0.72	0.78	0.79
400	0.63	0.65	0.64	0.73	-
450	0.26	0.52	0.45	0.49	-
500	0.20	0.27	0.21	0.27	0.29
550	0.08	0.15	0.11	0.14	0.15
600	0.02	0.10	0.04	0.07	0.08

Table 21 Retention factors of elastic modulus and yield stress for MS-1200 from transient-state tests.

T (°C)	$k_E$	$k_{0.2}$	$k_{0.5}$	$k_{1.5}$	$k_{2.0}$
100	1.10	0.89	0.92	-	-
150	1.05	0.75	0.85	-	-
200	0.95	0.70	0.78	0.90	-
250	0.88	0.63	0.71	0.83	0.87
300	0.57	0.61	0.57	0.63	0.67
350	0.36	0.49	0.38	0.52	-
400	0.23	0.37	0.28	0.37	-
450	0.18	0.20	0.15	0.24	-
500	0.10	0.09	0.09	0.11	0.13
550	0.04	0.06	0.04	0.06	0.07
600	0.02	0.05	0.02	0.03	0.04

### 3.6 Comparison and discussion

#### 3.6.1 Elastic modulus

Figure 24 plots the retention factors of elastic modulus. The elastic modulus decreases with increasing temperature. From steady-state tests, the DP-340 and DP-700 exhibit a similar reduction pattern between them when the temperature is below 500°C but some discrepancy is observed at 600°C and 700°C. For MS-1030 and MS-1200, the reduction curves are almost overlapping at

elevated temperature, except at 200°C where the MS-1200 shows a clear reduction of elastic modulus while the MS-1030 does not.

The retention factors of elastic modulus obtained from transient-state tests (Table 20 and **Error! Reference source not found.**) are compared with those obtained from steady-state tests. For DP-700, the two testing methods yield similar results up to 400°C, but at temperatures higher than 400°C the reduction in modulus is more marked for the transient-state tests than for the steady-state tests. At 600°C, DP-700 tested by steady-state method retains almost 32% of its elastic modulus at ambient temperature, while in transient-state test DP-700 retains less than 3% of its elastic modulus at ambient temperature. This may be due to the thermal creep effect [28] which becomes non-negligible when the temperature is higher than one third of the melting temperature of the material. Besides, the limited number of data points obtained from transient-state tests in the small strain range may also influence the measured elastic modulus. For MS-1200, the elastic modulus measured from transient-state test is higher than that from steady-state test for temperature lower than 300°C, beyond which the elastic modulus decreases at a higher rate in transient-state test than in steady-state test. This suggests that the thermal creep effect becomes noticeable at lower temperature for MS-1200 than for DP-700.

The retention factors of elastic modulus obtained in this study are also compared with design codes (EC3 [35] and AISC-360 [40]) and literature data in Figure 24. The AISC [40] is used for comparison for the US because, even though cold-formed steel that is not hollow tubes is generally designed by AISI standard [20], the AISI [20] currently does not provide information about material properties at elevated temperature. The figure also includes data from tests on cold-formed high-strength steels published in the literature. The retention factors provided in EC3 [35] are almost the same as those in AISC [40]. Generally, the retention factors predicted by EC3 [35]

and AISC [40] provide a higher bound for test results obtained in this study. This means the provisions in EC3 [35] and AISC [40] are not conservative for structural design using advanced AHSS steels. In addition, comparisons to previously published data also highlight that the behavior of the AHSS tested in this study is different from previously reported results on other steel types. The factors  $k_E$  given by Chen and Young [22] and Li and Young [28] are larger than these of the AHSS for temperature higher than 200°C. The  $k_E$  predicted by Lee et al. [27] show a similar reduction pattern as the DP steels in this study but are unconservative for MS steels. It is noteworthy that Li and Young [28] also provided results for both steady-state and transient-state tests. As in this study, Li and Young [28] found a significantly lower retention factor of elastic modulus from transient-state tests compared with steady-state tests when the elevated temperature exceeds 400°C, especially for the specimens with nominal yield stress of 900 MPa. This may be attributed to the thermal creep effect [28].

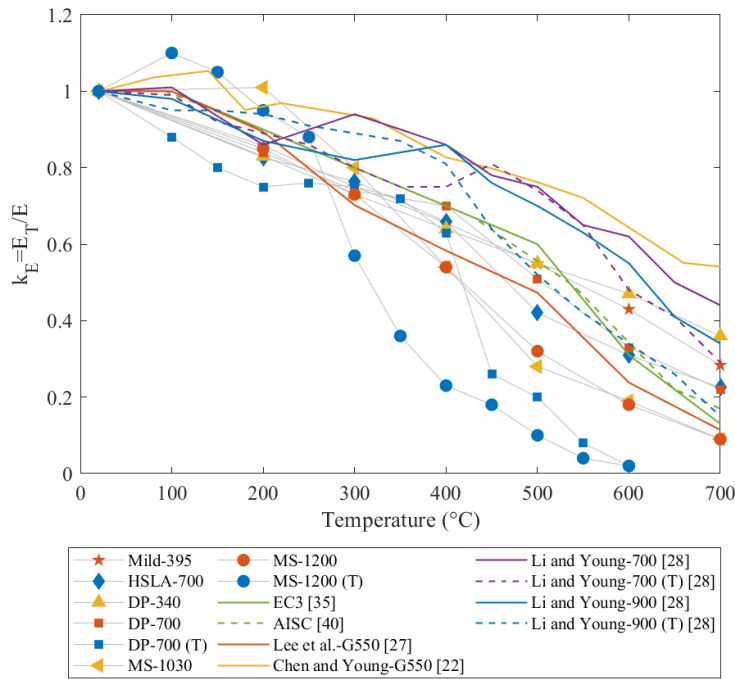


Figure 24. Comparison of elastic modulus (transient-state test results are marked with ‘T’ in the legend).

### 3.6.2 Yield stress

The elevated temperature retention factors for yield stress (given in Table 13 to Table 18) are plotted in Figure 10 for the 2% yield stress and in Figure 11 for the 0.2% proof stress. For Mild-395, HSLA-700, DP-340, and DP-700, the yield stress is maintained approximately at its ambient temperature level for temperatures up to 300°C. Once the temperature reaches 400°C, the yield stress starts to decrease noticeably, and it is less than 10% of its ambient temperature capacity for temperature higher than 700°C. For MS-1030 and MS-1200, the yield stress starts to decrease noticeably when the temperature reaches 300°C. Note that the 0.2% proof stress is dependent on the measured elastic modulus. When comparing the reduction of yield stress for steels of the same alloy (i.e. DP-340 to DP-700, and MS-1030 to MS-1200), the two tested grades of the same alloy

show similar reduction pattern. The minor observed difference is in the direction of the higher grade experiencing a slightly greater relative strength loss at elevated temperature.

The retention factors for 0.2% proof stress and for stress at 2.0% strain obtained from transient-state tests are close to those from steady-state tests. For DP-700 and MS-1200, the yield stresses obtained from the two test methods agree quite well for temperature up to 500°C while a slight discrepancy is observed beyond 500°C. Overall, unlike with the elastic modulus, there is no significant effect of the testing method (transient-state tests vs steady-state tests) on the yield stress retention factors.

The test data from this study are compared with the design codes EC3 [35] and AISC [40] and with data from the literature. For the 2.0% yield stress (Figure 25), the yield stress retention factors in EC3 [35] and AISC [40] are almost identical and are based on hot-rolled conventional grade steels. These code factors provide unconservative predictions for the cold-formed materials in this study, especially for temperatures of 400°C and higher. The retention factors obtained by Li and Young [28] and by Lee et al. [27] are also greater than those in this study. The retention factors obtained by Chen and Young [22] lie within the range of the results in this study, with a very large reduction at 500 °C. The 0.2% proof stress factors are compared with the prediction in EC3 [35] on cold-formed class 4 section (Figure 26). Data for the 0.2% proof strength of the mild-395 material tested in this study agrees well with the EC3 [35] class 4 curve, which provides a good benchmark for the testing campaign. However, for the AHSS, it is clear that the EC3 [35] provides unconservative predictions of the reduction in 0.2% proof stress with temperature. The retention factors obtained from this study are generally smaller than those from codes and from most of the other tests, which suggests that the cold-formed AHSS are more affected by elevated temperature and hence might be more vulnerable to fire.



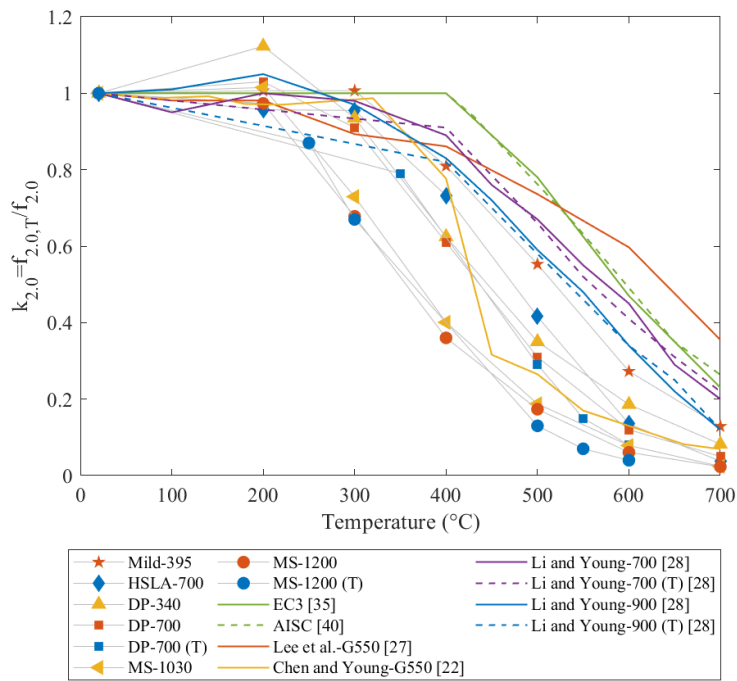


Figure 25. Comparison of 2.0% yield stress (transient-state test results are marked with ‘T’ in the legend).

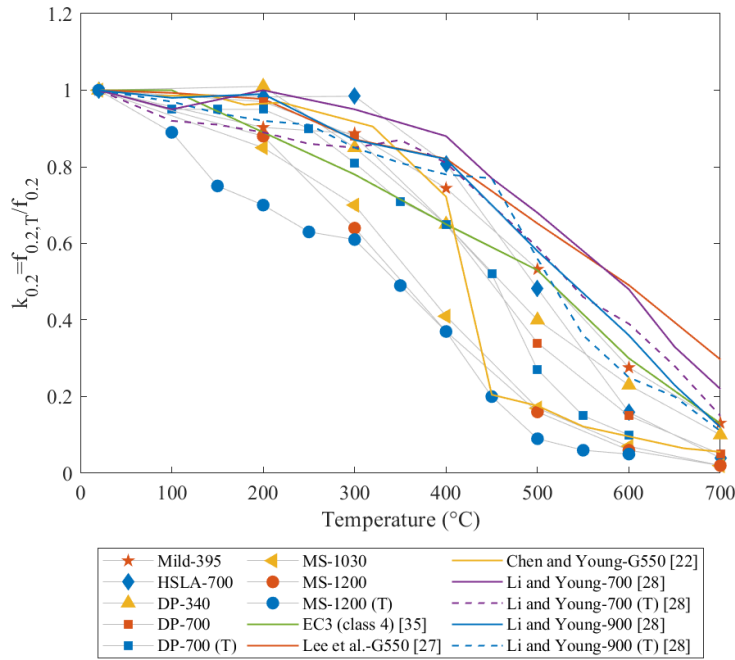


Figure 26. Comparison of 0.2% proof stress (transient-state test results are marked with ‘T’ in the legend).

### 3.6.3 Ultimate stress

The retention factors of ultimate stresses for the six steel types are summarized in Table 13 to Table 9. As shown in Figure 27, for Mild-395, HSLA-700, DP-340, and DP-700, the ultimate stress is maintained approximately at its ambient temperature level for temperature up to 300°C, and starts to decrease noticeably when the temperature reaches 400°C. For MS-1030 and MS-1200, the ultimate stress starts to decrease noticeably when the temperature reaches 300°C.

The retention factors of ultimate stress obtained from the steady-state tests are compared with the EC3 (Annex A) [35] and the AISC [40] and other ultimate stress data in the literature, as shown in Figure 27. The EC3 [35] predicts a larger reduction of ultimate stress at elevated temperature than the AISC [40]. Both standards provide unconservative predictions for the materials investigated in this study. The retention factors obtained by Li and Young [28] again provide an upper bound to

the data presented herein. The retention factors predicted by Chen and Young [22] show a somewhat similar reduction pattern as with the AHSS of this study, with a sudden reduction at 500°C.

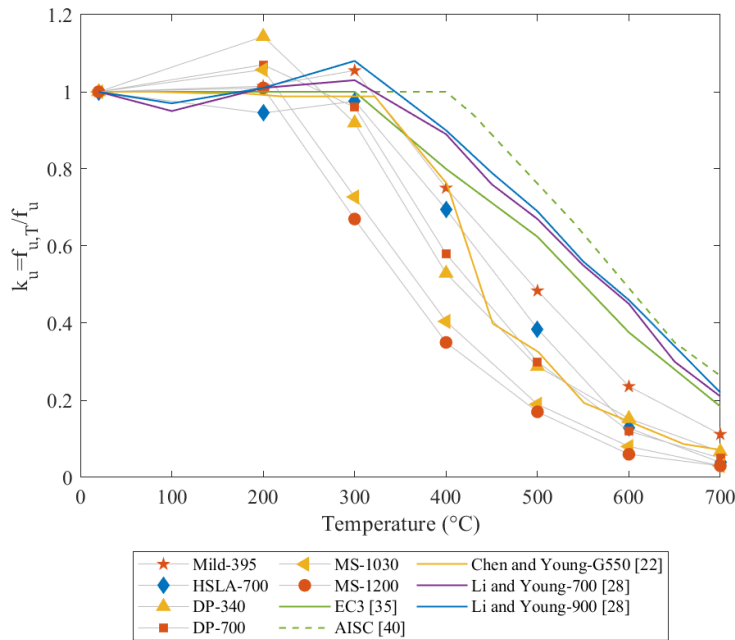


Figure 27. Comparison of ultimate stress obtained from steady-state tests.

### 3.6.4 Elongation at fracture

The elongation at fracture shows the ability of steel to deform and elongate plastically before fracture or failure. The measured values of elongation at fracture are shown in Figure 28. The maximum measurable strain limit was 40% due to the capacity of the DIC system. When the elongation at fracture was larger than 40%, a minimum value of 40% was marked (in Table 13 to Table 18) and the point was not reported in Figure 9. For Mild-395, DP-340, and DP-700, the elongation of fracture reduced at 200°C and then started to increase beyond that. For HSLA-700, the elongation at fracture was lower than ambient at 200°C, 300°C, and 400°C, and then increased

when the temperature reached 500°C and higher. For MS-1030 and MS-1200, the elongation at fracture increased with increasing temperature.

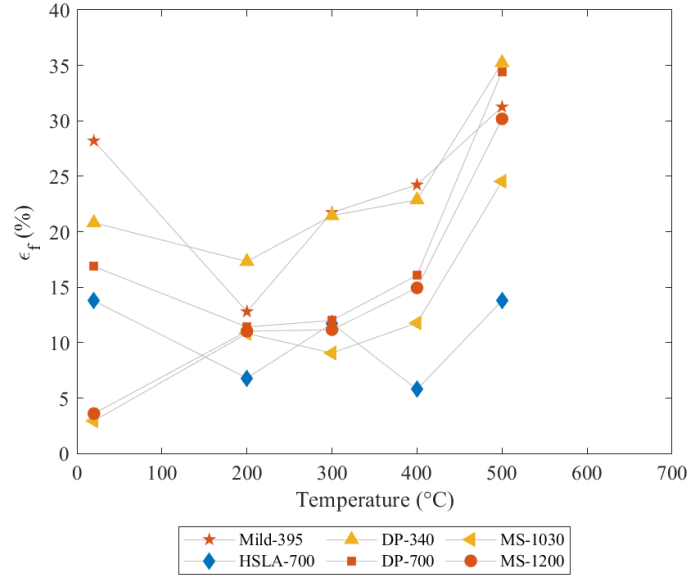


Figure 28. Elongation at fracture  $\epsilon_f$  obtained from steady-state tests. Note 40% is the maximum measurable strain in the test setup, which was exceeded at 600°C and 700°C.

### 3.7 Predictive models

Comparisons in Section 3.6 show that the tested AHSS exhibit larger reduction at elevated temperature than lower grade cold-formed steels, and the current provisions in design codes and standards are not applicable to the tested ASHSS. Thus, new predictive models are proposed to determine the mechanical properties of the cold-formed AHSS steels at elevated temperature in this section. A three-coefficient equation, derived from committee work with the American Iron and Steel Institute to determine the mechanical properties of normal grade cold-formed steels at elevated temperature [50], is adopted. As expressed in Eq. (6) and Eq. (7), the retention factor  $k_x$  is a function of temperature normalized within the temperature range of 20°C~700°C. The subscript  $X$  stands for the mechanical properties, namely elastic modulus  $E$ , 0.2% proof stress  $f_{0.2}$ ,

stress at 2.0% strain  $f_{2.0}$ , and ultimate stress  $f_u$ . This format has the advantage of using a single continuous function with a small number of coefficients to express the reduction trend of the mechanical properties at elevated temperature.

$$k_x = (1 - c) \cdot \frac{1 - x^b}{1 + ax^b} + c \quad (6)$$

$$x = \frac{T - T_1}{T_2 - T_1}, T_1 = 20^\circ\text{C}, T_2 = 700^\circ\text{C} \quad (7)$$

The coefficients a, b, and c are calibrated based on the test data in this study. For the tested AHSS in this study, DP-340 and DP-700 are sorted into the same group labelled ‘AHSS-DP’ due to the fact that they show very similar reduction trend in yield stress and ultimate stress at elevated temperature. MS-1030 and MS-1200 are sorted in another group labelled ‘AHSS-MS’. The calibrated coefficients to characterize the retention factors are given in Table 22. Comparisons showed that the testing method noticeably affect the measured elastic modulus of DP-700 and MS-1200, while it has no significant influence on the yield stress of the two steels. Thus, different coefficients are calibrated for the elastic modulus of AHSS, with one set of coefficients calibrated based on the steady-state test data and another set calibrated based on the transient-state test data. For the yield stress of AHSS, the coefficients are calibrated based on both steady-state and transient-state test data. The  $R^2$  value is also provided for each row in the table.

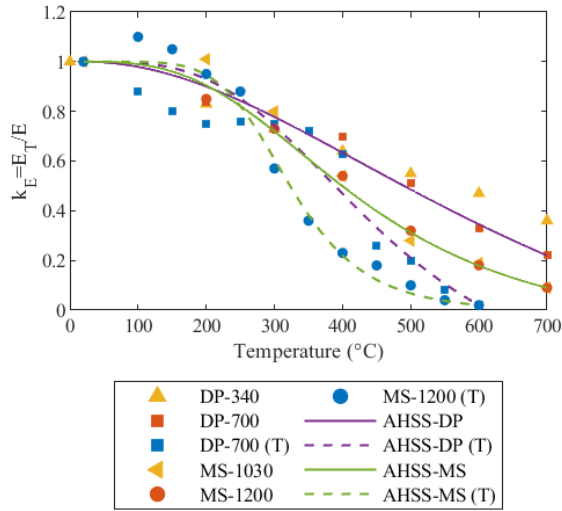
Table 22. Coefficients to determine the retention factors for the mechanical properties of cold-formed AHSS steels.

Properties	Data set	Test method	a	b	c	$R^2$
Elastic modulus	AHSS-DP	SS	0.95	2.0	0.22	0.926
		TS	2.6	3.3	0.02	0.774
	AHSS-MS	SS	4.4	2.9	0.09	0.984
		TS	35.0	5.5	0.02	0.919
0.2% proof stress	AHSS- DP	SS+TS	8.5	4.6	0.05	0.983
	AHSS- MS	SS+TS	9.2	3.0	0.02	0.962
Stress at 2.0% strain	AHSS- DP	SS+TS	17	6.1	0.05	0.987
	AHSS- MS	SS+TS	28.4	4.7	0.02	0.995

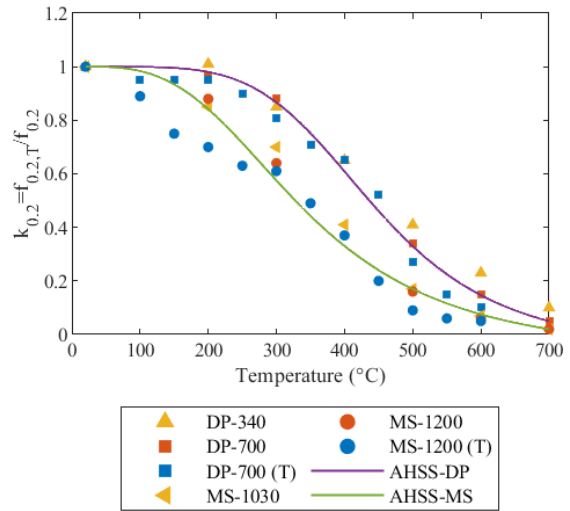
Ultimate stress	AHSS- DP	SS	23.8	5.9	0.05	0.981
	AHSS- MS	SS	30.4	4.8	0.03	0.990

Note: 'SS' stands for steady-state test; 'TS' stands for transient-state test.

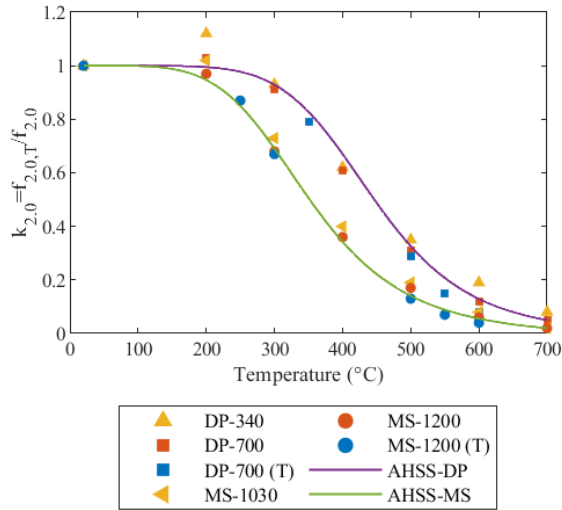
The proposed retention factors for elastic modulus  $k_E$ , 0.2% proof stress  $k_{0.2}$ , stress at 2.0% strain  $k_{2.0}$ , and ultimate stress  $k_u$  of the tested materials at elevated temperature are shown in Figure 29. For the elastic modulus, the predicted retention factors calibrated from transient-state tests are marked with dash lines. It is shown that the proposed retention factors generally provide a lower bound for the corresponding data set, hence are conservative for the tested cold-formed AHSS steels for temperature up to 700°C.



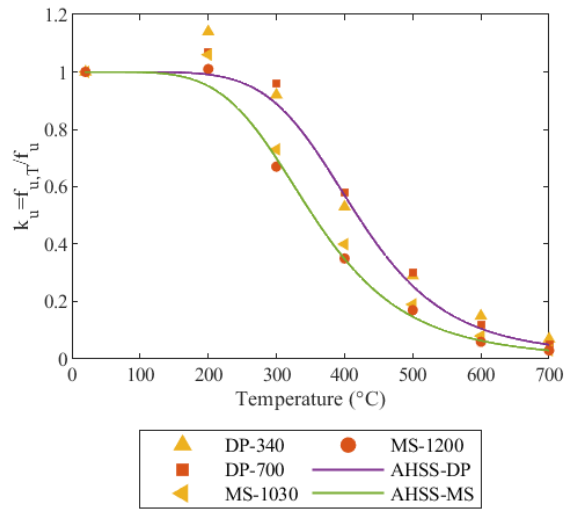
(1) elastic modulus



(2) 0.2% proof stress



(3) stress at strain level of 2.0%



(4) ultimate stress

Figure 29 Comparison of proposed retention factors with test data.

### 3.8 Conclusions

An experimental investigation was carried out on the mechanical properties of cold-formed steels at elevated temperature. Six steel types were investigated including conventional mild steel Mild-395 and high-strength low-alloy steel HSLA-700 and four types of advanced high-strength steels (AHSS), namely DP-340, DP-700, MS-1030, and MS-1200. A total of 66 steady-state tests and 22

transient-state tests were conducted. In steady-state tests, the specimens were first heated to elevated temperatures up to 700°C and then loaded until fracture. In transient-state tests, the specimens were first loaded to a given ratio of their nominal yield stress at ambient temperature and then heated until fracture. Stress-strain curves as well as material properties including elastic modulus, yield stress at different strain levels, ultimate stress, and elongation at fracture were obtained from the tests. Retention factors and predictive models for the material properties at elevated temperatures were provided for the different materials and testing regimes. The following main conclusions are drawn from the test data:

- Steady-state and transient-state test results show that the mechanical properties of AHSS are significantly influenced by elevated temperatures.
- Free thermal elongation of AHSS is independent of the steel type. The prediction of thermal elongation given by EC3 [35] is applicable for the tested AHSS steels for temperature up to 700°C.
- Comparing transient-state tests at 5°C/min heating rate with steady-state tests, the transient-state tests lead to greater reduction in elastic modulus (at a given temperature) than the steady-state tests once the temperature exceeds 300°C (MS) or 400°C (DP). However, the testing method did not noticeably affect the measured material yield stress.
- Comparing the test results with published literature data, it was shown that the tested cold-formed AHSS experience larger reduction of properties at elevated temperature than cold-formed steels of lower grade strength.
- Comparing the test results with the current provisions in design codes and standards, it appears that the published provisions are not applicable to the advanced high-strength steels tested in this research. The tested AHSS exhibit lower retention factors than the



published provisions, which shows the need for specific relationships for cold-formed AHSS elevated temperature properties.

- Predictive models based on a continuous three-coefficient equation were proposed to determine the mechanical properties of cold-formed advanced high-strength steels with nominal yield stress up to 1200 MPa at elevated temperature up to 700°C.

## **Chapter 4    Mechanical properties of advanced high-strength steels (AHSS) after cooling down**

### **4.1 Introduction**

As new types of steel alloys are made available, their behaviors after cooling down need to be characterized to enable post-fire safety assessment [51]. The material properties of conventional grade steel at elevated temperature can be found in design codes such as the European code (Eurocode3 part 1-2 [35]) and the American standard (AISC Specification 360 [40]). However, design guidance on the post-fire behavior of structural steels is limited. The Annex B of British Standard 5950 part 8 [41] provides suggestions on the reuse of structural steels after exposure to elevated temperature if the degradation of mechanical properties and member distortion are within appropriate engineering criteria. It specifies that hot rolled S235 and S275 steels can retain at least 90% of their original mechanical properties regardless of the exposure temperature. The S355 steels can be assumed to retain at least 75% of their original strength when the exposure temperature is higher than 600°C. The cold-formed steels with grades up to Z35 (BS EN 10143) can retain 90% of the original strength. However, there is no specific guidance in Eurocode 3 [35]. In the research literature, experimental investigations on the mechanical properties of various types of steels are presented both at elevated temperature [9,10,22,24,25,27–29,32] and in the post-fire situation [9,52–59], but the data for high strength steels and AHSS is limited. Further, predictive models can be found for cold-formed steels with nominal yield stress up to 900 MPa [55], but no model on the post-fire properties of AHSS steels is available. Yet such model is needed to enable the assessment of the residual reliability and potential reusability of steel structures after a fire event.

This chapter addresses the need for a model for characterizing the residual properties of cold-formed advanced high strength steels after exposure to elevated temperatures. First, a review of existing data on steel residual properties is conducted. The collected data includes tests on hot-rolled and cold-formed steels with grades varying from 235 MPa to 960 MPa. Second, a new experimental investigation is performed on AHSS. Two dual-phase (DP) steels and two martensitic (MS) steels with nominal yield stress ranging from 340 MPa to 1200 MPa and thickness of 1.4 mm and 1.0 mm were tested after exposure to temperatures up to 700°C. The tests were conducted on specimens cut per ASTM E8 [60] for pin-loaded tensile test. Post-fire mechanical properties including elastic modulus, yield stress at different strain levels, ultimate stress, and elongation at fracture were obtained. Third, the obtained retention factors were compared with literature data on hot-rolled and cold-formed steels. Since the AHSS tested in this study exhibit strength reductions after exposure to elevated temperature that differ from those of the cold-formed steels tested in the literature, a set of new equations is proposed to capture the post-fire properties of the AHSS with nominal yield stress up to 1200 MPa, based on calibration of a simple three-coefficient equation developed through committee work with the American Iron and Steel Institute [50].

## **4.2 Literature review**

### **4.2.1 Published residual properties for hot-rolled steels**

A summary of residual tests on hot-rolled steels is listed in Table 23. The Table specifies the steel type, thickness, heating rate, test temperature and cooling method used in the tests. The specimens range in nominal yield stress from 235 MPa to 960 MPa.

Qiang et al. [61,62] tested the residual mechanical properties of S460NL, S690QL, and S960QL after exposure to elevated temperature up to 1000°C and concluded that the post-fire performance

of structural steels is dependent on steel grade. Chiew et al. [63] investigated the post-fire mechanical properties of RQT S690 HSS and identified a threshold temperature of 600°C beyond which the strength would decrease significantly. Wang et al. [64] conducted an experimental investigation of the post-fire performance of Q460 and found that the Q460 maintains its original strength after exposure to temperature up to 700°C. Aziz and Kodur [65] tested the residual properties of ASTM A572 after exposure to temperature up to 1000°C and observed that the reduction of strength was dependent on the exposure temperature and cooling method. Lu et al. [57] conducted tests on post-fire properties of hot-rolled Q235, Q345, Q420 steels and cold-formed Q235 steel, and concluded that the post-fire properties were influenced by the manufacturing process (whether cold working is involved), exposure temperature, steel grade and cooling method, whereas the effect of cyclic heating-cooling was negligible. Sajid and Kiran [66] tested the post-fire properties of ASTM A36 steel with both air-cooling and water-cooling method, and found that the cooling method influenced the transformation of the ASTM A36 microstructure from temperature beyond 600°C. Li et al. [67] and Kang et al. [68] both tested the residual properties of Q690. Li et al. [67] found that the cooling method had a minor influence for temperature up to 700°C, but a noticeable influence when cooling down from temperatures above 700°C.

In summary, the existing literature on post-fire properties of hot-rolled steel shows a major influence of the exposure temperature and suggests the existence of a threshold beyond which the permanent loss increases at a greater rate with increasing temperature. The steel grade also has an influence. The cooling method has some level of influence when the exposure temperature has exceeded a threshold.

Table 23. Residual test information of hot-rolled steels.

Source	Time	Steel type	Nominal yield stress (MPa)	Thickness (mm)	Heating rate (°C/min)	Temperature (°C)	Cooling method
Qiang et al. [61]	2012	S460NL	460	5	10	20–1000	CIA*
		S690QL	690	5			
Qiang et al. [62]	2013	S960QL	960	5	10	20–1000	CIA
Chiew et al. [63]	2014	RQT S690	690	8	20	20–1000	CIA
Wang et al. [64]	2015	Q460	460	8	15	20-900	CIA, CIW*
Aziz and Kodur [65]	2015	ASTM A572	345	12.7	10	20–1000	CIA, CIW
		Q235	235	7.5			
Lu et al. [57]	2015	Q345	345	7.5	5-15	20–1000	CIA, CIW
		Q420	420	7			
Li et al. [67]	2017	Q690	690	10	5-20	20-900	CIA, CIW
Sajid and Kiran [66]	2018	ASTM A36	250	D=10*	10	20–1000	CIA, CIW
Kang et al. [68]	2018	Q690	690	10	5	20-900	CIA

Note: ‘CIA’ stands for cooling in air; ‘CIW’ stands for cooling in water; ‘D’ stands for the original diameter of the specimen.

#### 4.2.2 Published residual properties for cold-formed steels

A summary of residual tests on cold-formed steels is given in Table 24. The tested specimens range in nominal yield stress from 235 MPa to 900 MPa. Gunalan and Mahendran [52] tested the material properties of G300-1.00 mm, G500-1.15 mm, and G550-0.95 mm after exposure to temperature up to 800°C. They concluded that G500 and G550 steels suffered proportionally greater residual loss in strength (more than 40% of original strength after exposure to temperatures higher than 500°C) and elastic modulus than low grade G300 steel. Kesawan and Mahendran [53] explored the post-fire properties of G350 and G450 with thickness ranging from 2 to 6 mm cut from cold-formed steel hollow sections. They found that the hollow sections showed reduction in elastic modulus after exposure to temperature higher than 500°C, while their strength started to decrease noticeably when the exposure temperature was higher than 300°C. Li and Young [55] tested the post-fire properties of cold-formed high strength steels cut from tubular sections with nominal

yield stresses of 700 and 900 MPa and thickness of 4 mm and 6 mm. The tests revealed that the high strength cold-formed steel suffered relatively small reduction (<10%) in their elastic modulus after exposure to 1000°C, while the reduction in strength was higher than 40% when the exposure temperature was higher than 800°C. They also concluded that heating rate had a minor influence on the residual properties of the cold-formed steels. Chen et al. [54] tested Q345 and G550 cold-formed steels with thickness ranging from 0.75 to 1.9 mm. The G550 showed different residual properties compared with Q345, as G550 showed a sharp reduction in strength when the exposure temperature was higher than 500°C. Azhari et al. [69] tested the post-fire behavior of cold-formed steels cut from tubes with nominal yield stress of 350, 800, and 1200 MPa and thickness of 3.2mm. Azhari et al. [70] also tested the influence of extreme cooling rate on the three types of steels and concluded that water cooling, with much higher cooling rate than air cooling, was found to significantly affect the residual strength of the steel with 1200 MPa yield stress cooled from temperature higher than 700°C. It should be noted that a number of experimental investigations have been carried out on the post-fire mechanical properties of hot-rolled steels with high steel grades (460 MPa~960 MPa). However, investigations on the cold-formed steel is mainly focused on lower grade steels (235 MPa~550 MPa), except in [55,69].

In conclusion, the existing literature on post-fire properties of cold-formed steel shows a major influence of the exposure temperature. As with hot-rolled steel, there is a threshold beyond which the permanent loss effect becomes more marked, however this threshold seems to lie at a lower temperature for cold-formed steel (between 300°C and 500°C) compared with hot-rolled steel (between 550°C and 700°C). The steel grade also has an influence with higher grades suffering greater proportional loss, although the data is limited in the high-grade range. The heating rate and plate thickness do not seem to noticeably influence the post-fire properties.

Table 24. Residual test information of cold-formed steels.

Source	Time	Steel type	Nominal yield stress (MPa)	Thickness (mm)	Heating rate (°C/min)	Temperature (°C)	Cooling method
Outinen and Makelainen [9]	2004	S355J2 H	355	3	10, 20, 30	20-1000	CIA*
		G300	300	1			
Gunalan and Mahendran [52]	2014	G500	500	1.15	10-20	20-800	CIA
		G550	550	0.95			
		350	350				
Azhari et al. [69]	2015	800	800	3.2	10	20-600	CIA
		1200	1200				
Lu et al. [57]	2016	Q235	235	20, D=10*	5-15	20-800	CIA, CIW*
Kesawan and Mahendran [53]	2018	G350	350	2, 6	20	20-750	CIA
		G450	450	2, 2.5			
Li and Young [55]	2018	700	700	4, 6	10	20-1000	CIA
		900	900	4, 6			
		350	350				
Azhari et al. [70]	2018	800	800	3.2	20	-80-800	CIA, CIW*
		1200	1200				
Tekcham Gishan Singh [59]	2019	YSt-310	310	2.6, 2.9	20	20-800	CIA
Chen et al. [54]	2019	Q345	345	1.0, 1.5, 1.9	15	20-1000	CIA
		G550	550	0.75, 1.0			
Ren et al. [56]	2020	Q235	235	1.0, 2.0	35-40	20-800	CIA, CIW

Note: ‘CIA’ stands for cooling in air; ‘CIW’ stands for cooling in water; ‘D’ stands for the original diameter of the specimen.

### 4.3 Post-fire testing of AHSS: materials and method

#### 4.3.1 Specimens

Two different cold-formed alloys are studied, namely a dual phase steel (DP) and a martensitic steel (MS). The nominal thickness, nominal yield stress, and nominal ultimate stress of each specimen are listed in Table 25. The shape and dimensions of the specimen are in accordance with ASTM E8 [60] for pin-loaded tensile test, as shown in Figure 1.

Table 25. Steel grade with nominal properties and thickness of specimens.

Steel type	Thickness (mm)	Yield stress (MPa)	Ultimate stress (MPa)	Coating
DP-340	1.4	340	590	Uncoated

DP-700	1.4	700	980	Coated
MS-1030	1.0	1030	1300	Uncoated
MS-1200	1.0	1200	1500	Uncoated

## 4.3.2 Test procedure

### 4.3.2.1 Heating and cooling

The specimens were heated up by an ATS 3210 series high temperature furnace with a capacity of 1200°C, as shown in Figure 2. A total number of 7 target temperatures was selected to investigate the post-fire properties of DP and MS steels. The target temperatures include 20°C, 200°C, 300°C, 400°C, 500°C, 600°C, and 700°C.

The heating rate used in residual tests is typically chosen to provide a reasonable representation of the conditions the material would have experienced under a fire. However, as in-situ heating rate conditions vary with parameters such as the actual fire and the thickness and properties of the thermal insulation, different values have been used by different researchers. In the literature, some tests [29,71] were carried out with a heating rate of 10°C-20°C/min, which was reported to be similar to the rate of temperature for protected steel, while other tests were carried out with a higher heating rate (up to 30°C/min) that is closer to that of the initial part of the ISO-curve. It is noteworthy that the heating rate has been shown to have a minor influence on post-fire mechanical properties of high-strength cold-formed steels provided the soak time is long enough to ensure the stability and uniformity of temperature inside the specimens [55]. In this study, the specimens were heated to the target temperature with a heating rate of 25°C/min. During the heating process, the upper end of the specimen was pinned while the lower end was free to expand to prevent any thermally induced stress from building up. After the target temperature was reached, an additional 15~20 min of heating was maintained to ensure a uniform temperature distribution inside the specimens. The temperature history curves of the heating process are shown in Figure 30. Then,



the specimens were taken out of the furnace and placed in a tray to allow them to cool down to ambient temperature in the air. The same procedure was conducted on each specimen so that they followed the same cooling regime.

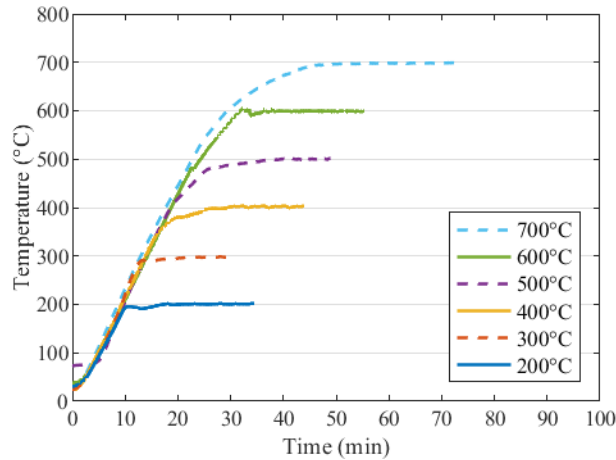


Figure 30. Measured temperature curves of the heating process.

#### 4.3.2.2 Tensile testing

After the specimens had cooled down to ambient temperature, the oxidation on the surface of the specimens was removed by sandpaper. An MTS material loading system with an MTS model 661.21A-03 load cell was used for the tensile testing at ambient temperature. The tension loading was applied in displacement control with a rate of 0.762 mm/min until fracture. The applied tension load on the specimen was directly output from the load cell. The strain was measured by two methods: a physical extensometer (-10%/20%) and by Digital Image Correlation (DIC) [46]. For the DIC method, a combination of white base paint and black dots was applied onto the surface of each specimen. During loading, the images were captured by the DIC camera and an open source MATLAB-based program *ncorr* [47] was used to analyze the strain.

### 4.3.3 Definition of material properties

From the tests, the stress was calculated by dividing the applied force output from the load cell by the measured cross-section area, while the strain was obtained from the extensometer and/or the DIC system. This resulted in the derivation of experimental stress-strain curves for the post-fire behavior of the tested specimens. The stress-strain curves are schematically presented in Figure 31, where two different types of curve shapes are observed. The first one is called a gradual shape, in which a definite yield point cannot be located. The second one is called a sharp shape, with an obvious yield plateau and yield point. The elastic modulus is established as follows from the measured stress-strain curve:

$$E_t = \frac{0.45f_{y,t} - 0.2f_{y,t}}{\varepsilon(\sigma = 0.45f_{y,t}) - \varepsilon(\sigma = 0.2f_{y,t})} \quad (8)$$

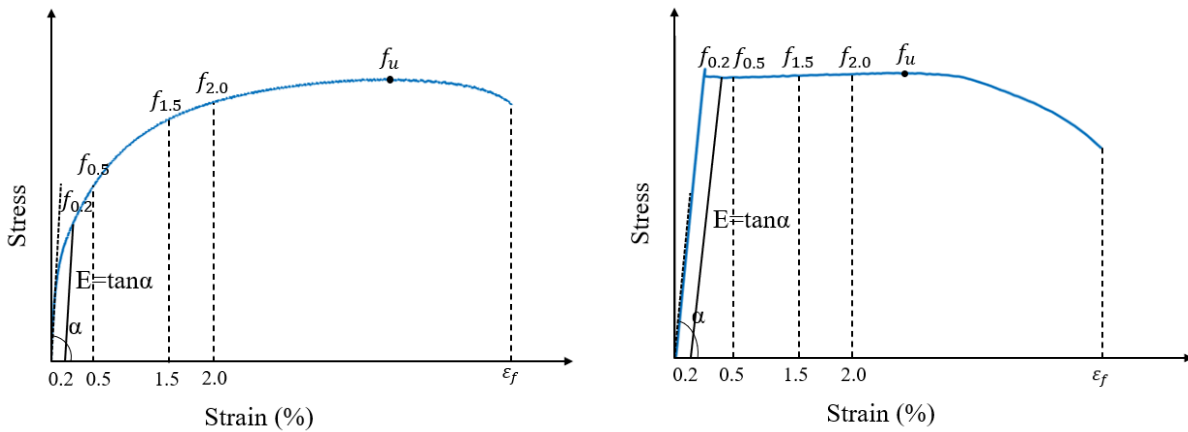
$$f_{y,t} = \frac{f_{u,t}}{f_{u,20}} f_{y,20} \quad (9)$$

where  $f_{y,t}$  is the nominal yield stress after exposure to elevated temperature;  $\varepsilon(\sigma = 0.2f_{y,t})$  is the strain measured when the stress is equal to 20% of the nominal yield stress after exposure to elevated temperature;  $f_{u,t}$  is the ultimate stress measured after exposure to elevated temperature;  $f_{y,20}$  is the nominal yield stress at ambient temperature;  $f_{u,20}$  is the measured ultimate stress at ambient temperature.

The yield stress is provided at several strain levels on the curves. This is useful to comprehensively describe the strength behavior as well as to limit the sensitivity of the reported results to variations in measurements at very small strain levels. The reported yield stresses are the 0.2% proof stress  $f_{0.2}$ , stress at 0.5% strain  $f_{0.5}$ , stress at 1.5% strain  $f_{1.5}$ , and stress at 2.0% strain  $f_{2.0}$ . The 0.2% proof stress  $f_{0.2}$  is determined by the intersection of the stress-strain curve with the line of slope equal to the initial elastic modulus passing by the point of zero stress and 0.2% strain. The stress

at 0.5% strain  $f_{0.5}$ , stress at 1.5% strain  $f_{1.5}$ , and stress at 2.0% strain  $f_{2.0}$  are stresses at strain levels of 0.5%, 1.5%, and 2.0%, respectively. The other material properties reported from the stress-strain curves include the elastic modulus  $E$ , ultimate stress  $f_u$ , and elongation at fracture  $\epsilon_f$ . The elastic modulus  $E$  is defined as the initial slope of the stress-strain curve. The ultimate stress  $f_u$  is the maximum stress value measured during the hardening. The elongation at fracture  $\epsilon_f$  is the strain at the onset of fracture (see Figure 31).

The post-fire properties are characterized by the definition of retention factors, defined as the ratio of the residual properties of steel after exposure to elevated temperature to their original value at ambient temperature. The retention factors are noted as  $k_E$  for elastic modulus,  $k_{0.2}$  for the 0.2% proof stress,  $k_{0.5}$  for the stress at 0.5% strain,  $k_{1.5}$  for the stress at 1.5% strain,  $k_{2.0}$  for the stress at 2.0% strain, and  $k_u$  for the ultimate stress.



(1) Gradual shape

(2) Sharp shape

Figure 31. Definition of symbols used for the material properties.

## **4.4 Post-fire testing of AHSS: data**

### **4.4.1 Failure mode**

The specimens after the residual tests are shown in Figure 32. The tested specimens experienced different extend of heat erosion and color change. As can be seen from the DP-340 and MS-1030 in Figure 32, at 200°C, the specimens generally displayed their original color. At 300°C, the specimens displayed a mixture of orange and blue colors. The blue color was due to the blue brittleness [72]. Beyond 500°C, the effect of heat erosion is visible as the specimens becomes quite dark and present a rough surface. The failure always occurred in the reduced section, as expected. For DP-340, the tested specimens showed ductile failure mode with clear necking. The tested DP-700 specimens showed a more ductile failure mode when the exposure temperature is higher than 400°C. At 700°C, DP-700 showed a more brittle failure. The difference exhibited between DP-340 and DP-700 was due to the larger amount of martensite in the latter, which increased the strength but decreased the ductility. For MS-1030 and MS-1200, the specimens did not show a clear necking up to 600°C, while they showed a more ductile failure mode with clear necking at 700°C. The brittleness of MS steels exhibited at lower exposure temperature is the result of martensite, which is a strong, hard, but brittle material. As the exposure temperature increased, the tempering effect occurs and the hard martensite decomposes to form ferrite, which increases the ductility of the steel [69].

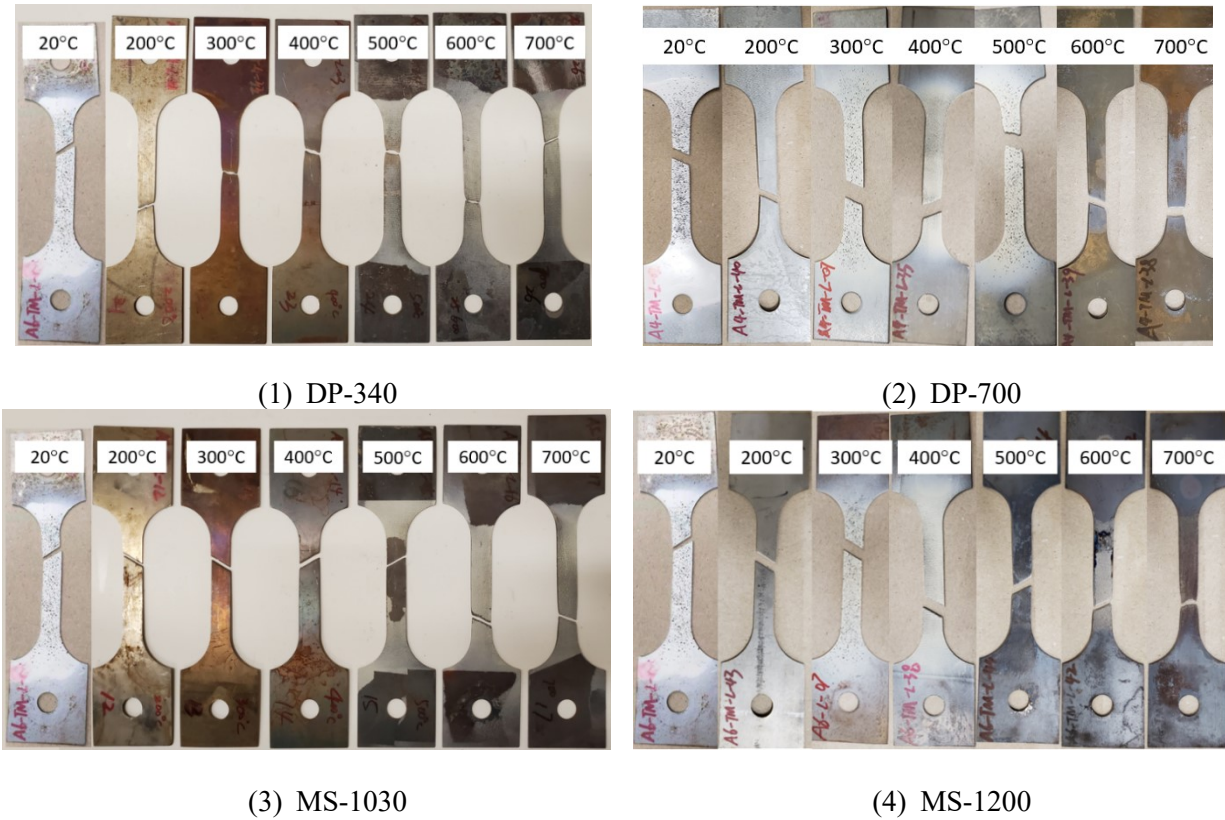


Figure 32. Failure modes of the specimen from residual tests. (White paint was used for improving contrast for the DIC)

#### 4.4.2 Test results

The stress-strain curves obtained from the residual tests are shown in Figure 33. For the four different steel types, the shape of the residual stress-strain curve is different depending on the exposure temperature. A general trend of decreasing strength (for all) and increasing ductility (particularly for the MS alloy) with temperature can be observed.

For the DP-340, the stress-strain curve at ambient temperature shows a gradual shape, while those at 200°C-700°C show a sharp shape with a clearly visible yield plateau. The residual strength slightly increases at 200°C compared with the strength at ambient temperature. Beyond 200°C, the residual strength of DP-340 decreases with increasing exposure temperature. For the DP-700, the stress-strain curves at ambient temperature and 200°C show a gradual shape, while those at 300°C-

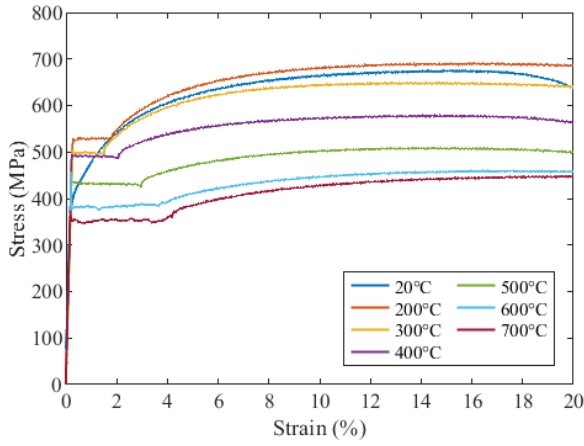
600°C show a sharp shape. The residual strength of DP-700 starts decreasing for exposure temperatures of 300°C and the reduction rate of DP-700 is higher than that of DP-340. At 700°C, the stress-strain curve of DP-700 shifts back to a gradual shape and presents significant nonlinearity and a gradual yielding process with hardening. A markedly rebound of strength is observed at 700°C for DP-700, with ultimate stress being almost close to that at 500°C. This behavior at 700°C observed for the DP-700 was not observed with the DP-340, for which the response was consistent as temperature increased from 200°C to 700°C.

The MS-1030 and MS-1200 show similar mechanical properties after exposure to elevated temperature. The stress-strain curves at ambient temperature and 200°C show a gradual shape, while those at 300°C-700°C show a sharp shape followed by a clear yield plateau. The strength of MS-1030 and MS-1200 decreases with increasing exposure temperature, while the elongation at fracture increases.

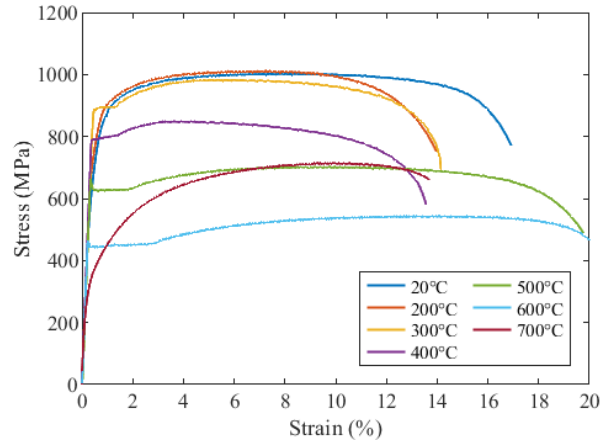
The ambient temperature mechanical properties of the tested steels are given in Table 26. The retention factors are listed in Table 27-Table 30 for the elastic modulus  $k_E$ , 0.2% proof stress  $k_{0.2}$ , stress at 0.5% strain  $k_{0.5}$ , stress at 1.5% strain  $k_{1.5}$ , stress at 2.0% strain  $k_{2.0}$ , and ultimate stress  $k_u$ . The measured value of elongation at fracture is provided in the tables as well.

Table 26. Mechanical properties obtained from ambient temperature tension testing.

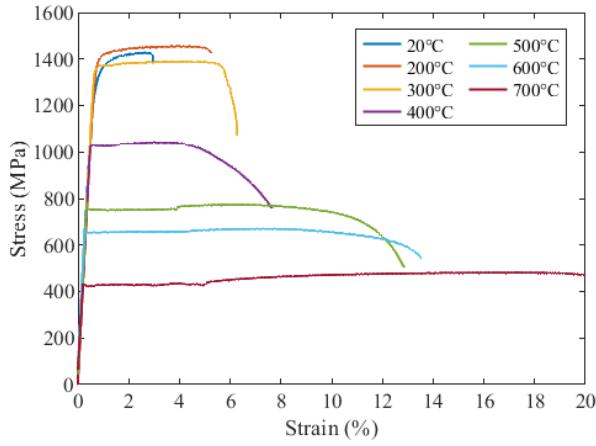
Steel type	Elastic modulus (MPa)	$f_{0.2}$ (MPa)	$f_{0.5}$ (MPa)	$f_{1.5}$ (MPa)	$f_{2.0}$ (MPa)	$f_u$ (MPa)	$\epsilon_f$ (%)
DP-340	206,800	422	431	514	542	675	20.8
DP-700	210,200	744	711	932	955	1009	16.9
MS-1030	215,600	1327	1085	1406	1418	1428	2.9
MS-1200	207,600	1387	1050	1516	1557	1595	3.6



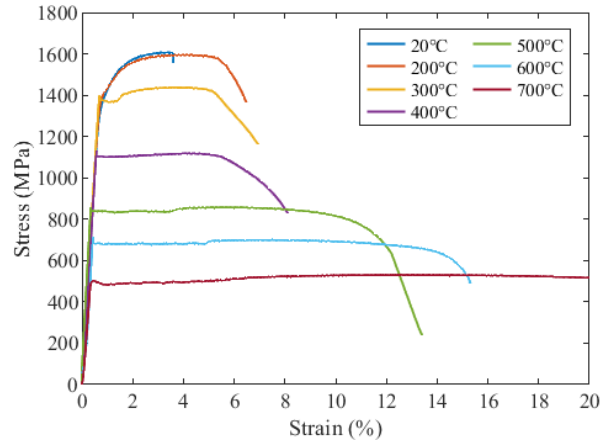
(1) DP-340



(2) DP-700



(3) MS-1030



(4) MS-1200

Figure 33. Stress-strain curve obtained from post-fire residual tests.

Table 27. DP-340 post-fire retention factors of elastic modulus and yield stress, and elongation at fracture.

T (°C)	$k_E$	$k_{0.2}$	$k_{0.5}$	$k_{1.5}$	$k_{2.0}$	$k_u$	$\epsilon_f$ (%)
20	1.00	1.00	1.00	1.00	1.00	1.00	20.81
200	1.03	1.24	1.22	1.03	1.01	1.02	24.56
300	0.93	1.18	1.16	0.97	0.99	0.96	23.83
400	1.06	1.16	1.14	0.96	0.90	0.86	23.62
500	1.00	1.02	1.01	0.84	0.80	0.75	24.96
600	1.00	0.90	0.88	0.74	0.71	0.68	29.43
700	0.94	0.84	0.81	0.69	0.65	0.66	38.29

Table 28. DP-700 post-fire retention factors of elastic modulus and yield stress, and elongation at fracture.

T (°C)	$k_E$	$k_{0.2}$	$k_{0.5}$	$k_{1.5}$	$k_{2.0}$	$k_u$	$\varepsilon_f$ (%)
20	1.00	1.00	1.00	1.00	1.00	1.00	16.87
200	0.99	1.08	1.07	1.01	1.01	1.00	13.98
300	1.02	1.20	1.25	0.98	0.98	0.97	14.24
400	1.00	1.06	1.11	0.87	0.86	0.87	13.65
500	1.07	0.84	0.88	0.67	0.66	0.70	19.77
600	1.04	0.61	0.64	0.49	0.48	0.55	20.65
700	0.78	0.48	0.53	0.54	0.58	0.71	13.68

Table 29. MS-1030 post-fire retention factors of elastic modulus and yield stress, and elongation at fracture.

T (°C)	$k_E$	$k_{0.2}$	$k_{0.5}$	$k_{1.5}$	$k_{2.0}$	$k_u$	$\varepsilon_f$ (%)
20	1.00	1.00	1.00	1.00	1.00	1.00	2.95
200	0.98	1.06	0.96	1.02	1.02	1.02	5.25
300	1.02	1.03	1.02	0.98	0.97	0.97	6.28
400	0.97	0.78	0.95	0.73	0.73	0.73	7.66
500	1.01	0.57	0.69	0.53	0.53	0.55	12.86
600	1.08	0.49	0.60	0.47	0.46	0.47	13.58
700	0.91	0.32	0.39	0.31	0.30	0.34	21.48

Table 30. MS-1200 post-fire retention factors of elastic modulus and yield stress, and elongation at fracture.

T (°C)	$k_E$	$k_{0.2}$	$k_{0.5}$	$k_{1.5}$	$k_{2.0}$	$k_u$	$\varepsilon_f$ (%)
20	1.00	1.00	1.00	1.00	1.00	1.00	3.61
200	0.98	1.02	0.99	1.00	1.00	1.00	6.48
300	1.01	0.99	1.01	0.92	0.91	0.90	6.96
400	0.99	0.80	0.95	0.73	0.71	0.71	8.13
500	1.10	0.60	0.80	0.55	0.54	0.54	13.41
600	1.02	0.51	0.68	0.46	0.45	0.48	15.51
700	0.91	0.36	0.47	0.32	0.31	0.32	22.33

## 4.5 Comparison and discussion

### 4.5.1 Elastic modulus

The retention factors of elastic modulus, calculated as the ratio of the residual elastic modulus of steel after exposure to elevated temperature to the original elastic modulus at ambient temperature,



are shown in Figure 34. DP-340 retains more than 93% of its elastic modulus up to 700°C, while DP-700 does not show significant reduction for exposure temperature up to 600°C (less than 1%). After exposure to 700°C, due to the nonlinear and gradual shape of the stress-strain curve, the elastic modulus of DP-700 decreases by 22% of its value at ambient temperature. The elastic modulus of MS-1030 and MS-1200 do not show significant reduction for exposure temperature up to 600°C (less than 3%), while the reduction becomes more noticeable at 700°C (about 10%). The retention factors of residual elastic modulus obtained for cold-formed AHSS are compared with residual test data on cold-formed steels from the literature in Figure 34. The data from this study is marked with empty markers joined by lines. Test data on conventional grade steels (defined as nominal yield stress ranging from 235 MPa to 450 MPa) are marked with filled black markers. Test data on high strength steels (defined as nominal yield stress higher than 460 MPa) are marked with filled red markers. The retention factors in this study align generally well with the literature data; notably the elastic modulus remains approximately unchanged after exposure to temperature up to 600°C. When exposed to 700°C, the residual modulus is reduced by a value that varies between 10% and 20% depending on the alloy.

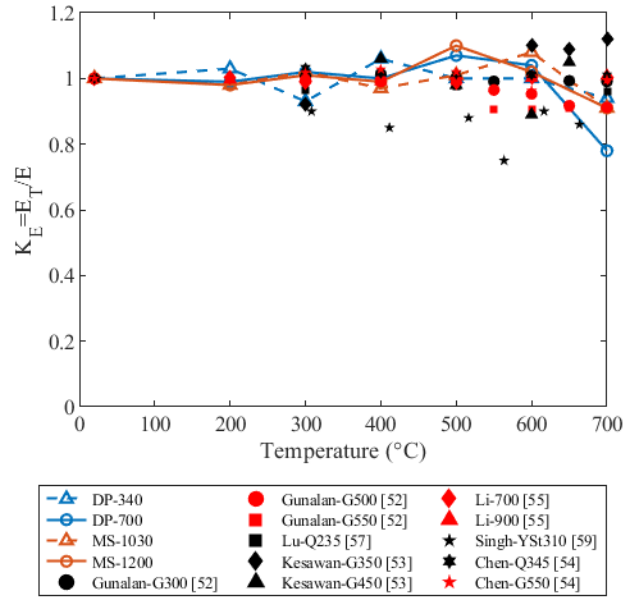


Figure 34. Retention factors for residual elastic modulus of cold-formed steels.

#### 4.5.2 Yield stress

The retention factors for the 0.2% proof stress (Table 27 to Table 30) are shown in Figure 35. Generally, 0.2% proof stress retention factors for DP-340 and DP-700 exhibit different trends after exposure to elevated temperature, while those for MS-1030 and MS-1200 align closely. For DP-340, the 0.2% proof stress remains relatively unchanged when the exposed temperature is lower than 500°C, beyond which the reduction is more noticeable. For DP-700, the 0.2% proof stress starts to reduce noticeably when the exposure temperature is 500°C or higher. For MS-1030 and MS-1200, the 0.2% proof stress starts to reduce noticeably at 300°C. The reduction of yield stress of MS-1030 and MS-1200 is close to 70% when the exposure temperature reaches 700°C.

The retention factors for the stress at 2.0% strain (Table 27 to Table 30) are shown in Figure 36. DP-340 retains more than 90% of its original stress at 2.0% strain after exposure to temperature up to 400°C, beyond which a more noticeable reduction is observed. DP-700, MS-1030, and MS-

1200 retain more than 90% of their original stress at 2.0% strain after exposure to temperature up to 300°C. A rebound of stress at 2.0% strain is observed for DP-700 when the exposure temperature exceeds 700°C. This may be attributed to the change in the crystal structure of the dual-phase steel, in which the martensitic microstructure is not very stable at high temperature.

The retention factors of residual 0.2% proof stress are also compared with residual test data on cold-formed steels from the literature in Figure 35. The data shows that below a threshold temperature the residual 0.2% proof stress is not affected by temperature exposure. The value of the threshold temperature depends on the steel grade and alloy but generally ranges between 300°C and 500°C. A number of tested steels show an increase of the 0.2% proof stress in the low range of elevated temperatures. Beyond the temperature threshold, a gradual reduction of residual stress is observed. Cold-formed steels with conventional grade maintain at least 75% of their ambient temperature yield stress after exposure to 700°C, while high strength steels exhibit larger reduction in yield stress. Notably the G500 and G550 steels by Gunalan and Mahendran [52] show reductions to about 50% of the ambient stress at 550°C. The data from this study on the DP-340 aligns with the conventional grade steel data from the literature. The DP-700, MS-1030, and MS-1200 show lower values of residual 0.2% proof stress than the literature data in the 300°C-500°C range, while they align with the lower dataset obtained by Gunalan and Mahendran [52] for the high strength G500 and G550 at 600°C and 700°C.

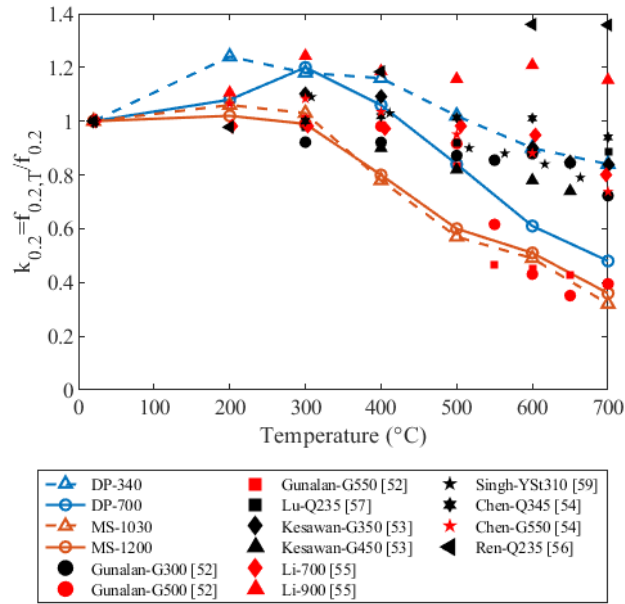


Figure 35. Retention factors for residual 0.2% proof stress of cold-formed steels.

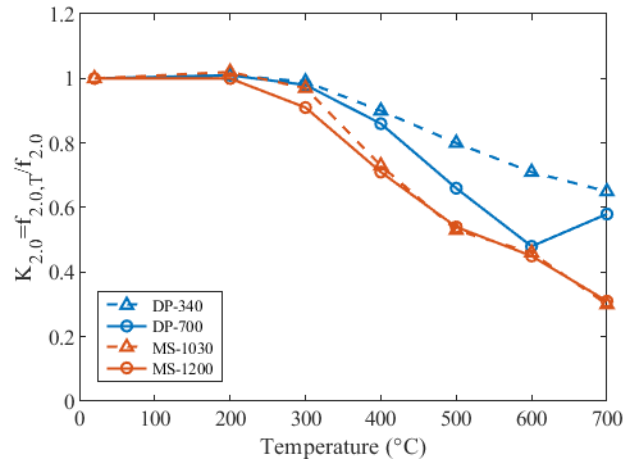


Figure 36. Retention factors for residual stress at 2.0% strain of cold-formed steels.

### 4.5.3 Ultimate stress

The retention factors of ultimate stress (Table 27 to Table 30), calculated as the ratio of the residual ultimate stress after exposure to elevated temperature to the original ultimate stress at ambient temperature, are shown in Figure 37. Generally, the ultimate stress of DP-340 and DP-700 show

similar reduction trend up to 400°C, beyond which the difference becomes noticeable. The ultimate stress of the DP steel is recoverable for exposure temperatures up to 300°C. Beyond 300°C, the post-fire ultimate stress reduces with increasing temperature. For DP-340 exposed to 700°C, the ultimate stress has reduced to about 65% of the ambient value. For DP-700, a rebound of ultimate stress is observed at 700°C. For MS-1030 and MS-1200, the ultimate stress starts to decrease when the temperature reaches 300°C and it reduces to about 30% of the ambient temperature value after exposure to 700°C.

The retention factors of residual ultimate stress are compared with residual ultimate stress data on cold-formed steels from the literature. Similar with the reduction trend of yield stress, an overall gradual reduction trend is observed from the plot for the ultimate stress once temperature exceeds a threshold. Conventional grade cold-formed steels maintain more than 80% of their original ultimate stress after exposure to temperatures up to 700°C. High strength steels generally exhibit larger reduction in ultimate stress than conventional grade steels. Compared with the conventional grade steels in the literature, DP-340 shows larger reduction of ultimate stress after exposure to elevated temperature. The retention factors of MS-1030 and MS-1200 steels in this study are generally smaller than those from most of the other tests, which means the tested AHSS suffer greater permanent loss in ultimate stress after fire than cold-formed steels of lower grade.

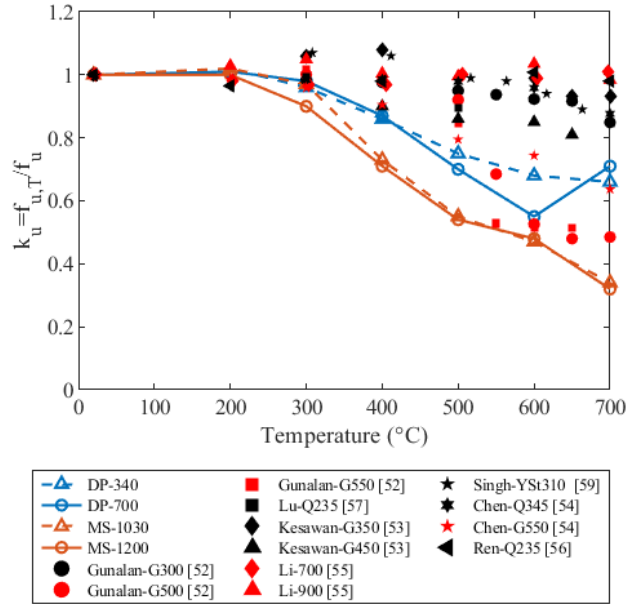


Figure 37. Retention factors of residual ultimate stress for cold-formed steels.

#### 4.5.4 Elongation at fracture

The elongations at fracture obtained from residual tests are plotted in Figure 38. A noticeable difference between DP-340 and DP-700 is observed, while MS-1030 and MS-1200 exhibit a similar trend. For DP-340, the elongation at fracture exhibits a slight increase at 200°C compared with ambient temperature, and then remains almost unchanged between 300°C-500°C, before gradually increasing as the temperature increases beyond 500°C. For DP-700, the post-fire elongation at fracture is minimally affected with varying exposure temperature, although it shows a slight increase at 500°C and 600°C. For MS-1030 and MS-1200, the trend is more apparent as the elongation at fracture gradually increases with increasing exposure temperature. Such increase in elongation at fracture is linked to the change in microstructures and reduction in dislocations due to heat treatment [72]. The increased ductility of the advanced high-strength steels after cooling down can positively influence the cross-sectional strength.

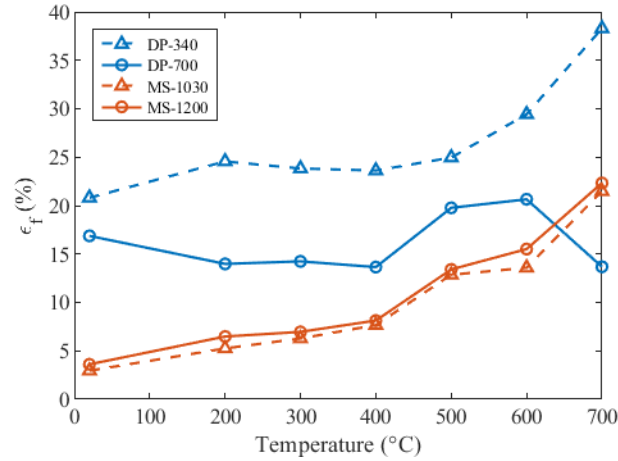


Figure 38. Elongation at fracture  $\varepsilon_f$  obtained from residual tests.

#### 4.5.5 Influence of cold working and steel grade

The post-fire retention factors for 0.2% proof stress and ultimate stress for cold-formed and hot-rolled steels are compared in Figure 39. The color shading in the plot shows the upper and lower boundaries of the retention factors. In the present study, conventional grade is defined as steels with nominal yield stress between 235 MPa and 450 MPa, while steels with a nominal yield stress higher than 460 MPa are categorized as high strength steels. It can be observed that steel grade has a significant influence on the post-fire mechanical properties of cold-formed steels, while it has minor influence on the post-fire properties of hot-rolled steels. For a given temperature exposure cold-formed steels made of high-strength grade exhibit proportionally greater permanent reductions in yield stress and ultimate stress than those made of conventional grade.

Besides the effect of the grade, the influence of cold working on the post-fire mechanical properties is also prominent. The permanent reduction in strength after exposure to temperature is more severe and starts at lower temperatures for cold-formed steels compared with hot-rolled steels. This can be explained by the change of microstructure during cold working and heating and cooling process. During cold working, more dislocations are generated within the metal in which

the dislocations interact and become pinned or tangled [72]. Thus, the mobility of dislocations is reduced, leading to higher strength. When cold-formed steels are exposed to elevated temperature, the heat treatment will induce the grains to recover, recrystallize, or grow in size, and reduce the strength and toughness of the steels.

Since the AHSS tested in this study exhibit strength reductions after exposure to elevated temperature that differ from those of the cold-formed steels tested in the literature, a set of new equations is proposed in the next section to determine the residual mechanical properties of the tested AHSS alloys.

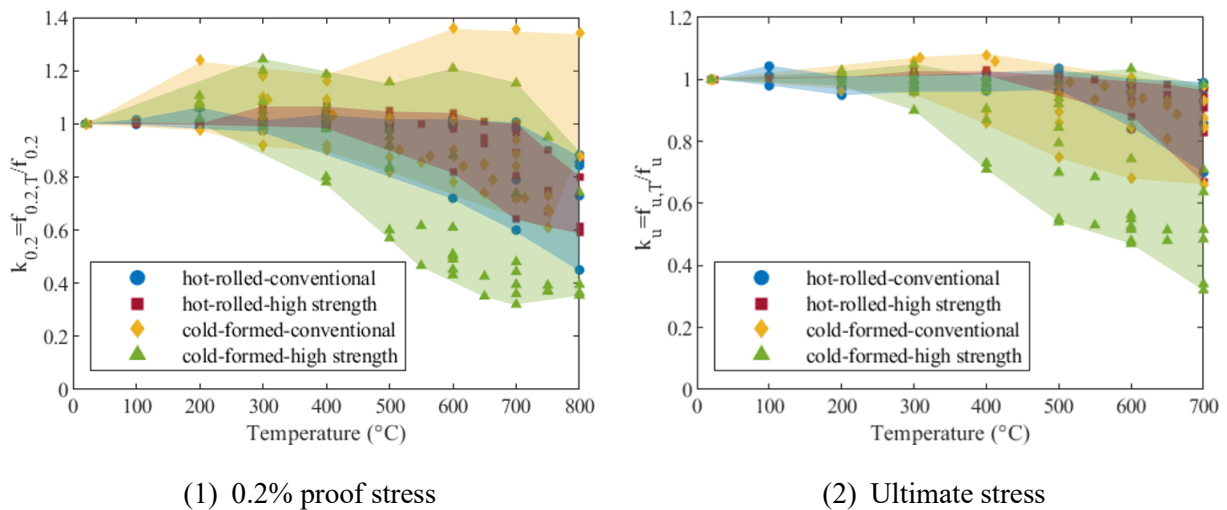


Figure 39. Residual retention factor of 0.2% proof stress and ultimate stress for hot-rolled and cold-formed steels.

## 4.6 Predictive equations for post-fire mechanical properties of AHSS

### 4.6.1 Elastic modulus

The elastic modulus of cold-formed steels in this study remains approximately unchanged after exposure up to 600°C, beyond which the reduction is more severe especially for DP-700. The format of piecewise linear function, as expressed in Eq. (10) to Eq. (13), proposed by Li and Young [55] are adopted in this study for design proposal.



For DP steels,

$$k_E = 1, \quad 20^\circ\text{C} < T < 600^\circ\text{C} \quad (10)$$

$$k_E = 1 - \frac{T - 600}{455}, \quad 600^\circ\text{C} < T < 700^\circ\text{C} \quad (11)$$

For MS steels,

$$k_E = 1, \quad 20^\circ\text{C} < T < 600^\circ\text{C} \quad (12)$$

$$k_E = 1 - \frac{T - 600}{1111}, \quad 600^\circ\text{C} < T < 700^\circ\text{C} \quad (13)$$

As shown in Figure 40, the proposed models are compared with other predictive models on high-strength cold-formed steels [52], [54,55]. The proposed models in this study generally agree well with the other models at temperature lower than 600°C, but the model for DP steels provides more conservative prediction at 700°C.

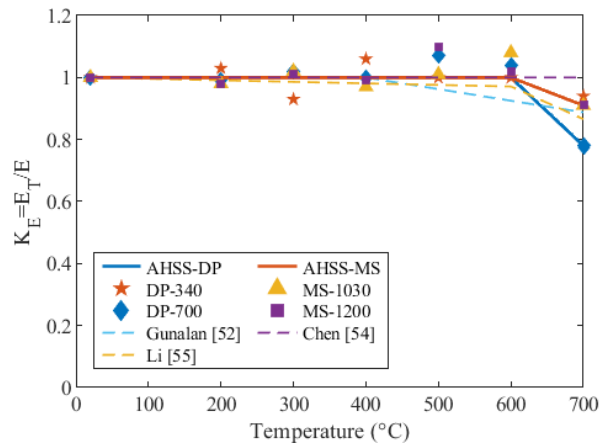


Figure 40. Proposed model for post-fire elastic modulus of AHSS.

#### 4.6.2 0.2% proof stress and ultimate stress

A three-parameter equation, expressed in Eq. (14) and Eq. (15), is adopted to predict the post-fire 0.2% proof stress and ultimate stress of AHSS. This equation has been derived through committee work with the American Iron and Steel Institute when developing retention factors for

conventional grade cold-formed steel at elevated temperature [50]. It is proposed here to adopt the same formulation by calibrating the coefficients to fit the AHSS data in post-fire conditions. In the equation the retention factor  $k_x$  is a function of temperature normalized within the range of the dataset temperatures, taken here as 20°C to 700°C.

$$k_x = (1 - c) \cdot \frac{1 - x^b}{1 + ax^b} + c \quad (14)$$

$$x = \frac{T - T_1}{T_2 - T_1}, T_1 = 20^\circ\text{C}, T_2 = 700^\circ\text{C} \quad (15)$$

The three coefficients  $a$ ,  $b$ , and  $c$  are calibrated from the test data. For the tested AHSS, the two MS steels are sorted into the same group named ‘AHSS-MS’ for their similar post-fire behavior, while the two DP steels are sorted into another group named ‘AHSS-DP’. The calibrated coefficients for the tested AHSS are given in Table 31. The  $R^2$  value is also provided for each row in the table.

Table 31. Proposed coefficients for residual properties of AHSS.

Properties	Data set	a	b	c	$R^2$
$k_{0.2}$	AHSS-DP	18	12	0.48	0.874
	AHSS-MS	10	6	0.32	0.967
$k_u$	AHSS-DP	10	6	0.52	0.917
	AHSS-MS	8	5	0.30	0.972

The proposed models are compared with other published models for the post-fire 0.2% proof stress and ultimate stress, respectively, of high strength cold-formed steels in the literature [52,54,55,72], as shown in Figure 41 and Figure 42. For the 0.2% proof stress, the proposed model for the DP steels lies within the published models, while that for the MS steels lies below the previously published models, which reflects the fact that the MS steel data shows lower residual retention factors than cold-formed steels of lower grades. Especially, the proposed model for MS steels yields noticeably lower predictions than existing models for exposure temperatures from 250°C to

550°C, while the predictions in 550°C-700°C align with the other models in the literature. For the ultimate stress, the proposed model for DP steels generally agrees with the models by Gunalan and Mahendran [52], and by Yu et al. [72]. The model does not capture the observed rebound for the DP-700 at 700°C. The proposed model for MS steels provides values lower than the existing models.

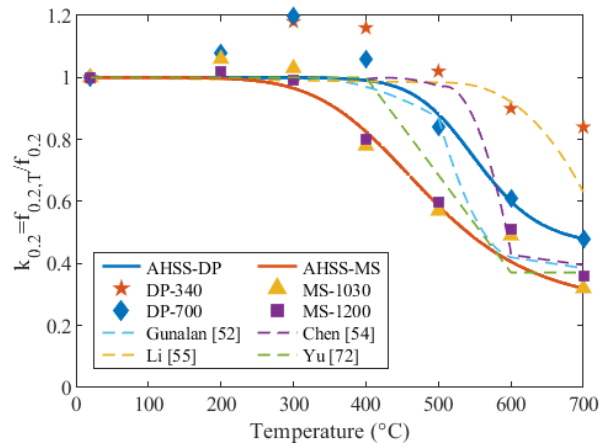


Figure 41. Proposed model for post-fire 0.2% proof stress of AHSS.

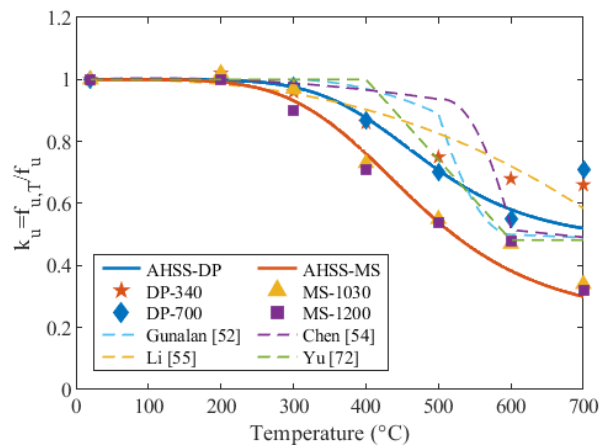


Figure 42. Proposed model for post-fire ultimate stress of AHSS.

## 4.7 Conclusions

This chapter presents an experimental investigation on the post-fire mechanical properties of four types of advanced high strength steels (AHSS), namely DP-340, DP-700, MS-1030, and MS-1200. The specimens were extracted from cold-formed dual phase (DP) and martensitic (MS) steel sheets with nominal yield stress ranging from 340 MPa to 1200 MPa and thickness of 1.4 mm and 1.0 mm. The specimens were heated to elevated temperatures up to 700°C, then allowed to cool down to ambient temperature in air, and finally tested in tensile loading until fracture. The mechanical properties including elastic modulus, yield stress, ultimate stress, and elongation at fracture were derived from the test measurements and retention factors were evaluated and compared with the published data in the literature. For the tested advanced high-strength cold-formed steels the following observations are formulated:

- The temperature exposure affects the shape of the residual stress-strain curve. While the ambient temperature stress-strain curves are gradual, the post-fire stress-strain curves after exposure to temperatures in the range of 300°C to 700°C exhibit a sharp shape with clear yield plateau and yield point (except for the stress-strain curve of DP-700 at 700°C).
- The residual elastic modulus is hardly affected by temperature exposure up to 600°C. After exposure to 700°C, the DP-340, MS-1030, and MS-1200 exhibit a permanent reduction of approximately 10% of their original elastic modulus, while the DP-700 exhibits a loss of about 20%.
- The permanent reduction in strength after exposure to elevated temperature is more severe and starts at lower temperatures for cold-formed steels compared with hot-rolled steels. For cold-formed steels the residual strength starts to reduce in the 300°C-500°C temperature range, while for hot-rolled steels it is in the 550°C-700°C range.

- The permanent reduction in yield and ultimate stress is proportionally larger for AHSS than for lower grade cold-formed steels. As a result, existing models calibrated on conventional cold-formed steels are not suitable to predict the post-fire properties of the tested AHSS.
- A new predictive model is proposed in this chapter to determine the post-fire mechanical properties of advanced high-strength cold-formed steels of the DP and MS types with nominal yield stress up to 700 MPa and 1200 MPa, respectively.

## **Chapter 5 Numerical modeling of localized fire exposure on structures: comparative study and application to open car park fires**

### **5.1 Introduction**

Performance-based structural fire design requires accurate representations of fires and subsequently thermal exposure conditions for structures. Most structural fire resistance is defined to resist high temperatures for certain fire duration based on standard fires or parametric fires, which assume a uniform temperature distribution at a given time inside the compartment. Where post-flashover phase of compartment fires is unlikely to happen, localized fire models are usually adopted. Localized fires typically occur in open or large compartments, such as open car parks, large transportation halls or industrial enclosures [73]. They also occur in the initial stage of a fire. The thermal exposure conditions created by localized fires depend markedly on the location in the compartment. Research has shown that localized fires can generate thermal conditions that threaten the stability of structures [74–77]. Therefore, numerical modeling approaches are needed for the fire design of structures subjected to localized fires [78,79].

Different localized fire models exist, notably the Heskestad model and Hasemi model in Eurocode EN1991-1-2 [80], and the LOCAFI model described by Tondini et al. [81]. To simulate complex fire scenarios, advanced numerical models based on computational fluid dynamics (CFD) are generally adopted [82]. Despite these valuable models, application of localized fire models to study the fire response of structures is still new and there is a need for further experimental validation of the numerical models. There is also a lack of guidance regarding the proper application and comparative merits of the different models and techniques.

To address this gap, this chapter focuses on the issue of numerical modeling of localized fire exposure on structures. A brief summary of the theories of the most commonly used fire models

is conducted. Based on the application field of each model, a numerical modeling strategy is proposed. Then, three experimental tests of structural members subjected to localized fires, collected from the literature, are simulated using the proposed modeling strategy. The predicted member temperatures are compared with the test measurements. At last, application of the proposed modeling strategy on the analysis of the temperatures reached in open car park steel framing members under fire is presented to demonstrate the benefits and limitations of simple models and exhibits the potential benefits of advanced numerical analysis for the performance-based design of open car parks in fire conditions. The parameters considered in the application study include the dimensions of the steel members, layout of burning vehicles, galvanization of the steel members, and the modeling approaches adopted. Both the simple analytical localized fire models and the advanced CFD-FEM coupling methods are used to evaluate the member temperatures. The predicted member temperatures by different modeling approaches are compared and discussed. Temperatures obtained can be used in structural FE analyses to design open car park structures for the fire situation.

## **5.2 Literature review**

### **5.2.1 Simple localized models**

The simple models are computationally efficient, but they have limited field of applications. Recently, Randaxhe et al. [83] used the LOCAFI model to investigate the effect of hydrocarbon pool fires on steel pipe-racks. Somnavilla and Tondini [84] conducted a thermo-mechanical analysis of an open car park subjected to localized fires using the LOCAFI and Hasemi models. Fang et al. [85] analyzed the robustness of a multi-story car park under vehicle fires using the Hasemi model to obtain the heat flux received by the structural members. Dai et al. [86] used the

Hasemi model to propose a traveling fire model. Other fire models have been proposed for structural systems such as bridges or tunnels. Guo et al. [87] developed a confined discretized solid frame model to calculate the heat flux impacted on the concrete tunnel liners due to vehicle fires. To better understand their applicable fields, the theories of the simple localized fire models are summarized here.

### 5.2.1.1 Heskestad model

The Heskestad method [88], which is implemented in Annex C of the Eurocode EN1991-1-2 [80], is applicable when the flame is not impacting the ceiling (if present) or for an open air fire. The method provides the temperature along the vertical centerline in the fire plume according to Eq. (16):

$$T_f(z) = \min(900 \text{ }^\circ\text{C}; 20 + 0.25 Q_c^{2/3} (z - z_0)^{-5/3}) \quad (16)$$

$$z_0 = -1.02D + 0.00524 Q^{2/5} \quad (17)$$

where  $T_f$  is the plume temperature along the vertical centerline of the fire ( $^\circ\text{C}$ ),  $Q_c$  is the convective part of the heat release rate ( $W$ ),  $z$  is the vertical distance to the fire source ( $m$ ), and  $z_0$  is the virtual origin ( $m$ ) given by Eq. (17). In the latter,  $D$  is the diameter of the fire ( $m$ ) and  $Q$  is the heat release rate ( $W$ ). The flame length ( $m$ ) of a localized fire is given by:

$$L_f = -1.02D + 0.0148 Q^{2/5} \quad (18)$$

The Eurocode does not specify how the temperature of the plume evaluated by Heskestad's method is to be used to calculate the heating of structural members. Assuming that the temperature in the flame is equal to that at the centerline of the plume (at each elevation), the Heskestad's temperatures of Eq. (16) can be used to evaluate the incident radiative heat flux ( $W/m^2$ ) received by a structural member based on the application of the theory of radiation with computation of



view factors. If the member is engulfed in the flame, the member temperature can be evaluated using the incident flux ( $W/m^2$ ) equation as follows:

$$\dot{q}_{inc} = \sigma \varepsilon (T_f(z) + 273)^4 + h_c T_f(z) \quad (19)$$

where  $\sigma$  is the Stefan-Boltzmann constant,  $\varepsilon$  is the emissivity of the fire,  $h_c$  is the convective heat transfer coefficient.

### 5.2.1.2 Hasemi model

When the flame hits the ceiling, the heat flux  $\dot{q}$  ( $W/m^2$ ) received by a unit surface area of the member at the ceiling level can be calculated with the Hasemi model [89]. This model is included in EN1991-1-2 Annex C [80] which provides Eq. (20) for the calculation of the flux:

$$\dot{q} = \begin{cases} 100000 & \text{if } y \leq 0.3 \\ 136300 - 121000 y & \text{if } 0.3 < y < 1.0 \\ 15000 y^{-3.7} & \text{if } y \geq 1.0 \end{cases} \quad (20)$$

$$y = \frac{d + H + z'}{L_h + H + z'} \quad (21)$$

where  $y$  is a non-dimensional variable,  $d$  is the horizontal distance between the centerline of the fire plume and the section of interest along the ceiling where the flux is calculated ( $m$ ),  $H$  is the ceiling height ( $m$ ), and  $z'$  is the vertical position of the virtual heat source ( $m$ ). Eq. (16) to Eq. (21) are valid for fire diameter up to 10 m and HRR up to 50 MW as specified in EN1991-1-2 [80].

The Hasemi flux  $\dot{q}$  is an absorbed heat flux. The net heat flux received by unit area of the fire exposed surface at the ceiling level is then computed by subtracting the re-emitted flux using Eq. (22).

$$\dot{q}_{net} = \dot{q} - h_c (T_s - T_{amb}) - \Phi \varepsilon_s \sigma ((T_s + 273)^4 - (T_{amb} + 273)^4) \quad (22)$$

where  $h_c$  and  $\varepsilon_s$  are the convection coefficient and emissivity of the exposed surface, respectively,  $\Phi$  is the configuration factor,  $\sigma$  is the Stefan-Boltzmann constant,  $T_s$  is the member temperature ( $^{\circ}\text{C}$ ), and  $T_{amb}$  is the ambient temperature generally taken as  $20^{\circ}\text{C}$ .

### 5.2.1.3 LOCAFI model

The LOCAFI model evaluates the radiative heat flux from a localized fire onto a structural member that is not engulfed in the flame. Since the member is outside the fire area, the surrounding gas is at ambient or close to ambient temperature, therefore the convective part of the received heat flux is neglected. This model uses the concept of virtual solid flame, taken as either a cylindrical or conical shape [81], as shown in Figure 43(a). If the fire area does not have a circular shape, it is approximated as a circular plan area with equivalent area. Radiative heat fluxes are emitted from the surfaces of the solid flame which is discretized into different vertical cylinders, as shown in Figure 43(b).

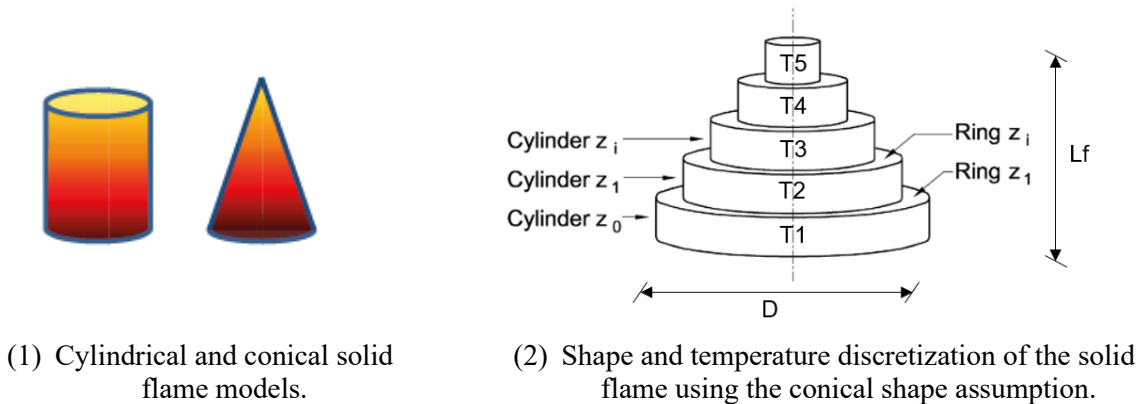


Figure 43. Virtual solid flame models [81].

The analytical model relies on the existing correlations described above for the Heskestad model. The flame height is calculated by Eq. (18). It is conservatively assumed that each cylinder is of

uniform temperature taken as that of the centerline; accordingly, the whole visible part of the flame has the same temperature as the vertical centerline, as computed by Eq. (16).

Once the solid flame model is defined with its temperature distribution, the incident radiative heat flux emitted by the fire surface A to an external surface B is computed as:

$$\dot{q}_{inc,A to B} = \Phi_{A to B} \varepsilon_A \sigma (T_A + 273)^4 \quad (23)$$

where  $\Phi_{A to B}$  is the configuration factor (details for its computation are provided in Tondini et al. [81]),  $\varepsilon_A$  is the emissivity of the fire surface A, which is conservatively taken as 1, and  $T_A$  is the temperature of the fire surface A (°C). The incident heat flux received by the external surface B is the sum of the radiative heat flux emitted by all fire surface visible to the external surface B:

$$\dot{q}_{inc,flame to B} = \sum_{i=1}^n \Phi_{i to B} \varepsilon_i \sigma (T_i + 273)^4 \quad (24)$$

where  $n$  is the number of cylinders,  $\Phi_{i to B}$  is the configuration factor from radiating surface  $i$  to surface B,  $\varepsilon_i$  is the emissivity of the fire surface  $i$ , and  $T_i$  is the temperature of the fire surface  $i$  (°C).

The LOCAFI model is valid within the same limitation of fire diameter and HRR as the Heskestad model and Hasemi model [81]. When evaluating the net heat flux received by the exposed surface B, the terms accounting for convective heat transfer with the air (generally at ambient temperature) and re-radiation toward the far field must be subtracted from the received radiative flux of Eq. (24).

The LOCAFI model has been implemented in the finite element software SAFIR. In this implementation, the net heat flux on each member surface is automatically computed, accounting for the view factors in the re-radiation term toward the far field.

### 5.2.2 CFD models

The Fire Dynamics Simulator (FDS) [90], a Large Eddy Simulation (LES) based CFD code developed by the NIST, has been widely used in fire engineering [91]. It solves the Navier-Stokes equations numerically for low-speed thermally driven fluid flow. Thermal radiation is modeled through the radiation transport equation for gray gas, which is solved by the Finite Volume Method (FVM).

CFD models need to be interfaced with finite element (FEM) models to import the thermal boundary conditions in the thermal-structural analysis. One commonly adopted method is through the use of the adiabatic surface temperature (AST) concept [92]. This method is robust and powerful to obtain the thermal boundary conditions, and has been used in several studies to investigate the behavior of structures subjected to different fire scenarios [93–97]. For example, Zhang et al. [77] used the AST method to transfer the thermal boundary information from FDS to a FEM thermal model and the predicted member temperature agreed with the test measurements. DeSimone and Jeffers conducted two case studies on steel members and provided recommendations for the use of the AST method [98]. Another method consists in exporting the temperatures and fluxes outputs computed by the CFD software in a format readable by the FEM software, which can apply them as thermal boundary conditions to the structural members. This method has been incorporated in the CFD software FDS and FEM software SAFIR [99] and is referred hereafter as the FDS-FEM interface method [100]. Charlier et al. [101] calibrated a FDS model representative of a travelling fire development in large compartment and adopted the FDS-FEM interface method to calculate the steel temperature in FEM software SAFIR. Good agreement was obtained between the steel temperature in the central column from the numerical analysis and the test data. Vassart et al. [100] used both the interface method and Hasemi model to perform the

fire analysis of an open car park and observed that Hasemi model yielded a more conservative prediction of the member temperatures. The theories of the two methods to interface the CFD models with finite element (FEM) models are summarized here below.

### 5.2.2.1 FDS-FEM AST

The AST proposed by Wickstrom [92] is used to transfer the convection and radiation information from a fire model to a thermal analysis. This fictitious temperature  $T_{AST}$  assumes that a surface is a perfect insulator, for which the net heat flux is zero. The value of  $T_{AST}$  depends on the incident radiative heat flux  $\dot{q}_{inc,rad}$  and the gas temperature near the surface  $T_g$ , and is calculated by solving Eq. (25):

$$\dot{q}_{net} = \varepsilon_{AST}(\dot{q}_{inc,rad} - \sigma(T_{AST} + 273)^4) + h_{c,AST}(T_g - T_{AST}) = 0 \quad (25)$$

where  $\varepsilon_{AST}$  is the surface emissivity and  $h_{c,AST}$  is the convection coefficient. Once  $T_{AST}$  is computed, it plays the role of an equivalent gas temperature for calculating the heat flux to an exposed structure. The net heat flux to a real surface with the same emissivity ( $\varepsilon_s = \varepsilon_{AST}$ ), the same convection coefficient ( $h_c = h_{c,AST}$ ), the same position and the same orientation as the adiabatic surface can be calculated as:

$$\dot{q}_{net} = \varepsilon_s \sigma ((T_{AST} + 273)^4 - (T_s + 273)^4) + h_c(T_{AST} - T_s) \quad (26)$$

where  $T_s$  is the temperature of the member surface. Hence, the net heat flux to a surface is calculated from the fictitious adiabatic surface temperature which contains the effects of both the gas temperature and the radiative heat fluxes from the fire. FDS allows two ways to output the AST: one way is to use the quantity command ‘adiabatic surface temperature’ and the second is to use the command ‘adiabatic surface temperature gas’. The first method requires the solid surface to be modeled in FDS and the sensor to be attached to the solid surface. Thermal properties of the

solid surface (emissivity and convective heat transfer coefficient) defined in the SURF line will be used to calculate the AST. The second method allows calculation of AST even when there is no actual solid surface. Emissivity, heat transfer coefficient and orientation of the sensor should be defined.

While the FDS-FEM AST method has been proven to be practical and powerful for structural fire analysis [73], it is expensive in terms of modeling since it requires applying a large number of sensors where the AST are recorded around the cross-sections of the structural members to capture thermal exposure conditions that vary in space and in direction.

#### **5.2.2.2 FDS-FEM interface**

Another method to transfer the thermal attack from the fire model to the thermal model, referred to as FDS-FEM interface, has been proposed to facilitate the interfacing in large models. FDS creates a transfer file containing the gas temperatures and radiant intensities at various positions and from various directions in the compartment [100]. These quantities can be output at each grid point of the FDS model or only at selected intervals of the grid points. The transfer file can then be read by a FEM software which interprets the quantities in terms of heat transfer boundary conditions. This integrated strategy has been written initially for interfacing between FDS and the software SAFIR, but it can be used with other software as long as the transfer file can be interpreted by the software. A trilinear interpolation is performed between the points of the grid and the position in the compartment where the information is needed. The incident radiative flux at the surface of the structural element,  $\dot{q}_{inc,rad}$ , is computed in the FEM software by integrating the radiant intensities, considering possible shadow effects in concave sections.

$$\dot{q}_{inc,rad} = \sum_{i=1}^{n_\alpha} \sum_{j=1}^{n_\beta} I_{FDS} \cos(\alpha) \cos(\beta) \frac{\beta_f - \beta_i}{n_\beta} \left( \sin\left(\alpha_1 + \frac{\pi}{n_\alpha}\right) - \sin\left((j-1)\frac{\pi}{n_\alpha} - \frac{\pi}{2}\right) \right) \quad (27)$$

where  $I_{FDS}$  is the radiative intensity ( $W/m^2$ ) from the direction  $(\alpha; \beta)$ ,  $\alpha$  is the angle between the normal to the surface and the direction of the radiant intensity, in the direction of the longitudinal axis of the beam element,  $\beta$  is the angle between the surface and the direction of the radiant intensity, in the direction perpendicular to the longitudinal axis of the beam element,  $n_\alpha = n_\beta =$

7. Knowing the incident radiative heat flux, the net heat flux can be obtained as:

$$\dot{q}_{net} = \varepsilon_s (\dot{q}_{inc,rad} - \sigma(T_s + 273)^4) + h_c (T_g - T_s) \quad (28)$$

where  $h_c$  and  $\varepsilon_s$  are the convection coefficient and emissivity of the exposed surface,  $T_g$  is the gas temperature, and  $T_s$  is the surface temperature of the section where the heat flux is computed. The re-radiating term in  $\sigma(T_s + 273)^4$  accounts for the shadow effect for each member surface, i.e., a surface of the structural member can only re-radiate energy toward the far field through the actual view factor with the far field. The interface method allows an automatic transfer of information from the fire model to the thermal model with a very fine spatial discretization. It is also efficient to capture the view factors and shadow effects in concave sections *a posteriori*, i.e. without the need to model the structural members in the fire model.

### 5.3 Proposed modeling strategy for structures subjected to localized fire

The models described in the previous section have their respective advantages and limitations. To provide guidance for structural fire design, a numerical modeling strategy for structures subjected to localized fires is proposed as a decision flowchart. To derive the flowchart, each fire model discussed in the previous section has been examined in terms of (i) the underlying theory and equations; (ii) the applicability limits and objectives of the model as stated by their authors; (iii)

available validation and benchmarking in the literature; and (iv) the results of modeling of three experimental tests as presented in detail in the next sections. Based on this information, the most suitable models were identified for different configurations, as discussed hereafter.

The decision flowchart is shown in Figure 44. It guides decision toward the adequate fire model, which can be either an advanced (CFD) model or a simple model. The CFD models refer to the FDS-FEM AST method and interface method, while the simple models refer to Heskestad, Hasemi and LOCAFI.

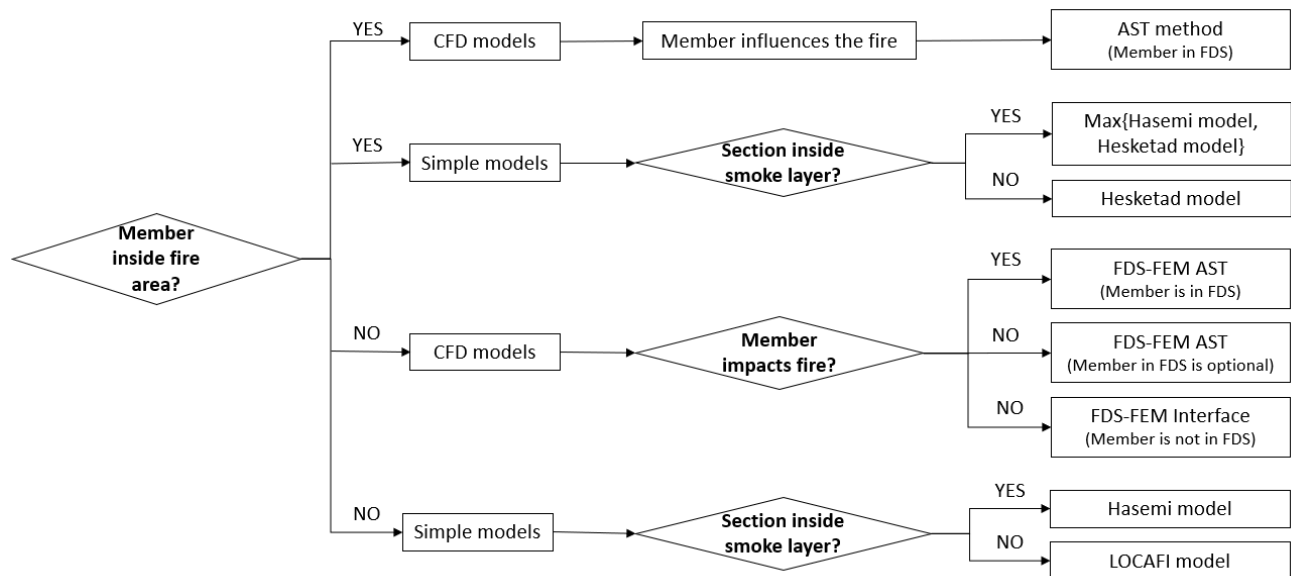


Figure 44. Modeling strategy for analyzing a structural member subjected to a localized fire.

The first consideration in the flowchart is whether the member is inside the localized fire area, i.e. the member is engulfed in the localized fire. This is determined based on the definition from see Figure 45. If it is, the presence of the structure influences the development and air flow of the fire plume.

If selecting CFD for a member inside the fire area, the structure must then necessarily be included in the CFD model. In that case, the FDS-FEM AST method should be adopted. The interface method is not suitable when the structural member is modeled in FDS as will be discussed later.



If selecting a simple model approach for a member inside the fire area, the next consideration is whether the member (or part of it) is inside the smoke layer (i.e. the ceiling jet gases). The smoke layer, or ceiling jet, refers here to the relatively rapid gas flow in a shallow layer beneath the ceiling surface. Note that it is not meant as the hot zone in a zone model, since this work deals with localized fires and the two zones have not yet developed. The smoke layer is typically controlled by members under the ceiling and its thickness depends on the member geometry, typically beam height. Otherwise, the thickness of the smoke layer is recommended to be 0.5 m for small compartments (office) and 1.0 m for large compartments (warehouse) [102]. The Heskestad model can be used to compute the temperature of the plume. The parts of the structural members that are below the smoke layer can be evaluated from heat transfer using Eq. (19), or conservatively taken at the temperature at the centerline of the plume. For members inside the smoke layer, the heat flux received should be taken as the maximum between that computed from the Hasemi model and the Heskestad model [102].

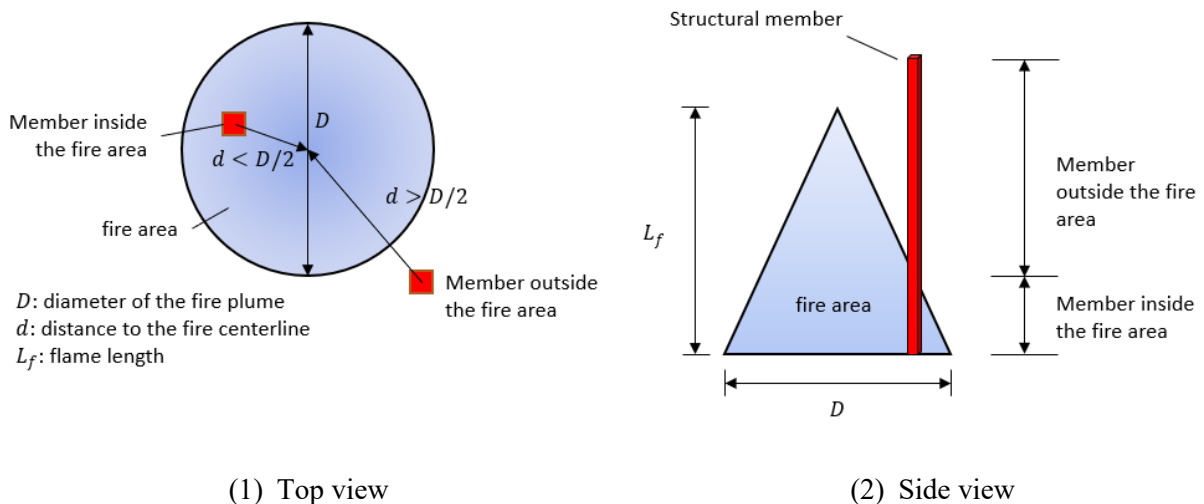


Figure 45. Relative position of fire area and structural member.

If, on the other hand, the member is outside the fire area, its presence may still influence the fire development, depending on the relative position of the fire and member. Whether a structural

member outside the fire area will influence the fire development is a case-by-case judgement that requires insights of fire dynamics. It largely depends on the dimensions of the member and the distance between the member and fire source. Structural walls and floor that form the boundaries of a compartment influence the fire development. However, a steel column at a 5 m distance of the flame of a localized fire has a negligible influence on the fire development. Generally, frame-type members that are outside the flames and do not noticeably affect the ceiling jet have negligible impact on the fire development in the context of the flowchart. In situations where the structural member is expected to affect the fire, the member must be included in the CFD model, and the FDS-FEM AST method is recommended. In contrast, when the member's presence has no significant effect on the fire development, it may or may not be included in the CFD model. In case the structural members are not modeled in FDS, both the AST method and the interface can be used. In other words, the FDS-FEM interface method is appropriate when the member has no significant influence on the fire development and provided the member was not included in the FDS model. In these situations, the interface's advantage is that it allows performing the fire development analysis independently from the thermal-mechanical analysis of the structure by neglecting the structural elements in the CFD model [103], while facilitating the transfer of information for big models compared with using a large number of AST sensors.

If a simple model is used to evaluate the thermal exposure on structural members located outside the fire area, a distinction is again made based on the position of the member in the smoke layer. If the member is outside the smoke layer (e.g., the lower part of a column), radiative heat flux is dominant. The LOCAFI model is then recommended. If the member is inside the smoke layer (e.g., a beam in the ceiling), the convective heat flux cannot be neglected and the Hasemi model should be used.

The flowchart applies to localized fire situations. It does not apply to traveling fires, which start locally but then spread across entire floor plates while becoming extinct at locations of origin as the fuel burns out; specific types of fire models not discussed here have been proposed for such situations [73]. The transient evolution of the localized fire may lead to different branches of the flowchart for a single analysis. When an advanced model is used, the entire analysis can be carried out at once using the FDS-FEM AST method with the member modeled in FDS. When simple models are used, it is necessary to change models as the situation changes during the analysis. The next section will illustrate such a case.

## **5.4 Case study: Steel beam under localized fire**

### **5.4.1 Description of the experiment**

The first case study is based on a test conducted by the NIST [104]. A W16×26 beam was heated by a 1.0 m square gas burner [77], as shown in Figure 46. The length of the beam is 6.17 m. The gas burner was placed at 1.0 m below the lower flange of the steel beam. The distance between the lower flange of the beam and the floor was 1.5 m. A series of tests were conducted on the steel beam with different support conditions, loading conditions, and fire exposures in accordance with ASTM A992/A992M-11 [105], ASTM A325-10e1 [106] and ASTM.E8/E8M-16a standards [60]. This study focuses on the transient-state Test no. 8. In this test, the steel beam was simply supported, with both the rotation about the longitudinal axis of the beam and the lateral displacement being restrained at the ends. At first, the beam was loaded to 67 % of the capacity at ambient temperature. Then, while the applied load was maintained constant, the beam was heated with the heat release rate (HRR) following a t-squared function ( $4.5t^2 + 250 \leq 1600kW$ , t in

min) until the beam failed. Thermocouples were installed to measure the surface temperatures of the lower flange, upper flange, and mid web.

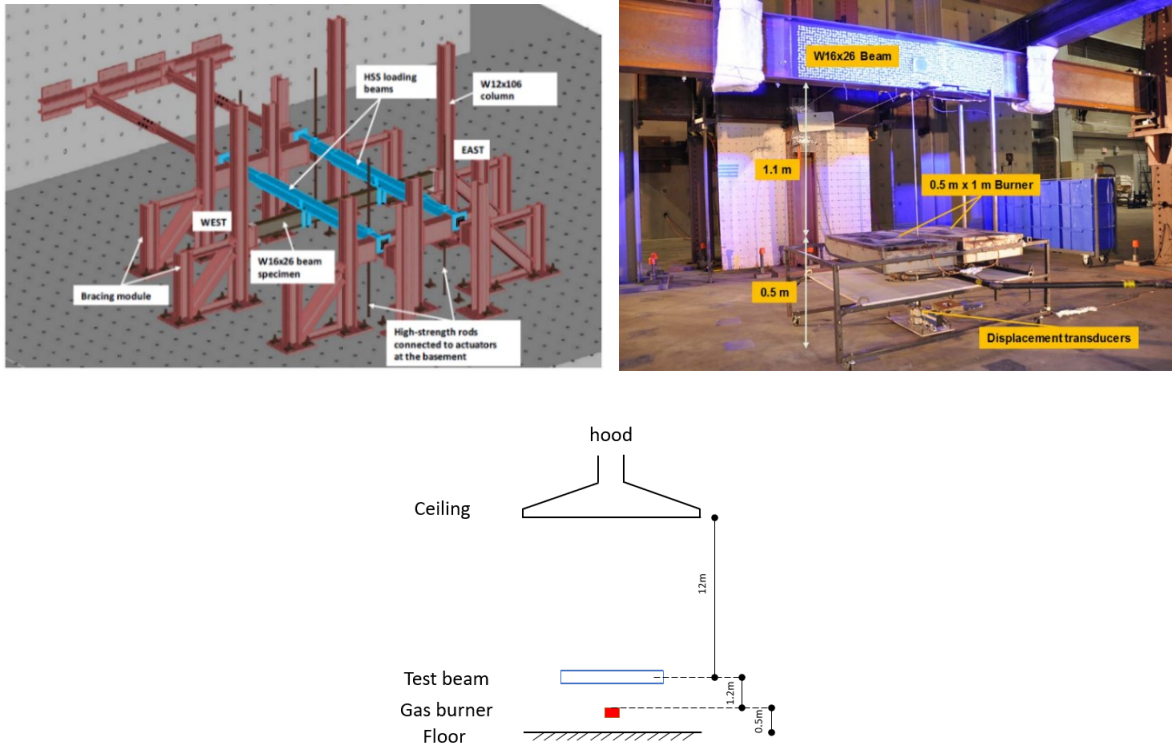


Figure 46. Experimental setup for the steel beam fire test [77].

#### 5.4.2 FDS-FEM model

Figure 47 shows the FDS numerical model for the steel beam test. The dimension of the computational domain was  $7.2 \times 1.2 \times 3.6$  m ( $X \times Y \times Z$ ). The steel beam, located right above the localized fire, affects the development of the fire plume and therefore it must be included in the FDS model. The steel beam was modeled by obstructions with zero thickness. A user-defined solid boundary condition was applied to the beam with thermal properties following the specifications in EC3 [35]. Thickness of the flange and web was also defined in the solid boundary condition. The default combustion model of methane was used as the fuel while the HRR of the heat source, defined as a function of time, followed the measured values during the test. Four side

boundaries and the top boundary were model as open, while the floor was assumed as a solid wall. The command DEVICE is used in FDS to output the data at selected points within the computational domain. Devices are evaluated using the cell centered or face centered values of the cell in which the device is located.

The mesh size or grid size is an important parameter of the numerical model. The special resolution  $R^*$  [90] of a numerical grid is defined as  $R^* = dx/D^*$ , where  $dx$  is the characteristic length of a cell for a given grid, and  $D^*$  is the characteristic diameter of a plume given by:

$$D^* = \left( \frac{\dot{Q}}{\rho_{\infty} c_p T_{\infty} \sqrt{g}} \right)^{\frac{2}{5}} \quad (29)$$

where  $\dot{Q}$  is the heat release rate,  $\rho_{\infty}$  is ambient density,  $c_p$  is the specific heat of air at constant pressure,  $T_{\infty}$  is ambient temperature, and  $g$  is acceleration of gravity. McGrattan et al. [90,107] suggest a cell size of 10 % of the plume characteristic length as adequate resolution. In Test 8, the heat release rate (HRR) is between 270 kW and 1590 kW. The other parameters are as follows:  $\rho_{\infty} = 1.2754 \text{ kg/m}^3$ ;  $c_p = 1.005 \text{ kJ/(kgK)}$ ;  $T_{\infty} = 300 \text{ K}$ ;  $g = 9.8 \text{ m/s}^2$ . Therefore,  $D^*$  is in the range of 0.35 m to 0.71 m. Based on the 10 % criterion, the required cell size is in the range of 0.035 m to 0.071 m. A sensitivity analysis was conducted considering three mesh sizes in the Y and Z directions, equal to 0.06 m (Case 1), 0.04 m (Case 2), and 0.03 m (Case 3). The mesh size in the X direction was kept at 0.12 m in the three cases. Figure 48 shows the time-averaged adiabatic surface temperatures at point 5 and 7 on the beam cross-section at the mid span. The sensitivity study on the mesh size shows that Case 2 and Case 3 give similar results, hence the grid size of Case 2 with 0.04 m (in Y and Z directions) is sufficient for the simulation. This mesh grid is adopted in the analyses.

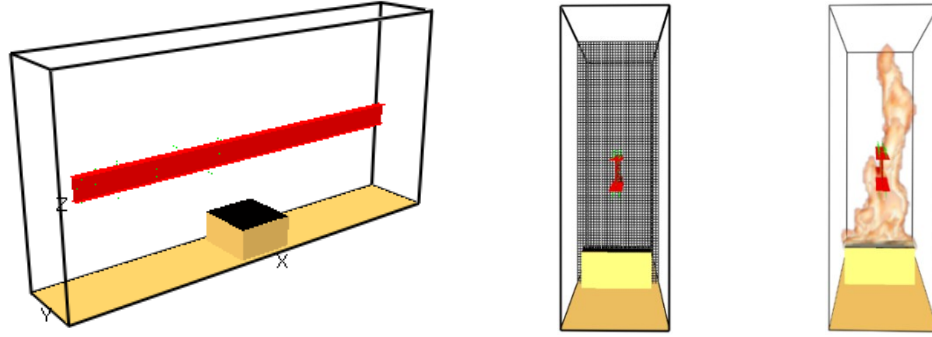


Figure 47. FDS numerical model of the steel beam fire test.

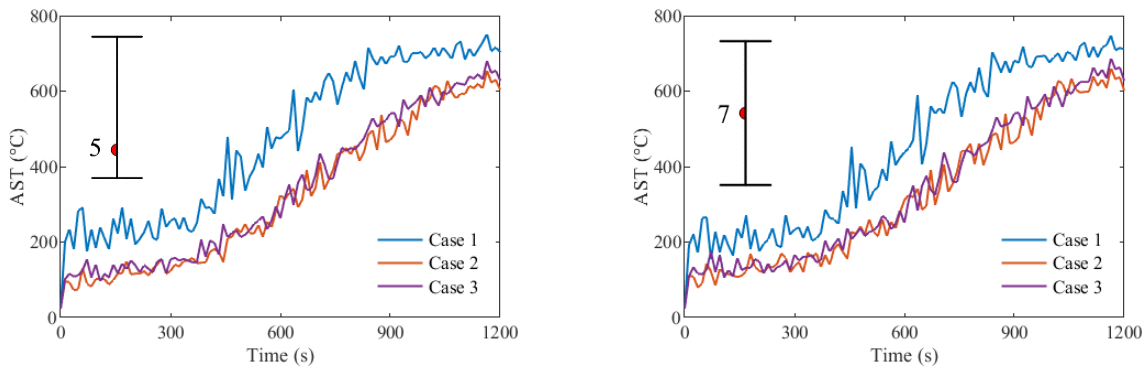


Figure 48. Effect of mesh size on the time-averaged adiabatic surface temperatures in the beam.

Since the structure is modeled in FDS, 14 sensors attached on the structural surface are used in the FDS analysis to compute the AST in the mid-span cross section of the steel beam using the first method discussed in Section 5.2.2.1, see Figure 7. The evolution of the AST is plotted in Figure 49, where some of the outputs have been omitted for readability. The AST output by FDS are then applied to the 2D thermal model as thermal boundary conditions for the FEM heat transfer analysis. Herein, the software SAFIR is used [99]. The AST are applied as temperature of the gas engulfing the profile (frontier conditions). The convection coefficients of the solid surfaces of the beam are taken as  $9 \text{ W/m}^2\text{K}$  for localized fires [108], and the emissivity is taken as 0.9 [77]. These values, which differ from the recommendation in the Eurocode, have been calibrated by other researchers when adopting a similar FDS-FEM AST method.

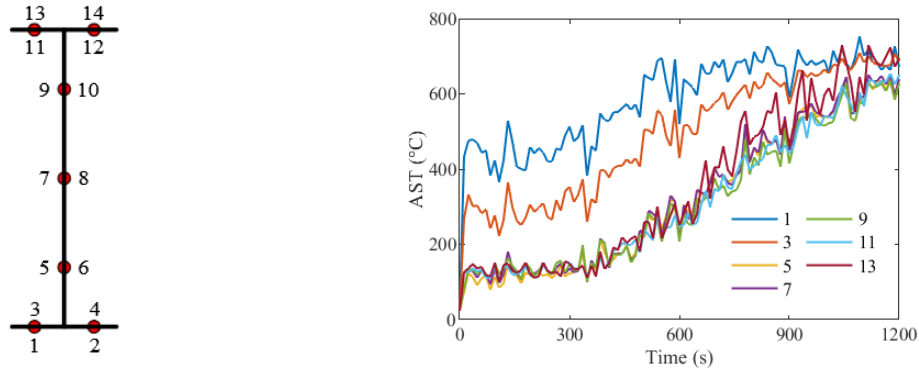


Figure 49. Location of adiabatic surface temperature sensors and time-averaged AST's from FDS.

The FDS-FEM interface method is also used for comparison, based on the same model in FDS (thus including the beam). The gas temperature and radiative intensities are output at each grid with a time step of 5 seconds and written into the transfer file. The number of solid angles is set as 100 by default. Then, the transfer file is applied onto the 2D thermal analysis model in SAFIR. A series of 2D thermal analysis are carried out at various positions along the length of the beam.

Steel temperatures calculated with the FDS-FEM AST method (labeled ‘AST-structure’) and the FDS-FEM interface method (labeled ‘Interface-structure’) are shown in Figure 50 to Figure 52.

The steel temperatures are provided at the lower flange, mid web, and upper flange of the mid-span section, and plotted aside the test measurements. It can be observed that the steel temperatures calculated with the AST method agree well with the test data at mid web and in the lower flange, while the AST method yields slightly higher temperature at the upper flange. The shielding effect of the lower flange to the mid web and upper flange is accurately captured by the AST method.

When the beam fails in Test 8, the predicted temperatures are 642 °C at the lower flange, 529 °C at the mid web, and 505 °C at the upper flange. At that time, the differences between the calculated temperatures and test data are -61 °C (-8.7 %) at lower flange, -5 °C (1.0 %) at mid web, and 95 °C (23.1 %) at upper flange, respectively.

The interface method provides different steel temperatures than the AST method especially at mid web and in the upper flange. This is due to the fact that, for the interface method, the gas temperature and radiative intensities are given at the center of the rectangular blocks of cells in FDS, while the geometry of the beam is modeled on the nodal points. Thus, a 3D Cartesian interpolation in space is needed to obtain the information at the beam surface nodes in the thermal model. However, this procedure leads to erroneous results if the values at the FDS nodes used for interpolation are significantly different, notably due to shielding from the beam itself. More discussion on the interface method is provided in the next case study to illustrate this limitation. At the time of failure, the differences between the calculated temperatures and test data are -48 °C (-6.8 %) at lower flange, 79 °C (14.8 %) at mid web, and 184 °C (44.8 %) at upper flange, respectively.

For completeness, the steel temperatures are then computed from FDS-FEM models where the steel beam is not included in the FDS simulation. These cases are referred to as ‘AST-no structure’ and ‘Interface-no structure’. The AST was calculated using the second method (AST-gas) when there is no solid surface modeled in FDS, as discussed in Section 5.2.2.1. The AST and interface methods yield very similar results when the structure is not included in FDS. This verifies the correct implementation of the two approaches: transferring the thermal boundary conditions through fictitious AST or through the transfer file of gas temperatures and radiative intensities yields the same results. When the structure does not influence the fire, either approach can be used. However, in this case study, these approaches lead to predicted temperatures at the mid web and upper flange that are much higher than the test measurements, because they incorrectly neglect the influence of the beam on the fire development.



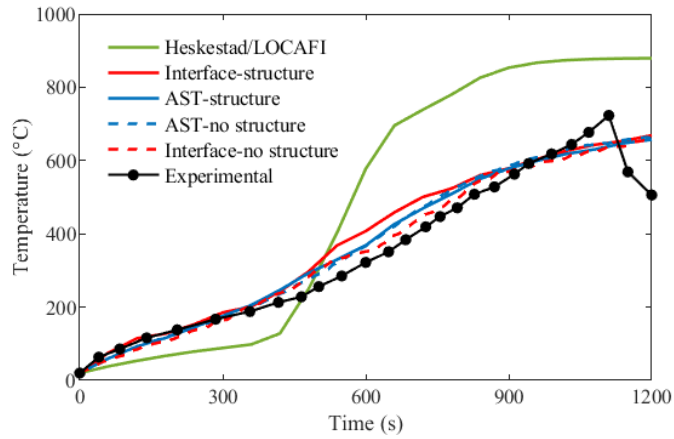


Figure 50. Test data and computed steel temperatures in the lower flange of the mid-span section.

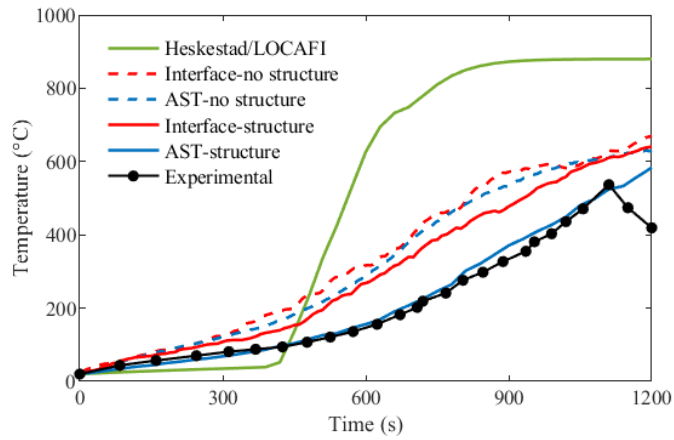


Figure 51. Test data and computed steel temperatures at mid web of the mid-span section.

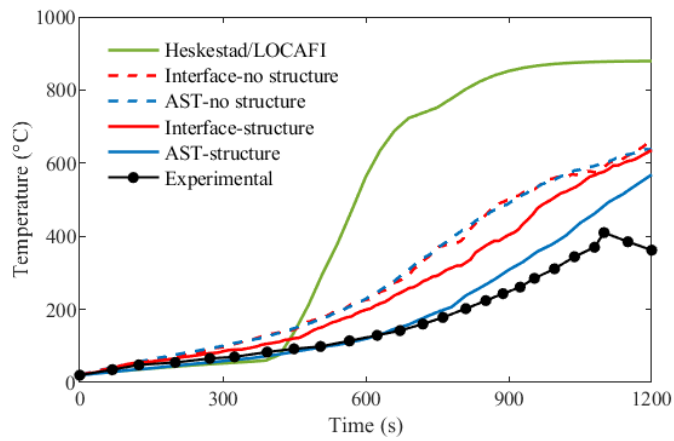


Figure 52. Test data and computed steel temperatures in the upper flange of the mid-span section.

### 5.4.3 Heskestad/LOCAFI model

The steel surface temperature for the beam test is then evaluated using simple models. As the HRR followed a t-squared function, the fire parameters were changing during the test. During the initial heating phase up to 392 s, the flame length was smaller than the distance between the fire source and the beam node line, which means the center section was outside the fire area and outside the smoke layer. In this case, the LOCAFI model (as introduced in Section 5.2.1) should be used. After 392 s, the flame became longer than the distance between the fire source and the beam node line, meaning that the beam was inside the fire area but outside the smoke layer. In the latter case, the Heskestad model (as introduced in Section 5.2.1) should be used.

The steel beam temperatures calculated by SAFIR using the simple fire models are plotted in Figure 50 to Figure 52. During the initial heating phase up to 392 s, the LOCAFI method gave lower prediction compared with the measured temperatures. The underestimation of the steel temperature during the initial phase may be due to the fact that LOCAFI neglects the convective flux. However, since the center section is right above the fire, the beam is heated by the hot gas that rises by buoyancy and therefore the convective effect is probably not negligible. After 392 s, the center section becomes inside the fire area. At that time, the radiative model introduced in Section 5.2.1.3 is no longer applicable and Heskestad is used. The member inside the fire area is surrounded by hot gas, of which the temperature is estimated by Eq. (16), and the incident heat flux to the member is computed from this flame temperature using Eq. (19). The flame temperature reached the limiting temperature 900 °C at 618 s, beyond which a more gradual increasing trend of steel temperature to 900 °C was observed. The overestimation by the Heskestad model when the flame engulfs the member is consistent with the observation by others that the Heskestad model overestimates the fire plume temperature along the centerline [109].

## 5.5 Case study: Steel column next to a localized fire

### 5.5.1 Description of the experiment

A square steel column (STKR400,  $0.1 \times 0.1 \times 1.6$  m, 3.2 mm thick) was heated by a 0.3 m square propane burner located next to the column [95], as shown in Figure 53. In the steady-state test carried out in accordance with the Japanese standards [95], the heat release rate was 52.5 kW. The height of the fire source was 0.25 m (from the bottom of the column). The base of the column was fixed. A constant load was applied on the other end which was fixed laterally but free to expand. The heating was applied for 60 min, after which the fire was extinguished. Temperature was measured by K-type thermocouples which were fixed on the column side surfaces with spot-welded steel foil.

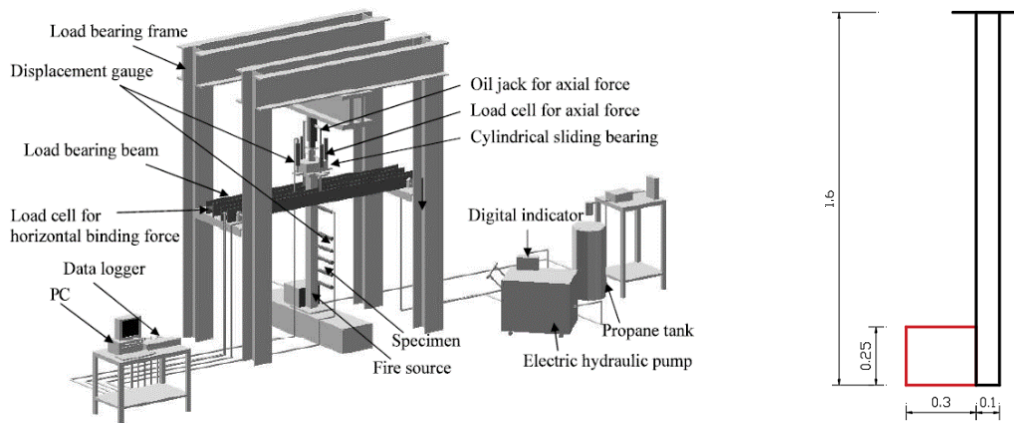


Figure 53. Experimental setup (unit: m) [95].

### 5.5.2 FDS-FEM model

The dimensions of the computational domain in FDS were  $0.75 \times 0.5 \times 1.8$  m ( $X \times Y \times Z$ ). A uniform grid size of 0.025 m was used, with  $R^*$  being about 1/12. Figure 54 shows the model in

FDS. The thermal properties of the steel were based on the specifications in EN1993-1-2 [35]. The emissivity of the steel was taken as 0.9 and the coefficient of convective heat transfer was taken as  $9 \text{ W/m}^2\text{K}$ .

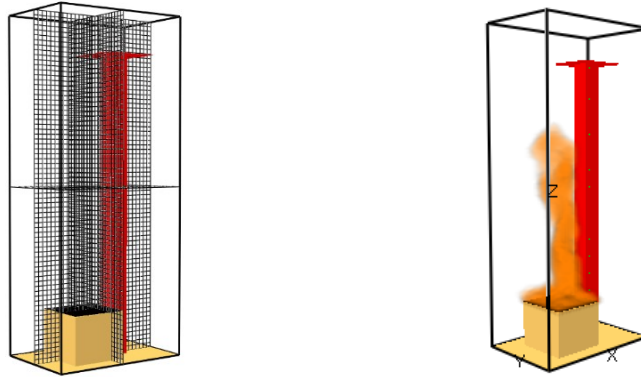


Figure 54. FDS model of steel column test.

A total number of 67 sensors are used to record the AST in 17 cross sections. Figure 55 shows the location of the 4 sensors on a cross section. It also plots the AST (averaged on time during the steady state part of the test) on the front, side, and back faces of the column, as a function of the vertical elevation above the burner. The maximum AST ( $666 \text{ }^\circ\text{C}$ ) occurs at the height of 0.5 m above the burner at the front surface that faces the flame directly. In contrast, as the back surface cannot see the flame, its AST is much lower than that of the front surface.

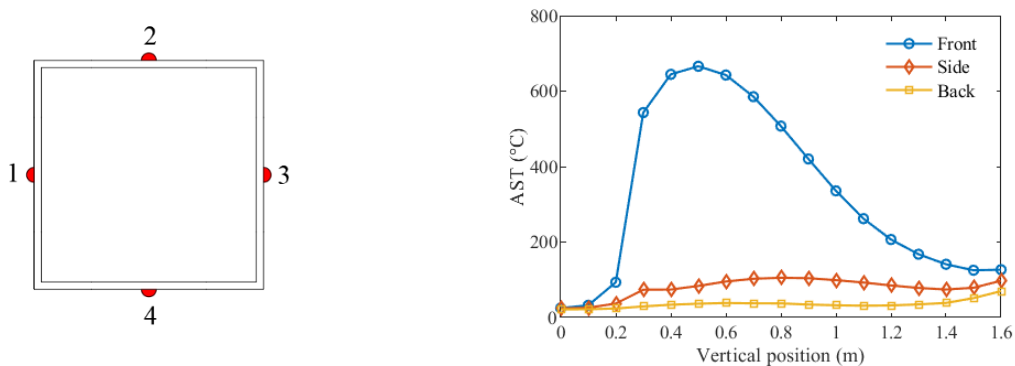


Figure 55. Location of adiabatic surface temperature sensors and time-averaged AST from FDS. Both the FDS-FEM AST method and the FDS-FEM interface method were used to transfer the thermal boundary information from FDS to SAFIR. The AST output by FDS were applied as gas temperature constraints to the 2D thermal model in SAFIR. The transfer file from the interface method was applied as 'Flux' constraints. Heat exchanges by convection and radiation within the cavity of the steel column were taken into account.

Figure 56 to Figure 58 show the comparison between the steel surface temperatures calculated from SAFIR and the test data. The computations using the FDS-FEM AST method provide reasonable agreement with the measured temperatures, although the computed temperatures are underestimated on the side and back surface. The heat transfer on the back surface is dominated by convection, but the equation used in FDS to calculate the adiabatic surface temperature is more suitable for the radiation dominated fire scenario [95]. This might explain the underestimation of the steel temperature on the back surface. The interface method yields much lower steel temperature on the front surface than the AST method. On the side and back surfaces, temperatures computed with the AST and interface methods are in better agreement.

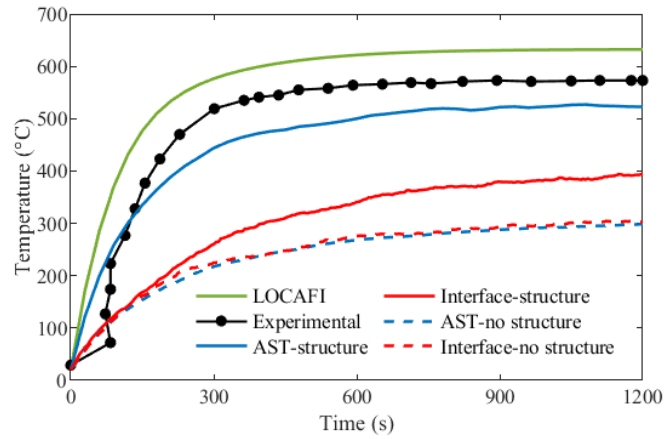


Figure 56. Test data and computed steel temperature on the front surface in the cross section at 0.4 m height.

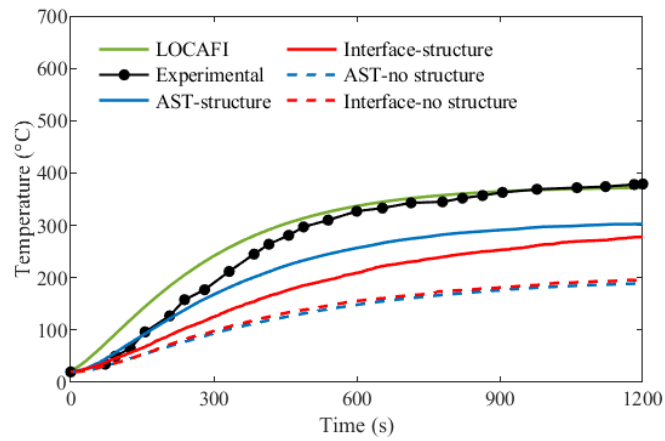


Figure 57. Test data and computed steel temperature on the side surface of the cross section at 0.6 m height.

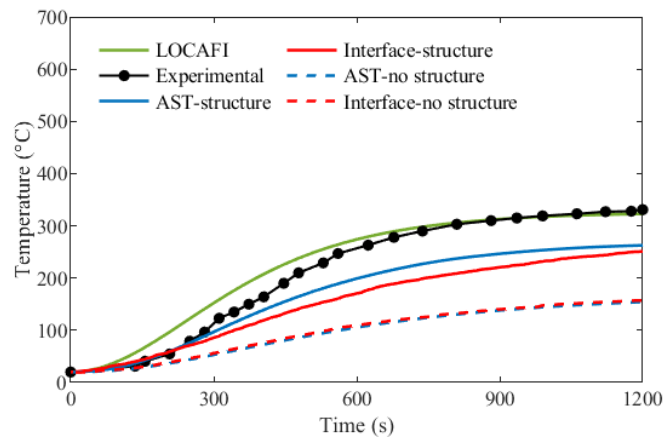


Figure 58. Test data and computed steel temperature on the back surface of the cross section at 0.6 m height.

### 5.5.3 LOCAFI model

The steel temperatures predicted by the LOCAFI method are plotted in Figure 56 to Figure 58. The LOCAFI predictions agree well with the experiment. The predicted steel temperature on the front and corner surface are slightly higher than the measured temperature, while the temperature on the side and back surface aligns with the test data. The slight overestimation of steel temperature on the front and corner surface may result from the idealization of the flame shape in LOCAFI with a uniform temperature distribution at a given flame height taken as that at the centerline. At the time of 1200 s, the differences between the calculated temperature and test data are 59 °C (10 %) on the front surface ( $z = 0.4$  m) and -8 °C (-2 %) on the back surface ( $z = 0.6$  m), respectively. This indicates a very good agreement for a relatively simple fire model.

### 5.5.4 Analysis of the effect of spatial interpolation in the FDS-FEM interface model

The discrepancy observed with the interface method on the front surface is due to the Cartesian interpolation in space. The cause of the inaccuracy of the method in this application is illustrated in Figure 59. The dashed lines represent the cell boundaries in FDS. The blue dots are the FDS cell nodes from which the gas temperature and radiative intensities are output and written in the transfer file. To conduct the thermal analysis in a FEM software such as SAFIR, the transfer file is applied onto the external boundary elements, shown by the red lines in Figure 59, as flux constraints. To obtain the thermal boundary information at the FEM structural nodes, a Cartesian interpolation of the nearby FDS nodes is conducted. For example, for the structural node S-1 on the boundary of the front surface, interpolation of the FDS cell nodes 1, 2, 3, and 4 is conducted

by the FEM software. As cell nodes 3 and 4 are inside the tubular profile, the gas temperature and incident heat flux at these nodes (recorded by FDS in the transfer file) are very low. Therefore, spatial interpolation in the transfer operation reduces the heat flux received by node S-1 by incorrectly ‘averaging’ values from the exposed surface (cell nodes 1 and 2) with values at nodes shielded from the fire (cell nodes 3 and 4).

Figure 60 (1) plots the gas temperatures recorded by FDS in the interface transfer file at the cell nodes 1, 3, 5, and 7 across a section of the tubular profile. As explained above, the gas temperature is much lower in cell node 3 than in cell node 1. Therefore, when the FEM software interpolates between the values at these two nodes to obtain the gas temperature applied on the exposed surface, it underestimates this temperature. The front surface in the heat transfer analysis thus receives a lower heat flux than expected, which results in a lower steel temperature on the front surface than the test data. The influence of interpolation is much less significant for the back surface, where the gas temperature and radiative intensities at node 5 and 6 are almost the same as those at node 7 and 8. As a result, the computed steel temperatures computed by the interface method are closer to those from the AST method on the back surface. This issue with the interpolation occurs when the structural member has been included in the FDS analysis.

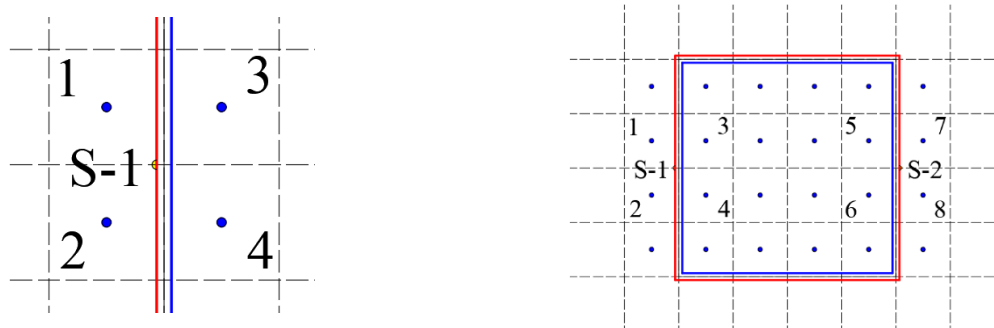
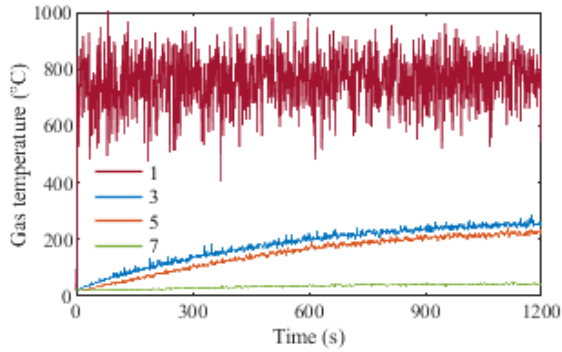
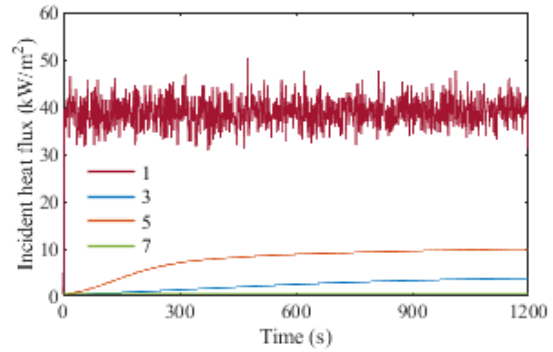


Figure 59. Interpolation in the domain to transfer information from the fire to the thermal model, based on the location of cell nodes in FDS (blue dots) and structural nodes in SAFIR (S-1).





(1) Gas temperature



(2) Incident heat flux

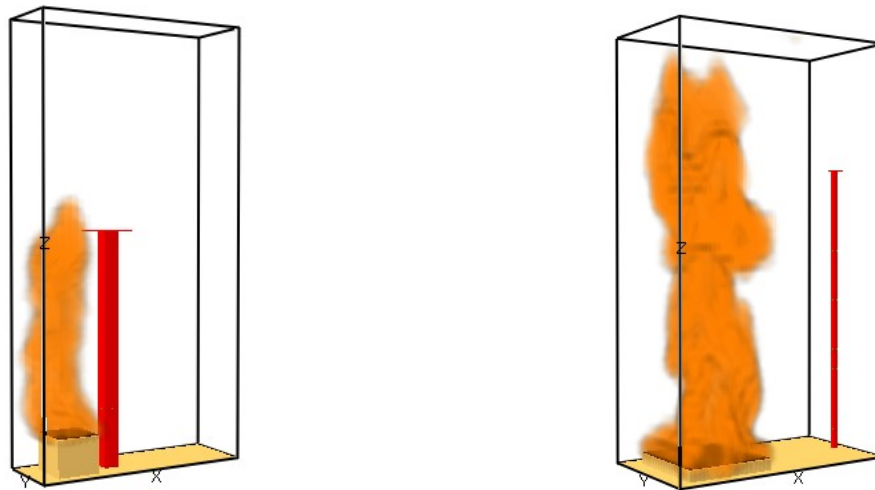
Figure 60. Gas temperature and incident heat flux output from FDS cell nodes.

In Figure 56 to Figure 58, the steel temperatures obtained with the FDS-FEM interface method without the structure in the FDS model (Interface-no structure) agree with those computed with the FDS-FEM AST method without the structure (AST-no structure). However, these results do not capture the measured temperatures, because in the experiment the presence of the column has a significant influence on the fire and on the thermal environment around its surfaces. Therefore, it is necessary to include the column in the FDS model, and for such situation, the interface does not lead to accurate results, because of the spatial interpolation as explained above.

The FDS-FEM interface is efficient when the structural member is further away from the localized fire. The fire analysis can then be performed independently from the thermal-mechanical analysis, without the need to include the member in the fire model. Any eventual change of the member design will not impact the fire simulation. The shadow effects and view factors are accounted for automatically through integration of the radiant intensities.

To illustrate an application where the interface is applicable, two variations of the column case study are studied. In Case 1, the test column is shifted away from the fire with an offset distance of 0.1 m. The HRR is 400 kW. In Case 2, the column is shifted away from the fire with an offset distance of 2 m, and the dimension of the fire is increased to  $1.77 \times 1.77 \text{ m}^2$ . The HRR is 20 MW. For each case, four advanced models are considered: either with or without the column present in

the FDS model, and either using the AST or interface method to transfer the thermal boundary information from FDS to SAFIR. The LOCAFI model implemented in SAFIR is also used to predict the steel temperature. As can be observed in Figure 61, the fire plume shape is more of a cylindrical shape, thus the ‘CYLINDRIC’ plume type was used for the LOCAFI model in SAFIR.



(1) Case 1 with HRR of 400 kW

(2) Case 2 with HRR of 20 MW

Figure 61. FDS models of case study with structure modeled in FDS.

The steel temperature on the front and back surfaces are plotted in Figure 62 and Figure 63 for Case 1 and 2, respectively. The FDS-FEM AST method with structure present in FDS (‘AST-structure’) has been validated based on the previous simulations and is thus used as benchmark. For Case 1, the interface method yields lower temperatures than the benchmark for the front surface, due to the spatial interpolation discussed above. The LOCAFI model yields more conservative predictions than the FDS-FEM models. This is probably due to the fact that the temperature at the surface of the solid flame in this model is taken as the one in the centerline whereas FDS is able to capture a temperature gradient in the horizontal direction in the flame. For Case 2, The AST method yields approximately the same temperatures regardless of whether the structure is included in FDS or not, which indicates that the column is far enough from the fire and

it does not noticeably influence it. In this case, the results from the interface method with no structure ('Interface-no structure') in FDS agree with those from the AST method. This shows that the interface method can be used for such applications where the structural member does not influence the fire. It is noteworthy that the interface with the structure in FDS ('Interface-structure') yields again lower temperatures than the benchmark, due to the spatial interpolation, confirming that in the interface method the structure should not be included in FDS.

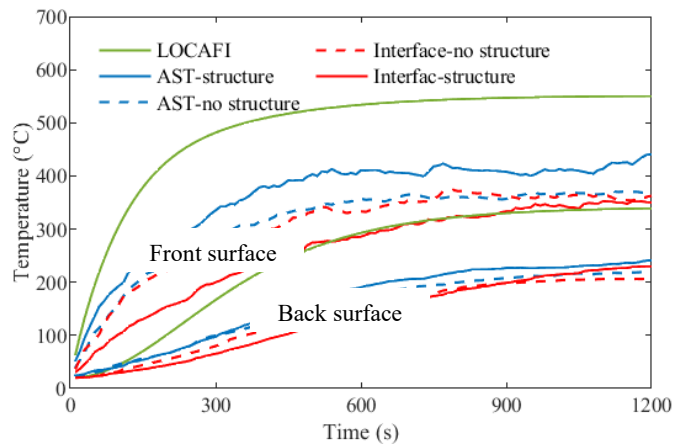


Figure 62. Computed steel temperatures in the cross section at 0.4 m height, Case 1.

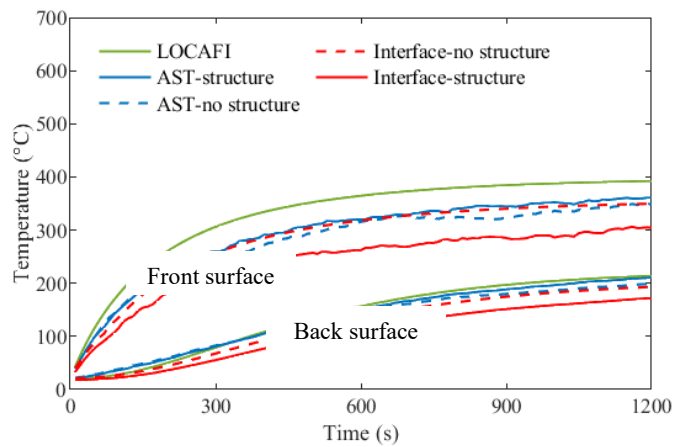


Figure 63. Computed steel temperatures in the cross section at 3 m height, Case 2.

## 5.6 Case study: Steel beam under ceiling subjected to localized fire

### 5.6.1 Description of the experiment

A H-section bare steel beam beneath the ceiling was heated by a 1.0 m square porous propane burner [89], as shown in Figure 64. The dimension of the steel beam was  $3.6 \times 0.075 \times 0.15$  m ( $X \times Y \times Z$ ), and the thickness was 5 mm in the web and 6 mm in the flange. The ceiling was made of mineral fiber Perlite board with dimension of  $3.6 \times 1.83 \times 0.024$  m ( $X \times Y \times Z$ ). The distance from the burner to the lower flange of the beam was 1.2 m. Different scenarios were carried out in the test campaign to investigate the transient domain ( $1 < L_h/H < 2.5$ ) for the heat flux at the stagnation point (beam center) according to the Japanese test standards [89]. The case with heat release rate of 900 kW, for which temperature measurements after 7 min of exposure were provided, is considered herein.

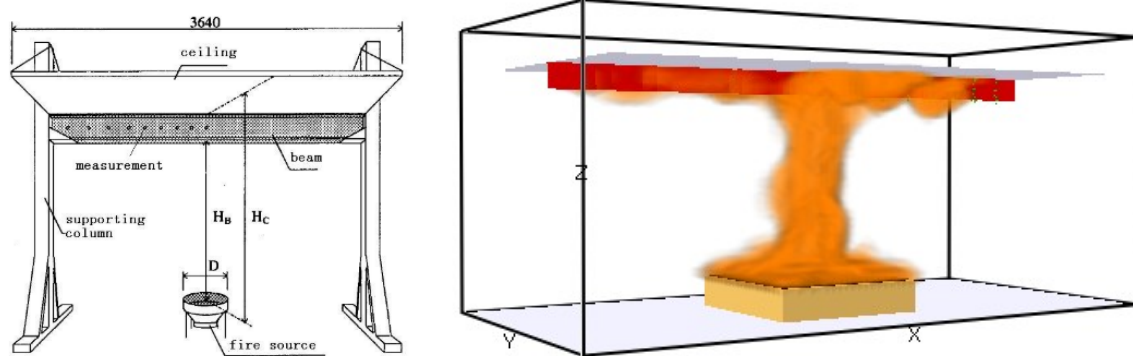


Figure 64. Experimental setup and FDS model of Hasemi test [89].

### 5.6.2 FDS-FEM model

The computational domain in FDS is  $4 \times 2 \times 1.8$  m ( $X \times Y \times Z$ ). The boundary condition at four sides of the domain was opening. The mesh size was 5 cm in all directions and the resolution was 1/18. The thermal properties of the steel were based on the specifications in EC3 [35]. The

emissivity of the steel was taken as 0.9 and the coefficient of convective heat transfer was taken as  $9 \text{ W/m}^2\text{K}$ .

Both the FDS-FEM AST method and FDS-FEM interface methods were used to compute the steel temperature along the horizontal axis of the steel beam. Figure 65 to Figure 67 show the predicted steel surface temperature at the lower flange, mid web, and upper flange of the center section, along with the test measurements after heating for 7 min. The results obtained with the AST method agree with the test measurements. The interface method, with the beam included in the FDS model given its influence on the fire, yields steel temperature lower than the AST method by about  $100^\circ\text{C}$ . Results obtained with the FDS-FEM interface method without including the steel beam in FDS are also provided (label 'Interface-no structure'). The ceiling (directly above the beam) is included in the FDS model. Higher temperature than the test measurements are obtained at the mid web and upper flange of the center section with 'Interface-no structure'. This observation is consistent with the findings from the NIST steel beam case study above and reflects the effect of neglecting the influence of the presence of the beam when computing the fire development. However, the difference between 'Interface-no structure' and test data is much less significant here than in the NIST beam case study (especially in the flanges), probably due to the presence of the ceiling in this FDS model. This observation suggests that the FDS-FEM interface method could be conservatively used to predict the temperature of steel members located at the ceiling level [100] provided the steel members are not included in FDS but the ceiling is.

### **5.6.3 Hasemi model**

The steel temperatures predicted by the Hasemi model at the lower flange, mid web, and upper flange of the center section are shown in Figure 65 to Figure 67. The height in the Hasemi model

was taken as the distance from the fire source and the ceiling. The Hasemi model yields very conservative results compared to the test data, which is in line with findings by others [100]. When using the Hasemi model, all the boundary elements on the center section receive the same heat flux (temperature calculated at the node line) and no shadow effect is considered.

#### **5.6.4 Maximum heat flux between Hasemi model and Heskestad model**

Since the center section of the beam is in the fire area and is in the smoke ceiling jet, the total heat flux received is taken as the maximum between the heat flux calculated using Hasemi model and the heat flux calculated with the Heskestad model, according to Figure 44. The computed steel temperatures are shown in Figure 65 to Figure 67 (labeled ‘Max(Hasemi, Heskestad)’). Among the four different numerical methods, this method yields the most conservative results for the steel beam under the ceiling. As the point of integration is inside the flame, the whole section receives the same heat flux, and no shadow effect is considered.

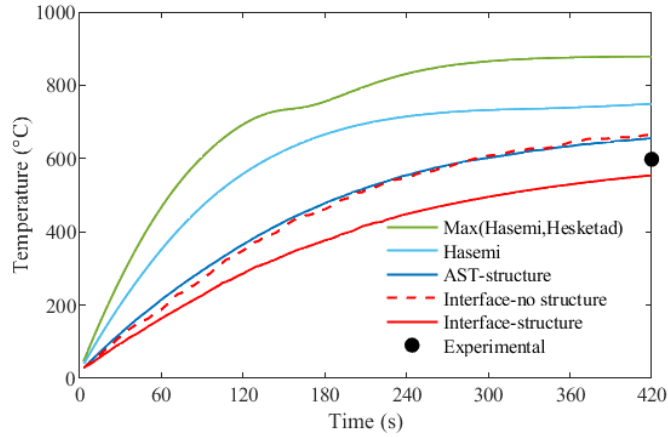


Figure 65. Comparison of the steel surface temperatures at lower flange of the center section.

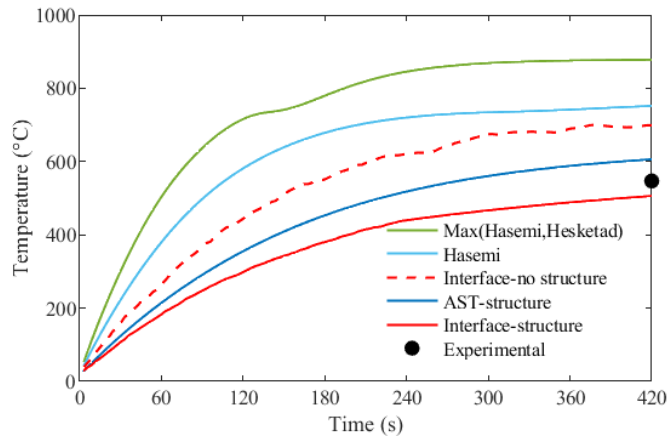


Figure 66. Comparison of the steel surface temperatures at mid web of the center section.

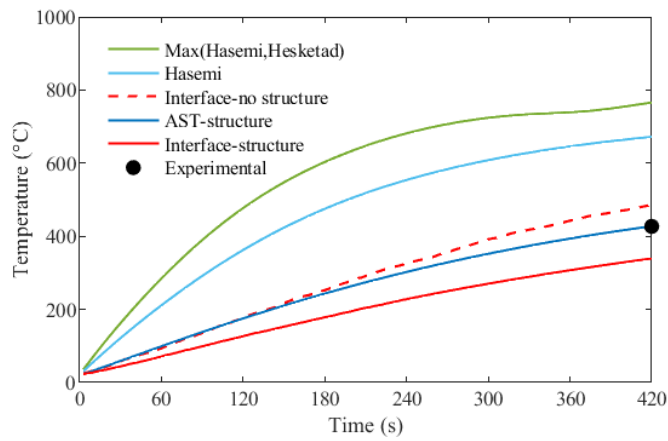


Figure 67. Comparison of the steel surface temperatures at upper flange of the center section.

## 5.7 Application: Open car park fires

### 5.7.1 Car park

Performance-based design approaches are well suited for assessment of open car parks behavior in case of fire. Localized fire models are applied to represent the burning cars and assess the heating of the adjacent structural members. Indeed, in open car parks, a flashover is unlikely to happen and considering uniformly distributed temperatures is thus not deemed to properly represent the fire event. This observation, however, does not hold for underground car parks, or aboveground car parks with few openings (i.e., not meeting the requirements to be classified as open). The definition of open car park depends on the country or jurisdiction under consideration [110], but it usually relies on a ratio of openings to surface of the boundaries of enclosure. Openings present on opposite façades also have an influence.

To conduct the parametric study on the temperatures reached in typical steel framing members under open car park fires, a medium-sized multi-story open car park is adopted [100]. The distance between the floor and the bottom part of the ceiling is 2.5 m. The floor plan of the car park is 60 × 48 m, with 5 × 2.5 m standard parking bays. The structure is a steel-concrete composite structure with steel framing and concrete flat slabs. One situation is based considering a steel hot rolled profile IPE450 for the beam (common design in composite steel-concrete car parks for 16 m primary beams spaced 2.5 meters apart), and another one considering a steel hot rolled profile HE600A (common design for 16 m primary beams spaced 5 meters apart) [100]. The column is a HE240M hot rolled steel profile [84] and the concrete slab has a thickness of 0.2 m. The dimensions of the IPE450, HE600A, and HE240M profiles are shown in Figure 68. No fire protection is applied to the structure.



To study the influence of galvanization on steel temperatures, the analysis is conducted for both ungalvanized profiles (UNGALVA) and galvanized profiles (GALVA). The emissivity of ungalvanized steel is taken as 0.7, independent of temperature, according to EN 1993-1-2 [19]. The thermal behavior of the galvanized steel is the same as that of ungalvanized steel except that the emissivity is 0.35 up to first heating to 500 °C, and 0.7 beyond. This is because the zinc coating applied on the surface of the steel irreversibly melts at a temperature of 500 °C.

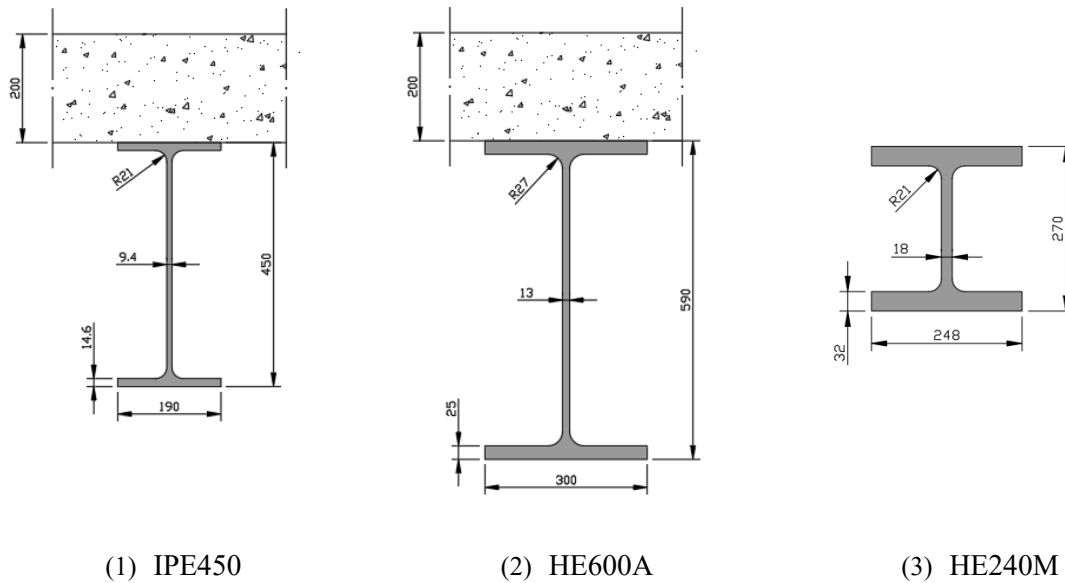


Figure 68 Dimensions of the steel profiles (unit: mm).

### 5.7.2 Fire scenarios

The heat release rate (HRR) for burning cars is adopted from the CTICM recommendation as the HRR curve for a Class 3 car [111]. The classification of cars is based on the potential calorific value of cars [112]. According to the study by INERIS [113], Class 3 cars can be used to evaluate the structural stability of open car parks under fire, with the requirement that the stability of the structure should be ensured during the whole fire scenario. The heat release rate of Class 3 car was experimentally obtained from a car fire test campaign conducted in 1995 at the CTICM laboratory.

The Class 3 vehicles were tested under a calorimetric hood in their operating state and showed a maximum heat release rate of 8.3 MW during the test.

The fire scenarios for the heating of steel beams and columns are shown in Figure 69. In the first scenario, a single car is burning, and it is positioned right below the beam. In the second scenario, three cars are burning underneath the beam, which axis is aligned with the middle car. When multiple cars are involved in a fire scenario, a time shift of fire propagation between nearby cars is observed [112]. Thus, the ignition of cars next to the first car igniting the fire is delayed by 12 min. In this scenario, the car in the middle is the first to ignite, followed by the two other cars after a delay of 12 min [112]. For the steel columns, the considered scenario has the column located in the middle of 4 car park spots [111]. The fire starts from one car, and spreads to the adjacent cars with a delay of 12 min. Finally, the car on the diagonal from the first ignited car starts burning at 24 min from the start. The heat release rate of each burning car follows the CTICM curve.

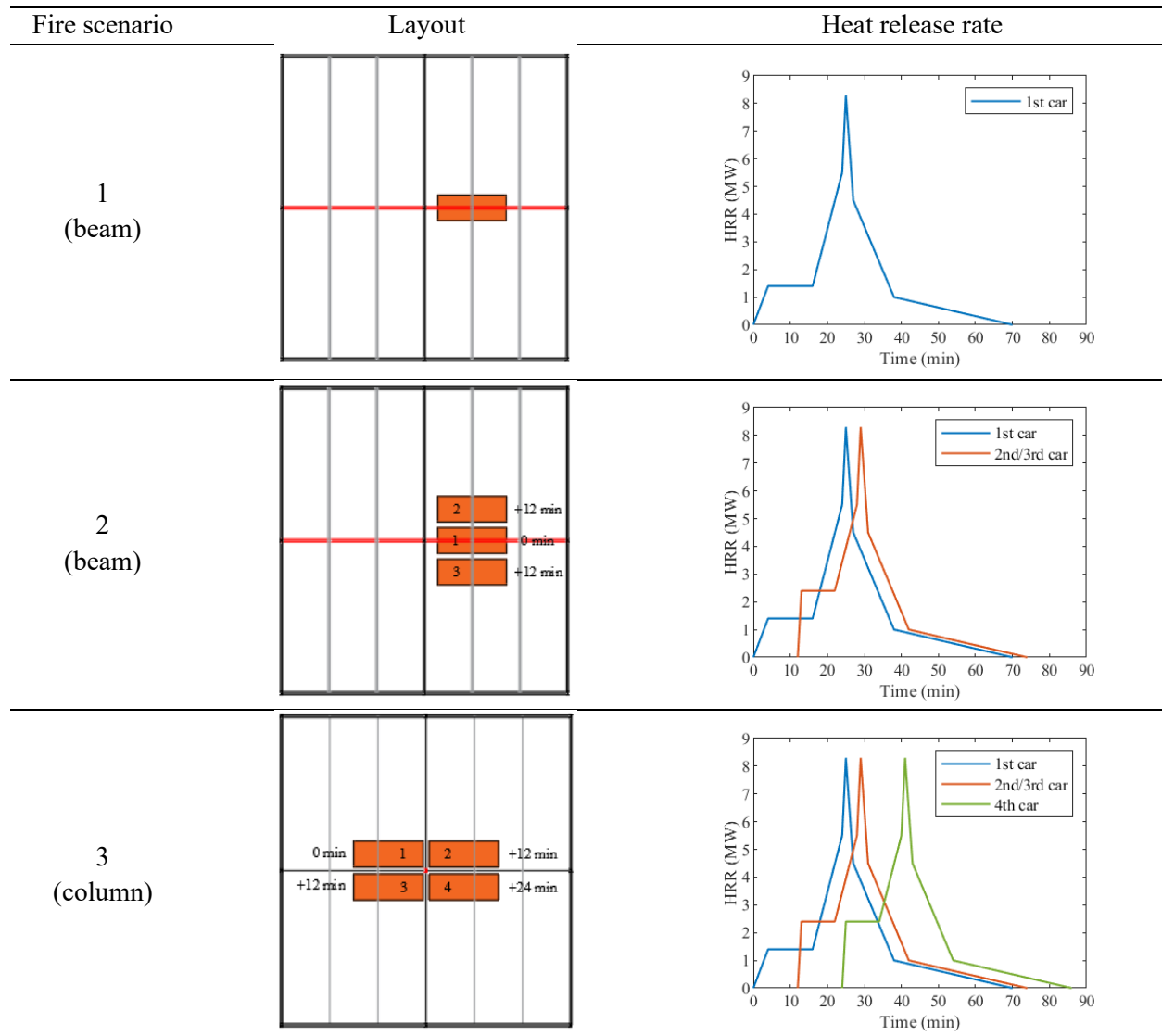


Figure 69 Fire scenarios considered for the modeling of the thermal exposure on steel beams and columns (burning cars are shown in orange, structure of interest is shown in red).

### 5.7.3 Methods for fire-thermal modeling

Figure 70 shows the applicable fire models based on the configuration between the localized fire and the steel member. The steel beams at the ceiling are inside the smoke layer. When using simple models for analyzing beam sections outside the fire area (section 'B1' and 'B2'), the heat flux should be taken from the Hasemi model. However, if beam sections are inside the fire area (section

‘B3’), the heat flux should be taken as the maximum between the Hasemi flux and the flux computed based on the flame temperature from the Heskstad model.

For steel beams, when selecting CFD-based modeling approaches, the FDS-FEM AST method is applicable to all configurations. The structural frame members should be included in the FDS model when adopting the AST method. The FDS-FEM interface method is applicable for structural members that are far from the fire source (section ‘B1’); the relevant distance being such that the presence of the structural members does not noticeably affect the continuity of the temperature and radiative fields. These frame members should be omitted in the FDS model when using the interface method. The ability to omit the frame members from the FDS simulation and to rely on an automatic transfer file between FDS and a FEM software is advantageous in terms of modeling effort. For sections closer to the heat source, which significantly influence the mass flow or radiative flow in the compartment (section ‘B2’), the frame members should be included in the FDS model and the AST method is preferred for the transfer of thermal information; except if the section is right above the heat source (section ‘B3’), in which case owing to symmetry both FDS-FEM AST and FDS-FEM interface methods are applicable.

The steel columns of a car park are outside the fire area (burning car), and a distinction is made based on the position of column in the smoke layer. For the lower part, which is outside the smoke layer, the radiative heat flux is dominant, thus the LOCAFI model should be applied. For the upper part of a column, which is inside the smoke layer, the convective heat flux from the hot smoke is not negligible, so the Hasemi model should be applied. When selecting CFD-based models, the FDS-FEM AST method is applicable regardless of the respective configuration between the column and the fire, but requires including the column in the FDS model and using a sufficient amount of AST sensors around the sections. When the column is away from the fire and the

presence of the column does not impact the fire development (column ‘C1’), the FDS-FEM interface provides an alternative method; the column is omitted from the FDS model in that case.

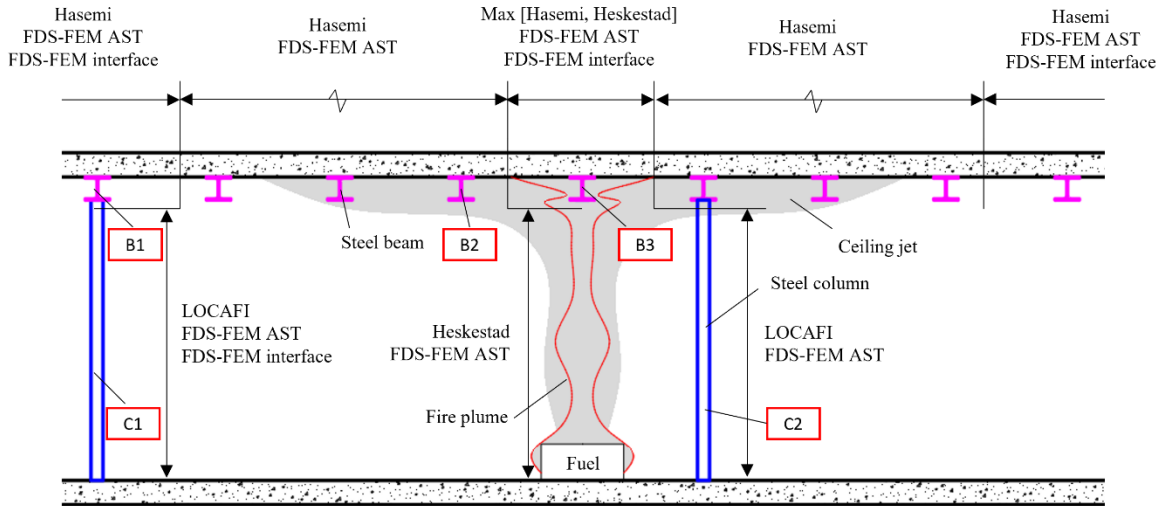


Figure 70 Application domain of localized fire modeling approaches for car park fires (not to scale) (adapted from [114]).

#### 5.7.4 Fire analysis

The computational domain in FDS is  $30 \times 22.5 \times 3$  m (length  $\times$  width  $\times$  height) for the simulations of fire scenarios for the steel beam, as shown in Figure 83. It is  $20 \times 10 \times 3$  m (length  $\times$  width  $\times$  height) for the simulations pertaining to the steel column. A sensitivity analysis was conducted on the computation domain to minimize the border effects with respect to the smoke flow. Burning cars are modeled as rectangular blocks with dimension of  $4.8 \times 1.8 \times 0.3$  m each. The heat release rate of the burning car is taken as the heat flux curves in Figure 69. Based on research for car fires, the soot yield is set to 0.22 [115], and heat of combustion is set to 44.4 MJ/kg, typical of gasoline [100]. A mesh size of  $0.1 \times 0.2 \times 0.1$  m is selected. The special resolution  $R^* = dx/D^*$ , where  $dx$  is the characteristic length of a cell for a given grid and  $D^*$  is the

characteristic diameter of a plume, calculated with the selected mesh size falls into a reasonable range of  $1/10 \sim 1/20$  [90].

The heat transfer analysis to the steel member is conducted in the FEM software SAFIR [99]. The software SAFIR allows applying thermal boundary conditions to the surfaces of the steel members which are imported from FDS simulations or from the simple localized fire models provided in the Eurocodes, i.e., Hasemi, Heskestad, and LOCAFI (i.e., solid flame).

To transfer thermal boundary information from FDS to the FEM software, two methods are used: the adiabatic surface temperature (AST) and the automatic interface. The steel member is included in the FDS analysis when using the AST method, while it is not included when using the interface method. To capture the thermal gradient, 14 sensors are attached onto the structural surface of cross sections at an interval of 0.2 m in the longitudinal direction to measure the AST. Then, the AST outputs from FDS are applied onto the 2D thermal model as thermal constraint for the FEM thermal analysis. For the interface method, the gas temperature and radiant intensities are output from FDS at the grids surrounding the structural member with a time step of 10 seconds and written into a transfer file. The transfer file is applied onto the 2D thermal model in SAFIR as thermal constraint. Then, 2D thermal analyses are conducted at each longitudinal integration point of the structural member.

The steel member temperatures are also investigated with the simple models described above. The burning car is modeled by a 3.2 m-diameter circular plan area with equivalent fire area. The axis of the localized fire is at the center of car. The heat release rate of the burning car is consistent with the heat flux curves in Figure 69. In SAFIR, a flux constraint 'Hasemi' is available for the heat transfer analysis. It computes the flux applied to each point of integration of the steel beams based on the simple Hasemi model. This flux constraint is also applied to the upper part of the

column, which is located inside the smoke layer. For the lower part of the column, the LOCAFI model is applied. SAFIR evaluates the flux using the solid flame model and assuming that the burning car is represented by a cone shape fire. For members in the axis of the flame, the Heskestad model is applied. The equations from Eurocode EN1991-1-2 are used to evaluate the flame temperature along the vertical axis of the fire. The heat flux to the member is then evaluated considering both the convective and radiative heat flux. It is worth noting that the Heskestad model is embedded in the flux constraint named 'LOCAFI' in SAFIR. With the flux constraint 'LOCAFI' applied, the heat transfer computation in SAFIR automatically shifts between the virtual solid flame model and the Heskestad model considering the relative position of the point of integration and the fire flame. When the point of integration (POI) is located in the flame, a convective flux with the flame temperature and radiative heat flux with this temperature and a view factor of 1 are considered. The flame temperature is calculated by the Heskestad model in the centerline of the flame at the height of the POI. When the POI is located outside the flame, only the radiative heat flux is considered with the LOCAFI model.

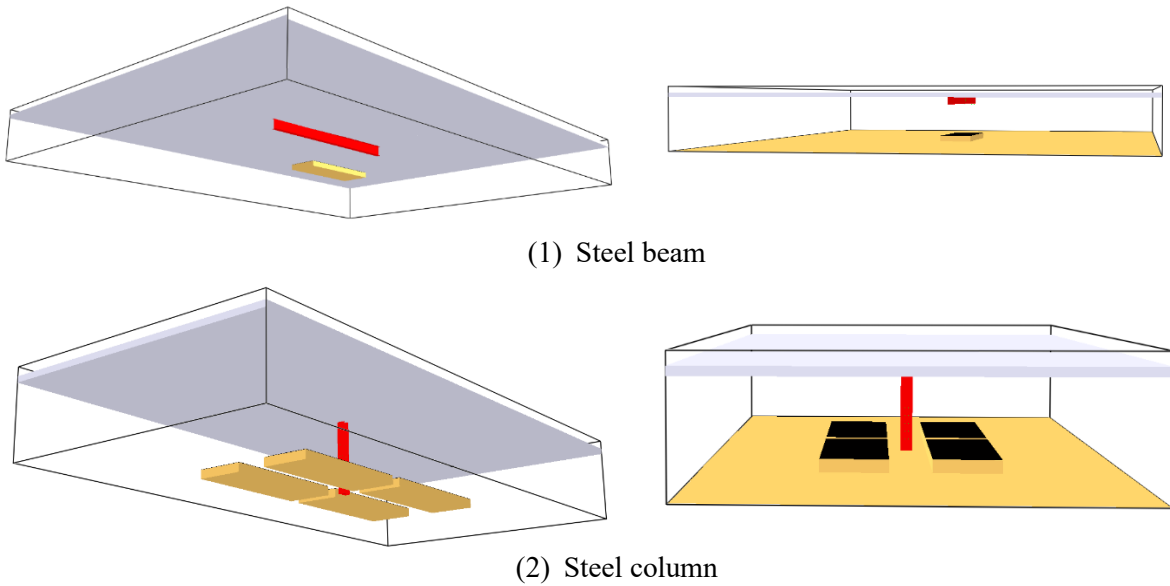


Figure 71 FDS modeling domains for the open car park fire analyses.

### 5.7.5 Thermal analysis

Thermal analysis of the steel beam and column under open car park fires is conducted in SAFIR [99]. Different types of boundary conditions can be assigned to the steel sections in the thermal analysis. For the FDS-FEM AST method, the AST temperatures are applied to the surface of the cross section as temperature-time Frontier constraints. This boundary condition is the same as used when applying a temperature-time curve, e.g., from a standard fire curve or an OZone post-flashover model; except that here the temperature is the AST. For the FDS-FEM interface method, the transfer file is interpreted by SAFIR to compute heat flux at the boundaries (applied as Flux constraints in the thermal analysis). The treatment of the transfer file involves spatial and temporal interpolation as well as integration of the radiant intensities, which is completed by the software. For simple models, the thermal boundary condition is also applied as Flux constraints. Flux constraints are named either ‘Hasemi’ or ‘LOCAFI’ as detailed in Section 5.7.4 (with ‘LOCAFI’ encompassing both the virtual solid flame model and Heskestad model).



The thermal properties of the steel are in accordance with Eurocode EN1993-1-2 [14]. The convection coefficient is taken as 35 W/m<sup>2</sup>K, in accordance with Eurocode EN1991-1-2 for natural fire exposures. Emissivity of the ungalvanized profiles is taken as 0.7. For the galvanized profiles, a newly developed material type named GALVASTEEL is implemented in SAFIR. The new material GALVASTEEL is such that the emissivity is taken as 0.35 up to 500 °C and then 0.7 beyond that. A mesh size of 0.01 m is adopted for all the thermal analyses, as shown in Figure 72.

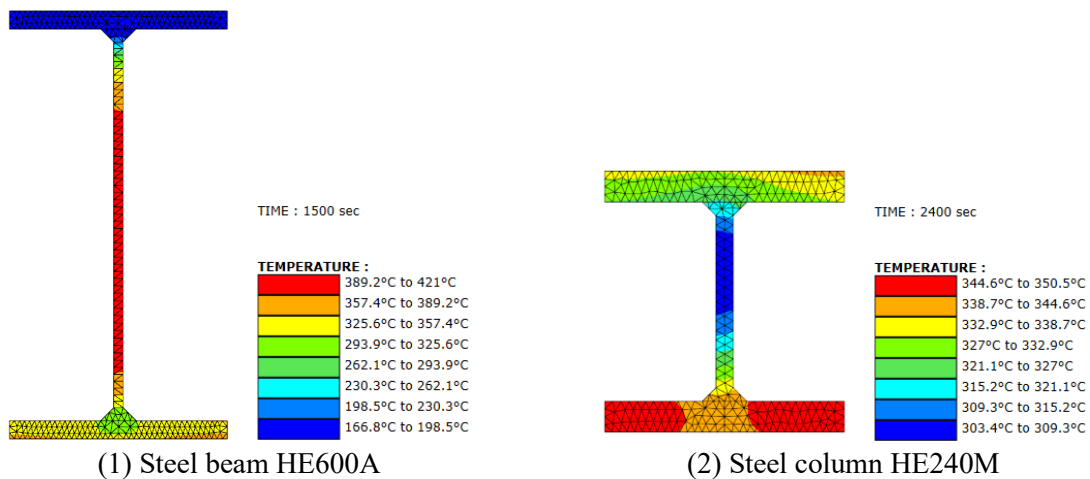


Figure 72 Finite element thermal analysis.

## 5.7.6 Results

### 5.7.6.1 Fire scenario 1: steel beam

The steel beam temperatures at the mid-span cross section under localized fire scenario 1 are shown in Figure 73. Solid lines are used for the ungalvanized profiles, while dashed lines are used for galvanized profiles. The FDS-FEM AST method has been validated against test data in Section 5.4 to Section 5.6 and is thus used as benchmark.

For the car park fire scenario 1, both FDS-FEM methods yield similar results for the IPE450 profile, while the interface method is slightly more conservative than the AST method for the HE600A profile. This verifies that for the structures located at the ceiling level and right above the heat

source, the interface method is applicable, as shown in Figure 70 B3. In the FDS interface simulation, the beam is not modeled in FDS, but the flat slab ceiling is. When comparing the member temperatures reached in different profiles, the IPE450 experiences temperatures higher by almost 120 °C than HE600A due to the higher section factor.

Both the AST method and interface method correctly yield reduced temperatures when the profile is galvanized. Due to galvanization, the peak temperature is reduced by 53 °C in the web and 69 °C in the flange of IPE450 at the center section. As for the HE600A profile, the peak temperature is reduced by 68 °C in the web and 73 °C in the flange at the center section. The time to reach the peak temperature is also delayed by about 1 minute for IPE450 and 2 minutes for HE600A due to galvanization. This is consistent with the fact that a lower emissivity leads to reduced heat transfer at the boundaries of the steel beam.

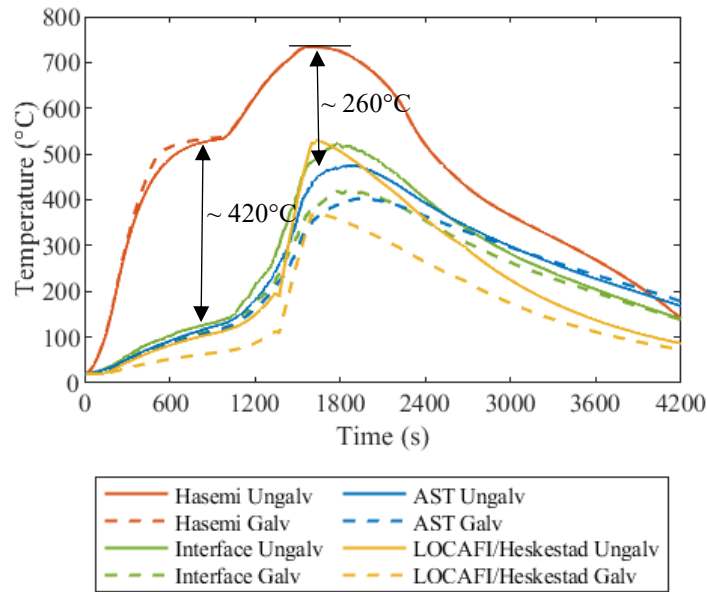
Simple models are also adopted to predict the member temperatures. The center section of the beam is in the axis of the fire and at the ceiling level. For such situation, two analyses are completed. One simple model approach is to apply the Hasemi model. Strictly speaking, the Hasemi model only applies when the flame touches the ceiling, while in the early stage of the fire this is not the case. Evaluating the heat flux throughout the localized fire event with the Hasemi model (“Hasemi” flux boundary condition in SAFIR) is thus expected to yield conservative results. Another approach is to evaluate the flux based on the flame temperature from the Heskstad model. This second approach (“LOCAFI” flux boundary condition in SAFIR) evaluates the flame temperature along the vertical axis of the fire, then applies either the virtual solid flame model to compute radiative flux to the beam at the early stage of the fire when it is outside the flame or computes the convective and radiative flux to the beam once it is inside the flame. In this second approach, the finite element software automatically transitions from the former flux computation to the latter

based on the flame height. To indicate that both LOCAFI and Heskestad models are combined in this second approach, the curves in Figure 73 are labelled as LOCAFI/Heskestad.

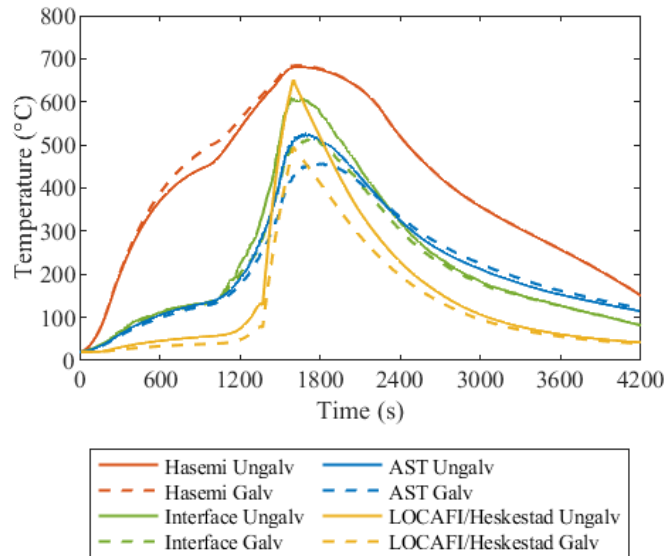
The Hasemi model significantly overestimates the steel temperatures, compared to the FDS-FEM AST/interface method. The overestimation is greatest during the initial heating phase. For example, at 15 min, the temperature difference between the Hasemi model and AST method reaches 420 °C in the lower flange of the ungalvanized HE600A profile, as shown in Figure 73 (1). A clear discrepancy in peak temperature between the Hasemi model and FDS-FEM models is also observed. For instance, the peak temperature difference between Hasemi model and AST method can be as much as 260 °C in the lower flange of ungalvanized HE600A profile, as shown in Figure 73 (1).

Another issue with the Hasemi model is that it erroneously represents the influence of galvanization on the member temperature. Contrary to the observation with FDS-FEM, Hasemi yields slightly higher steel temperature in the galvanized profile compared with the ungalvanized one. The causes for these shortcomings of the Hasemi model will be discussed in Section 5.7.7.2. Regarding the LOCAFI/Heskestad model (“LOCAFI” flux boundary condition in SAFIR), during the initial stage when the HRR from the burning car is small and the analyzed section is outside the flame, lower temperatures are obtained compared with the FDS-FEM AST method. In this initial stage, the flux is computed based on the virtual solid flame, hence convection is neglected. After the flame touches the ceiling and the section is inside the flame, both the convective and radiative heat flux are taken into account, evaluated based on the flame temperature from the Heskestad model. The model yields similar estimations of the peak temperatures reached in the profiles as the FDS-FEM AST method. The ability of this implementation of the simple model to transition from virtual solid flame when the member is outside the flame to convection and

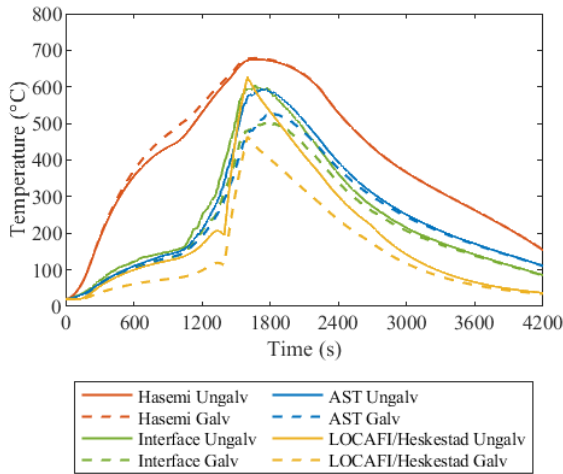
radiation once the member becomes engulfed is clearly visible in the results, with a sudden increase in temperatures that matches that obtained with FDS. It also captures the influence of galvanization with lower emissivity leading to lower temperature.



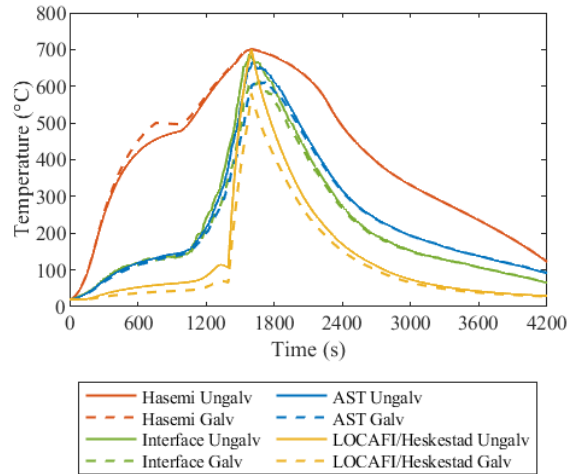
(1) Lower flange of HE600A



(2) Web of HE600A



(3) Lower flange of IPE450



(4) Web of IPE450

Figure 73. Temperature evolution in the web and lower flange of HE600A and IPE450 in fire scenario 1 (results obtained from FDS-FEM AST method is used as benchmark).

### 5.7.6.2 Fire scenario 2: steel beam

The steel beam temperatures at the mid-span cross section obtained from various methods under localized fire scenarios 2 are shown from Figure 74. The FDS-FEM interface method yields lower member temperatures than the FDS-FEM AST method, especially at the lower flange. This discrepancy indicates that when the section is not right above the heat source (the second and third burning cars in scenario 2), the influence of the presence of the structural member cannot be neglected. Thus, the interface method is not recommended for this situation. Both the AST method and interface method correctly yield reduced temperatures when the profile is galvanized. In fire scenario 2, the galvanization has less dominant effect on the peak temperature due to the more intense heating. When comparing the member temperatures in different profiles, IPE450 experiences temperatures about 60 °C to 100 °C higher than the HE600A due to the different section factor.

The Hasemi model again overestimates the member temperatures compared with the FDS-FEM AST method. It is on the conservative side, with discrepancies not as large as for scenario 1, but

still possibly making it overconservative for design. As observed previously, the Hasemi model also yields erroneous results on the effect of galvanization, because it cannot correctly capture the effect of a change in emissivity on the absorbed heat flux.

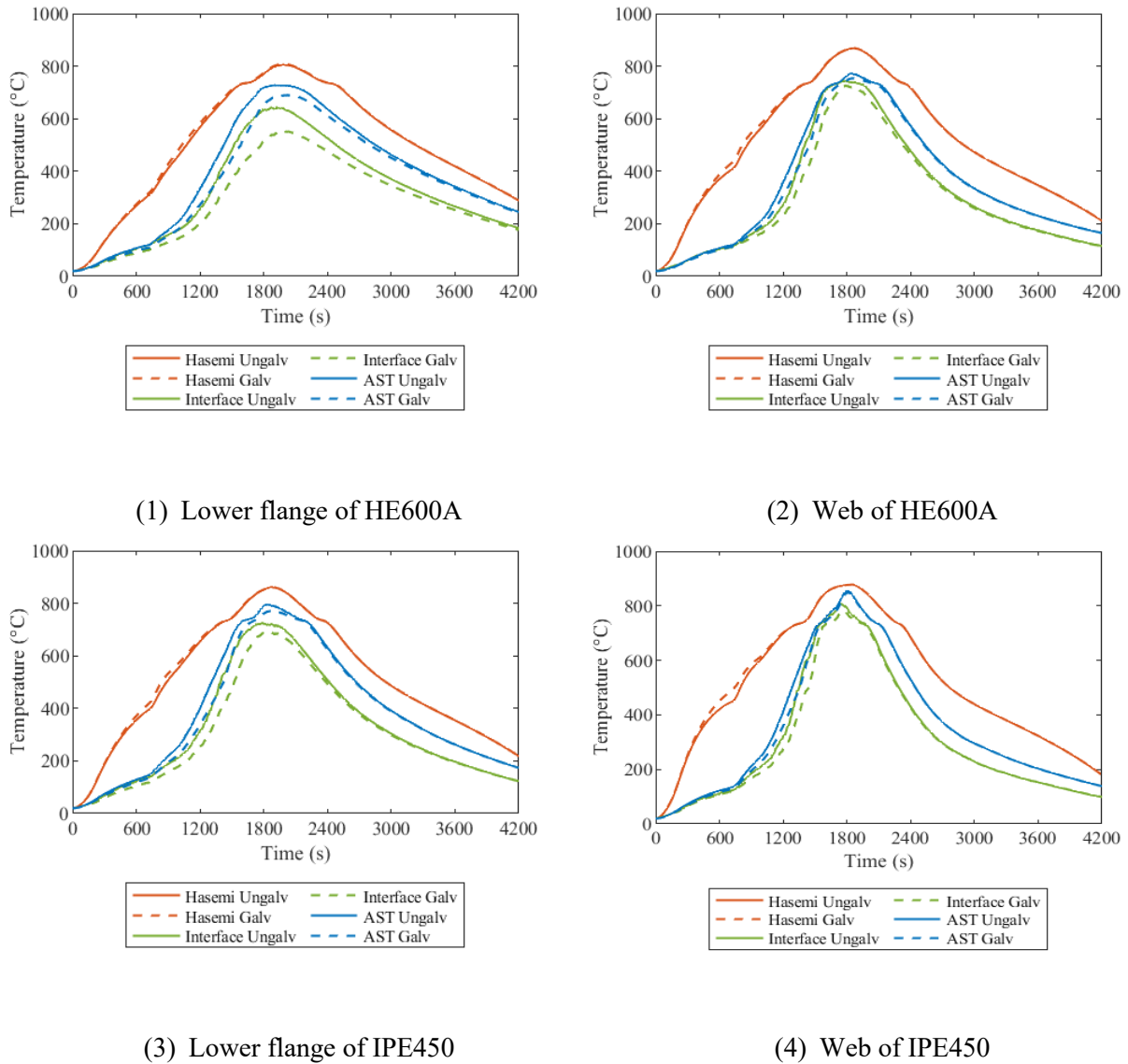


Figure 74. Temperature evolution in the web and lower flange of HE600A and IPE450 in fire scenario 2 (results obtained from FDS-FEM AST method is used as benchmark).

The CTICM conducted experiments on a similar open car park fire scenario as the scenario 2 in this study in 2000 [116]. Three Class 3 cars were involved in the test and the central one was ignited initially, as shown in Figure 75. The difference between the test and fire scenario 2 in this

study is that the beam in the test was in the middle of two parking bays. The maximum temperature in the tested IPE550 beam at the mid distance of a car was around 700 °C. This value is comparable with the maximum temperatures of 772 °C and 855 °C computed with the FDS-AST methods in the webs of the ungalvanized HE600A and IPE450, respectively. The lower value obtained in the CTICM experiment compared to the numerical simulations in this study could be due to the offset of the beam in the test, while the simulation assumes a burning car directly underneath the axis of the beam.

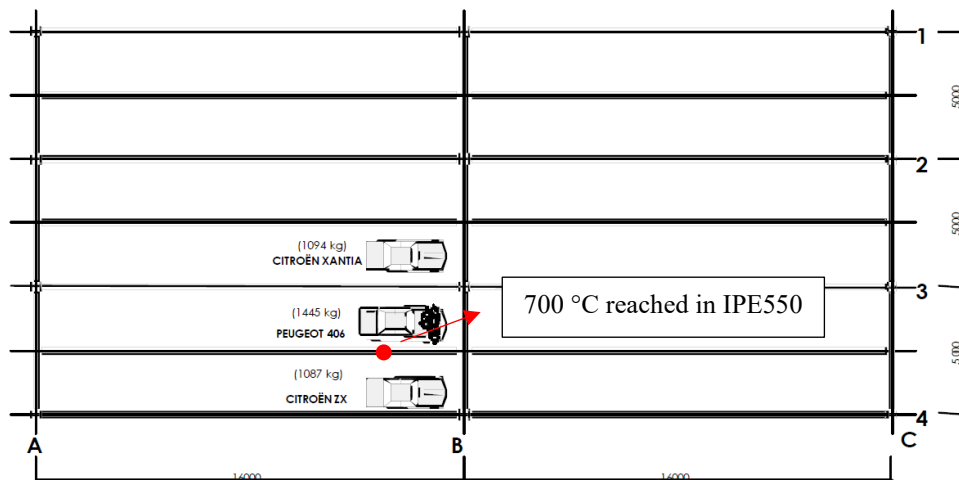


Figure 75 Fire scenario and location of maximum temperature tested by CTICM [116].

### 5.7.6.3 Fire scenario 3: steel column

The steel column temperatures in the flanges and web at 0.7, 1.9, and 2.4 m elevations under localized fire scenarios 3 are shown from Figure 76. The temperatures predicted by the FDS-FEM AST method are denoted by the solid lines, those predicted by the interface method are denoted by the dotted lines, and those predicted by simple methods are denoted by the dashed lines.

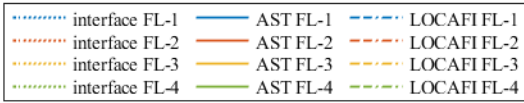
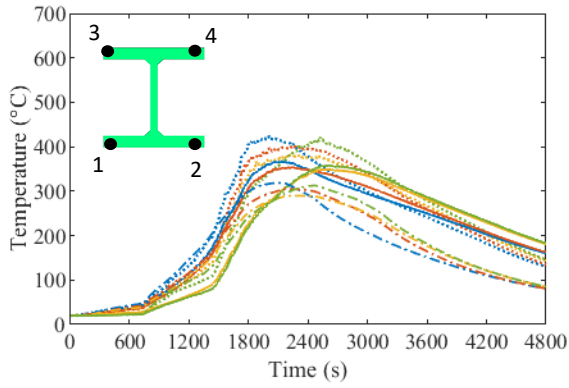
The heating sequence in the flanges is consistent with the fire propagation from the first vehicle to the surrounding vehicles. The peak flange temperatures reached in points 1 and 4 are slightly

higher than those in points 2 and 3. In terms of the modeling approaches, the FDS-FEM interface method yields slightly higher temperature in the flanges and web at different elevations of the column than the AST method.

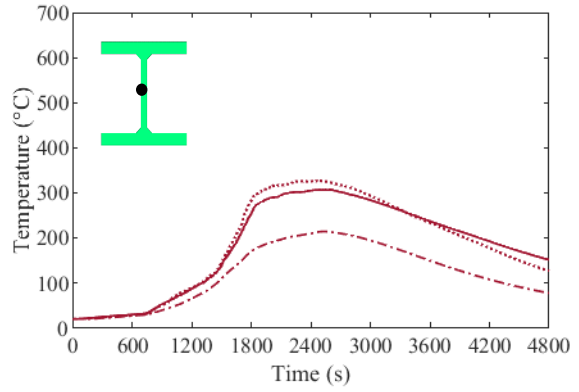
For the lower part of the column (outside the smoke layer), the LOCAFI model yields lower member temperatures than the AST and interface methods, especially in the web, as shown in Figure 76. For example, the difference of peak temperature from the AST method and the LOCAFI model can be as much as 200 °C in the web of the column at 1.9 m elevation.

For the upper part of the column (inside the smoke layer), the Hasemi model yields higher member temperatures than the AST or interface method. The difference of peak temperature from the AST method and the Hasemi model can be as much as 175 °C in the flange of the column at 2.4 m elevation. Meanwhile, the Hasemi model is not able to capture the shadow effect and the whole section receives the same heat flux, thus the four flanges exhibit the same temperature, as shown in Figure 76 (5).

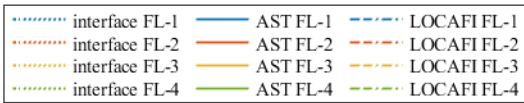
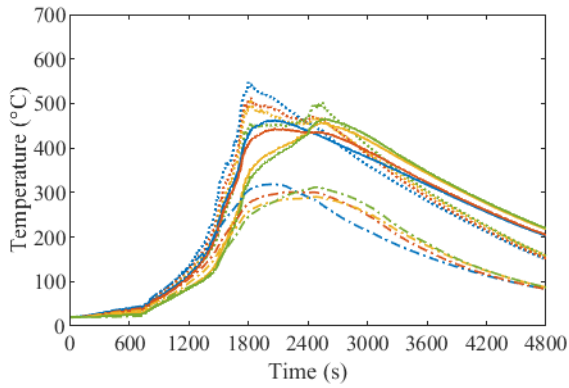




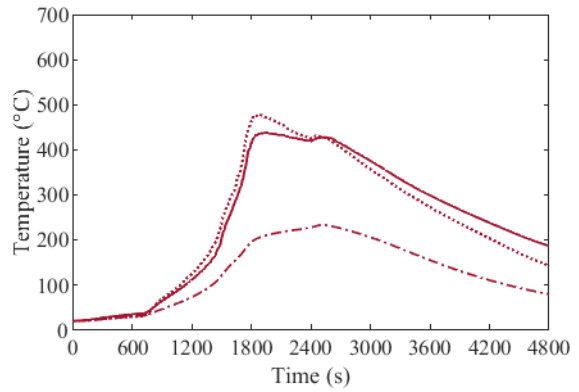
(1) Flange at the height of 0.7 m



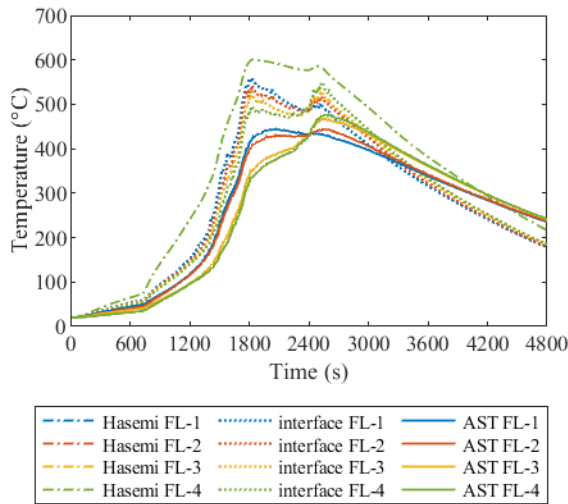
(2) Web at the height of 0.7 m



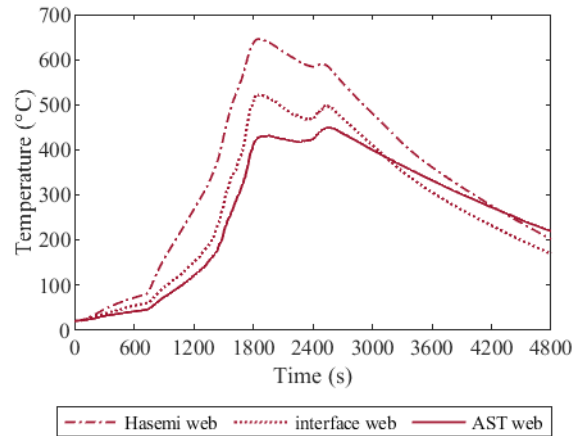
(3) Flange at the height of 1.9 m



(4) Web at the height of 1.9 m



(5) Flange at the height of 2.4 m



(6) Web at the height of 2.4 m

Figure 76 Temperature in the HE240M in fire scenario 3 (results obtained from FDS-FEM AST method is used as benchmark).

## 5.7.7 Discussion

### 5.7.7.1 Temperatures reached in the steel members

The peak and average temperatures obtained from the FDS-FEM AST method are summarized in Table 10. The size of the structural member and the location and number of burning vehicles influence the temperatures reached in the steel beam profiles. Under the same localized fire scenario, the peak temperature reached in the profile depends on the dimension of the profile, with higher peak temperature reached in more slender profile. In the fire scenario 1, the member temperatures in IPE 450 profile are generally 120 °C higher than HE600A, while in fire scenarios 2, the difference is more than 70 °C. The peak temperatures reached in the profiles above three burning vehicles (scenario 2) are higher than those reached above a single burning vehicle (scenario 1) due to the higher heat release rate with multiple burning cars. For example, the peak temperature at the lower flange of ungalvanized HE600A is increased from 476 °C under fire scenario 1 to 728 °C under fire scenario 2.

When subject to open car park fires, galvanization has the effect of delayed heating and reduced peak temperature. As listed in Table 32, the peak temperatures in HE600A are reduced by more than 60 °C and those in IPE450 are reduced by more than 50 °C under localized fire scenarios 1 when galvanization is applied to the steel members. The influence of galvanization on reduced peak temperature is less dominant in localized fire scenarios 2, because the zinc coating applied on the surface of the steel melts at a temperature of 500 °C, so the member temperatures gradually catch up with the fire temperature for severe fire exposures. For the steel column investigated in this study, the peak temperatures are reduced by more than 40 °C under localized fire scenario 3. Table 32. The peak temperature is taken as the maximum temperature reached on any cross section in the longitudinal direction of the structural members. The average temperature of the steel beam is taken as the arithmetical average of the temperatures at the bottom of lower flange, center of lower flange, mid web, and bottom of upper flange, while the average temperature of the steel column is taken as the arithmetical average of the temperatures at the four flanges and the mid web, as shown in Figure 77.



Figure 77 Temperatures distribution on the cross section.

The size of the structural member and the location and number of burning vehicles influence the temperatures reached in the steel beam profiles. Under the same localized fire scenario, the peak temperature reached in the profile depends on the dimension of the profile, with higher peak temperature reached in more slender profile. In the fire scenario 1, the member temperatures in IPE 450 profile are generally 120 °C higher than HE600A, while in fire scenarios 2, the difference

is more than 70 °C. The peak temperatures reached in the profiles above three burning vehicles (scenario 2) are higher than those reached above a single burning vehicle (scenario 1) due to the higher heat release rate with multiple burning cars. For example, the peak temperature at the lower flange of ungalvanized HE600A is increased from 476 °C under fire scenario 1 to 728 °C under fire scenario 2.

When subject to open car park fires, galvanization has the effect of delayed heating and reduced peak temperature. As listed in Table 32, the peak temperatures in HE600A are reduced by more than 60 °C and those in IPE450 are reduced by more than 50 °C under localized fire scenarios 1 when galvanization is applied to the steel members. The influence of galvanization on reduced peak temperature is less dominant in localized fire scenarios 2, because the zinc coating applied on the surface of the steel melts at a temperature of 500 °C, so the member temperatures gradually catch up with the fire temperature for severe fire exposures. For the steel column investigated in this study, the peak temperatures are reduced by more than 40 °C under localized fire scenario 3.

Table 32 Peak and average temperatures of galvanized and ungalvanized profiles under localized fire scenarios (obtained from FDS-FEM AST method).

Fire scenario	Profile		Peak temperature (°C)		Average temperatures (°C)
			Flange	Web	
1 (beam)	HE600A	Ungalva	476	526	428
		Galva	403	458	369
		Difference	73	68	59
	IPE450	Ungalva	595	665	551
		Galva	526	612	494
		Difference	69	53	57
2 (beam)	HE600A	Ungalva	728	772	671
		Galva	690	754	628
		Difference	38	18	43
	IPE450	Ungalva	795	855	749
		Galva	770	848	718
		Difference	25	7	31
3 (column)	HE240M (at z=2.3m)	Ungalva	474	464	470
		Galva	425	420	412
		Difference	49	44	58

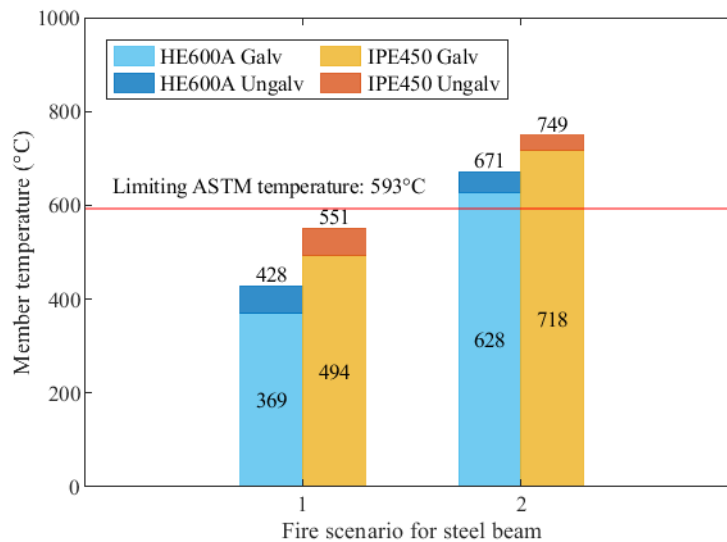


Figure 78 Average temperatures reached in HE600A and IPE450.

### 5.7.7.2 Limitations of the Hasemi model

Comparison of the temperature evolution in the steel beam at the ceiling level show that Hasemi model is more conservative than the FDS-FEM coupling methods. The main reasons of this

noticeable difference are the following: (i) The Hasemi model assumes that the flame touches the ceiling, but as can be observed in FDS modeling, the flame touches the ceiling during only one sixth of the whole fire duration, as shown in Figure 79. (ii) The Hasemi model was derived from experimental tests in which the ceiling was made of perlite boards. The energy absorbed by perlite boards is lower than that absorbed by the concrete slabs in a car park structure. The latter behave as a heat sink that absorbs a large amount of energy, which causes a decrease in gas temperature at the ceiling level. (iii) The Hasemi model does not capture the shadow effect, i.e., all boundaries of the section receive the same heat flux with the value calculated at the point of integration in FEM software. For open sections with concave parts, the received heat flux evaluated by the Hasemi model is therefore overestimated, which leads to higher member temperatures.

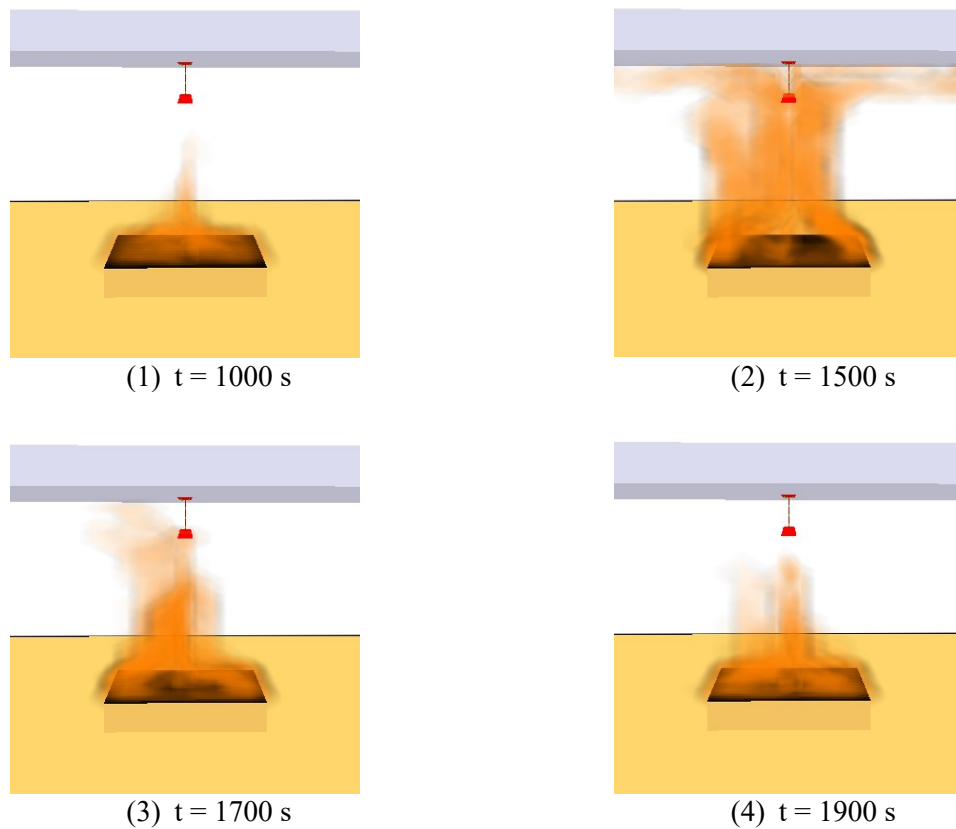


Figure 79 The FDS simulation of the localized fire scenario 1 shows that the flame does not touch the ceiling for most of the fire duration.

Besides, the Hasemi model gives erroneous results when applied to a material with different thermal properties than the ones for which the model was calibrated. More specifically, Hasemi model gives higher member temperatures with lower emissivity. This is due to the fact that the heat flux given by the Hasemi model is in fact inherently an absorbed heat flux, meaning that it does not depend on the thermal properties of the receiving member (because it is already implicitly multiplied by the thermal properties of the material for which it was calibrated). When using the Hasemi model, the net heat flux on the boundary of a solid is evaluated with Eq. (22). As can be seen in Eq. (22), the incoming (absorbed) part is independent of the thermal properties of the solid, whereas the outgoing (re-emitted) part depends on  $h_c$  and  $\varepsilon_s$ .

In this study, the steel member is analyzed in two configurations: ungalvanized ( $\varepsilon = 0.7$ ) and galvanized ( $\varepsilon = 0.35$ ). The incoming flux  $\dot{q}_{hasemi}$  is the same for the two configurations, which does not capture the fact that reducing emissivity physically leads to less radiant heat absorbed in a solid. The outgoing flux, in contrast, accounts for the term  $\varepsilon$  and therefore will be larger for the material with larger emissivity (as the latter is able to re-radiate more heat to the far field as its temperature increases). The result is that the net heat flux on the boundary of the ungalvanized steel would be smaller than that of the galvanized steel. This contradicts the physics and erroneously leads to higher temperatures in galvanized steel members than in (otherwise identical) ungalvanized members.

### 5.7.7.3 Implications for performance-based fire design

The performance-based design approach has been increasingly adopted in recent years for the structural fire design of car parks. This approach provides several potential advantages over the

traditional prescriptive design approach, including a more quantifiable level of safety and potential cost saving and design optimization [117]. It relies on rational analysis to explicitly evaluate the response of the structure in fire and then assess whether the design can achieve the required performance objectives. Thermal analysis, which evaluates the temperatures inside the structural member under certain fire exposure conditions, is a key step in the performance-based fire design procedure. The accuracy of the thermal analysis has a direct and significant impact on the following structural analysis. The structural analysis adopts the temperatures from the thermal analysis in the assessment of the response throughout the fire exposure which eventually determines the required amount of fire protection for the steel members.

For reference, the temperatures obtained in this study can also be compared with the critical temperature specified in ASTM E119 standard [118] for a prescriptive design of structural members in fire. In the open car park fire scenarios 1, the peak temperatures in the investigated ungalvanized steel beams are lower than 704 °C and the average temperatures are lower than 593 °C, i.e., they satisfy the prescriptive thermal requirements from ASTM E119 without thermal protection. However, when subjected to multiple localized fires (localized fire scenario 2), the temperatures are higher than the limiting temperature. As a result, either thermal protection is applied to the steel beams in a simplified approach of single element analysis, or the structural fire response of the structure needs to be assessed under these temperatures to check the performance. Completing a 3D FE model of the structure may allow demonstrating that the beams may be left unprotected through load redistribution in the structure (e.g., tensile membrane action of the composite floors). In the localized open car park fire scenario 3, the average temperature of the steel column is lower than 538 °C and the peak temperature on any cross section is lower than 649 °C, suggesting that no thermal protection is needed for the steel column in a simple element



approach. In general, completing a structural fire analysis is recommended to explicitly assess the response of the structure under fire exposure, as the limiting temperature criteria are a simplification intended for prescriptive design.

From the perspective of modeling approaches, both the simple models and advanced numerical modeling can be used for the performance-based fire design. Simple models tend to provide more conservative results and have limited field of applications, but they are generally computationally efficient. As an alternative to simple models, advanced numerical modeling approaches, especially the CFD-based models can provide more accurate results and can possibly enable optimization of the structure. For example, the peak temperature predicted by the Hasemi model in the upper part of the steel column under localized fire scenario 3 is 601 °C, while with the FDS-FEM AST method it is 474 °C. However, advanced numerical thermal analysis generally has higher demand for computational and modeling efforts.

## **5.8 Conclusions**

This chapter investigates the use of different numerical modeling approaches, based on advanced (CFD) and simple fire models, to predict the temperature in steel members subjected to localized fires. The concepts of adiabatic surface temperature (AST) and that of an interface transfer file were adopted to transfer the thermal boundary information from CFD models to FEM models. Simple models, based on fire plume theories validated against experimental data, were used to calculate the heat flux received by a structural member from a localized fire. A decision flowchart was proposed to recommend the suitable numerical modeling strategy as a function of the characteristics of the fire and structure. Then, three case studies were carried out with unprotected steel members to benchmark the different modeling strategies against experimental data. The

localized fire scenarios discussed in the case studies cover a wide range of potential fire situations, such as beam beneath the roof, columns in car park fires, or bridges under fires. The results show that the proposed flowchart can provide guidance for structural fire engineers to apply the models in adequate manner and ensure the safety requirements for structures subjected to localized fires. Then, application study of the proposed model strategy was carried out on the temperatures reached in steel framing members subjected to open car park fire scenarios considering the influence of the steel profiles, layout and number of burning vehicles, galvanization of the steel, and the modeling approaches adopted. The following conclusions are drawn:

- The FDS-FEM AST method proved versatile and accurate for the type of case studies investigated here. It allowed accurate prediction of the temperatures in unprotected steel beams and columns subjected to localized fires. With this method, the structural member must be included in FDS if its presence is expected to influence the fire development, and can be included or not if it has no influence on the fire. The main limitation of this method lies in the modeling effort when the thermal boundary conditions have to be evaluated in large structures, because of the required number of AST sensors and associated boundary conditions in the thermal analysis.
- The FDS-FEM interface method provides accurate results in structural members which presence does not significantly influence the localized fire development. Therefore, use of this method should be restricted to such situations, such as that of a column or a beam located away from the fire source. With this method, the structural member in which the temperatures will be evaluated should not be modeled in FDS, since the member presence was not foreseen when developing the spatial interpolation technique from the FDS grid to

the FEM surface. Slabs, walls and ceilings should be included in the FDS model given that they influence the fire development.

- The LOCAFI model is able to accurately predict the temperature of structural members outside the fire areas and outside the smoke layer. The virtual solid flame model is shown to give good predictions against experimentally measured temperatures. Implementation of the LOCAFI model can take into account the geometry of the structural members to account for the shadow effect in the received flux.
- The Heskestad model can be adopted if the structural members are inside the fire areas and outside the smoke layer. It seems to overestimate the member temperatures.
- The Hasemi model can be adopted if the structural members are under the ceiling and inside the smoke ceiling jet. It leads to conservative prediction of the member temperature. As the Hasemi model directly provides the flux absorbed by the member, it does not allow capturing the effect of the geometry of the member (shadow effect) or of its thermal properties on the received flux.
- In the investigated open car park fire scenarios, the location and number of burning vehicles influence the peak temperature reached in the structural steel members. When subjected to multiple vehicle fires, higher temperatures are reached in the steel beams compared to the case of a single burning vehicle due to the higher heat release rate.
- When subject to localized open car park fire, galvanization has the effect of delayed heating and reduced peak temperature.
- In terms of modeling approach, the Hasemi model is overconservative in predicting the temperatures in the steel beams at the ceiling level under open car park fires. Another

limitation of the Hasemi model is that, since it provides an absorbed heat flux, it incorrectly predicts that reduced steel emissivity leads to higher steel temperatures.

## **Chapter 6    Numerical study of local buckling behavior of cold-formed high-strength steel hollow section columns at elevated temperatures**

### **6.1 Introduction**

Research on the behavior of cold-formed AHSS members notably needs to address the issue of structural fire response. At the material level, cold-formed steels tend to lose proportionally more of their yield strength and modulus at a given temperature than hot rolled steels due to the release of cold-working dislocation with heating [72]. Test data show that CFS is more susceptible to temperature than hot rolled, as the increased strength caused by cold-forming fades away [8,9]. Furthermore, experiments on AHSS steel coupons, presented in Chapter 3, have shown that the reduction in strength and modulus with temperature is more pronounced for AHSS than for mild steel. As a result, the elevated temperature capacity of cold-formed AHSS members needs to be studied, as it may reduce quickly [119]. To support the use of members made from AHSS in cold-formed steel construction, the structural fire behavior of these members must be understood.

In this chapter, finite element models (FEM) are calibrated on experimental data for SHS and RHS [120] to capture the local buckling behavior of cold-formed SHS and RHS columns at ambient and elevated temperatures. A parametric study is then carried out with the FE models covering a range of width-to-thickness, plate width ratios, cross section dimensions, member thicknesses, and steel grades. The ultimate capacities gathered from the numerical results are then used to evaluate the applicability of the DSM specified in AISI S100 [12] as well as to explore possible modifications of DSM in the context of cold-formed SHS and RHS columns made of advanced high strength steels.

## 6.2 Literature review

While experimental and numerical research have been conducted on the compressive capacity of cold-formed steel square and rectangular hollow section (SHS and RHS) columns at ambient temperature [121–125], relatively few studies have focused on the structural response at elevated temperatures. Balarupan [120] conducted experimental and numerical study on the local buckling behavior of cold-formed hollow section columns at elevated temperatures. Based on his results, he concluded that the Direct Strength Method (DSM) [126] in AISI S100 [12] needed modifications to be applicable to hollow section columns. Mohammed and Afshan [127] conducted numerical investigations on the flexural buckling behavior and fire resistance design of cold-formed square, rectangular, and circular hollow section columns with different stainless steel grades and member slenderness. They compared their numerical results with the design approach in EN 1993-1-2 [14] and proposed new buckling equations. Martins et al. [128] investigated the global and local buckling behavior of stainless steel square, rectangular, circular, and elliptic hollow section columns under fire conditions. Arrais et al. [129] investigated stainless steel circular hollow section columns. The two latter studies concluded that the current design method in EN 1993-1-2 [14] should be improved for these members. Rokilan and Mahendran [130] studied the effect of nonlinear stress-strain characteristics on the global buckling capacities of cold-formed steel SHS columns at elevated temperatures. Recently, Couto et al. compared design methodologies for the cross-section capacity of SHS and RHS at elevated temperature and showed that the cross-sectional classification procedure in the fire situation from Eurocode and AISC specifications is inconsistent for these sections [131,132]. From this review, it appears that design methods currently provided in standards for the elevated temperature behavior of cold-formed steel members are not necessarily applicable, or accurate, for hollow sections.

Meanwhile, design methods need to address higher strength steels [133]. As the steel grade increases, the local buckling slenderness also increases. At ambient temperature, Foroughi and Schafer et al. [7] have investigated the behavior of CFS studs made of AHSS and showed that the DSM was adequate for members failing in isolated local or distortional buckling, while further investigation was needed for local-global or distortional-global interaction. In the fire situation, while research has been published on cold-formed steel SHS and RHS columns made of normal grades or stainless steels [134,135], the behavior of AHSS members still requires investigations.

### **6.3 Finite element model**

#### **6.3.1 Method and experimental data for benchmarking**

Finite element analysis has proven to be a powerful alternative to experimental testing in capturing the structural behavior of cold-formed steel members in fire conditions [136]. In this study, finite element modeling is used in parametric analyses to assess the local buckling capacity of SHS and RHS columns at elevated temperature. The finite element software SAFIR [99] is used.

The FE models are validated against experimental data from the thesis by Balarupan [120]. The experimental test considered as benchmark used the cold-formed SHS column shown in Figure 80 (1). The experiments studied the behavior of the SHS column made of G450 steel at temperature from 20 to 700 °C. The column failed by local buckling. In the experiments, the ends of the columns were welded to rigid endplates. The rigid plates were bolted to the shafts with high strength tensile bolts. The author of the experiments reported the axial load-deflection curves obtained experimentally and with modeling using ABAQUS. Prior to the parametric study, these experiments are thus modeled using SAFIR to validate the modeling approach on SHS members at elevated temperatures.

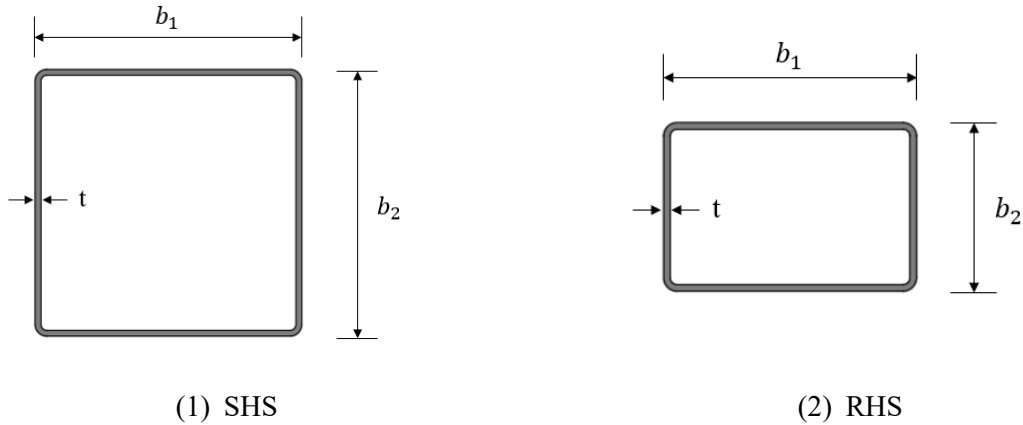


Figure 80 Cross section of SHS and RHS.

### 6.3.2 Description of the finite element model

#### 6.3.2.1 Element type and mesh size

The SHS and RHS columns are modeled using nonlinear quadrilateral shell elements in SAFIR [99]. The dimensions of the column used for validation of the model, as tested by Balaruban [120], are listed in Table 33. The rounded corner is considered with a radius of twice the thickness. A mesh size sensitivity study was conducted by Balaruban [120] with different mesh sizes to determine the optimal mesh size that yields the best accuracy with reasonable computational efficiency. Based on his recommendations, a mesh size of 4 x 4 mm is adopted for the flat elements of the columns and a finer mesh size of 2 x 4 mm is adopted for the rounded corner.

The shell element is a quadrangle based on four nodes, each bearing three translations and three rotations. Integration on the section is numerically done by four points of Gauss. Integration on the thickness is numerically done by up to ten points of Gauss. The capability of SAFIR to model local buckling with shell elements was validated by Talamona and Franssen [137,138], and this technique has been used in a number of studies [139–143].

Table 33 Dimensions of the column used for validation of the model.

Column	Length (mm)	Width $b_1$ (mm)	Width $b_2$ (mm)	Thickness $t$ (mm)
--------	-------------	------------------	------------------	--------------------



90x90x2	270	90	90	2.0
---------	-----	----	----	-----

### 6.3.2.2 Boundary and loading conditions

As the ends of the columns were welded to rigid endplates bolted to the shafts in the experiments [120], fixed end supports are applied in the numerical model. Nodal restraints, as shown in Figure 81, are used to implement the boundary conditions, which has proven to yield the same buckling load as rigid-fixed Multiple Point Constraints (MPCs) for fixed end supports [120]. At the loading end, the transversal displacements (X and Y) and three rotations (X, Y and Z) are restrained at each node, while all the three (X, Y and Z) displacements and rotations are restrained at the supporting end of the columns. An axial displacement in negative z direction is applied uniformly at the nodes of the flat elements at the loading end to avoid stress concentration, as shown in Figure 81. The axial displacement is increased until failure of the column. Failure is deemed to occur when the nonlinear analysis is unable to converge, and it is marked by a reduction in the axial force and a sudden increase in the transversal displacement of the plates at the location of local buckling.

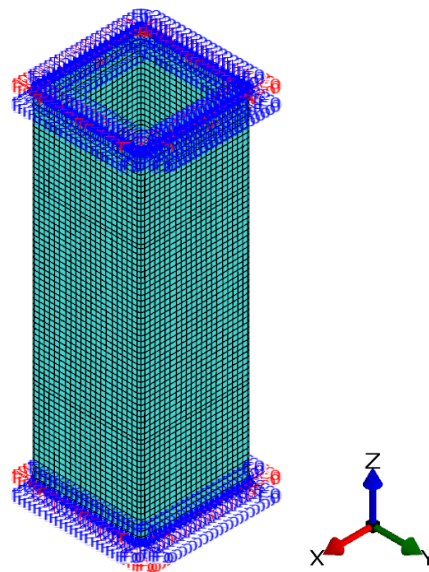


Figure 81 Boundary conditions for the fixed-fixed SHS column under controlled axial displacement.

### 6.3.2.3 Material properties

For comparison between the numerical model and the experiments, the material properties used in the model are the ambient temperature and elevated temperature mechanical properties of G450 steel reported by Balarupan [120] based on experimental measurements. These mechanical properties are listed in Table 34. The stress-strain relationship specified in Eurocode EN 1993-1-2 [14] is used. This stress-strain relationship has a nonlinear gradual yielding region and does not consider strain hardening.

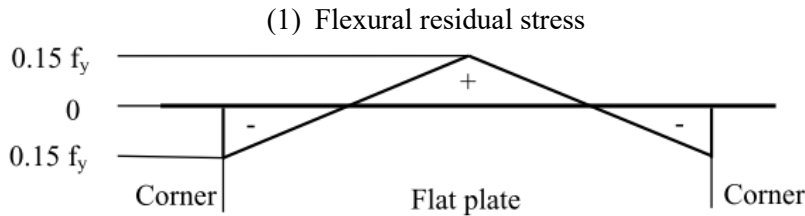
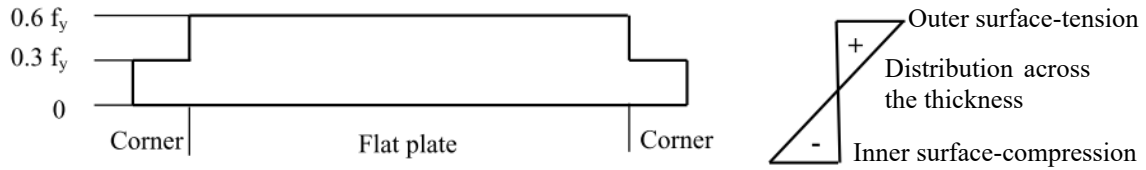
Table 34 Material properties of G450 generated from the test at ambient and elevated temperatures [120].

T (°C)	Elastic modulus (MPa)	0.2% proof stress (MPa)
20	184770	430
200	179749	419
400	144163	371
500	106132	277
600	73243	154
700	45158	56

### 6.3.2.4 Initial geometric imperfections and residual stresses

Geometric imperfections influence the accuracy of numerical models of cold-formed steel columns [144]. These imperfections come from the manufacturing, transportation, and handling processes. The accurate implementation of imperfections in the models influences the predicted capacity and failure mode of columns. Since the columns studied here are subjected to local buckling, only the local imperfections are considered. The first buckling mode generated from the buckling analysis in ABAQUS [145] is used as the shape of the geometry imperfections. For comparison between the numerical model and the experiments, the magnitude of the imperfection is taken as the measured local imperfection as specified by the author of the tests in Appendix H of the thesis [120].

Residual stresses are another factor that may impact the accuracy of the numerical modeling. These stresses are induced by the cold-forming process and the uneven cooling due to the welding process for hollow section. An idealized residual stress model, as shown in Figure 82, was proposed by Balaruban [120] based on previous research [146,147]. To investigate the effect of residual stress on the compressive capacity, a study is conducted on the 90x90x2 column, adding the membrane and flexural residual stresses separately to the FE models. Table 35 shows the ultimate capacities of the 90x90x2 column with and without residual stress considered in numerical modeling. It can be observed that the incorporation of membrane residual stresses in the model increases the capacity, while the flexural residual stress has a negative effect on the capacity. Yet, research has shown that the flexural residual stresses are implicitly included in the stress-strain relationships of the material if the specimens are not straightened by plastic bending prior to testing [148]. Hence, explicitly adding flexural residual stresses to the shell elements while adopting stress-strain relationships calibrated on material test data that implicitly included the effects of these residual stresses would amount to double counting the effect. Meanwhile, the effect of membrane residual stress is limited and neglecting it is conservative. Therefore, no explicit modeling of residual stress was included in the models for the simulated cold-formed steel hollow section columns.



(2) Membrane residual stress

Figure 82 Idealized residual stress model proposed for hollow sections [120].

Table 35 Ultimate capacities of 90x90x2 column with and without residual stress.

Temperature (°C)	No residual stress (kN)	With membrane residual stress only		With flexural residual stress only	
		Capacity (kN)	% difference	Capacity (kN)	% difference
20	221.9	227.8	2.7%	201.1	-9.4%
200	215.6	220.8	2.4%	200.8	-6.9%
400	181.9	185.7	2.1%	173.9	-4.4%
500	134.9	137.7	2.1%	129.0	-4.4%
600	83.26	84.84	1.9%	77.98	-6.3%

### 6.3.3 Validation of the finite element model against experimental data

The results in terms of ultimate capacities and force-displacement curves are compared with the test measurements and numerical results reported by Balarupan [120]. The axial loading vs. axial shortening curves are shown in Figure 83. The curves obtained from SAFIR in this research agree with the curves obtained from the numerical analysis in ABAQUS by Balarupan [120], both in terms of peak load and axial shortening at the peak load. At temperatures of 400 °C and higher, the ABAQUS simulations converge for larger deformations post-buckling compared to the SAFIR simulations. This may be due to the different material models used in the numerical modeling. Compared with the experiments, the curves from the two FEM software show larger stiffness at the initial loading phase and less ductility at failure than the test measurements.

The failure modes of the columns at ambient and elevated temperature are shown in Table 36. All columns fail by local buckling at ambient and elevated temperatures. The failure modes from the simulation agree with those of the tests. The only difference between the tests and the numerical results is the location of local buckling. Due to the symmetric geometry imperfection applied to the numerical models, the columns in SAFIR develop local buckling at the center of the column where the magnitude of imperfection is the largest. In contrast, the location of the local buckling in the test varies between the specimens.

The ultimate capacities of the columns at ambient and elevated temperatures are listed in Table 37. The results obtained with SAFIR agree well with those obtained with ABAQUS. The numerical models predict slightly higher capacities than the experiments except at 600 °C. The experimental value at 700 °C should be discarded according to the author of the test. Overall, this comparison with experimental data validates the ability of the numerical model to capture the local buckling failure mode and ultimate capacity of SHS and RHS section columns at ambient and elevated temperature.

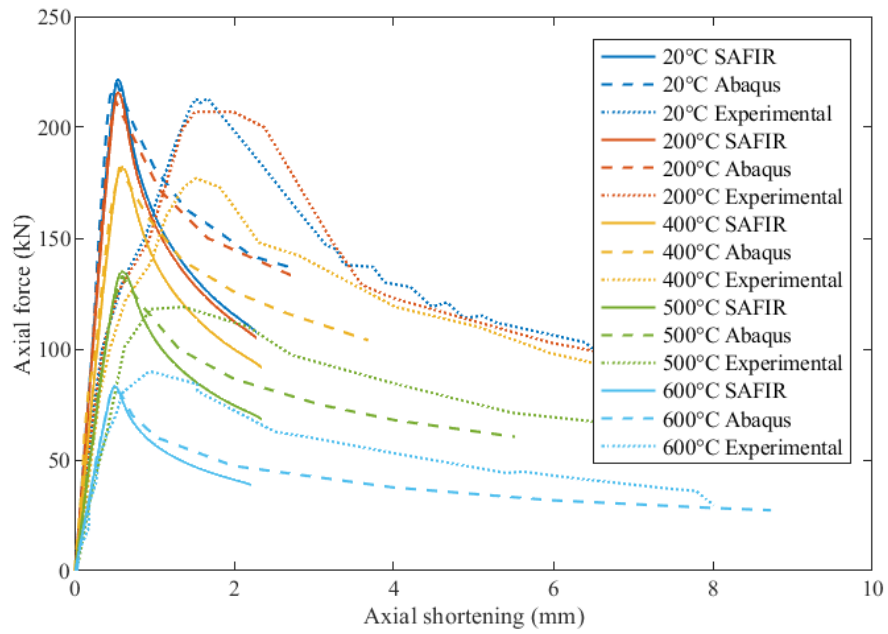


Figure 83 Axial force-displacement curves for the 90x90x2 SHS column loaded to failure at different temperatures (experimental measurements and numerical results from Abaqus are reported by Balarupan [120]).

Table 36. Failure modes for 90x90x2 column.

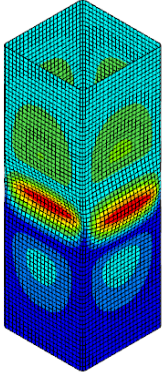
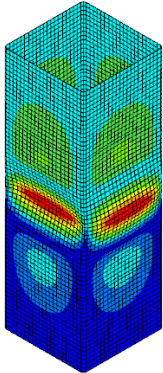
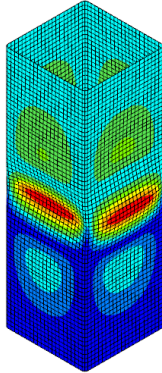



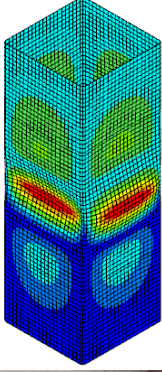
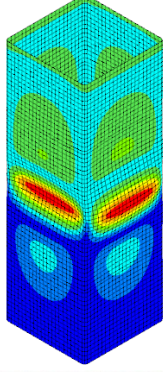


Temperature (°C)	20	200	400
Failure mode in SAFIR			
Failure mode in test (from [120])			
Temperature (°C)	500	600	
Failure mode in SAFIR			
Failure mode in test (from [120])			

Table 37. Comparison of ultimate capacities.

Temperature (°C)	FEM SAFIR (kN)	Test [120] (kN)	FEM Abaqus [120] (kN)	SAFIR/Test	SAFIR/Abaqus
20	221.9	212.6	221.0	104.4%	100.4%
200	215.6	207.0	213.0	104.2%	101.2%
400	181.9	178.3	181.0	102.0%	100.5%
500	134.9	119.4	133.0	113.0%	101.4%
600	83.26	89.9	82.2	92.6%	101.3%
700	35.01	46.6*	33.8	75.1%	103.6%

\*Due to unexpected problems in the test, the authors of the tests stated that this value should be ignored [120].

## 6.4 Parametric study

### 6.4.1 Approach for the parametric study

The modeling procedure and results discussed in Section 6.3 validate that the FE models are able to capture both the buckling mode and capacities of the tested columns at ambient and elevated temperatures. To investigate the behavior of the cold-formed hollow section columns manufactured with normal and advanced high-strength steels (AHSS) at elevated temperature, a parametric study is conducted in this section. The main parameters include the section dimensions, mechanical properties, and temperatures. The section dimensions include both square hollow section (SHS) and rectangular hollow section (RHS). 16 SHS and 30 RHS are studied. The steel grades include G450, DP-700, and MS-1200. Each column is investigated under uniform temperature ranging from ambient temperature up to 700 °C.

### 6.4.2 Material properties

The steel grades investigated in the study include one conventional cold-formed steel (G450) and two advanced high-strength steels (DP-700 and MS-1200). The elastic modulus and yield stress at elevated temperatures are determined by the predictive models proposed in Chapter 2 and Chapter 3.



Retention factors for the different grades adopt the same generic formulation, with coefficients provided as a function of the grade. The retention factors  $k$  of the material properties, defined as the ratio of the measured value at elevated temperature to that at ambient temperature, follow the standardized format of Eq. (30):

$$k = (1 - c) \frac{1 - x^b}{1 + ax^b} + c \quad (30)$$

where

$$x = \frac{T - T_1}{T_2 - T_1} \quad (31)$$

The dimensionless coefficients  $a$ ,  $b$  and  $c$  are calibrated from the test data.  $T_1$  and  $T_2$  are the limiting temperatures specifying the applicable range of the equation.  $T$  is the steel temperature in °C. The coefficients and limiting temperatures are listed in Table 38.

Table 38 Coefficients for the predictive model of retention factors.

Material	Properties	$a$	$b$	$c$	$T_1$ (°C)	$T_2$ (°C)
G450	Elastic modulus	8	3	0.04	20	1000
	0.2% proof stress	20	4	0.03	20	1000
DP-700	Elastic modulus	0.95	2	0.22	20	700
	0.2% proof stress	8.5	4.6	0.05	20	700
MS-1200	Elastic modulus	4.4	2.9	0.09	20	700
	0.2% proof stress	9.2	3.0	0.02	20	700

The retention factors for the 0.2% proof stress ( $k_y$ ) and elastic modulus ( $k_E$ ) are plotted in Figure 84 for the three steel grades investigated in this research. At a given temperature, the normalized retention factors decrease as the grade increases (i.e., from G450 to DP-700 to MS-1200), which indicates that the retained strength and modulus is proportionally lower for high strength steels than for the G450. It can also be observed that, for G450, the strength and modulus properties follow approximately the same normalized reduction with temperature. In contrast, for

the advanced high strength steel grades, the reduction in strength is greater than the reduction in elastic modulus at a given temperature.

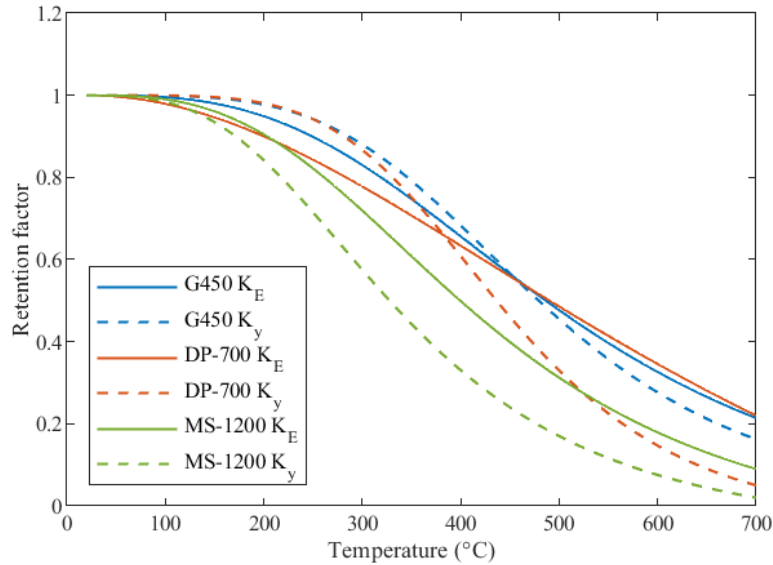


Figure 84 Retention factors for cold-formed steels of different grades, from Chapter 2 and Chapter 3.

### 6.4.3 Finite element models

46 cold-formed hollow section (16 SHS and 30 RHS) columns are analyzed using the finite element modeling approach validated in Section 6.3. The dimensions of the columns are listed in Table 39. The columns are named by the dimensions of the cross section and the thickness. The lengths of the columns are chosen as three times the buckling half-wavelength to achieve local buckling at ambient temperature. The width of the cross sections ranges from 65 mm to 400 mm for SHS and 50 mm to 400 mm for RHS. The thickness ranges from 1.6 mm to 12.5 mm. The width-to-thickness ratio  $b/t$  of the sections ranges from 27 to 71.

Table 39 Cold-formed steel SHS and RHS columns in the parametric study.

Section	Length (mm)	b/t	Section	Length (mm)	b/t
65x65x1.6	186	36.6	125x75x2.5	322	32.5
65x65x2	183	28.5	125x75x3	320	45
75x75x2	213	33.5	127x51x3.5	295	32.5
90x90x2	270	41	150x50x2	355	58.5
90x90x2.5	255	32	150x50x2.5	352	46
100x100x2	300	46	150x50x3	350	37.7
100x100x2.5	285	36	150x50x4	348	45
100x100x3	282	29.3	150x100x4	375	36.7
200x200x5	570	35	200x100x4	498	58.5
200x200x6	564	28.3	200x100x5	495	46
250x250x6	714	36.7	200x100x6	492	36
300x300x8	852	32.5	250x150x5	620	29.3
350x350x8	1002	38.8	250x150x6	615	45
350x350x10	990	30	300x200x6	762	35
400x400x10	1140	35	300x200x8	756	28.3
400x400x12.5	1125	27	350x250x8	906	45
75x50x1.6	200	45	350x250x10	900	35
75x50x2	200	35	400x200x8	966	27
100x50x1.6	235	27	400x200x10	960	32.3
100x50x2	235	38.8	400x200x12.5	955	71
100x50x2.5	230	30	400x300x8	1055	56
100x50x3	230	42.9	400x300x10	1050	46
125x75x2	324	33.5	400x300x12.5	1045	32.5

Similar to the validation models, fixed end support conditions are applied to the models. The mesh size is 4 x 4 mm for the flat elements and 2 x 4 mm or 1x4 mm for the corner. Residual stresses are not considered in the parametric study for the reasons detailed in Section 6.3. As for the initial geometry, the magnitude of local imperfection is taken as  $b/250$  [120], where  $b$  is the width of the cross sections. This value was proposed based on a probabilistic approach for the prediction of imperfection [144]. Based on the collected imperfection measurements of cold-formed steel hollow sections in [120], the probability that the section has an imperfection of less than  $b/250$  is more than 95%. Thus, the value of  $b/250$  is used in this study.

The reduced material properties, determined through multiplication of the ambient temperature elastic modulus and yield stress by the corresponding retention factors at elevated temperature, are used in the elevated temperature simulations. The elastic modulus and yield stress of the studied materials at ambient temperature are listed in Table 40. The retention factors of G450 are based on the models proposed for the new appendix for AISI S100 discussed in [8], while those of DP-700 and MS-1200 are based on the experimental data generated in the test campaign in [18]. The columns are axially loaded until failure. The ultimate capacities are taken as the maximum axial reactions during the loading process.

Table 40 Material properties at ambient temperature.

Material	Elastic modulus (MPa)	0.2% proof stress (MPa)
G450	200000	450
DP-700	209772	762
MS-1200	208609	1387

#### 6.4.4 Ultimate capacities of cold-formed SHS and RHS columns at elevated temperatures

All the columns exhibit local buckling failure at ambient and elevated temperatures from the numerical modeling. As expected, the ultimate capacities of the columns decrease with increasing temperature. However, this reduction is not uniform for different steel grades.

Figure 85 plots the retention factor of ultimate capacity of the columns with temperature, which is defined for each column as the ratio of the capacity at elevated temperature over that at ambient temperature. For the columns with G450, despite the various width-to-thickness ratio  $b/t$  considered in the parametric analysis, the proportional reduction of the ultimate capacity follows a similar trend; the curves for the 46 columns are almost superposed. In contrast, for the columns with DP-700 and MS-1200, even though the reduction of the capacities follows similar trend, there is certain variability in the retention factor of the capacity at temperatures higher than 400 °C.

Most noticeably, the retention factor of ultimate capacity is much larger for the MS-1200 than for the other grades, and it is larger for the DP-700 than for the G450. The SHS and RHS columns made of higher grade steels progressively lose more of their local buckling capacity than those made of lower grade steels as the temperature increases. This behavior results from the lower material retention factors for AHSS, see Figure 84.

To understand the effect in terms of absolute value of the capacity (rather than proportionally to the ambient capacity), Figure 86 plots the evolution of the compressive strength of the 90x90x2 column with temperature. At ambient temperature, replacing the G450 by DP-700 or MS-1200 results in an increase in ultimate capacity of 46% and 107%, respectively. However, as the reduction of the mechanical properties of AHSS steels at elevated temperature is more significant than that of the conventional cold-formed steels, the advantage in ultimate capacity with AHSS over the conventional steels is lost at temperatures higher than 400-500 °C.

Figure 87 shows, for each steel grade, the retention factor of the section capacity alongside the material retention factors for yield stress and elastic modulus. It can be observed that the effect of the yield stress prevails over that of the modulus on the ultimate capacity of the hollow section columns. For the AHSS materials, the yield stress reduction with temperature is more severe than the modulus reduction.

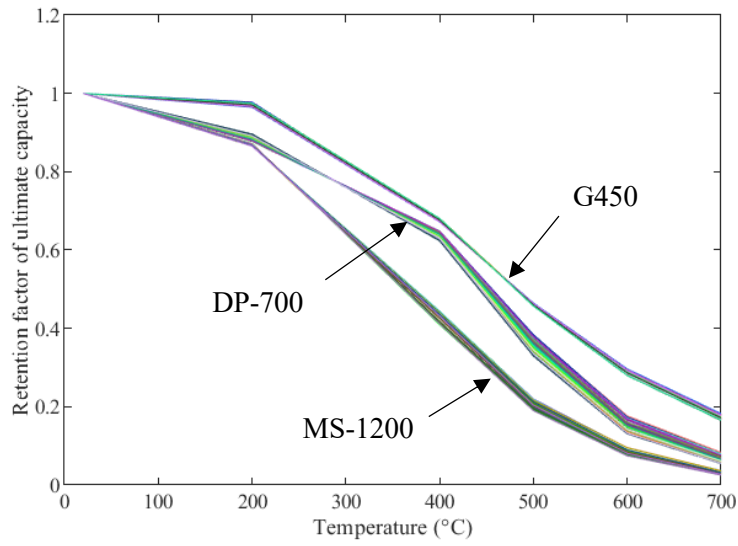


Figure 85 Normalized reduction of ultimate capacity with temperature for the SHS and RHS columns.

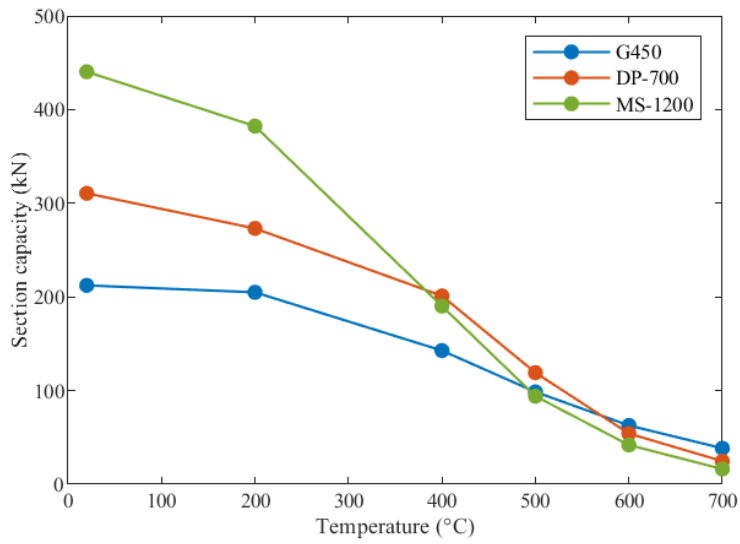


Figure 86 Ultimate capacity in local buckling at elevated temperature for the 90x90x2 section column with steel grades G450, DP-700, MS-1200.

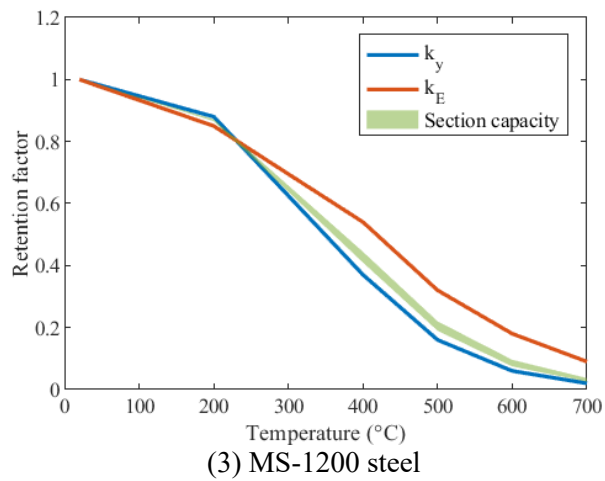
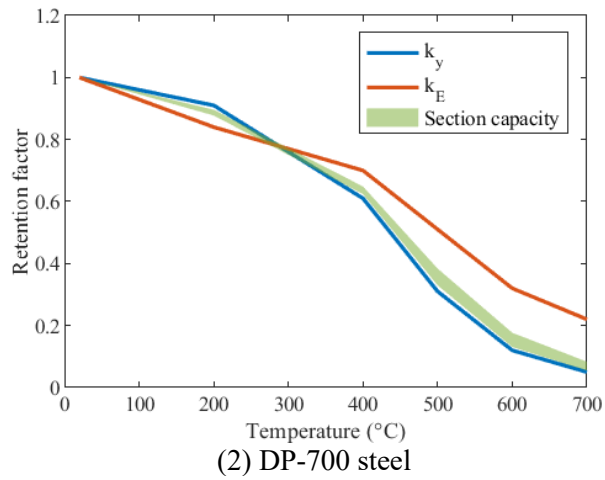
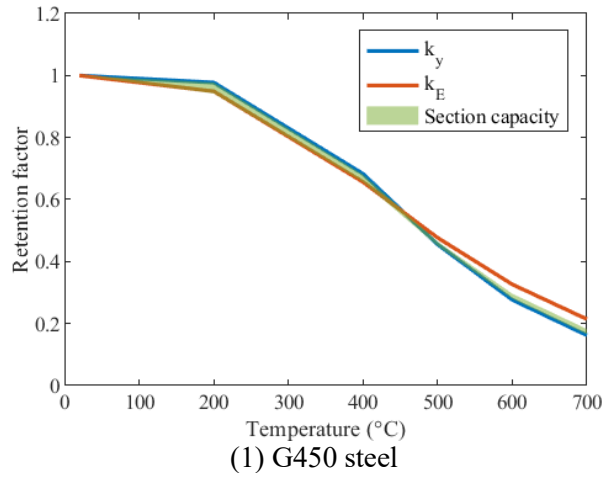


Figure 87 The normalized reduction with temperature of section capacity in local buckling lies in between the retention factors for yield strength and elastic modulus.

## 6.5 Comparison between FE analysis and Direct Strength Method

### 6.5.1 At ambient temperature

The Direct Strength Method (DSM) proposed by Schafer [11] and incorporated in AISI S100 [12] is used to predict the ultimate capacity of the cold-formed SHS and RHS columns at ambient temperature. The elastic buckling strength is obtained from the finite strip analysis in CUFSM [149], while the ultimate capacities are calculated with the DSM equations. The comparison of the capacities obtained from FEM to the those from the DSM at ambient temperature are plotted in Figure 88. The averaged ratio of FEM analysis to DSM prediction are summarized in Table 41; AVG-SHS refers to the ratio for the SHS columns only, AVG-RHS if for the RHS columns only, while AVG-ALL is the averaged ratio over the whole dataset of hollow section columns.

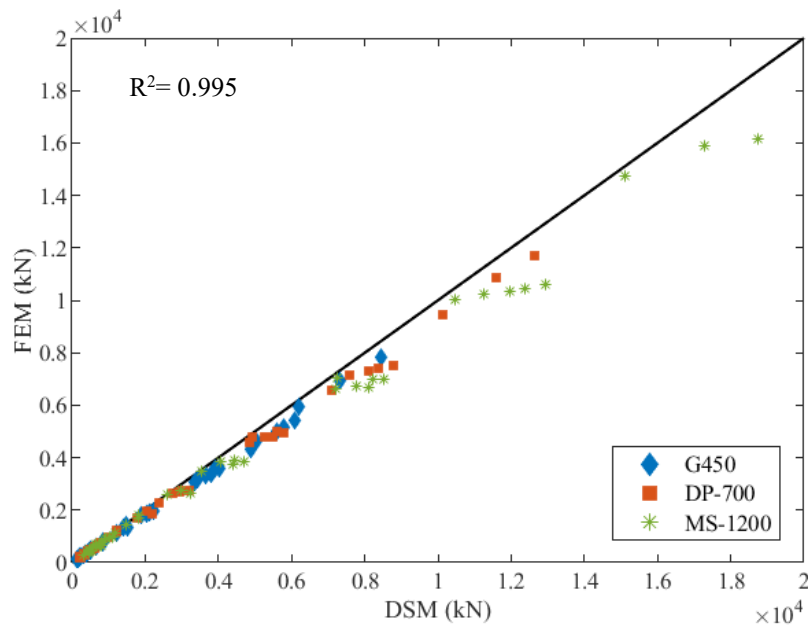


Figure 88. At ambient temperature, the DSM predicts higher section capacities than the FE model for the hollow sections, both for conventional and advanced high-strength steels.

The values of ultimate capacities predicted by the DSM for the hollow section columns are slightly, but consistently, higher than those obtained by the FE analysis. It is important to note that the DSM



is calibrated on cold-formed open sections. It accounts for the beneficial effect of interaction between plate elements during and post-buckling. However, with hollow sections, there is less room for the interaction of plate elements during buckling when the ratio of slenderness of the web and flange is much smaller than that of the open sections. As can be observed from Table 41, the DSM agrees better with the FE results for RHS than for SHS columns. This can be explained by the fact that the ratio of the web to flange slenderness is equal to 1 for SHS columns, and accordingly, the buckling of the four plate elements will occur approximately simultaneously, with little reserve in strength. For RHS columns, two plate elements have higher slenderness than the other two and their buckling will cause stress redistribution, which contributes to the post-buckling behavior.

Figure 89 plots the ratios of the ultimate capacities obtained by FE analysis and DSM, as a function of the plate width ratio  $b_1/b_2$ . The sections with the lowest  $b_1/b_2$  ratio have the most unconservative predictions from DSM. As sections become more rectangular (with higher  $b_1/b_2$ ), there is more possibility for post-buckling redistribution as is the case in open sections, and the DSM results agree better with the FE results. This suggests that the DSM, which was developed for open sections and to take into account this beneficial effect of post-buckling behavior, requires adaptation to apply to SHS and RHS columns, for which there is much less of this effect.

When looking at the influence of steel grade, the SHS columns with higher steel grade generally have more unconservative predictions from DSM at ambient temperature, as shown in Table 41. On the other hand, the FEM analysis to DSM prediction ratios do not vary much with different plate width-to-thickness ratio  $b/t$  within the investigated range of 27 to 71, as shown in Figure 90.

Table 41 Averaged ratios of FEM to DSM evaluations of capacity at ambient and elevated temperatures. A ratio lower than 1.00 indicates that the FEM predicts a lower capacity than the DSM.

Material	Section	Temperature (°C)					
		20	200	400	500	600	700
G450	AVG-SHS	0.90	0.90	0.90	0.90	0.91	0.91
	AVG-RHS	0.94	0.94	0.94	0.94	0.94	0.94
	AVG-ALL	0.93	0.93	0.93	0.93	0.93	0.93
DP-700	AVG-SHS	0.89	0.88	0.89	0.90	0.93	0.96
	AVG-RHS	0.96	0.96	0.95	0.94	0.93	0.95
	AVG-ALL	0.93	0.93	0.93	0.93	0.93	0.95
MS-1200	AVG-SHS	0.84	0.84	0.87	0.89	0.91	0.93
	AVG-RHS	0.95	0.95	0.96	0.95	0.94	0.94
	AVG-ALL	0.91	0.91	0.93	0.93	0.93	0.93

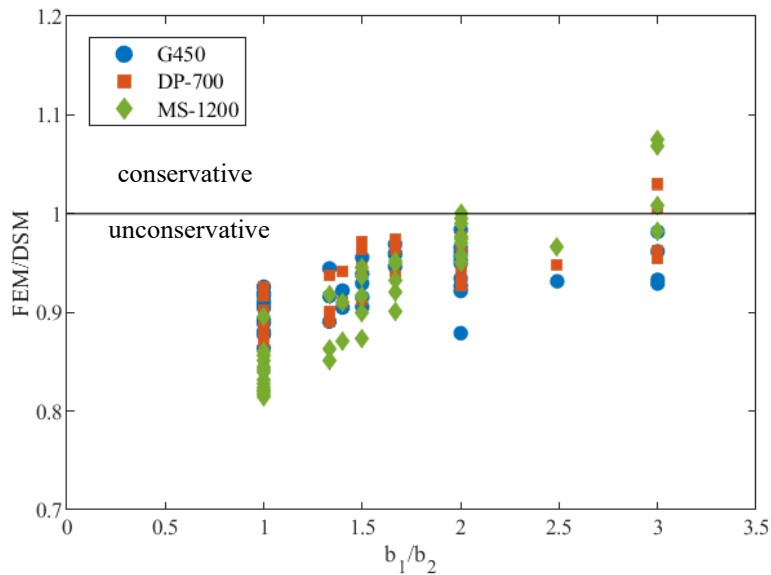


Figure 89. At ambient temperature, the DSM predicts higher capacities than the FE model for hollow sections, especially when the plates width ratio ( $b_1/b_2$ ) is close to 1.

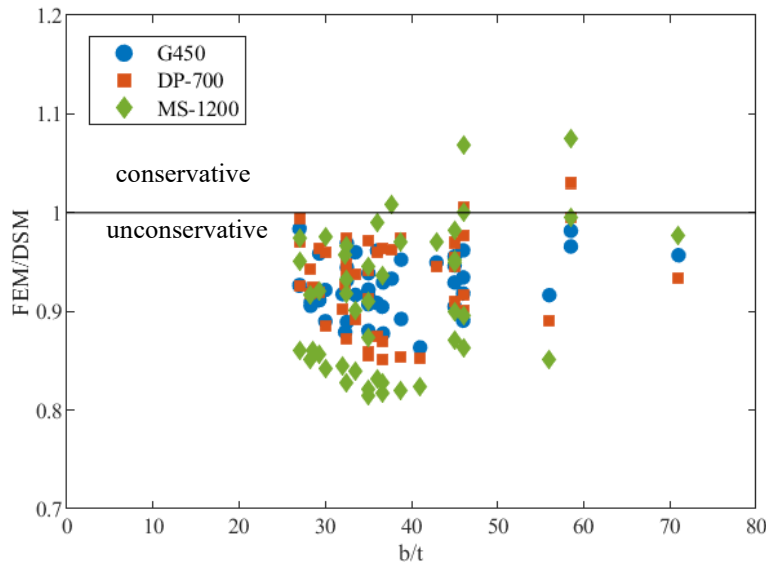


Figure 90. At ambient temperature, the plate width-to-thickness ratio ( $b/t$ ) of the hollow sections does not noticeably influence the ratio between the DSM and FE predictions of the ultimate capacity.

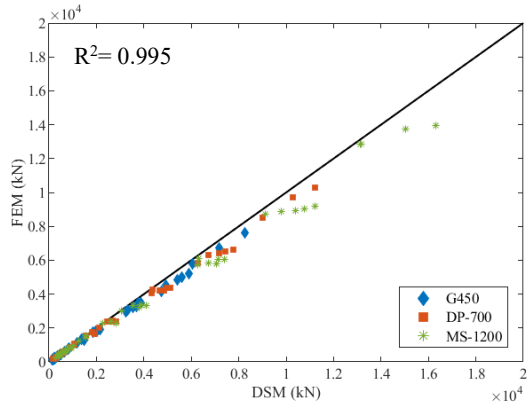
### 6.5.2 At elevated temperatures

To evaluate the capacity of the hollow section columns at elevated temperature with the DSM, the reduced mechanical properties determined with the retention factors in Eq. (30) are used in CUFSM and with the DSM equations. The values of elevated temperature capacity obtained with the DSM are then compared with the values from the finite element simulations for the 46 columns at temperatures from 200 C to 700 C. The comparison of the capacities of the cold-formed SHS and RHS columns obtained from FEM with those from DSM at elevated temperature are plotted in Figure 91. A general agreement is observed, with  $R^2$  values higher than 0.995 across all temperatures and steel grades. Yet similar to ambient temperature, the DSM provides consistently higher values of ultimate capacities at elevated temperatures compared with the FE analysis, as indicated by the points lying under the bisector in the plots. The overestimation by the DSM generally lies within 5-15% as shown by the averaged ratio of FEM to DSM predictions given in

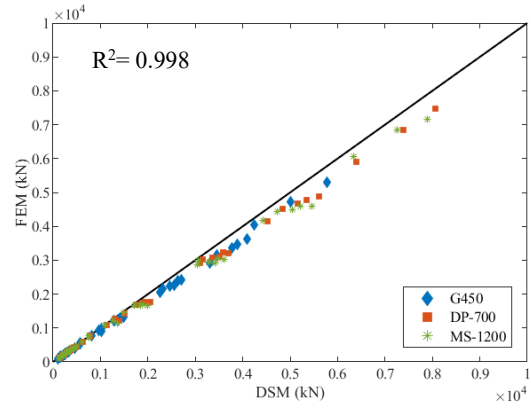
Table 41. Possible reasons of this overestimation by the DSM, compared with the FE model, have been discussed in Section 6.5.1.

Figure 92 plots, for each of the 46 columns, the evolution of the ratios between the FEM and DSM predictions of capacities as a function of the temperature. For the columns with G450, the ratios of capacities predicted by the two approaches do not vary much up to 400 °C. For higher temperatures, larger variations are observed. For the columns with AHSS, the ratios exhibit variation at much lower temperature (200 °C) and at larger magnitude than the columns with G450. The variations of the ratio do not show clear discrepancies between the SHS and RHS columns but show certain inconsistency. As proposed in the research by Balarupan [120] and Couto et al. [150], possible factor of the observed inconsistent variation at elevated temperature can be the difference in yield stress to elastic modulus retention factors with temperature. As shown in Figure 84, the elastic modulus shows similar reduction trend as the yield stress for G450 up to 400 °C, after which a slightly larger reduction in yield stress is observed. For the AHSS steels, the yield stress shows much larger reduction than the elastic modulus at temperatures higher than 200 °C for MS-1200 and 400 °C for DP-700. This inconsistent reduction of mechanical properties may result in incorrect classification of the sections. To confirm this hypothesis, the elevated temperature ultimate capacity to yield capacity ( $P_u/P_y$ ) versus  $\lambda_l = \sqrt{P_{ne}/P_{crl}}$  (where  $P_{ne}$  is the global buckling strength;  $P_{crl}$  is the critical elastic local buckling load) curves obtained from DSM are shown in Figure 93. The plots show that using the ambient temperature design method DSM with elevated temperature material properties categorizes some SHS and RHS into Class 1-3 sections ( $P_u = P_y$ ) at elevated temperature while the FE analysis always shows local buckling ( $P_u < P_y$ ). Thus, it may be necessary to adjust the limiting slenderness in order to properly cover the influence of local buckling at elevated temperatures.

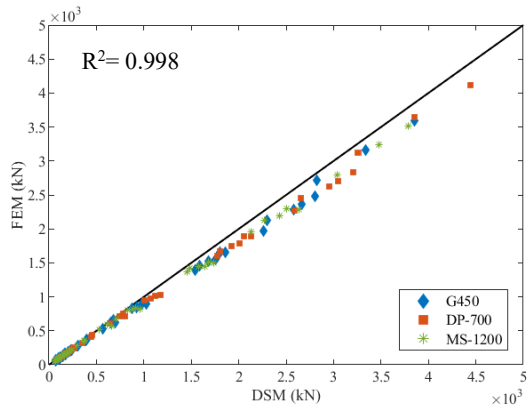
The averaged ratio of FEM analysis to DSM prediction of the investigated SHS columns only, RHS columns only, and the whole dataset of investigated hollow section columns at elevated temperatures are summarized in Table 41. The ratio for RHS columns does not noticeably depend on the steel grade, neither on the temperature. The DSM provides estimates of capacity higher by about 6% than the FEM for the RHS columns. In contrast, the ratio for SHS columns varies across temperatures for the AHSS grades. The DSM estimates of capacity for the SHS columns generally exceed the FEM estimates by about 5-10% depending on the temperature.



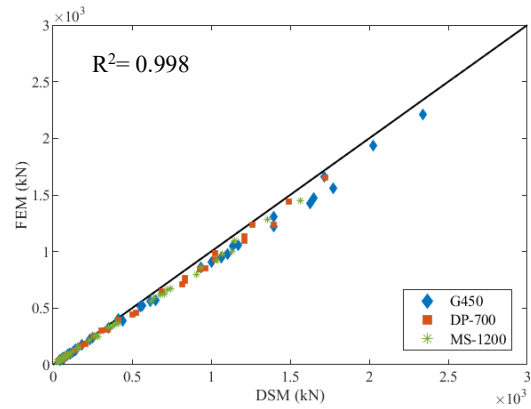
(1) 200 °C



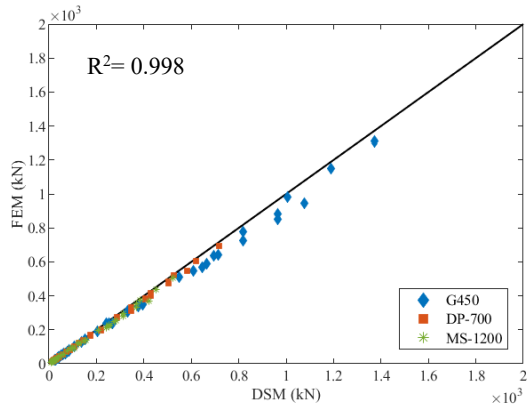
(2) 400 °C



(3) 500 °C

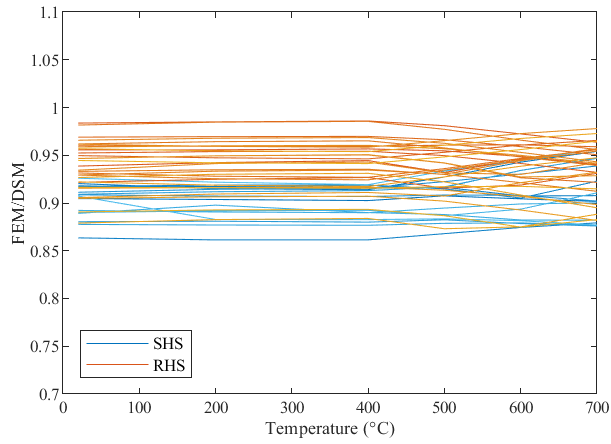


(4) 600 °C

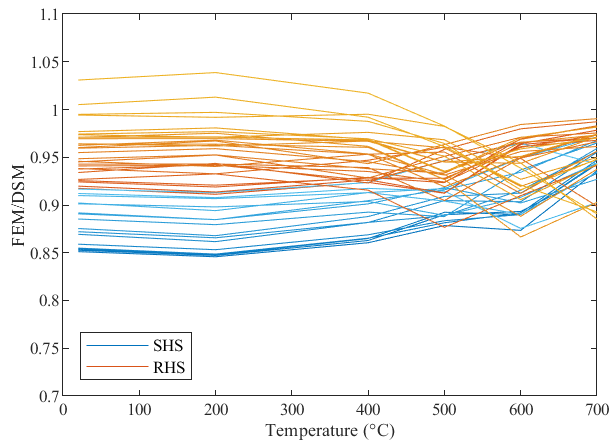


(5) 700 °C

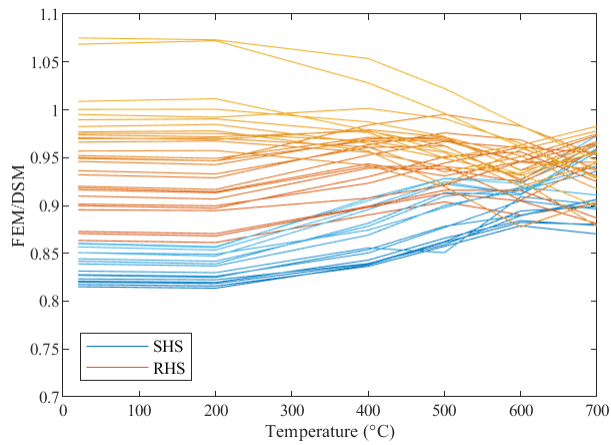
Figure 91 Section capacities obtained from FEM and DSM at elevated temperature. (Note the vertical scale is adjusted on each plot for readability.)



(1) G450

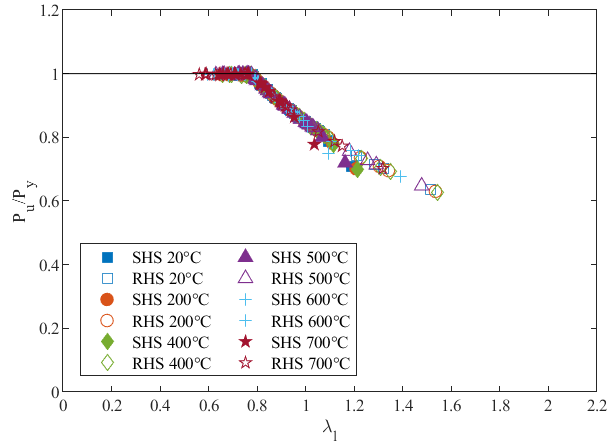


(2) DP-700

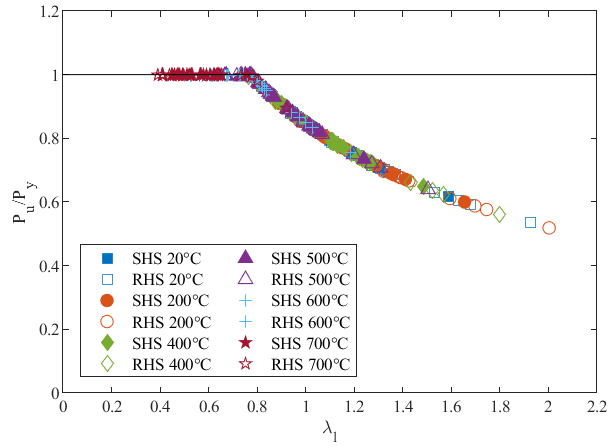


(3) MS-1200

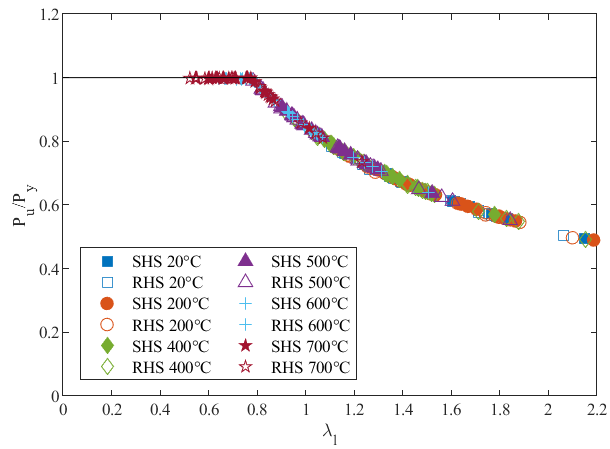
Figure 92. Variation of the ratio between FE and DSM predictions of the capacity for each of the 46 hollow sections as a function of temperature.



(1) G450



(2) DP-700



(3) MS-1200

Figure 93  $P_u/P_y$  versus  $\lambda_l$  at elevated temperatures obtained from DSM.



## 6.6 Modified Direct Strength Method for SHS and RHS columns

Based on the results presented in the above sections, the DSM tends to overestimate the local buckling capacities of cold-formed hollow section columns when compared to shell finite element models. The DSM yields higher estimates than the FE models with both conventional G450 and AHSS steels, and both at ambient and elevated temperature. Therefore, it is recommended to modify the formulation of the Direct Strength Method to be used in the design of cold-formed SHS and RHS columns. It is noteworthy that this observation was already made by Balarupan [120], who proposed modified DSM equations based on the data derived in his thesis for cold-formed steel SHS and RHS section columns with G450. However, his data only covered local slenderness up to 1.6 and the proposed equations in the thesis do not work well with the larger range of slenderness for higher steel grades investigated in this study.

Different sets of coefficients in the same format of DSM for local buckling behavior of thin-walled columns in compression have been proposed by other researchers [120,151–153]. Among them, the Bridge formula [151] was calibrated based on test data of local buckling capacities of thin-walled square steel tubular columns at ambient temperature. The width-to-thickness ratios in Bridge's test campaign ranged between 37.3 and 130.7 and the plate local buckling slenderness spanned from 0.5 up to 2.5, both of which are similar to the parameters investigated in this study. Thus, a modified Direct Strength Method is proposed based on the Bridge formula [151] to predict the capacities of the cold-formed SHS and RHS columns investigated in this study. The modified DSM local buckling equations are as follows:

For  $\lambda_l \leq 0.561$ ,

$$P_{nl} = P_{ne} \quad (32)$$

For  $\lambda_l > 0.561$ ,

$$P_{nl} = \left[ 1 - 0.25 \left( \frac{P_{crl}}{P_{ne}} \right)^{0.6} \right] \left( \frac{P_{crl}}{P_{ne}} \right)^{0.6} P_{ne} \quad (33)$$

where  $\lambda_l = \sqrt{\frac{P_{ne}}{P_{crl}}}$ ;  $P_{nl}$  is the local buckling strength;  $P_{crl}$  is the critical elastic local buckling load;

$P_{ne}$  is the global buckling strength.

The  $P_u/P_{ne}$  versus  $\lambda_l$  curves obtained with the original DSM and modified DSM at ambient and elevated temperatures are plotted in Figure 94. Compared with the original DSM, the modified DSM based on Bridge formula [151] provides a more accurate and mostly conservative estimate of the local buckling capacities of cold-formed SHS and RHS columns. The proposed modified DSM works best from ambient temperature to 500 °C. At 600 °C and 700 °C, it yields higher predictions than the FE model for very low values of the slenderness. Yet, it is worth noting that the actual capacities of the hollow section columns may be expected to be slightly higher than the capacities predicted by the FEM due to strain hardening, lower imperfection magnitude than the  $b/250$  used in the model, less severe imperfection shape than the first eigen mode used in this study, and possible higher yield stress in the corner regions.

In sum, the proposed modified DSM can appropriately be used to predict the ultimate capacity in local buckling of hollow sections, both square and rectangular, made of G450 and AHSS DP-700 and MS-1200, in the temperature range of 20-700 °C. This modified DSM requires very limited adjustments compared with the DSM currently implemented in AISI S100, and these adjustments rely on the established Bridge formula.

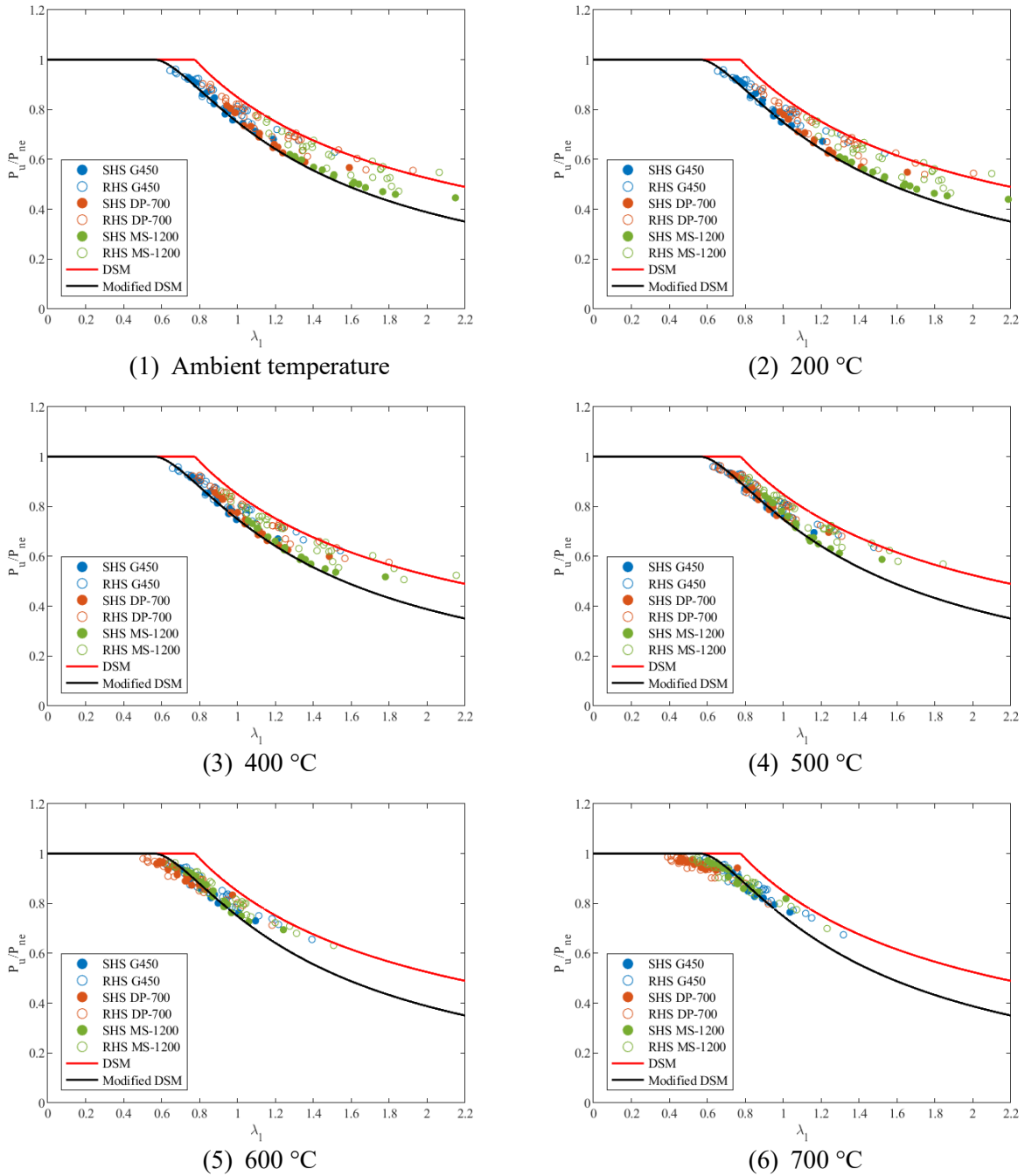


Figure 94 Comparison of DSM and modified DSM curves and FEM data for the SHS and RHS columns.

## 6.7 Conclusions

This chapter presents a numerical study on the local buckling behavior of cold-formed steel square and rectangular hollow section columns made of normal and advanced high-strength steels (AHSS)

at elevated temperatures. Finite element models based on shell elements were developed and validated against test data from the literature. A parametric study was conducted with the finite element models on 46 SHS and RHS columns with various width-to-thickness ratios, plate width ratios, cross section dimensions, and three steel grades (G450, DP-700, and MS-1200). The retention factors of the mechanical properties for the normal and advanced high-strength steels were based on data recently collected by the authors. The ultimate capacities obtained from the numerical modeling were compared with the strengths calculated with the Direct Strength Method (DSM) in AISI S100. The following conclusions can be drawn:

- The shell finite element model is able to reproduce the experimental behavior of a SHS cold-formed steel column failing in local buckling at temperatures ranging from 20 °C to 700 °C. The model captures the failure mode and the section capacity, but underestimates the axial shortening at peak load and post-buckling ductility. This level of agreement between the numerical model and the experiments is obtained while the model relies on some simplifying assumptions including from adopting the Eurocode 3 stress-strain relationship and not including explicitly residual stresses.
- The dual-phase and martensitic advanced high-strength steels experience proportionally greater reductions in strength than the G450 with temperature. As a result, the gain in section capacity of the SHS and RHS columns obtained by replacing G450 with AHSS, which can reach 100% at ambient temperature, is entirely lost at temperatures of 500 °C and higher.
- The Direct Strength Method yields higher estimates of the section capacity than the finite element models at ambient and elevated temperatures. The overestimation is greater for square sections (SHS) than for rectangular sections (RHS), and within rectangular sections

it increases as the plate width ratio decreases. The overestimation by the DSM is observed for all steel grades and temperatures and is of the order of 10-15% for SHS and 5% for RHS. The DSM was calibrated for open sections which exhibit interaction of plate elements during buckling, contrary to square hollow sections. This observation corroborates previous observations from other authors who have noted that SHS and RHS do not benefit from interaction effects after buckling.

- For the AHSS steels, the proportional reduction in yield stress largely exceeds that in elastic modulus at elevated temperatures. The application of current design procedures at ambient temperature results in inconsistent section classification for the SHS and RHS at elevated temperatures, which shows the need to adjust the limiting slenderness to properly cover the influence of local buckling at elevated temperatures.
- Therefore, a modification to the Direct Strength Method equations from AISI S100 is proposed for the local buckling capacity of SHS and RHS columns. The modification is based on the Bridge formula which was originally calibrated on test data of local buckling capacities of thin-walled square steel tubular columns at ambient temperature. Results show that the proposed equation provides accurate estimates for the SHS and RHS section capacities for the different steel grades at ambient and elevated temperatures up to 700 °C.

## **Chapter 7    Structural design of cold-formed steel C-shaped column assemblies under fire conditions**

### **7.1 Introduction**

Performance-based design for fire conditions has been increasingly adopted for different structural systems. This approach offers several potential advantages over the prescriptive fire design, including flexibility for engineers and architects, a more harmonized and quantified level of safety, potential cost savings and optimization, and the ability to demonstrate equivalency of solutions varying from a reference standard fire rated assembly. For cold-formed steel structures, however, application of performance-based structural fire design remains uncommon.

This chapter aims to investigate the application of analysis-based methods to evaluate the behavior of cold-formed steel column assemblies taken as part of a realistic cold-formed steel building structure in the fire situation. Analysis-based methods allow explicit evaluation of the anticipated response under fire loading. A performance-based fire design approach can therefore be adopted where the achievement of the desirable performance objectives in the event of a fire is explicitly evaluated [6]. By adopting a prototype metal building structure designed by industry partners and conducting a complete performance-based structural fire design procedure on selected assemblies part of this structure, the study aims to describe a systematic methodology that can be applied to design realistic cold-formed steel structures for fire. Explicit analysis of assemblies not qualified through standard fire resistance testing provides data about their expected fire performance and supports their use as solutions equivalent to current fire rated assemblies. Finally, the application of several methods of analysis also allows drawing conclusions on their applicability and usefulness to complete such structural fire assessment.

## 7.2 Literature review

Methods to analyze the fire behavior of cold-formed steel members and assemblies have been studied and proposed by several researchers [37,154–156]. These include numerical methods, mostly based on the finite element method (FEM), to evaluate the temperature development in the assemblies and the structural response. These also include analytical methods to evaluate the capacity at elevated temperature under some simplifying assumptions [157].

The methods of analyses applied in this chapter rely on the work of several scholars. Most notably, finite element analyses of cold-formed steel members have been conducted by [130,158,159]. Many of these studies have been validated against experimental tests [160,161] and provide valuable data to calibrate material properties [120] and model parameters [162]. Analytical methods adopted in this research for capacity assessment rely on the Direct Strength Method (DSM), which has been originally proposed (at ambient temperature) by Schafer [11]. A few studies have previously shown the applicability of the DSM for evaluating elevated temperature capacity of cold-formed steel members subjected to uniform temperature elevation, providing appropriate material retention factors are applied [71,126,157]. Herein, the chapter adopts these different methods to design assemblies from a prototype metal building for explicit performance objectives in the fire situation.

The structure of the study follows the methodology illustrated in Figure 95. This methodology is adapted from the steps listed in ISO 24679-1:2019 [163] for the performance-based assessment of structures exposed to fire and has also been applied to other structural systems [164]. The first step is to identify the goal and performance objectives. Performance objectives, which depend on the project specificities, must be defined at the outset of a project, with the relevant stakeholders. They must be explicit so their fulfillment can be assessed at the end of the process. The second step

consists in selecting (a range of) design fires. These design fires are based on identified fuel loading and building characteristics. Third, once the thermal exposure conditions have been quantified, their effect on the structure needs to be assessed. Assessment of the structure response requires two steps, namely the thermal (heat transfer) analysis to evaluate temperatures inside the members, and the structural analysis to evaluate internal forces and displacements. Herein, these evaluations are conducted through both numerical and analytical analyses. Finally, the predicted response is checked against the required performance.

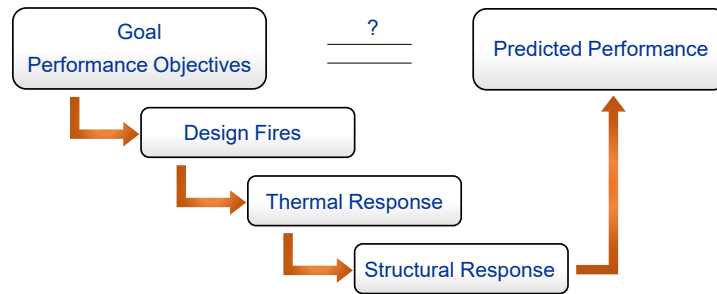


Figure 95. Performance-based design procedure.

### 7.3 Scope and fire design objectives

#### 7.3.1 Prototype building

The prototype building is a one-story warehouse located in Greeley, Colorado, as shown in Figure 96. It is designed in accordance with the 2018 International Building Code [165]. The floor plan is 22.86 m × 36.58 m (75 ft × 120 ft). The eave height is 6.096 m (20 ft), and the roof has a symmetric gable roof configuration with 1:12 slope. The external walls are corrugated metal panels. About 10 % of the wall area are openings for windows and doors. An interior partition wall divides the building into a large warehouse and a small office area. The dimensions of the warehouse area are 22.86 m × 32.92 m (75 ft × 108 ft), as shown in Figure 97.





Figure 96. Prototype warehouse building.

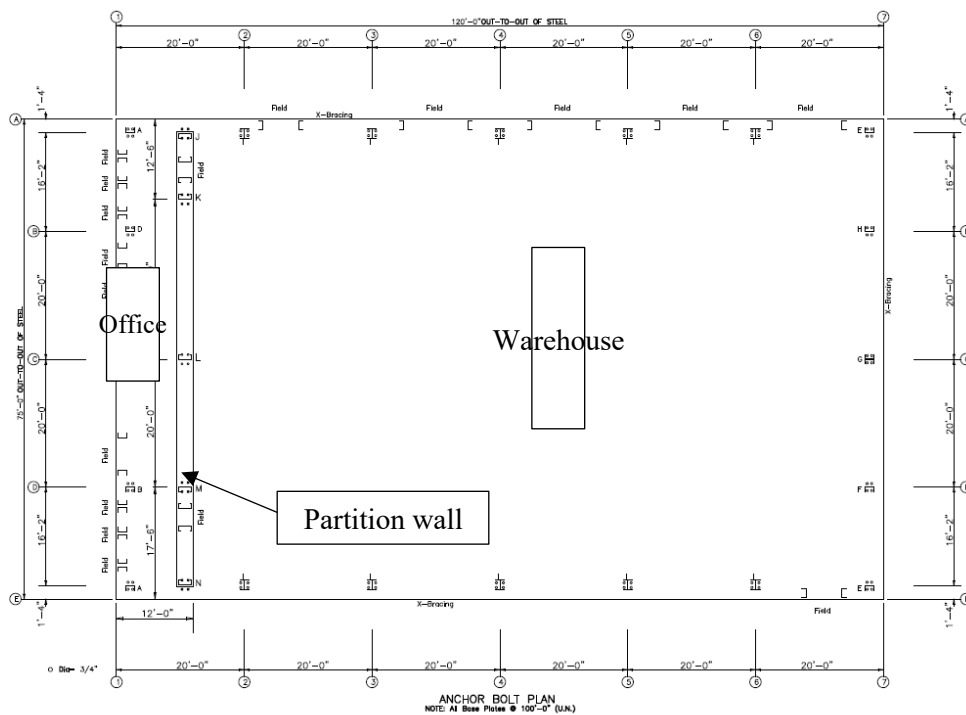


Figure 97. Floor plan of the warehouse.

### 7.3.2 End wall columns

The study focuses on two end walls of the prototype building structure. The structure is designed as Type IIB Construction and moderate-hazard storage, Use Group S-1, under the building code. The end walls are framed with cold-formed steel columns and beams. The end wall framing on Line 1 is shown in Figure 98. The columns are composed of single and double C-shaped sections,

as shown in Figure 99. Dimensions of the columns are listed in Table 42. Wall girts are placed at three elevations: 2.29 m (7.5 ft), 4.11 m (13.5 ft), and 5.18 m (17 ft), which also provides bracing to the columns. In-line attachments between girts and columns are used for the end wall framing line 1, i.e., the girts are in plane with the columns. Bypass girt attachments are used for the end wall framing line 7. The unbraced length for the major and minor axis bending of each column is given in Table 42.

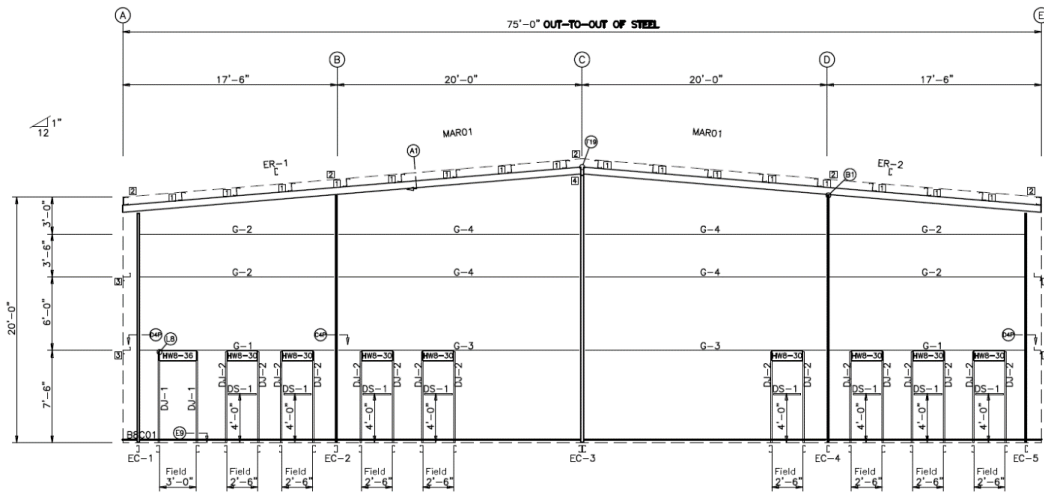
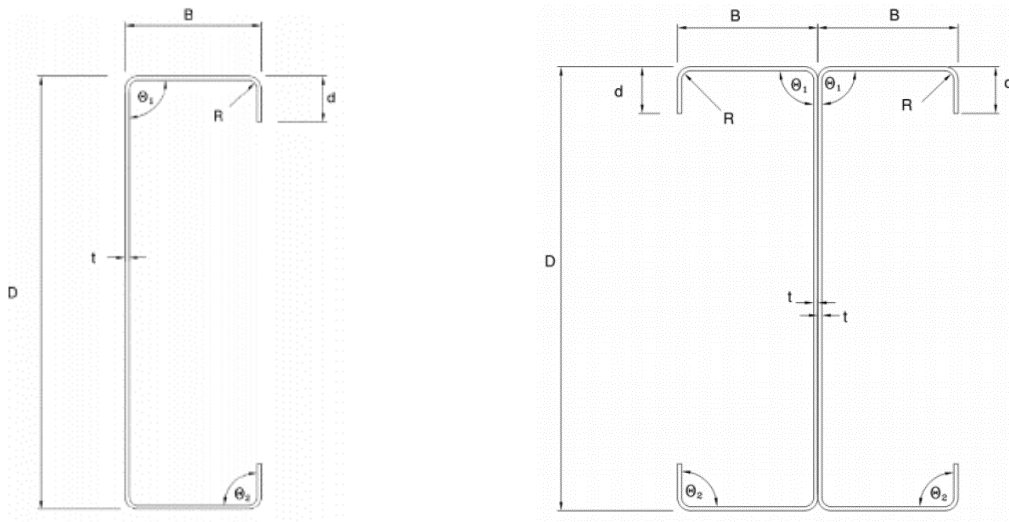


Figure 98. End wall framing line 1.



(1) Single C-shaped section

(2) Double C-shaped section

Figure 99. C-shaped sections used for the columns of the end walls.

Table 42 Section dimensions and unbraced length of the end wall columns.

Location	Column	Grade (ksi)	Part	D (in.)	B (in.)	R (in.)	d (in.)	t (in.)	L major (ft)	L minor (ft)
End wall framing line 1	EC-1	55	W08S075	8	3.78	0.25	0.992	0.075	18.4	7.5
	EC-2	55	W08S120	8	3.78	0.25	1.101	0.120	19.8	7.5
	EC-3	55	W08SD099	8	3.78	0.25	1.050	0.099	21.5	7.5
	EC-4	55	W12S099	12	3.63	0.25	1.049	0.099	19.8	7.5
	EC-5	55	W08S075	8	3.75	0.25	0.992	0.075	18.4	7.5
End wall framing line 7	EC-6	55	W08S075	8	3.78	0.25	0.992	0.075	18.4	7.5
	EC-7	55	W08S120	8	3.78	0.25	1.101	0.120	19.8	7.5
	EC-8	55	W08SD099	8	3.78	0.25	1.050	0.099	21.5	7.5
	EC-9	55	W12S099	12	3.63	0.25	1.049	0.099	19.8	7.5
	EC-10	55	W08S075	8	3.75	0.25	0.992	0.075	18.4	7.5

### 7.3.3 Fire protection assemblies

The columns of the end wall framing are based on fire-resistance-rated assemblies for a 1-hour duration. This is the requirement by code if the building separation distance is less than 30 feet. The fire protection enclosure is based on the 1-hour rated UL X530 design with 2 layers of 15.8-mm (5/8-inch) Type X gypsum board, as given in Table 43, but variations of this qualified assembly are adopted. The different fire protection configurations (N1, N2, and N3) derived from this reference assembly and used in this research are shown in Figure 100.

The assembly N2, for the single C-shaped columns EC-2 and EC-4, differ from the qualified UL X530 by the layout of the gypsum boards. The assemblies N1 and N3, for the double C-shaped columns EC-3 and EC-8, are not rated either because no standard qualified fire protection assemblies exist for double C-shaped cold-formed steel columns. In the absence of standard testing, the analysis-based methods that are applied in this chapter for determining the fire performance are therefore needed to justify the adequacy of these assemblies.

Table 43 Fire protection assemblies of the cold-formed steel columns.

Location	Column	Fire protection	
End wall framing line 1	EC-1	UL X530	[1 HR]
	EC-2	X530-N2	[1 HR]
	EC-3	X530-N3	[1 HR]
	EC-4	X530-N2	[1 HR]
	EC-5	UL X530	[1 HR]
End wall framing line 7	EC-6	UL X530	[1 HR]
	EC-7	UL X530	[1 HR]
	EC-8	X530-N1	[1 HR]
	EC-9	UL X530	[1 HR]
	EC-10	UL X530	[1 HR]

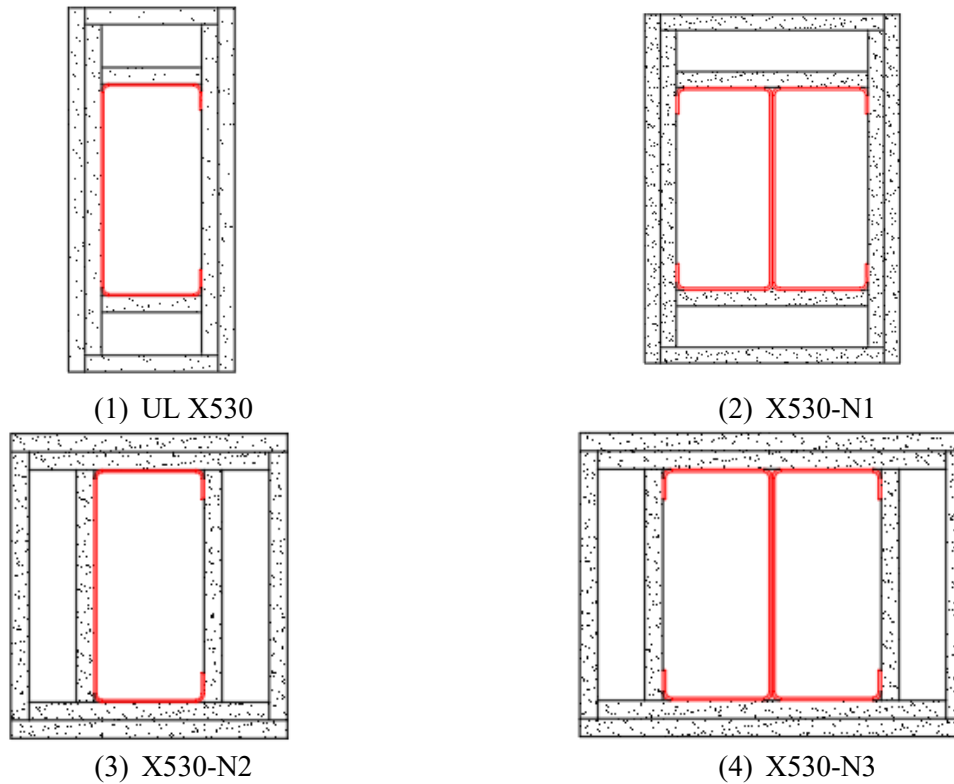


Figure 100 Fire protection assemblies for the columns.

### 7.3.4 Performance objectives

The study focuses on the loadbearing stability of the fire resistance rated members of the end walls of the prototype building. In structural fire engineering analyses, a range of performance objectives may be specified, including specific duration of fire endurance, survival to burnout, up to and

including resiliency and re-use of the structure. For a one-story warehouse building, however, it is normally not deemed economical to design the structure to survive in the unlikely event of a fire. Instead, maintaining stability for the time required for occupants to evacuate and fire brigades to arrive on site and mitigate the risk of spread to adjacent structures, is generally deemed an adequate target.

In this study, the required structural performance is to maintain stability for 1 hour duration of exposure to the design-basis fires which include the ASTM E119 fire [118] as well as natural fires determined through applicable fire models. This objective is selected in consensus with industry representatives and taking into consideration code requirements. The goal of the performance-based fire design is to demonstrate through analysis of the thermal-structural response of the cold-formed steel assemblies that the selected design achieves the abovementioned objective of stability. Alternatively, in a prescriptive setting, the acceptance criterion prescribed in the ASTM E119 standard for fire resistance rating of columns tested without applied loads is a maximum steel average temperature of 1,000 °F (538 °C) or maximum individual temperature of 1,200 °F (649 °C) [118].

### **7.3.5 Design loads**

Loads on the structure and internal forces in the members of the end walls were determined from structural analysis using the applicable load combinations from ASCE 7 [4]. For the fire analysis and design, the load combination for extraordinary events is used. For the end walls of the prototype building, this combination leads to:  $1.2 \text{ Dead} + 1.2 \text{ Collateral} + 0.2 \text{ Snow}$ . (Note: there is no live load generating forces in the end wall structure because the columns support only

a roof). Application of this load combination provides the required strength of the structure and its elements for the Load and Resistance Factor Design (LRFD) [120].

The applied forces in the end wall columns in the fire situation are summarized in Table 44. As can be seen, the columns are only subjected to axial force in the fire situation, which results from the absence of horizontal loads in the combination.

Table 44 Applied design forces for LRFD in the end wall columns under the load combination applicable in the fire situation.

Location	Column	Axial force (kN)	Shear force (kN)	Moment (kN·m)
End wall framing line 1	EC-1	4.0	0	0
	EC-2	13.7	0	0
	EC-3	10.1	0	0
	EC-4	13.7	0	0
	EC-5	4.0	0	0
End wall framing line 7	EC-6	4.0	0	0
	EC-7	13.6	0	0
	EC-8	10.1	0	0
	EC-9	13.6	0	0
	EC-10	4.0	0	0

#### 7.4 Design-basis fires

Besides the standard ASTM E119 fire curve, design-basis fires based on modeling are also considered to assess the fire response of the building structure. The fire modeling software OZone [166] is used to calculate the gas temperature development in the warehouse. OZone relies on the zone model theory, where the differential equations that express the mass balance and the energy balance are numerically integrated on time. The temperature and pressure are considered as spatially uniform in each zone. The amount of combustible material present in the compartment (fuel load), heat release rate (HRR), openings, thermal properties of the boundaries of enclosure, and fire propagation rate are specified as inputs in the model.

To estimate the fuel load in the warehouse, different approaches can be adopted. The fuel load can be evaluated from tabulated data in standards, which provide statistics as a function of the building

occupancy. However, neither Eurocode EN1991-2 [14] nor NFPA 557 [167] report values for storage facilities. The British BS 7974 Part 1 [168] provides values of fuel load density for manufacturing and storage occupancies, with average of  $1,180 \text{ MJ/m}^2$  and the 95% percentile at  $2,690 \text{ MJ/m}^2$ . The large variability reflects the fact that the fuel load in a storage facility depends heavily on the type of content stored. For an existing building, the fuel load can also be measured through surveying [169], but this is not a viable approach in the design stage or when the content is expected to vary significantly over time. Here, the fuel load is conservatively assumed from an estimation of the maximum amount of combustible material that could be stored in the warehouse. This estimation provides an upper bound to evaluate the most severe design-basis fire that could develop in the warehouse. The designer can then decide to adopt a certain quantile of this upper bound to design for a reasonable reliability target.

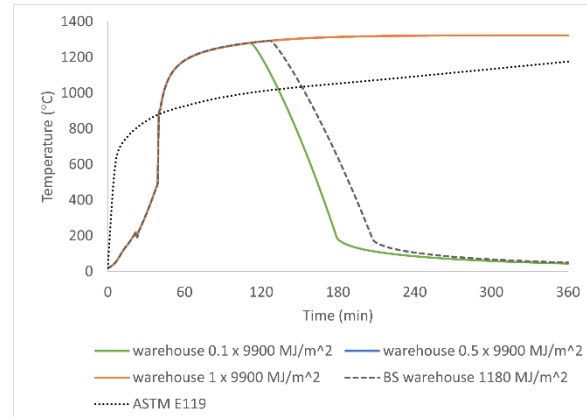
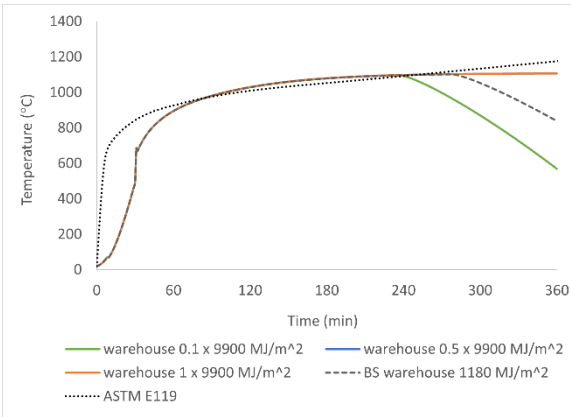
As the warehouse is used for moderate-hazardous materials based on the IBC classification [165], stored content may include books, clothing, or lumber, for example. The calorific value,  $H$ , of these materials is conservatively estimated as  $20 \text{ MJ/kg}$  [170]. The fuel load then depends on the amount of material in the warehouse. The highest possible value is obtained by assuming full efficiency of storage and a packed material, such as stacked wood panels. A utilization ratio of 25% of the warehouse volume is assumed for storage optimization while enabling operation and staff movement. Assuming an average density of  $550 \text{ kg/m}^3$  for cross laminated timber panels, the maximum fuel load density is obtained by multiplying the material volume by its density and calorific value, yielding  $9,900 \text{ MJ/m}^2$ . This should be seen as the highest physically possible value from which design values can be derived. This value is significantly higher than the 95% percentile from the British standard ( $2,690 \text{ MJ/m}^2$ ) and the maximum measured value in a recent office room survey ( $3,451 \text{ MJ/m}^2$ ) [169].

Zone fire models include a wall model that captures the heat transfer between the air of the compartment and the surrounding walls. Herein, the lining material of the walls is 15.9 mm (5/8'') thick gypsum boards. The floor is 101.6 mm (4'') thick normal weight concrete, while the roof structure includes two layers of fiberglass insulation, 203.2 mm (8'') and 88.9 mm (3.5'') thick. Doors and windows are also modeled as zone fire models account for the transfer of mass through the openings.

Parametric analyses are then used to generate a set of design-basis fire curves using OZone. The fuel load is varied from 10% to 100% of the upper bound estimate of  $9,900 \text{ MJ}/\text{m}^2$ . To study the effect of ventilation on fire severity, simulations are run with openings (i.e., doors and windows) either fully open or half-open.

Gas temperature-time curves are plotted in Figure 101. The ASTM E119 fire curve is also shown. The temperatures from the simulated fires follow a similar trend for the heating phase when the fuel load is modified at constant ventilation. Indeed, the heating phase is governed by the fire growth rate and the available oxygen. The fuel load influences the fire duration, with larger fuel loads leading to longer fires. In contrast with the OZone fires, the ASTM E119 curve is a post-flashover curve, which heats up very fast without capturing the incipient and growing phases of the fire. As a result, within the 1-hour duration of interest, the ASTM E119 curve appears more severe than the design-basis fires obtained through modeling. This will be confirmed by modeling the heat transfer in the steel assemblies under the different fires.





(1) Openings at 50% open during the fire

(2) Openings fully open during the fire

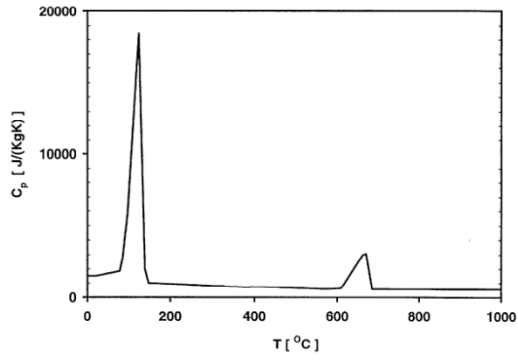
Figure 101 Gas temperature – time curves obtained from fire modeling with OZone for a range of fuel loads and two ventilation conditions.

## 7.5 Thermal response of cold-formed steel columns

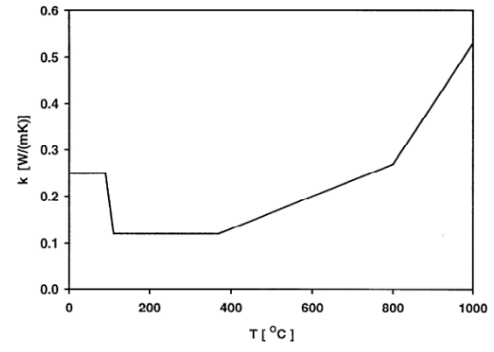
### 7.5.1 Thermal properties

The finite element software SAFIR [99] is used to conduct the thermal analysis using temperature-dependent material properties. Thermal properties of the steel are taken from Eurocode EN1993-1-2 [14].

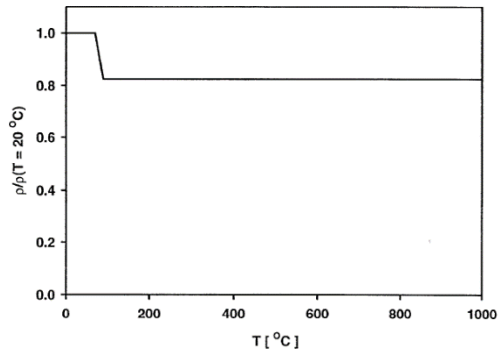
Thermal properties of the Type X gypsum board are based on the research by Cooper [171]. The thermal properties are shown in Figure 102. The properties provided by Cooper originated from Sultan's [172] work at the NRC Canada on Type X boards. The density of the Type X gypsum is taken as  $648 \text{ kg/m}^3$  at ambient temperature.



(1) Specific heat



(2) Thermal conductivity



(3) Density

Figure 102 Thermal properties of Type X gypsum board.

## 7.5.2 Finite element model

The protected columns are modeled using 4 elements across the thickness of each gypsum board layer, as shown in Figure 103. The columns are exposed to the design-basis fires on all 4 sides. The radiation and convection within the cavities of the assemblies are considered. The emissivity of the gypsum board is taken as 0.8. The convective coefficient is taken as  $25 \text{ W/m}^2\text{K}$  for columns subjected to ASTM E119 fire and  $35 \text{ W/m}^2\text{K}$  for those subjected to design-basis fires, according to Eurocode [14].

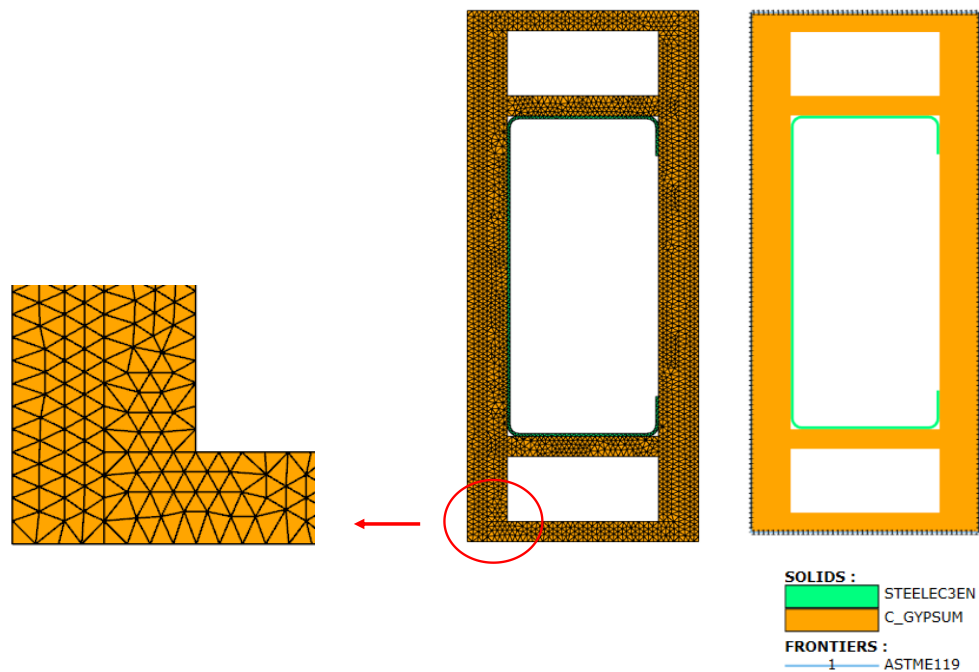


Figure 103 Finite element model of columns subjected to fire on 4 sides.

## 7.5.3 Thermal analysis of the column assemblies

### 7.5.3.1 Subjected to ASTM E119 fire

The temperature distributions of each column assembly at 60 minutes are shown in Figure 104. The temperature in the flange and web of each column at 60 minutes is summarized in Table 45. The temperature in the steel profile is approximately uniform, except a relatively larger

discrepancy is observed in the double C-shaped sections EC-3 and EC-8, where the web heats up more slowly than the flanges due to the geometry.

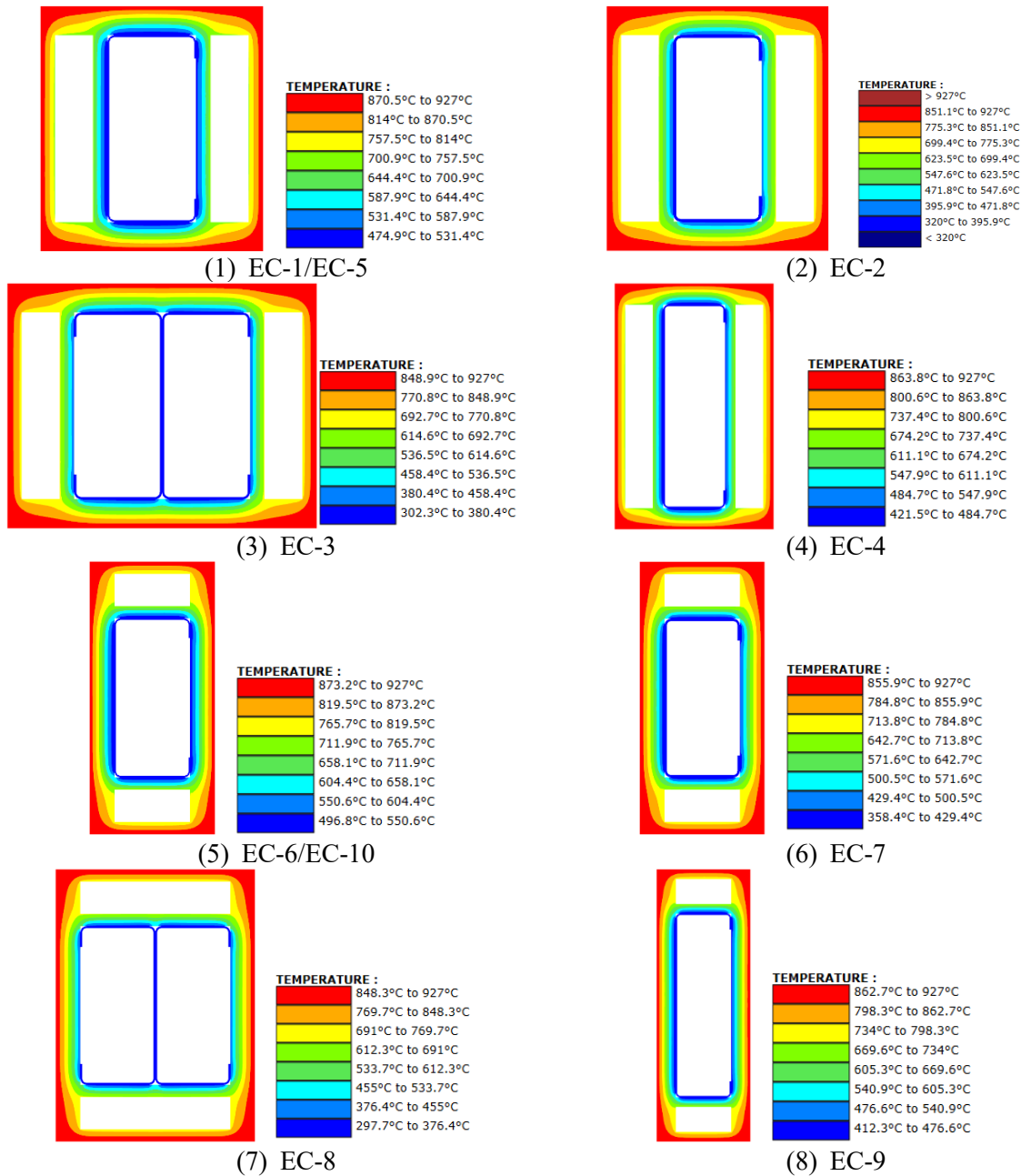


Figure 104 Temperature distribution in the cold-formed steel column assemblies after 60 minutes of exposure to the ASTM E119 fire.

Table 45 Steel temperature in the end wall columns at 60 minutes under ASTM E119 fire.

Location	Column	Flange (°C)	Web (°C)
End wall framing line 1	EC-1	475	478
	EC-2	375	378
	EC-3	347	302
	EC-4	421	426
	EC-5	475	478
End wall framing line 7	EC-6	499	497
	EC-7	397	395
	EC-8	344	297
	EC-9	455	457
	EC-10	499	497

### 7.5.3.2 Subjected to the design-basis fires

Thermal analyses were also conducted considering the design-basis fires obtained from modeling with OZone (Figure 101). However, under these fires, temperatures in the steel remain moderate after 60 minutes of exposure. Table 46 reports the temperatures in the flange and web after 60 minutes of exposure considering the two assumptions on openings. Note that the assumed fuel load does not affect the values at 60 minutes, it only affects the duration of the heating phase thereafter. The effect of these temperatures, below 150 °C, on the capacity is not significant. Comparing Table 45 and Table 46, the ASTM E119 fire results in a more onerous scenario for the fire performance assessment than the design-basis fires derived from modeling. This is because the assessment only considers the first 60 minutes, and the former has a faster rate of temperature increase in the early stage of the time-temperature curve than the latter. Therefore, the mechanical analysis needs only focusing on the steel temperatures resulting from the ASTM E119 fire.

Table 46 Temperature in the end wall columns at 60 minutes under OZone fires. Note: the different considered fuel loads do not affect the temperatures at 60 min.

Location	Column	50% Ventilation		100% Ventilation	
		Flange (°C)	Web (°C)	Flange (°C)	Web (°C)
End wall framing line 1	EC-1	92	91	120	90
	EC-2	92	89	100	88
	EC-3	89	76	99	71
	EC-4	93	89	103	89
	EC-5	92	91	120	90
End wall framing line 7	EC-6	92	92	90	132
	EC-7	88	92	90	105
	EC-8	83	71	86	72
	EC-9	91	96	93	120
	EC-10	92	92	90	132

### 7.5.3.3 Fire rating of the assemblies based on limiting steel temperature under ASTM E119 fire

In this work, the thermal analyses of the assemblies are conducted to evaluate steel temperatures that are then input in a structural model, for an explicit assessment of the structural fire response. However, in prescriptive design, a limiting steel temperature criterion is adopted (during the furnace testing) to determine a standard fire rating. According to the standard, the condition of acceptance is that the rise in average temperature of the steel does not exceed 538 °C (1,000 °F) and the rise in any measured point does not exceed 649 °C (1,200 °F). Comparing the temperatures obtained from analysis with this criterion is informative to evaluate whether the assemblies would pass the prescriptive rating test. Notably, this is interesting for the assemblies that have not been fire-rated through standardized physical testing, as is the case of the double-C shapes used for columns EC-3 and EC-8.

As a parametric numerical analysis, different layers and thickness of Type X gypsum boards were considered for the cold-formed steel columns of the end wall line 7. These included 1 layer of 25.4 mm (1'') gypsum, 2 layers of 12.7 mm (½'') gypsum, 2 layers of 15.9 mm (5/8'') gypsum, 3 layers

of 15.9 mm (5/8'') gypsum, and 2 layers of 25.4 mm (1'') gypsum. The average steel temperatures at 60 minutes under ASTM E119 fire are given in Table 47. The proposed Type X assembly based on UL X530 (i.e., 2 layers of 15.9 mm (5/8'') gypsum) satisfies the limiting temperature criteria as evaluated through thermal analysis for all columns. For the double C-shaped section EC-8, the 1-hour rating can also be achieved using 2 layers of 12.7 mm (1/2'') gypsum. This represents a reduction in the thickness of the gypsum boards as compared with what is required for single C-shaped sections for the same fire rating. This is due to the more favorable section factor of the double C-shaped section, which results in the lower steel temperatures as quantified by the heat transfer analysis.

Table 47 Average steel temperatures (°C) at 60 minutes under ASTM E119 fire in the columns of the end wall line 7 using different fire protection assemblies.

Assembly	1 x 1''	2 x 1/2''	2 x 5/8''	3 x 5/8''	2 x 1''
EC-6/EC-10	716	705	<b>499</b>	87	81
EC-7	620	607	<b>397</b>	82	76
EC-8	556	<b>535</b>	<b>344</b>	70	71
EC-9	671	661	<b>457</b>	85	80

## 7.6 Structural response of cold-formed steel columns

Simple methods and advanced methods of analysis have been proposed for the evaluation of the performance of cold-formed steel structural members at elevated temperatures. Herein, the fire performance of the cold-formed steel columns from the end walls is evaluated with the Direct Strength Method (DSM) as an application of a simple analytical method, and with finite element modeling (FEM), as an application of an advanced numerical method.

## 7.6.1 Analysis by Direct Strength Method/AISI S100

### 7.6.1.1 The Direct Strength Method within AISI S100

The Direct Strength Method (DSM) [11] and AISI S100 [11] is used to assess the loadbearing stability of the columns under fire exposure. For members subjected to uniform and near-uniform temperature distribution, as is the case here, the ambient temperature design capacity rules can be used with reduced mechanical properties at elevated temperature.

The column design rules of DSM that consider the global, local, and distortional buckling at elevated temperatures are shown in Eq. (34).

$$P_{DSM} = \min(P_{ne}, P_{nl}, P_{nd}) \quad (34)$$

where  $P_{ne}$  is the nominal axial strength for overall buckling (i.e., flexural, torsional, or flexural–torsional);  $P_{nl}$  is the nominal axial strength for local buckling; and  $P_{nd}$  is the nominal axial strength for distortional buckling. The DSM is a procedure within the AISI S100 that provides nominal values of the strength. Calculation of each buckling strength in Eq. (34) follows the procedure described in AISI S100. Cross-section properties are calculated from the open-source program CUFSM [149,173]. At elevated temperature, retention factors for the steel properties are used in the DSM equations. Note that for fire design, the nominal strength values are considered as the design strength. The nominal strength calculated with the DSM is compared to the required strength determined from the gravity load combination defined in Section 7.3.5.

### 7.6.1.2 Capacity of the columns at ambient temperature by DSM

The capacities of the columns at ambient temperature evaluated by DSM are given in Table 48. The double C-shaped columns EC-3 and EC-8 were not structurally designed as an interconnected member but as two individual single C-shaped columns. Thus, the listed capacity for EC-3 and



EC-8 is twice that of an individual single C-shaped column. The failure mode at ambient temperature is local buckling for all columns. The load ratio is provided as the ratio between the required strength in the fire situation (see Section 7.3.5) and the available strength (taken as the nominal strength value evaluated by DSM, as the resistance factor is taken as 1.0 for fire design). This load ratio is lower than 10%, meaning the columns have significant reserve in strength at the time the fire starts. It is worth noting that the load combination applicable in a fire as per ASCE 7 does not include wind load, which is the dominant load for column design at ambient temperature. The columns are not oversized for ambient temperature design, but when considering the load combination for the fire situation, the demand over capacity is initially low.

Table 48 Capacity of the columns at ambient temperature as evaluated by DSM.

Location	Columns	DSM (kN)	Load ratio Load <sup>b</sup> / DSM
End wall framing line 1	EC-1/EC-5	93.4 (L <sup>a</sup> )	0.04
	EC-2	202.6 (L)	0.06
	EC-3	140.2 (L)	0.07
	EC-4	161.1 (L)	0.08
End wall framing line 7	EC-6/EC-10	93.4 (L)	0.04
	EC-7	202.6 (L)	0.06
	EC-8	140.2 (L)	0.07
	EC-9	161.1 (L)	0.08

Note: <sup>a</sup>'L' refers to local buckling. <sup>b</sup>'Load' refers to the applied load under load combination applicable in the fire situation (from ASCE 7).

### 7.6.1.3 Capacity of the columns at elevated temperature by DSM

The mechanical properties of the steel decreases at elevated temperature, resulting in lower capacity of the columns in fire. Based on the results of the heat transfer analysis, the temperature in the cross section of the columns is approximately uniform after 60 minutes of exposure to ASTM E119. Accordingly, the steel temperature is assumed as uniform and taken at the maximum value across the steel cross section, as reported in Table 50. The temperature-dependent retention relationships for the mechanical properties of cold-formed steel are adopted from the study in

Chapter 2. These retention factors are given in Eq. (35). Mechanical properties for elastic modulus  $E$ , shear modulus  $G$ , yield stress  $F_y$ , and tensile stress  $F_u$  of cold-formed steels at elevated temperature can be obtained by multiplying the ambient temperature properties by retention factors  $k_E, k_G, k_y, k_u$ , respectively

$$k_E, k_G, k_y, k_u = (1 - c) \frac{1 - x^b}{1 + ax^b} + c \quad (35)$$

where  $x = \frac{T - T_1}{T_2 - T_1}$ ,  $T$  is the steel temperature,  $T_1 = 68 \text{ }^\circ\text{F}$  ( $20 \text{ }^\circ\text{C}$ ),  $T_2 = 1832 \text{ }^\circ\text{F}$  ( $1000 \text{ }^\circ\text{C}$ ), and the coefficients  $a, b, c$  are defined in Table 49.

Table 49 Coefficients for retention factors of steel mechanical properties.

Retention factor	$a$	$b$	$c$
$k_E, k_G$	8	3	0.04
$k_y$	20	4	0.03
$k_u$	185	7	0.04

The retention factors are used in the application of the DSM equations from AISI S100 for evaluating the elevated temperature capacity. The capacity of the columns at 60 minutes under ASTM E119 fire are given in Table 50. The calculations show that the capacity of the columns at 60 minutes is still significantly larger than the demand; the demand-to-capacity ratio does not exceed 15%. As a result, the analysis based on the DSM shows that the 1-hour fire-resistance-rated assemblies for the end wall columns do indeed maintain stability for much longer than 1 hour under fire.

Table 50 Capacity of the columns at 60 minutes subjected to ASTM E119 by DSM.

Location	Columns	Temperature (°C)	DSM (kN)	Load ratio Load <sup>b</sup> / DSM
End wall framing line 1	EC-1/EC-5	478	47.9 (L <sup>a</sup> )	0.09
	EC-2	378	142.3 (L)	0.10
	EC-3	347	106.1 (L)	0.10
	EC-4	426	98.8 (L)	0.14
End wall framing line 7	EC-6/EC-10	499	44.3 (L)	0.09
	EC-7	397	135.0 (L)	0.10
	EC-8	344	106.9 (L)	0.09
	EC-9	457	88.8 (L)	0.15

Note: <sup>a</sup>'L' refers to local buckling. <sup>b</sup>'Load' refers to the applied load under load combination applicable in the fire situation (from ASCE 7).

#### 7.6.1.4 Failure temperature and failure time by DSM

The failure temperature is obtained by searching for the temperature at which the column demand-to-capacity load ratio becomes equal to 1. The procedure is as follows: 1) Input the section temperature; 2) Calculate the resulting retention factors; 3) Calculate the capacity at that temperature with the DSM equations from AISI S100; 4) Evaluate the utilization ratio as demand / capacity; 5) Find the failure temperature by iteratively repeating steps 1-4 until the utilization ratio is equal to 1.0; 6) Find the failure time from the finite element thermal analysis as the time at which the failure temperature is reached.

The failure temperatures and failure times of each column are given in Table 51. The failure temperatures are high at approximately double the steel temperatures reached after 60-minutes of the fire exposure, which results from the low values of the load ratio in Table 50 at that time exposure for these end wall columns. Based on the thermal analysis discussed in Section 7.5, the failure time of a column is taken as the time step when the corresponding column reaches the failure temperature. The failure time of each column is much longer than 60 minutes, indicating that the columns satisfy the fire resistance rating and achieve stability under the ASTM E119 fire

for a least 1 hour. The longest failure times occurred for the double C-shaped columns EC-3 and EC-8, whose loadbearing stability was maintained for more than 2 hours.

Table 51 Failure temperature and failure time by DSM for ASTM E119 fire.

Location	Columns	Failure time (minutes)	Failure temperature (°C)
End wall framing line 1	EC-1/EC-5	116	979
	EC-2	116	911
	EC-3	127	903
	EC-4	101	861
End wall framing line 7	EC-6/EC-10	116	981
	EC-7	116	912
	EC-8	127	904
	EC-9	100	862

## 7.6.2 Analysis by finite element modeling

### 7.6.2.1 Numerical model

The structural stability of the end wall columns is also assessed by finite element modeling, for comparing the results with those of the DSM. Shell finite elements are used in the nonlinear FE software SAFIR [99] to analyze the behavior of the columns under fire exposure. The elements are quadrilateral nonlinear thin shell elements. The length of the columns in the model is 2.286 m (7.5 ft) and the columns are pinned-pinned. The mesh size is  $10\text{ mm} \times 20\text{ mm}$ . The loading is applied through an end plate at the top of the column for uniform distribution of the load. Both global imperfections and local imperfections are included in the model through modification of the initial coordinates of the nodes in the model to give initial deformed shapes that follow the buckling eigenmodes of the columns. An elastic buckling analysis is carried out in Abaqus, and global imperfections are applied according to the deformed shape of the global eigenmode with a maximum magnitude of  $L/1000$  ( $L$  is the unbraced length). Local imperfections are applied according to the web and flange eigenmode for local buckling with a maximum magnitude of

$b/200$  (where  $b$  is the width of the flange for flange eigenmode and the depth of the web for web eigenmode). These local imperfections are scaled to 70% as recommended in the Eurocode EN1993-1-5 for combination of global and local modes [174]. The eigenmodes obtained from Abaqus for the column EC-6 are shown in Figure 105.

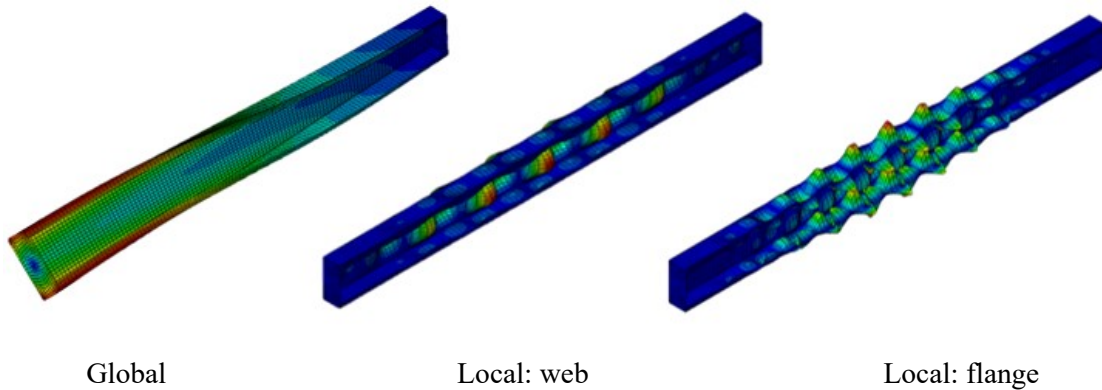


Figure 105 Global and local eigenmodes obtained from elastic buckling analysis in Abaqus.

#### 7.6.2.2 Capacity of the columns at ambient temperature by FE analysis

The capacity of the columns at ambient temperature are evaluated with the FE model by increasing the load to failure. Structural failure is defined as the last converged time step, i.e., failure is deemed to occur when the implicit nonlinear analysis cannot find a stable converged solution. Runaway out-of-plane displacements associated with instability are observed at that time. Results are given in Table 52. These capacities obtained by FE analysis are compared with the capacities obtained by application of the DSM method. The capacity obtained with the two methods agree very well with relative differences of only about 5%. The DSM generally provides slightly lower estimates (conservative) of the ambient temperature capacity than the FE analysis, except for the EC-4 and EC-9 columns, which are deeper open section columns. The deformed shape at failure

of the columns is shown in Figure 106. The columns generally fail by interaction of local and distortional buckling.

Table 52 Capacity of the columns at ambient temperature by FE analysis and DSM.

Location	Columns	DSM (kN)	SAFIR/Shell FE (kN)
End wall framing line 1	EC-1/EC-5	93.4	98.3
	EC-2	202.6	212.9
	EC-3	140.2	149.8
	EC-4	161.1	154.1
End wall framing line 7	EC-6/EC-10	93.4	98.3
	EC-7	202.6	212.9
	EC-8	140.2	149.8
	EC-9	161.1	154.1

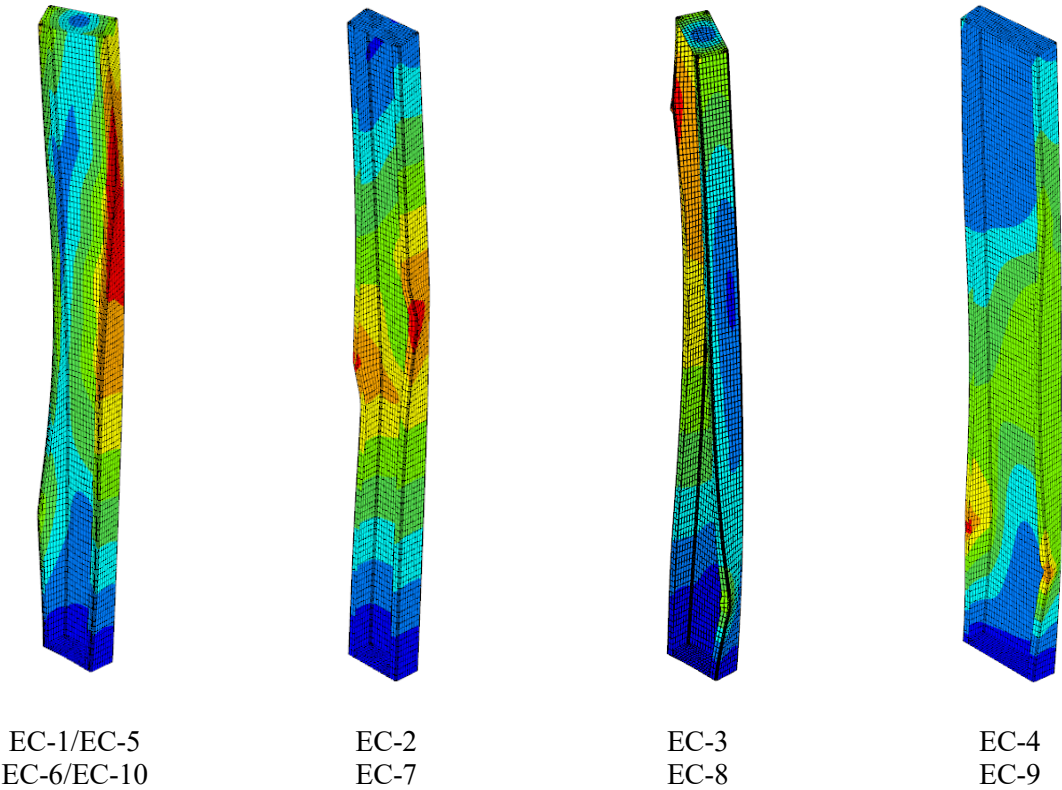


Figure 106 Failure modes of columns at ambient temperature.

### 7.6.2.3 Failure temperature and failure time by FE analysis

The failure time for each column is computed through a transient analysis with the FE model by applying the applicable load under load combination for fire and letting the member temperature increase with time according to the heat transfer analysis results for the ASTM E119 standard fire. SAFIR allows automatic coupling of the heat transfer outputs into the mechanical analysis. Results of failure time and failure temperature are given in Table 53. The results obtained from the FE analysis agree with those obtained from application of the DSM procedure in AISI S100. For EC-1, EC-5, EC-6 and EC-10, the simulation stopped when the member temperature reached 1,000 °C, because this is the upper limit of applicability of the steel mechanical property models from Eq. (35). Therefore, the failure temperatures of these columns are marked as ‘1,000+’. The results from the FE analysis confirm that the end wall columns maintain stability well over 1 hour under the standard fire. As mentioned above, the very high failure temperature obtained in this study results from the application of the load combination from ASCE 7 for the fire situation. As the cold-formed steel columns carry little gravity loads, their load ratio in the fire situation is low, hence their failure temperature is high. This shows the usefulness of explicitly considering the structural response and applicable loading in the fire design, as opposed to the prescriptive method.

Table 53 Failure temperature and failure time by FEM analysis for ASTM E119 fire

Location	Columns	DSM		SAFIR/Shell FE	
		Failure time (min)	Failure temperature (°C)	Failure time (min)	Failure temperature (°C)
End wall framing line 1	EC-1/EC-5	116	979	120+	1,000+
	EC-2	116	911	113	887
	EC-3	127	903	126	899
	EC-4	101	861	98	829
End wall framing line 7	EC-6/EC-10	116	981	120+	1,000+
	EC-7	116	912	112	889
	EC-8	127	904	127	900
	EC-9	100	862	96	830

## **7.7 Verification of the fire performance of the metal steel building end walls**

This chapter has evaluated through analysis the design-basis fires, thermal response, and mechanical response at elevated temperature of the cold-formed steel columns that compose the end walls of a prototype building. The required structural performance for these columns was to maintain loadbearing stability for 1-hour duration of exposure to fire.

The thermal analysis based on finite element modeling has shown that consideration of the ASTM E119 fire led to higher temperatures in the steel members at 60 minutes than other design-basis fires, even with very large values of fuel loads, because the latter had a slower growth phase at the early stage. Therefore, verification of the column stability was made using the ASTM E119 fire. The temperature in the steel remained lower than 500 °C at 60 minutes due to the fire protection. The temperature in the C-shaped steel members is approximately uniform.

The mechanical analysis was performed using two methods: the DSM procedure in AISI S100 and finite element modeling. Both methods demonstrate that the required performance is achieved, i.e., the columns maintain their loadbearing stability for more than 60 minutes of the standard fire exposure. The DSM calculates the nominal strength (capacity) at 60 minutes considering the reduction in steel mechanical properties at high temperatures. The demand-to-capacity ratio between this elevated temperature capacity at 60 minutes and the loading resulting from the applicable load combination from ASCE 7 does not exceed 15%. This is mainly because the applicable load combination for fire does not include wind, and therefore the columns are subjected to low force demands as compared with their capacity. The FE analysis calculates the time of failure for the columns subjected to the applicable loading and the transient temperature increase from the fire. The failure time exceeds 90 minutes for all columns and even reached 2 hours for



half of the columns. This suggests possibility of optimizing the fire protection design strategy for the end wall members in this specific building prototype.

In conclusion, application of the analysis method, i.e., performance-based structural fire engineering approach, to the case of the end wall columns for the prototype building allowed explicitly demonstrating satisfactory performance of the cold-formed steel assemblies. As the design considered some assemblies for which no standard fire rating is available, the approach provided flexibility. The designed column assemblies can maintain stability for over one hour of fire exposure, thereby achieving the performance objective agreed upon for the prototype building.

## **7.8 Conclusions**

A performance-based structural fire analysis was conducted in this chapter to evaluate cold-formed steel assemblies from a prototype one-story warehouse building in the fire situation. The assessment of the performance of the load-bearing column assemblies under elevated temperatures due to fire conditions was presented step-by-step including the definition of performance objectives, design-basis fires, thermal analysis, and structural strength analysis at elevated temperature. This approach of fire design by analysis is included in the newly proposed Appendix 4 to AISI S100 on ‘Structural design for fire condition’ and its application here illustrated the usefulness for cold-formed steel fire design based on a practical case study. The following conclusions are drawn from the study:

- Design-basis fires derived from physically-based zone models may result in severe thermal exposure conditions in a warehouse containing a large amount of fuel. The fuel load influences the fire duration while the ventilation conditions influence the peak gas temperatures. However, as the performance objective focused on the first 60 minutes, the

standard ASTM E119 fire resulted in more onerous thermal exposure than the design-basis fires for this case study, because of the fast initial heating rate of the former. Therefore, consideration of the standard ASTM E119 time-temperature curve was conservative for this study.

- The heat transfer analysis by the FE method of the columns subjected to ASTM E119 fire led to steel temperatures ranging from 315-500 °C after 60 minutes. These results are consistent with the expected performance for the C-shaped cold-formed steel sections protected by gypsum board based on the UL X530 1-hour fire-resistance-rated assembly. As the steel temperature was approximately uniform in the C-shaped columns heated on four faces, assessment of the strength at elevated temperature could rely on ambient temperature methods with the appropriate material reduction factors.
- For a double C-shaped assembly (EC-3 and EC-8) for which no standard fire resistance rating exists, FE thermal analyses showed that the 1-hour fire rating based on the ASTM E119 limiting temperature criteria is achieved with 2 layers of 15.9 mm (5/8") Type X gypsum boards assembled according to the UL X530 assembly. The temperature increase in the double C-shaped member is slower than that in the equivalent single C-shaped member owing to the favorable section factor of the former as compared with the latter. For single C-shaped assemblies with a layout of gypsum boards modified from the qualified assembly UL X530 (EC-2 and EC-4), the FE model showed similar performance as the reference UL X530 assembly. These examples illustrate how the analysis methods can be used to study variations of qualified assemblies to demonstrate performance or determine appropriate adjustments in fire protection.

- For assessing the structural response in fire, the AISI S100 Direct Strength Method was applied and showed that the strength of the columns after 60 minutes of ASTM E119 exposure remains larger than the applied forces resulting from the ASCE 7 load combination for the fire situation. The verification was also made in the time domain by evaluating the failure time for each column, which ranged between 100 minutes and 127 minutes. Finite element analysis with shell elements confirmed the results obtained with the AISI S100 DSM. The failure time and failure temperature obtained with the two methods are close and both methods allow demonstrating achievement of the required performance.
- For this prototype building, the analysis shows that the end wall columns with the UL X530 1-hour fire rating protection could maintain loadbearing stability for significantly longer than 1 hour of ASTM E119 fire exposure. This is because the required strength of the columns determined from the load combination in ASCE/SEI 7 for extraordinary events is much lower than the available strength for these columns for which the design at ambient temperature is governed by wind loads. As a result of the relatively low load ratio in the fire situation, the failure temperature of the columns is larger than the standard limiting steel temperature used in furnace testing. This eventually results in a longer duration of stability. This study thus demonstrates that the fire resistance depends on the applied loading. Most standard fire resistance rated column assemblies have been developed from unloaded test specimens and based on the limiting steel temperatures specified in ASTM E119. Other types of wall, floor, roof and beam assemblies are usually tested with maximum design loads. Therefore, for elements and structures which are lightly loaded in

the fire situation, analysis methods can be used to demonstrate superior performance compared to a given fire resistance rating.

## **Chapter 8    Conclusions and future work**

### **8.1 Summary**

This thesis has presented an extensive investigation into several key aspects of performance-based fire design of cold-formed steel structures made of new high-strength steels. The three main steps of performance-based fire design lie in real fire behavior, accurate thermal analysis, and engineering-based structural analysis and design.

As for the real fire behavior and accurate thermal analysis, the research in this thesis mainly focuses on the effect of localized fire exposure on structures. A numerical modeling strategy has been proposed and validated against experimental data. Application of the modeling strategy on the open car park fires demonstrate the benefits and limitations of simple models and exhibits the potential benefits of advanced numerical analysis for the performance-based design of structure in fire conditions.

As for the engineering-based structural analysis, the thesis explores the elevated temperature and post-fire mechanical properties of conventional and advanced high-strength cold-formed steels. The proposed retention factors combined with the stress-strain relationships lie the foundation of the following structural analysis. With the proposed elevated temperature properties of cold-formed steels, the local buckling behavior of CFS hollow section columns in fire conditions is explored. Finally, the performance-based design framework to evaluate the behavior of cold-formed steel column assemblies taken as part of a realistic cold-formed steel building structure in the fire situation is investigated.

The main contributions of this work satisfy the research objectives established in Chapter 1. The main findings are summarized in this chapter.

Chapter 2 reviewed the current experimental study on the elevated temperature properties of cold-formed steels. Based on the collected data, a simple three-coefficient equation format has been proposed to capture the reduction of mechanical properties of cold-formed steel with temperature. The coefficients were derived from test data. The established relationships are applicable to material grades up to 550 MPa and thickness up to 3.5 mm, at temperatures up to 1000°C.

Chapter 3 presented an experimental investigation on the mechanical properties of cold-formed steels at elevated temperatures. Six steel types were investigated including conventional mild steel Mild-395 and high-strength low-alloy steel HSLA-700 and four types of advanced high-strength steels (AHSS), namely DP-340, DP-700, MS-1030, and MS-1200. Steady-state and transient-state test results show that the mechanical properties of AHSS are significantly influenced by elevated temperatures. Compared with cold-formed steels of lower grade strength, the tested cold-formed AHSS experience larger reduction of properties at elevated temperature, while current design provisions are not applicable to the advanced high-strength steels tested in this research. Thus, predicted models in the same format in Chapter 2 have been proposed to determine the mechanical properties of cold-formed advanced high-strength steels with nominal yield stress up to 1200 MPa at elevated temperatures up to 700 °C.

Chapter 4 presented an experimental investigation on the post-fire mechanical properties of four types of advanced high strength steels (AHSS), namely DP-340, DP-700, MS-1030, and MS-1200. The residual test results show that the temperature exposure affects the shape of the residual stress-strain curve, with post-fire stress-strain curves changing from a gradual shape to a sharp shape with clear yield plateau and yield point after exposure to certain temperatures. The residual elastic

modulus is hardly affected by temperature exposure, while the permanent reduction in strength after exposure to elevated temperature is more severe and starts at lower temperatures for cold-formed steels compared with hot-rolled steels. Thus, predicted models in the same format in Chapter 2 have been proposed to determine the post-fire mechanical properties of advanced high-strength cold-formed steels of the DP and MS types with nominal yield stress up to 700 MPa and 1200 MPa after exposure to temperatures up to 700 °C.

Chapter 5 presented a numerical study on the use of different numerical modeling approaches, based on advanced (CFD) and simple fire models, to predict the temperature in steel members subjected to localized fires. A decision flowchart was proposed to recommend the suitable numerical modeling strategy as a function of the characteristics of the fire and structure. The decision flowchart was validated against test measurements by three case studies. Application study of the proposed decision flowchart was carried out on the temperatures reached in steel framing members subjected to open car park fire scenarios. The application study demonstrated the benefits and limitations of simple models and exhibits the potential benefits of advanced numerical analysis for the performance-based design of structure in fire conditions.

Chapter 6 presented a numerical study on the local buckling behavior of cold-formed steel square and rectangular hollow section columns made of normal and advanced high-strength steels (AHSS) at elevated temperatures. Finite element models were developed and validated against test data from the literature. A parametric study including temperature-dependent mechanical properties generated in Chapter 2 and 3 was conducted on the hollow section columns with various width-to-thickness ratios, plate width ratios, cross section dimensions, and three steel grades (G450, DP-

700, and MS-1200). The ultimate capacities obtained from the numerical modeling were compared with the strengths calculated with the Direct Strength Method (DSM) in AISI S100. Results show that DSM yields higher estimates of the section capacity than the finite element models at ambient and elevated temperatures. Therefore, a modified DSM was proposed for the local buckling capacity of SHS and RHS columns with different steel grades at ambient and elevated temperatures up to 700 °C.

Chapter 7 presented a performance-based structural fire analysis on the cold-formed steel assemblies from a prototype one-story warehouse building in the fire situation. The analysis-based assessment of the cold-formed load-bearing column assemblies at elevated temperatures was reported following the framework of performance-based fire design including definition of performance objectives, design-basis fires, thermal analysis, and structural strength analysis at elevated temperature. The examples illustrate how the analysis methods can be used to study variations of qualified assemblies to demonstrate performance or determine appropriate adjustments in fire protection.

## **8.2 Conclusions and future work**

The following conclusions can be drawn:

- Newly manufactured CFS steels may exhibit different elevated temperature and post-fire response than conventional CFS steels. Therefore, their material properties at elevated temperature and after cooling down need to be tested. New material models are needed and should be made available in building code to enable engineers to adopt them in the design. This thesis demonstrates the testing method and procedure to achieve this.



- With performance-based fire design, engineers should consider realistic fire scenarios. Localized fire scenarios lead to vastly different thermal behavior than standard fires in design codes. While modeling localized fire scenarios is more demanding, it can yield more accurate and often less onerous thermal behavior for the structures. As such, it can offer the opportunity to efficiently allocate fire protection, thereby reduce the carbon and economic costs of the design.
- Simple design methods for CFS members at ambient temperature need to be adapted to account for the elevated temperature effect and the application of new materials. Experimental and numerical work needs to be carried out to validate the simple methods under uniform heating conditions. Research on the effect of thermal gradient is going on to investigate the effect of non-uniform heating. Simple design methods for the structural system at elevated temperatures are also needed to incorporate the impact of thermal induced deformation, forces, and moments.
- Performance-based fire design is still rarely used in CFS design. Yet with this progress in analytical and numerical methods, methodology has been made available to engineers to adopt this approach. It allows a more harmonized and quantified level of safety and the ability to demonstrate equivalency of solutions varying from a reference standard fire rated assembly.

It is suggested that future research for the development of performance-based fire design of cold-formed steel structures should be conducted on the following topics:

- Assessment of structural performance under realistic heating conditions, especially under non-uniform heating conditions or localized fires. The non-uniform heating can result in

the neutral axis shift and thermal bowing. The moments induced by thermal gradient and their second-order effect should be quantified. The DSM method for structures under non-uniform heating conditions should be further investigated.

- Influence of non-linear stress-strain characteristics including nonlinearity between proportional limit stress and yield strength, strain hardening between yield and ultimate strengths on the structural behavior of cold-formed steel members in fire. The stress-strain relationships of CFS at ambient and elevated temperatures may exhibit significant differences. The application of ambient temperature design rules with elevated temperature mechanical properties to predict the behavior of CFS members in fire can be questionable.
- Performance of cold-formed structural systems such as cold-formed steel stud shear wall and cold-formed steel frame under realistic fire conditions. The standard approach for assessing the walls or floors is based on standard fire test which assumes uniform heating conditions. One side heating (structural systems are exposed to fire only on one side) or localized fire exposure can result in significantly different thermal behavior.
- Prediction of the performance of cold-formed steel structures under fire conditions through the application of artificial intelligence and machine learning tools. While experimental tests and finite element analysis can be time consuming and expensive, application of machine learning using dataset of numerical results can provide a powerful and accurate choice for the design of CFS structures in fire conditions.

## References

- [1] American Society of Civil Engineers, Performance-Based Structural Fire Design: Exemplar Designs of Four Regionally Diverse Buildings using ASCE 7-16, Appendix E, Reston, VA, 2020. <https://doi.org/10.1061/9780784482698>.
- [2] N.N. Brushlinsky, M. Ahrens, S. V Sokolov, P. Wagner, World fire statistics, Cent. Fire Stat. 10 (2016).
- [3] J. Zhuang, V.M. Payyappalli, A. Behrendt, K. Lukasiewicz, Total cost of fire in the United States, Fire Protection Research Foundation Buffalo, NY, USA, 2017.
- [4] ASCE/SEI 7-16, Minimum Design Loads for Buildings and Other Structures, ASCE/SEI 7, Structural Engineering Institute of ASCE, Reston, VA, 2013. <https://doi.org/10.1061/9780784412916>.
- [5] R. Kuziak, R. Kawalla, S. Waengler, Advanced high strength steels for automotive industry, Arch. Civ. Mech. Eng. 8 (2008) 103–117.
- [6] S. Keeler, M. Kimchi, Advanced high-strength steels application guidelines V5, WorldAutoSteel, 2015.
- [7] H. Foroughi, B.W. Schafer, Simulation of conventional cold-formed steel sections formed from advanced high strength steel (AHSS), in: Annu. Stab. Conf. Struct. Stab. Res. Counc., San Antonio, TX, 2017.
- [8] X. Yan, J.C.B. Abreu, R.S. Glauz, B.W. Schafer, T. Gernay, Simple Three-Coefficient Equation for Temperature-Dependent Mechanical Properties of Cold-Formed Steels, J. Struct. Eng. 147 (2021) 4021035.
- [9] J. Outinen, P. Mäkeläinen, Mechanical properties of structural steel at elevated temperatures and after cooling down, Fire Mater. 28 (2004) 237–251. <https://doi.org/10.1002/fam.849>.

- [10] T. Ranawaka, M. Mahendran, Experimental study of the mechanical properties of light gauge cold-formed steels at elevated temperatures, *Fire Saf. J.* 44 (2009) 219–229. <https://doi.org/10.1016/j.firesaf.2008.06.006>.
- [11] B.W. Schafer, Review: The Direct Strength Method of cold-formed steel member design, *J. Constr. Steel Res.* 64 (2008) 766–778. <https://doi.org/10.1016/j.jcsr.2008.01.022>.
- [12] AISI S100-16, North American Cold-Formed Steel Specification for the Design of Cold-Formed Steel Structural Members, Washington, DC, 2016.
- [13] Australia Standards, AS/NZS 4600, Cold-Formed Steel Structures, 2005.
- [14] Eurocode 1993-1-2, Eurocode 3: Design of steel structures - Part 1-2: General rules - Structural fire design, Brussels, 2005.
- [15] ASTM A1003/A1003M-15, ASTM A1003 / A1003M - 15 Standard Specification for Steel Sheet, Carbon, Metallic- and Nonmetallic-Coated for Cold-Formed Framing Members, American Society for Testing and Materials, West Conshohocken, USA, 2015. <https://www.astm.org/Standards/A1003.htm> (accessed October 22, 2020).
- [16] ASTM A653/A653M-15, ASTM A653 / A653M - 20 Standard Specification for Steel Sheet, Zinc-Coated (Galvanized) or Zinc-Iron Alloy-Coated (Galvannealed) by the Hot-Dip Process, ASTM International, West Conshohocken, USA, 2015. <https://www.astm.org/Standards/A653> (accessed October 22, 2020).
- [17] ASTM E21, Standard Test Methods for Elevated Temperature Tension Tests of Metallic Materials, American Society for Testing and Materials, West Conshohocken, USA, 2009.
- [18] X. Yan, Y. Xia, H.B. Blum, T. Gernay, Elevated temperature material properties of advanced high strength steel alloys, *J. Constr. Steel Res.* 174 (2020) 106299.
- [19] J.C. Batista Abreu, B.W. Schafer, Fire performance of cold-formed steel walls, 2015.

[http://gateway.library.qut.edu.au/login?url=http://search.proquest.com/docview/1859071359?accountid=13380%0Ahttp://sf5mc5tj5v.search.serialssolutions.com/?ctx\\_ver=Z39.88-2004&ctx\\_enc=info:ofi/enc:UTF-8&rfr\\_id=info:sid/ProQuest+Dissertations+%26+Theses+Glo](http://gateway.library.qut.edu.au/login?url=http://search.proquest.com/docview/1859071359?accountid=13380%0Ahttp://sf5mc5tj5v.search.serialssolutions.com/?ctx_ver=Z39.88-2004&ctx_enc=info:ofi/enc:UTF-8&rfr_id=info:sid/ProQuest+Dissertations+%26+Theses+Glo).

- [20] AISI, North American standard for cold-formed steel structural framing, 2015.
- [21] ASTM E8/E8M-16, Standard Test Methods for Tension Testing of Metallic Materials, ASTM International, West Conshohocken, USA, 2016.
- [22] J. Chen, B. Young, Experimental investigation of cold-formed steel material at elevated temperatures, *Thin-Walled Struct.* 45 (2007) 96–110. <https://doi.org/10.1016/j.tws.2006.11.003>.
- [23] H.D. Craveiro, J.P.C. Rodrigues, A. Santiago, L. Laím, Review of the high temperature mechanical and thermal properties of the steels used in cold formed steel structures - The case of the S280 Gd+Z steel, *Thin-Walled Struct.* 98 (2016) 154–168. <https://doi.org/10.1016/j.tws.2015.06.002>.
- [24] M. Imran, M. Mahendran, P. Keerthan, Mechanical properties of cold-formed steel tubular sections at elevated temperatures, *J. Constr. Steel Res.* 143 (2018) 131–147. <https://doi.org/10.1016/j.jcsr.2017.12.003>.
- [25] N.D. Kankanamge, M. Mahendran, Mechanical properties of cold-formed steels at elevated temperatures, *Thin-Walled Struct.* 49 (2011) 26–44. <https://doi.org/10.1016/j.tws.2010.08.004>.
- [26] A. Landesmann, F.C.M. da Silva, E. de M. Batista, Experimental investigation of the mechanical properties of ZAR-345 cold-formed steel at elevated temperatures, *Mater. Res.* 17 (2014) 1082–1091. <https://doi.org/10.1590/1516-1439.297014>.

- [27] J.H. Lee, M. Mahendran, P. Makelainen, Prediction of mechanical properties of light gauge steels at elevated temperatures, *J. Constr. Steel Res.* 59 (2003) 1517–1532. [https://doi.org/10.1016/S0143-974X\(03\)00087-7](https://doi.org/10.1016/S0143-974X(03)00087-7).
- [28] H.T. Li, B. Young, Material properties of cold-formed high strength steel at elevated temperatures, *Thin-Walled Struct.* 115 (2017) 289–299. <https://doi.org/10.1016/j.tws.2017.02.019>.
- [29] F. McCann, L. Gardner, S. Kirk, Elevated temperature material properties of cold-formed steel hollow sections, *Thin-Walled Struct.* 90 (2015) 84–94. <https://doi.org/10.1016/j.tws.2015.01.007>.
- [30] M. Rokilan, M. Mahendran, Elevated temperature mechanical properties of cold-rolled steel sheets and cold-formed steel sections, *J. Constr. Steel Res.* (2019) 105851. <https://doi.org/10.1016/j.jcsr.2019.105851>.
- [31] S. Shakil, W. Lu, J. Puttonen, Experimental studies on mechanical properties of S700 MC steel at elevated temperatures, *Fire Saf. J.* (2020) 103157. <https://doi.org/10.1016/j.firesaf.2020.103157>.
- [32] J. Ye, W. Chen, Elevated Temperature Material Degradation of Cold-Formed Steels under Steady- and Transient-State Conditions, *J. Mater. Civ. Eng.* 25 (2012) 947–957. [https://doi.org/10.1061/\(asce\)mt.1943-5533.0000640](https://doi.org/10.1061/(asce)mt.1943-5533.0000640).
- [33] M. Seif, J. Main, J. Weigand, F. Sadek, L. Choe, C. Zhang, J. Gross, W. Luecke, D. McColskey, Temperature-Dependent Material Modeling for Structural Steels: Formulation and Application, Gaithersburg, MD, 2016. <https://doi.org/10.6028/NIST.TN.1907>.
- [34] N.E. 1993-1-2/NA, Eurocode 3 - Design of steel structures - Part 1-2 : general rules - Structural fire design - National Annex to NF EN 1993-1-2:2005, (2007).

- <https://www.boutique.afnor.org/standard/nf-en-1993-1-2-na/eurocode-3-design-of-steel-structures-part-1-2-general-rules-structural-fire-design-national-annex-to-nf-en-1993-1-22005-general/article/741913/fa149357> (accessed October 23, 2020).
- [35] Eurocode 1993-1-2, Eurocode 3: Design of Steel Structures - Part 1-2: General Rules – Structural Fire Design, European Committee for Standardization (CEN), Brussels, 2005.
- [36] M. Feng, Y.-C. Wang, J.M. Davies, Axial strength of cold-formed thin-walled steel channels under non-uniform temperatures in fire, *Fire Saf. J.* 38 (2003) 679–707.
- [37] S. Gunalan, M. Mahendran, Finite element modelling of load bearing cold-formed steel wall systems under fire conditions, *Eng. Struct.* 56 (2013) 1007–1027.
- [38] F. Arrais, N. Lopes, P.V. Real, Behaviour and resistance of cold-formed steel beams with lipped channel sections under fire conditions, *J. Struct. Fire Eng.* (2016).
- [39] C. Couto, P.V. Real, Numerical investigation on the influence of imperfections in the local buckling of thin-walled I-shaped sections, *Thin-Walled Struct.* 135 (2019) 89–108.
- [40] AISC 360-16, Specification for Structural Steel Buildings, Chicago, 2016.
- [41] BS 5950-8: 2003, Structural use of steelwork in building—part 8: code of practice for fire resistant design, British Standards Institution (BSI), British Standard BS, 2003.
- [42] Australian Standard 4100, Steel Structures, Australian Standard, Australia, 1998.
- [43] CECS (China Association for Engineering Construction Standardization), Technical specification for stainless steel structure, CECS 410:2, China Planning Press, Beijing, 2015.
- [44] W. Chen, K. Liu, J. Ye, J. Jiang, C. Xu, L. Jin, M. Zhang, High-temperature steady-state experiments on G550 cold-formed steel during heating and cooling stages, *Thin-Walled Struct.* 151 (2020) 106760. <https://doi.org/10.1016/j.tws.2020.106760>.
- [45] ASTM E21, Standard Test Methods for Elevated Temperature Tension Tests of Metallic

- Materials, American Society for Testing and Materials, West Conshohocken, USA, 2009.
- [46] J.D.M. William Luecke, Stephen W. Banovic, High-temperature tensile constitutive data and models for structural steels in fire, NIST Tech. Note 1714. (2011) 137. <https://doi.org/10.1088/1674-1056/22/6/068503>.
- [47] J. Blaber, B. Adair, A. Antoniou, Ncorr: open-source 2D digital image correlation matlab software, *Exp. Mech.* 55 (2015) 1105–1122.
- [48] D. Ba, S. Duy, J.L. Torero, V.T.N. Dao, Application of digital image correlation system for reliable deformation measurement of concrete structures at high temperatures, *Eng. Struct.* 192 (2019) 181–189. <https://doi.org/10.1016/j.engstruct.2019.05.009>.
- [49] Y. Huang, B. Young, The art of coupon tests, *J. Constr. Steel Res.* 96 (2014) 159–175. <https://doi.org/10.1016/j.jcsr.2014.01.010>.
- [50] X. Yan, J.C. Batista Abreu, R.S. Glauz, B.W. Schafer, T. Gernay, Simple three-coefficient equation for temperature dependent mechanical properties of cold-formed steels (Under review), (2020).
- [51] C. Maraveas, Z. Fasoulakis, K.D. Tsavdaridis, Post-fire assessment and reinstatement of steel structures, *J. Struct. Fire Eng.* (2017).
- [52] S. Gunalan, M. Mahendran, Experimental investigation of post-fire mechanical properties of cold-formed steels, *Thin-Walled Struct.* 84 (2014) 241–254. <https://doi.org/10.1016/j.tws.2014.06.010>.
- [53] S. Kesawan, M. Mahendran, Post-fire mechanical properties of cold-formed steel hollow sections, *Constr. Build. Mater.* 161 (2018) 26–36. <https://doi.org/10.1016/j.conbuildmat.2017.11.077>.
- [54] W. Chen, J. Ye, J. Peng, B. Liu, Experimental Investigation of Postfire Mechanical



- Properties of Q345 and G550 Cold-Formed Steel, *J. Mater. Civ. Eng.* 31 (2019) 1–13. [https://doi.org/10.1061/\(ASCE\)MT.1943-5533.0002791](https://doi.org/10.1061/(ASCE)MT.1943-5533.0002791).
- [55] H.T. Li, B. Young, Residual mechanical properties of high strength steels after exposure to fire, *J. Constr. Steel Res.* 148 (2018) 562–571. <https://doi.org/10.1016/j.jcsr.2018.05.028>.
- [56] C. Ren, L. Dai, Y. Huang, W. He, Experimental investigation of post-fire mechanical properties of Q235 cold-formed steel, *Thin-Walled Struct.* 150 (2020) 106651. <https://doi.org/10.1016/j.tws.2020.106651>.
- [57] J. Lu, H. Liu, Z. Chen, X. Liao, Experimental investigation into the post-fire mechanical properties of hot-rolled and cold-formed steels, *J. Constr. Steel Res.* 121 (2016) 291–310. <https://doi.org/10.1016/j.jcsr.2016.03.005>.
- [58] Y. Huang, B. Young, Mechanical properties of lean duplex stainless steel at post-fire condition, *Thin-Walled Struct.* 130 (2018) 564–576. <https://doi.org/10.1016/j.tws.2018.06.018>.
- [59] T.G. Singh, K.D. Singh, Post-fire mechanical properties of YSt-310 cold-formed steel tubular sections, *J. Constr. Steel Res.* 153 (2019) 654–666. <https://doi.org/10.1016/j.jcsr.2018.11.014>.
- [60] ASTM E8M-16, Standard Test Methods for Tension Testing of Metallic Materials, ASTM International, West Conshohocken, PA, 2016.
- [61] X. Qiang, F.S.K. Bijlaard, H. Kolstein, Post-fire mechanical properties of high strength structural steels S460 and S690, *Eng. Struct.* 35 (2012) 1–10. <https://doi.org/10.1016/j.engstruct.2011.11.005>.
- [62] X. Qiang, F.S.K. Bijlaard, H. Kolstein, Post-fire performance of very high strength steel S960, *J. Constr. Steel Res.* 80 (2013) 235–242. <https://doi.org/10.1016/j.jcsr.2012.09.002>.

- [63] S.P. Chiew, M.S. Zhao, C.K. Lee, Mechanical properties of heat-treated high strength steel under fire/post-fire conditions, *J. Constr. Steel Res.* 98 (2014) 12–19. <https://doi.org/10.1016/j.jcsr.2014.02.003>.
- [64] W. Wang, T. Liu, J. Liu, Experimental study on post-fire mechanical properties of high strength Q460 steel, *J. Constr. Steel Res.* 114 (2015) 100–109. <https://doi.org/10.1016/j.jcsr.2015.07.019>.
- [65] E.M. Aziz, V.K. Kodur, Effect of temperature and cooling regime on mechanical properties of high-strength low-alloy steel, *Fire Mater.* 40 (2016) 926–939. <https://doi.org/10.1002/fam.2352>.
- [66] H.U. Sajid, R. Kiran, Influence of stress concentration and cooling methods on post-fire mechanical behavior of ASTM A36 steels, *Constr. Build. Mater.* 186 (2018) 920–945. <https://doi.org/10.1016/j.conbuildmat.2018.08.006>.
- [67] G.Q. Li, H. Lyu, C. Zhang, Post-fire mechanical properties of high strength Q690 structural steel, *J. Constr. Steel Res.* 132 (2017) 108–116. <https://doi.org/10.1016/j.jcsr.2016.12.027>.
- [68] L. Kang, M. Suzuki, H. Ge, B. Wu, Experiment of ductile fracture performances of HSSS Q690 after a fire, *J. Constr. Steel Res.* 146 (2018) 109–121. <https://doi.org/10.1016/j.jcsr.2018.03.010>.
- [69] F. Azhari, A. Heidarpour, X.L. Zhao, C.R. Hutchinson, Mechanical properties of ultra-high strength (Grade 1200) steel tubes under cooling phase of a fire: An experimental investigation, *Constr. Build. Mater.* 93 (2015) 841–850. <https://doi.org/10.1016/j.conbuildmat.2015.05.082>.
- [70] F. Azhari, A.A. Hossain Apon, A. Heidarpour, X.L. Zhao, C.R. Hutchinson, Mechanical response of ultra-high strength (Grade 1200) steel under extreme cooling conditions, *Constr.*

- Build. Mater. 175 (2018) 790–803. <https://doi.org/10.1016/j.conbuildmat.2018.04.191>.
- [71] J.C. Batista Abreu, L.C.M. Vieira, A.L. Moreno, T. Gernay, B.W. Schafer, Experiments on load-bearing cold-formed steel sheathed studs at elevated temperatures, *Thin-Walled Struct.* 156 (2020) 106968. <https://doi.org/10.1016/j.tws.2020.106968>.
- [72] Y. Yu, L. Lan, F. Ding, L. Wang, Mechanical properties of hot-rolled and cold-formed steels after exposure to elevated temperature: A review, *Constr. Build. Mater.* (2019). <https://doi.org/10.1016/j.conbuildmat.2019.04.062>.
- [73] A.A. Khan, A. Usmani, J.L. Torero, Evolution of fire models for estimating structural fire-resistance, *Fire Saf. J.* 124 (2021) 103367. <https://doi.org/10.1016/j.firesaf.2021.103367>.
- [74] B. Jiang, G.Q. Li, A. Usmani, Progressive collapse mechanisms investigation of planar steel moment frames under localized fire, *J. Constr. Steel Res.* 115 (2015) 160–168. <https://doi.org/10.1016/j.jcsr.2015.08.015>.
- [75] J. Alos-Moya, I. Paya-Zaforteza, A. Hospitaler, P. Rinaudo, Valencia bridge fire tests: Experimental study of a composite bridge under fire, *J. Constr. Steel Res.* 138 (2017) 538–554. <https://doi.org/10.1016/j.jcsr.2017.08.008>.
- [76] T. Gernay, A. Gamba, Progressive collapse triggered by fire induced column loss: Detrimental effect of thermal forces, *Eng. Struct.* 172 (2018) 483–496. <https://doi.org/10.1016/j.engstruct.2018.06.060>.
- [77] C. Zhang, H.X. Yu, L. Choe, J. Gross, G.H. Li, Simulating the fire-thermal-structural behavior in a localized fire test on a bare steel beam, *Eng. Struct.* 163 (2018) 61–70. <https://doi.org/10.1016/j.engstruct.2018.02.036>.
- [78] J.M. Franssen, D. Pintea, J.C. Dotreppe, Considering the effects of localised fires in the numerical analysis of a building structure, *Fire Saf. J.* 42 (2007) 473–481.

- <https://doi.org/10.1016/j.firesaf.2007.04.006>.
- [79] L. Jiang, A. Usmani, Computational performance of beam-column elements in modelling structural members subjected to localised fire, *Eng. Struct.* 156 (2018) 490–502. <https://doi.org/10.1016/j.engstruct.2017.11.008>.
- [80] Eurocode 1991-1-2, Eurocode 1: Actions on structures–Part 1-2: General actions–Actions on structures exposed to fire, *Eur. Stand.* (2002).
- [81] N. Tondini, C. Thauvoys, F. Hanus, O. Vassart, Development of an analytical model to predict the radiative heat flux to a vertical element due to a localised fire, *Fire Saf. J.* 105 (2019) 227–243. <https://doi.org/10.1016/j.firesaf.2019.03.001>.
- [82] N. Hua, A. Tessari, N. Elhami-Khorasani, Quantifying Uncertainties in the Temperature–Time Evolution of Railway Tunnel Fires, Springer US, 2021. <https://doi.org/10.1007/s10694-020-01007-8>.
- [83] J. Randaxhe, N. Popa, N. Tondini, Probabilistic fire demand model for steel pipe-racks exposed to localised fires, *Eng. Struct.* 226 (2021) 111310. <https://doi.org/10.1016/j.engstruct.2020.111310>.
- [84] M. Somavilla, N. Tondini, Fire performance of a steel open car park in the light of the recent development of the localised fire model" LOCAFI", (2020).
- [85] C. Fang, B.A. Izzuddin, R. Obiala, A.Y. Elghazouli, D.A. Nethercot, Robustness of multi-storey car parks under vehicle fire, *J. Constr. Steel Res.* 75 (2012) 72–84. <https://doi.org/10.1016/j.jcsr.2012.03.004>.
- [86] X. Dai, L. Jiang, J. Maclean, S. Welch, A. Usmani, A conceptual framework for a design travelling fire for large compartments with fire resistant islands, *Proc. 14th Int. Interflam Conf.* (2016) 1039–1050.

- [87] Q. Guo, K.J. Root, A. Carlton, S.E. Quiel, C.J. Naito, Framework for rapid prediction of fire-induced heat flux on concrete tunnel liners with curved ceilings, *Fire Saf. J.* 109 (2019) 102866. <https://doi.org/10.1016/j.firesaf.2019.102866>.
- [88] G. Heskestad, Engineering relations for fire plumes, *Fire Saf. J.* 7 (1984) 25–32. [https://doi.org/10.1016/0379-7112\(84\)90005-5](https://doi.org/10.1016/0379-7112(84)90005-5).
- [89] A. Pchelintsev, Y. Hasemi, T. Wakamatsu, Y. Yokobayashi, Experimental and numerical study on the behaviour of a steel beam under ceiling exposed to a localized fire, *Fire Saf. Sci.* 5 (1997) 1153–1164.
- [90] K. McGrattan, S. Hostikka, R. McDermott, J. Floyd, C. Weinschenk, K. Overholt, Fire dynamics simulator user's guide, NIST Spec. Publ. 1019 (2013).
- [91] N. Johansson, M. Ekholm, Variation in Results Due to User Effects in a Simulation with FDS, *Fire Technol.* 54 (2018) 97–116. <https://doi.org/10.1007/s10694-017-0674-y>.
- [92] U. Wickström, D. Duthinh, K. McGrattan, Adiabatic surface temperature for calculating heat transfer to fire exposed structures, in: *Proc. Elev. Int. Interflam Conf. Intersci. Commun.* London, 2007.
- [93] J. Alos-Moya, I. Paya-Zaforteza, M.E.M. Garlock, E. Loma-Ossorio, D. Schiffner, A. Hospitaler, Analysis of a bridge failure due to fire using computational fluid dynamics and finite element models, *Eng. Struct.* 68 (2014) 96–110. <https://doi.org/10.1016/j.engstruct.2014.02.022>.
- [94] S. Šulc, V. Šmilauer, B. Patzák, K. Cábová, F. Wald, Linked simulation for fire-exposed elements using CFD and thermo-mechanical models, *Adv. Eng. Softw.* 131 (2019) 12–22. <https://doi.org/10.1016/j.advengsoft.2019.02.007>.
- [95] C. Zhang, J.G. Silva, C. Weinschenk, D. Kamikawa, Y. Hasemi, *Simulation Methodology*

- for Coupled Fire-Structure Analysis: Modeling Localized Fire Tests on a Steel Column, *Fire Technol.* 52 (2016) 239–262. <https://doi.org/10.1007/s10694-015-0495-9>.
- [96] J. Alos-Moya, I. Paya-Zaforteza, A. Hospitaler, E. Loma-Ossorio, Valencia bridge fire tests: Validation of simplified and advanced numerical approaches to model bridge fire scenarios, *Adv. Eng. Softw.* 128 (2019) 55–68. <https://doi.org/10.1016/j.advengsoft.2018.11.003>.
- [97] K. Prasad, H.R. Baum, Fire Structure Interface and Thermal Response of the World Trade Center Towers, US Department of Commerce, Technology Administration, National Institute of ..., 2005.
- [98] A. DeSimone, A.E. Jeffers, Best practices for modeling structural boundary conditions due to a localized fire, *Fire Mater.* 44 (2020) 409–422. <https://doi.org/10.1002/fam.2774>.
- [99] J.-M. Franssen, T. Gernay, Modeling structures in fire with SAFIR®: Theoretical background and capabilities, *J. Struct. Fire Eng.* (2017).
- [100] O. Vassart, A. Morbioli, N. Tondini, J.-M. Franssen, S. Lechêne, An integrated modelling strategy between a CFD and an FE software, *J. Struct. Fire Eng.* 7 (2017) 217–233. <https://doi.org/10.1108/jsfe-09-2016-015>.
- [101] M. Charlier, A. Glorieux, X. Dai, N. Alam, S. Welch, J. Anderson, O. Vassart, A. Nadjai, Travelling fire experiments in steel-framed structure: numerical investigations with CFD and FEM, *J. Struct. Fire Eng.* (2021). <https://doi.org/10.1108/JSFE-11-2020-0034>.
- [102] C. Brasseur, M; Zaharia, R; Obiala, R; Franssen, J. M; Hanus, F; Zhao, B; Pintea, D; Sanghoon, H; Vassart, O; Nadjai, A; Scifo, A; Thauvoye, Temperature assessment of a vertical steel member subjected to localised fire (LOCAFI), 2017. <https://doi.org/10.2777/67601>.
- [103] N. Tondini, O. Vassart, J.-M. Franssen, Development of an interface between CFD and FE

- software, in: Proc. 7th Int. Conf. Struct. Fire, ETH Zürich, 2012: pp. 459–468.
- [104] L. Choe, L. Choe, S. Ramesh, M. Hoehler, M. Seif, J. Gross, C. Zhang, M. Bundy, National fire research laboratory commissioning project: testing steel beams under localized fire exposure, US Department of Commerce, National Institute of Standards and Technology, 2018.
- [105] ASTM A490-14a, Standard Specification for Structural Bolts, Alloy Steel, Heat Treated, 150 ksi Minimum Tensile Strength, West Conshohocken, PA, 2012.  
[https://doi.org/10.1520/A0992\\_A0992M-11](https://doi.org/10.1520/A0992_A0992M-11).
- [106] ASTM A325-10e1, Standard Specification for Structural Bolts, Steel, Heat Treated, 120/105 ksi Minimum Tensile Strength, West Conshohocken, PA, 2010.  
<https://doi.org/10.1520/A0325>.
- [107] K. McGrattan, S. Hostikka, J. Floyd, R. McDermott, M. Vanella, Fire dynamics simulator Validation Guide :, 2006.  
<https://nvlpubs.nist.gov/nistpubs/Legacy/SP/nistspecialpublication1018.pdf>.
- [108] C. Zhang, G.Q. Li, R. Wang, Using adiabatic surface temperature for thermal calculation of steel members exposed to localized fires, *Int. J. Steel Struct.* 13 (2013) 547–556.  
<https://doi.org/10.1007/s13296-013-3013-2>.
- [109] N. Tondini, J.M. Franssen, Analysis of experimental hydrocarbon localised fires with and without engulfed steel members, *Fire Saf. J.* 92 (2017) 9–22.  
<https://doi.org/10.1016/j.firesaf.2017.05.011>.
- [110] Fire Safety of Steel Structures. European Convention for Constructional Steelwork. Technical Committee 3, Fire Safety in Open Car Parks: Modern Fire Engineering, in: European Convention for Constructional Steelwork, 1993.

- [111] B. Zhao, M. Roosefid, Guide pour la vérification du comportement au feu de parcs de stationnement largement ventilés en superstructure métallique, CTICM document (SRI – 11/110h– MR-BZ/NB), 2014.
- [112] D. Joyeux, J. Kruppa, L.-G. Cajot, J.-B. Schleich, P. Van De Leur, L. Twilt, Demonstration of real fire tests in car parks and high buildings, EUR. (2002) 1–171.
- [113] C. Cwiklinski, Parcs de Stationnement en Superstructure Large Ment ventilés–Avis d’expertsur les scénariosd’incendie, Rapp. Final. INERIS DRA-CCw/MCh-2001-Cgr22984. (2001) 26.
- [114] X. Yan, T. Gernay, Numerical modeling of localized fire exposures on structures using FDS-FEM and simple models, Eng. Struct. 246 (2021) 112997. <https://doi.org/10.1016/j.engstruct.2021.112997>.
- [115] X. Deckers, S. Haga, N. Tilley, B. Merci, Smoke control in case of fire in a large car park: CFD simulations of full-scale configurations, Fire Saf. J. 57 (2013) 22–34. <https://doi.org/10.1016/j.firesaf.2012.02.005>.
- [116] D. Joyeux, J. Kruppa, L.G. Cajot, J.B. Schleich, P. van de Leur, L. Twilt, Demonstration of real fire tests in car parks and high buildings, European Commission, 2002.
- [117] X. Yan, T. Gernay, Structural fire design of load-bearing cold-formed steel assemblies from a prototype metal building, Structures. (2022).
- [118] ASTM E119-18c, Standard test methods for fire tests of building construction and materials, West Conshohocken, PA, 2018.
- [119] S. Gunalan, Y. Bandula Heva, M. Mahendran, Local buckling studies of cold-formed steel compression members at elevated temperatures, J. Constr. Steel Res. 108 (2015) 31–45. <https://doi.org/10.1016/j.jcsr.2015.01.011>.



- [120] M. Balarupan, Structural behaviour and design of cold-formed steel hollow columns under simulated fire conditions, PhD Thesis, Thesis. (2015).
- [121] P.W. Key, S.W. Hasan, G.J. Hancock, Column behavior of cold-formed hollow sections, *J. Struct. Eng.* 114 (1988) 390–407.
- [122] X. Meng, L. Gardner, Behavior and Design of Normal- and High-Strength Steel SHS and RHS Columns, *J. Struct. Eng.* 146 (2020) 04020227. [https://doi.org/10.1061/\(asce\)st.1943-541x.0002728](https://doi.org/10.1061/(asce)st.1943-541x.0002728).
- [123] H. Fang, T.M. Chan, B. Young, Structural performance of cold-formed high strength steel tubular columns, *Eng. Struct.* 177 (2018) 473–488. <https://doi.org/10.1016/J.ENGSTRUCT.2018.09.082>.
- [124] J.L. Ma, T.M. Chan, B. Young, Cold-formed high strength steel tubular beam-columns, *Eng. Struct.* 230 (2021) 111618. <https://doi.org/10.1016/j.engstruct.2020.111618>.
- [125] E. Ellobody, B. Young, Structural performance of cold-formed high strength stainless steel columns, *J. Constr. Steel Res.* 61 (2005) 1631–1649. <https://doi.org/10.1016/j.jcsr.2005.05.001>.
- [126] B.W. Schafer, Advances in the Direct Strength Method of cold-formed steel design, *Thin-Walled Struct.* 140 (2019) 533–541. <https://doi.org/10.1016/j.tws.2019.03.001>.
- [127] A. Mohammed, S. Afshan, Numerical modelling and fire design of stainless steel hollow section columns, *Thin-Walled Struct.* 144 (2019) 106243. <https://doi.org/10.1016/j.tws.2019.106243>.
- [128] A.D. Martins, R. Gonçalves, D. Camotim, Numerical simulation and design of stainless steel columns under fire conditions, *Eng. Struct.* 229 (2021). <https://doi.org/10.1016/j.engstruct.2020.111628>.

- [129] F. Arrais, N. Lopes, P.V. Real, Numerical study of fire resistance of stainless steel circular hollow section columns, *J. Fire Sci.* 38 (2020) 156–172. <https://doi.org/10.1177/0734904119888823>.
- [130] M. Rokilan, M. Mahendran, Effects of nonlinear elevated temperature stress-strain characteristics on the global buckling capacities of cold-formed steel columns, *Thin-Walled Struct.* 160 (2021). <https://doi.org/10.1016/j.tws.2020.107352>.
- [131] C. Couto, T. Coderre, P. Vila Real, N. Boissonnade, Cross-section capacity of RHS and SHS at elevated temperatures: Comparison of design methodologies, *Structures.* 34 (2021) 198–214. <https://doi.org/10.1016/j.istruc.2021.07.072>.
- [132] C. Couto, P.V. Real, N. Lopes, B. Zhao, Effective width method to account for the local buckling of steel thin plates at elevated temperatures, (2014). <https://doi.org/10.1016/j.tws.2014.06.003>.
- [133] Y. Zhong, Y. Sun, O. Zhao, L. Gardner, Structural Response and Residual Capacity of S700 High-Strength Steel CHS Columns after Exposure to Elevated Temperatures, *J. Struct. Eng.* 148 (2022) 4022050.
- [134] Y. Huang, B. Young, Finite element analysis of cold-formed lean duplex stainless steel columns at elevated temperatures, *Thin-Walled Struct.* 143 (2019) 106203. <https://doi.org/10.1016/j.tws.2019.106203>.
- [135] N. Tondini, B. Rossi, J.M. Franssen, Experimental investigation on ferritic stainless steel columns in fire, *Fire Saf. J.* 62 (2013) 238–248. <https://doi.org/10.1016/j.firesaf.2013.09.026>.
- [136] J. Chen, B. Young, Cold-formed steel lipped channel columns at elevated temperatures, *Eng. Struct.* 29 (2007) 2445–2456. <https://doi.org/10.1016/j.engstruct.2006.12.004>.

- [137] D. Talamona, J.-M. Franssen, A quadrangular shell finite element for concrete and steel structures subjected to fire, *J. Fire Prot. Eng.* 15 (2005) 237–264.
- [138] D. Talamona, L. Lim, J.-M. Franssen, Validation of a shell finite element for concrete and steel structures subjected to fire, in: *Proc. 4th Int. Semin. Fire Explos. Hazards*", Universities Press, 2004: pp. 577–588.
- [139] N. Lopes, P. Vila Real, L. Simões da Silva, J.-M. Franssen, Numerical modelling of thin-walled stainless steel structural elements in case of fire, *Fire Technol.* 46 (2010) 91–108.
- [140] J.-M. Franssen, B. Zhao, T. Gernay, Experimental tests and numerical modelling on slender steel columns at high temperatures, *J. Struct. Fire Eng.* (2016).
- [141] C. Couto, P.V. Real, N. Lopes, B. Zhao, Numerical investigation of the lateral–torsional buckling of beams with slender cross sections for the case of fire, *Eng. Struct.* 106 (2016) 410–421.
- [142] J. Ferreira, T. Gernay, J. Franssen, O. Vassant, Discussion on a systematic approach to validation of software for structures in fire-Romeiro Ferreira Joao Daniel, in: *SiF 2018 10th Int. Conf. Struct. Fire*, Belfast, 2018.
- [143] S. Ni, X. Yan, M.S. Hoehler, T. Gernay, Numerical modeling of the post-fire performance of strap-braced cold-formed steel shear walls, *Thin-Walled Struct.* 171 (2022) 108733. <https://doi.org/10.1016/j.tws.2021.108733>.
- [144] B.W. Schafer, T. Peköz, Computational modeling of cold-formed steel: Characterizing geometric imperfections and residual stresses, *J. Constr. Steel Res.* 47 (1998) 193–210. [https://doi.org/10.1016/S0143-974X\(98\)00007-8](https://doi.org/10.1016/S0143-974X(98)00007-8).
- [145] D. Systèmes, Abaqus analysis user's manual, Simulia Corp. Provid. RI, USA. 40 (2007).
- [146] P.W. Key, G.J. Hancock, A theoretical investigation of the column behaviour of cold-

- formed square hollow sections, *Thin-Walled Struct.* 16 (1993) 31–64.  
[https://doi.org/10.1016/0263-8231\(93\)90040-H](https://doi.org/10.1016/0263-8231(93)90040-H).
- [147] J.L. Ma, T.M. Chan, B. Young, Material properties and residual stresses of cold-formed high strength steel hollow sections, *J. Constr. Steel Res.* 109 (2015) 152–165.  
<https://doi.org/10.1016/j.jcsr.2015.02.006>.
- [148] L. Gardner, R.B. Cruise, Modeling of Residual Stresses in Structural Stainless Steel Sections, *J. Struct. Eng.* 135 (2009) 42–53. [https://doi.org/10.1061/\(asce\)0733-9445\(2009\)135:1\(42\)](https://doi.org/10.1061/(asce)0733-9445(2009)135:1(42)).
- [149] Z. Li, B.W. Schafer, Buckling analysis of cold-formed steel members with general boundary conditions using CUFSM conventional and constrained finite strip methods, (2010).
- [150] C. Couto, P. Vila Real, N. Lopes, B. Zhao, Resistance of steel cross-sections with local buckling at elevated temperatures, *J. Constr. Steel Res.* 109 (2015) 101–114.  
<https://doi.org/10.1016/j.jcsr.2015.03.005>.
- [151] R.Q. Bridge, M.D. O’Shea, Behaviour of thin-walled steel box sections with or without internal restraint, *J. Constr. Steel Res.* 47 (1998) 73–91. [https://doi.org/10.1016/S0143-974X\(98\)80103-X](https://doi.org/10.1016/S0143-974X(98)80103-X).
- [152] Winter\_1952.pdf, (n.d.).
- [153] T. Peköz, Development of a unified approach to the design of cold-formed steel members (Draft), (1986).
- [154] A. Shahbazian, Y.C. Wang, Calculating the global buckling resistance of thin-walled steel members with uniform and non-uniform elevated temperatures under axial compression, *Thin-Walled Struct.* 49 (2011) 1415–1428.
- [155] J.C.B. Abreu, L.M.C. Vieira, M.H. Abu-Hamd, B.W. Schafer, development of

- performance-based fire design for cold-formed steel, *Fire Sci. Rev.* 3 (2014) 1–15.
- [156] L. Laím, J.P.C. Rodrigues, Fire design methodologies for cold-formed steel beams made with open and closed cross-sections, *Eng. Struct.* 171 (2018) 759–778. <https://doi.org/10.1016/j.engstruct.2018.06.030>.
- [157] A. Shahbazian, Y.C. Wang, Direct Strength Method for calculating distortional buckling capacity of cold-formed thin-walled steel columns with uniform and non-uniform elevated temperatures, *Thin-Walled Struct.* 53 (2012) 188–199.
- [158] J.H. Zhu, B. Young, Design of cold-formed steel oval hollow section columns, *J. Constr. Steel Res.* 71 (2012) 26–37. <https://doi.org/10.1016/j.jcsr.2011.11.013>.
- [159] X. Yun, X. Meng, L. Gardner, Design of cold-formed steel SHS and RHS beam–columns considering the influence of steel grade, *Thin-Walled Struct.* (2021) 108600. <https://doi.org/10.1016/j.tws.2021.108600>.
- [160] T. Ranawaka, M. Mahendran, Distortional buckling tests of cold-formed steel compression members at elevated temperatures, *J. Constr. Steel Res.* 65 (2009) 249–259. <https://doi.org/10.1016/j.jcsr.2008.09.002>.
- [161] S. Gunalan, Y.B. Heva, M. Mahendran, Flexural-torsional buckling behaviour and design of cold-formed steel compression members at elevated temperatures, *Eng. Struct.* 79 (2014) 149–168. <https://doi.org/10.1016/j.engstruct.2014.07.036>.
- [162] Y. Tao, M. Mahendran, A. Ariyanayagam, Numerical study of LSF walls made of cold-formed steel hollow section studs in fire, *Thin-Walled Struct.* 167 (2021) 108181. <https://doi.org/10.1016/j.tws.2021.108181>.
- [163] ISO 24679-1:2019 International Organization for Standardization, Fire Safety Engineering – Performance of Structures in Fire – Part 1, General, Geneva, Switzerland, 2019.

- [164] T. Gernay, N.E. Khorasani, Recommendations for performance-based fire design of composite steel buildings using computational analysis, *J. Constr. Steel Res.* 166 (2020) 105906.
- [165] International Code Council, *International Building Code*, Brea, CA, 2018.
- [166] J.-F. Cadorin, J.-M. Franssen, A tool to design steel elements submitted to compartment fires—OZone V2. Part 1: pre-and post-flashover compartment fire model, *Fire Saf. J.* 38 (2003) 395–427.
- [167] NFPA 557, *Standard for determination of fire loads for use in structural fire protection design*, 2020th ed., 2012.
- [168] BSI, BS 7974:2019 *Application of fire safety engineering principles to the design of buildings*, BSI, London, 2019.
- [169] N. Elhami-Khorasani, J.G.S. Castillo, E. Saula, T. Josephs, G. Nurlybekova, T. Gernay, Application of a digitized fuel load surveying methodology to office buildings, *Fire Technol.* 57 (2021) 101–122.
- [170] N. Elhami-Khorasani, J.G. Salado Castillo, T. Gernay, A digitized fuel load surveying methodology using machine vision, *Fire Technol.* 57 (2021) 207–232.
- [171] L.Y. Cooper, *The Thermal Response of Gypsum-panel/steel-stud Wall Systems Exposed to Fire Environments: A Simulation for Use in Zone-type Fire Models*, US Department of Commerce, Technology Administration, National Institute of Standards and Technology, 1997.
- [172] M.A. Sultan, A model for predicting heat transfer through noninsulated unloaded steel-stud gypsum board wall assemblies exposed to fire, *Fire Technol.* 32 (1996) 239–259.
- [173] B.W. Schafer, S. Ádány, Buckling analysis of cold-formed steel members using CUFSM:

conventional and constrained finite strip methods, in: Eighteenth Int. Spec. Conf. Cold-Formed Steel Struct. Orlando, FL, Citeseer, 2006.

[174] Eurocode 1993-1-5 CEN, Eurocode 3 - Design of steel structures - Part 1-5: Plated structural elements, 2006.